3D RADIATIVE TRANSFER MODELING OF EMBEDDED PROTOSTELLAR REGIONS

STEFFEN KJÆR JACOBSEN

Dissertation submitted for the degree of

PHILOSOPHIÆ DOCTOR

Centre for Star and Planet Formation
Niels Bohr Institute & Natural History Museum of Denmark
Faculty of Science
University of Copenhagen

This thesis has been submitted to the PhD School of The Faculty of Science, University of Copenhagen

Title	3D Radiative Transfer Modeling of Embedded Protostellar Regions,
Author	Steffen Kjær Jacobsen
Date of Submission	16 April, 2018
Department	Centre for Star and Planet Formation, Niels Bohr Institute & Natural History Museum of Denmark, Faculty of Science, University of Copenhagen
Academic Advisor	Assoc. Prof. Jes Kristian Jørgensen

Typeset using the Palatino and Euler type faces by Hermann Zapf
Layout and typography by the author with $\LaTeX 2_\varepsilon$ using the class "classicthesis" developed by André Miede
Cover:

To friends and family

ENGLISH ABSTRACT

The formation of stars and planetary systems is a physical as well as a chemical process. Through decades of research, our understanding of star formation has greatly improved, though many aspects are still unknown or heavily debated. Stable, rotationally supported disks of gas and dust around protostars are routinely observed in the intermediate and later stages of star formation. However, the exact details of how early and how they form, are still open questions. Concurrently with these issues, Complex Organic Molecules (COMs), and even prebiotic molecules such as simple sugars, have been observed in the gas phase of early, protostellar cores. Their exact formation route and the physical origin of their arrival to the gas phase are heavily debated. It is not known if the observed COMs are linked to the warm disk atmosphere of settled protoplanetary disks, or if they predominantly exist in the gas phase in the warmest, inner regions of protostellar cores, before the emergence of a protoplanetary disk. These questions are important, as the protostellar chemistry acts as a chemical precursor for the composition of the material that ends up in planet formation, and may explain the rich chemistry we see in our own Solar System. Using high angular resolution observations with the Atacama Large Millimeter/submillimeter Array (ALMA), together with complex 3D radiative transfer codes, we can investigate the innermost environment of young protostars, and hopefully answer some of the questions stated above.

In this thesis I present research focusing on the two low-mass protostellar cores, IRAS 16293-2422 and L483, in terms of their dust and gas density, temperature structures, and chemistries. Two of the three research papers presented in this thesis concentrate on IRAS 16293-2422, with one focusing on the 3D modeling of the envelope, the bridge of dust and gas conjoining the two protostars, and the disk-like emission around each protostar, as well as their individual luminosities. A 3D dust density model is presented, which morphologically matches the 868 μm continuum emission and explains the observed $C^{17}O$ emission through a jump abundance model. This model emulates freeze-out of molecules upon the dust grains, when the temperature drops beneath the sublimation temperature of CO on the dust ice-mantles. The individual luminosities of the deeply embedded protostars in IRAS 16293-2422 are found to be $L_A \geqslant 18\ L_\odot$ and $L_B \leqslant 3\ L_\odot$, for radiation source A and B, respectively, which presents the first estimation of the individual luminosities.

The second research paper on IRAS 16293-2422 focuses on the outflows and the kinematics of the observed gas line emission from the

different molecules in the gas phase, and their relation to the bridge of dust and gas. Molecular gas line emission of CO, H_2CO, HCN, CS, SiO and C_2H reveal that only the dust continuum and $C^{17}O$ emission have a physical origin in the bridge of dust and gas, while all other molecular transitions are found to be related to the outflows emanating from radiation source A. The lack of outflow activity from radiation source B leads us to conclude that it is likely on a lower evolutionary stage than radiation source A.

The last research paper describes $\sim 0.1''$ observations of L483 with ALMA, which reveal that the COMs observed towards L483 reside in the innermost hot region of the envelope, within 40–60 au of the central protostar, and arise from thermal sublimation of the icy mantle around the dust grains. By analyzing the kinematics of the $H^{13}CN$ J = 4–3 and CS J =7–6 gas line emission, the presence of a Keplerian disk is excluded down to at least a 15 au radius. This means that the observed COMs cannot come from an abrupt transition region between the collapsing envelope and a Keplerian disk, as hypothesized by an earlier research team, or from a warm disk atmosphere. Within 15 au, a small Kepler disk could hypothetically reside.

Suggestions are made for future research projects targeting IRAS 16293-2422 and L483, to further constrain the spatial distribution of COMs (which constrains their formation routes), and the timeline for the emergence of protoplanetary disks.

DANSK RESUMÉ

Dannelsen af stjerner er en fysisk, såvel som en kemisk proces. Takket være åtiers forskning er vores forståelse af stjernedannelse blevet betragteligt bedre på trods af, at mange aspekter stadig er ukendte eller omdiskuterede. Stabile, rotationelt understøttede protoplanetariske skiver af støv og gas omkring protostjerner bliver rutinemæssigt observeret i de mellemste og sene stadier af stjernedannelse. Dog er de præcise detaljer omkring, hvordan og hvor tidligt de dannes, stadig åbne spørgsmål. Samtidig med disse problemer, så er komplekse organiske molekuler (KOMs) og selv prebiotiske molekyler såsom simple slags sukker, blevet observeret i gasfasen i tidlige protostellare kerner. Deres præcise formationsrute og den fysiske mekanisme bag deres ankomst til gasfasen, er kraftigt debateret. Det vides ikke, om de observerede KOMs er tilstede i den varme atmosfære af en flad protoplanetarisk skive, eller om de mestendels eksisterer i den varme gasfase i de varmeste, inderste områder af protostellare kerner, før protoplanetariske skiver opstår. Disse spørgsmål er vigtige, da den protostellare kemi agerer som en forgænger for sammensætningen af det materiale, der indgår i planet dannelse, hvilket muligvis kan forklare den komplekse kemi vi ser i vores eget solsystem.

Ved at bruge høj opløsnings observationer fra Atacama Large Millimeter/submillimeter Array (ALMA), sammen med komplekse 3D strålingstransports koder, kan vi undersøge de inderste regioner af unge protostjerner og forhåbentligt besvare nogle af de spørgsmål vi har stillet ovenover. I denne afhandling præsenterer jeg forskning vedrørende de to lav-masse protostellare kerner, IRAS 16293-2422 og L483, deres støv og gasdensitet, temperaturfordeling og kemi.

To ud af de tre forskningsartikler, som bliver præsenteret i denne afhandling omhandler IRAS 16293-2422, hvor den ene fokuserer på 3D modellering af selve skyen, broen af støv og gas, der sammenbinder de to protostjerner, og den skivelignende emission omkring hver protostjerne, såvel som deres individuelle luminositet. En 3D støvdensitets-model præsenteres, som morfologisk svarer til 868 μm kontinuum emissionen, og forklarer den observerede $C^{17}O$ emission vha. en springmodel i mængden af molekyler i gasfasen. Denne model efterligner effekten af udfrysning af molekyler på overfladen af støvkorn, når temperaturen på støvkornene falder under sublimationstemperaturen af CO. De individuelle luminositeter af de dybt indlejrede protostjerner i IRAS 16293-2422 bestemmes til at være $L_A \geqslant 18\ L_\odot$ og $L_B \leqslant 3\ L_\odot$, for henholdsvist strålingskilde A og B, hvilket er første gang de individuelle luminositeter estimeres.

Den næste forskningsartikel om IRAS 16293 fokuserer på udstrømningerne af materiale og kinematikken af den observerede gaslinje-

emission fra de forskellige molekyler i gasfasen, og deres relation til broen af støv og gas. Molekylær gaslinje-emission fra CO, H_2CO, HCN, CS, SiO og C_2H afslører, at kun støvkontinuumet og $C^{17}O$ emissionen har et fysisk ophav i broen af støv og gas, imens emissionen fra alle andre molekylære overgange er relateret til udstrømningerne af gas fra strålingskilde A. Manglen på udstrømninger fra strålingskilde B får os til at konkludere, at den sandsynligvis er på et lavere evolutionært stadie end strålingskilde A.

Den sidste forskningsartikel omhandler ~0.1″ observationer af L483 med ALMA, som afslører at de observerede KOMs i L483 befinder sig i det inderste, varme område af skyen, indenfor 40–60 au af den centrale protostjerne, og kommer af den termale sublimation af islaget omkring støvkornene. Igennem en analyse af kinematikken fra $H^{13}CN$ J = 4–3 og CS J =7–6 gaslinje-emissionen, kan tilstedeværelsen af en Kepler skive ned til i hvert fald 15 au udelukkes. Dette betyder at de observerede KOMs ikke kan komme fra et abrupt overgangsområde imellem den kollapsende sky og en Kepler skive, som foreslået af et tidligere forskningshold, ej heller fra en varm skive atmosfære. Indenfor 15 au kan en lille Kepler skive hypotetisk set eksistere.

Til slut bliver der givet foreslag til fremtidige forskningsprojekter, der retter sig imod IRAS 16293-2422 og L483, som bedre vil kunne bestemme den rumlige fordeling af KOMs (hvilket giver mere information omkring formationsruterne), samt bedre bestemme tidslinjen for dannelsen af protoplanetariske skiver.

A prudent man should always follow
in the path trodden by great men
and imitate those who are most excellent.
— Niccolò Machiavelli

ACKNOWLEDGMENTS

I want thank my supervisor Jes Jørgensen for his guidance and support throughout my PhD studies. I am also indebted to my colleagues at StarPlan for their advice and help whenever I needed it. Special thanks are given to Lars Kristensen, Hannah Calcutt, Jon Ramsay, and Christian Brinch. I also want to thank our administrators Marianne Bentsen and Lene Bentzen, the submm group at StarPlan, and all the other members of StarPlan. I am very grateful to Matthijs van der Wiel for our collaboration, useful discussions, and for allowing me to visit and work with him at ASTRON in the Netherlands. Likewise, I am thankful to Daniel Harsono for letting me visit and work with him at Leiden. I am grateful to Søren Frimann for his help during my PhD, and for helping me with the LaTeX template of this thesis. I want to thank my parents for their support and encouragement. Thanks are given to the rest of my family, and all my friends.

CONTENTS

LIST OF FIGURES

LIST OF TABLES

ACRONYMS

PP-DISK Proto-planetary Disk

RSD Rotationally Supported Disk

PMS Pre-main-sequence

YSO Young Stellar Object

IR Infrared

SED Spectral Energy Distribution

ISM Interstellar Medium

COM Complex Organic Molecule

PAH polycyclic aromatic hydrocarbons

LTE Local Thermal Equilibrium

FT Fourier Transform

ALMA Atacama Large Submillimeter/millimeter Array

ACA Atacama Compact Array

SNR Signal-to-Noise Ratio

IRAS Infrared Astronomical Satellite

FAST Five-hundred-meter Aperture Spherical radio Telescope

Part I

INTRODUCTION

1 SCIENTIFIC BACKGROUND

And those who were seen dancing
were thought to be insane
by those who could not hear the music.
— Friedrich Nietzsche

1.1 INTRODUCTION

Astronomy (from Greek; "law of the stars") has been practiced by some of the first civilizations known, such as ancient Egypt and Babylon. It has found use in all major civilizations up to the present day, with the movement of celestial lights inspiring countless legends and creation myths. Through the ages, humans have fashioned different tools and instruments to look closer at the mystical domain of their gods, while utilizing astronomical observations to benefit their communities. The ancient Greeks created the first known analogue computer, the Antikythera, exclusively for predicting the dates of important astronomical positions and events, while seafaring nations through the ages have used the positions of celestial bodies to navigate the seas. Constructions found in Macchu Picchu, Peru, the sacred temple of the Inkan empire, were used to observe the sky and track the winter and summer solstices. This was vital for knowing when to plant and when to harvest, which was critical for an agricultural civilization such as the Inkan Empire. The Renaissance and the following scientific revolution ushered in advancements in Mathematics, Physics and Astronomy, which, together with more advanced instruments than previously built, such as Galileo's telescope, transformed our understanding of the Cosmos. Now, after thousands of years of research, we are slowly unveiling the heart of our existence. We are exploring the birth of the stars and their planets, including our Sun and the Earth, like a frog climbing out of the well to ponder the Great Ocean.

1.2 CONTEXT

After the Big Bang, the first generation of stars fused the primordial elements of predominantly hydrogen and helium into larger atoms. These stars formed in enormous clouds of gas, residing in the interstellar medium (ISM) which fills the space between stars in galaxies. With the violent death of these stars, the surrounding medium was enriched with their produce, which was then reused in a new generation of stars. This lead to star forming regions with an increasingly

Figure 1.1: Optical image of the Milky Way center, obscured by bands of interstellar material. Credit: ESO/S. Brunier.

larger proportion of atoms with higher atomic numbers. The ISM in our galaxy, the Milky Way, is a complex environment consisting of a range of different states of density, temperature and ionization.

The cold neutral regions of the ISM are dominated by neutral hydrogen (HI), which makes up the bulk mass of the galaxy. In contrast, *molecular clouds* (number densities $n_{tot} \geqslant 10^2$ cm^{-3}), are composed primarily of molecular hydrogen (H_2). Interspersed with the gas population are large amounts of small, micron-sized dust grains, found in the ISM to have a gas-to-dust mass ratio of 100 (Bohlin et al., 1978). The massive amounts of dust in the galaxy results in a high extinction of optical light, which can be seen as dark bands on the night sky towards the galaxy center (Fig. 1.1). The relatively high column density of molecular clouds shield the molecules inside against external stellar UV-radiation. This allows H_2 to form on dust grains in the ISM, from combination of two hydrogen atoms on the dust surface (Hollenbach & Salpeter, 1970). Molecular clouds are predominantly found in complexes called *Giant Molecular Clouds*, with masses and diameters on the order of 10^5 $M_\odot$ and 50 pc, respectively, such as the ones residing in the Orion constellation, see Fig. 1.2. These are gigantic star forming regions with complex physics and chemistry. Giant molecular clouds are mostly diffuse, with a mean number density of $\sim 10^2$ cm^{-3}, where the clouds gravity keeps the structure cohesive, with negligible internal thermal pressure. Inside the cloud exists *dense cores* (also called *prestellar cores*), components of higher densities ($> 10^4$ cm^{-3}) and low temperatures ($T \sim 10$ K), favorable to gravitational collapse (e.g., Stahler & Palla, 2005).

Gravitational collapse occurs when the gravitational potential energy of the cloud is greater than the internal kinetic energy, which, for a spherical, isothermal gas cloud, is described by the *Jeans cri-*

Figure 1.2: The Orion Molecular Cloud Complex harbors two separate giant molecular clouds with active star formation. The red color highlights emission from the narrow hydrogen α filter, at 0.656 μm. Credit: Rogelio Bernal Andreo.

terion (Jeans, 1902). This criterion states that collapse occurs if the cloud mass is larger than the *Jeans mass* M_J, given by

$$M_J = \left(\frac{\pi c_s^2}{G}\right)^{3/2} \rho^{-1/2}, \tag{1.1}$$

where ρ is the cloud density, c_s is the cloud sound speed, and G is the gravitational constant. The sound speed is given by,

$$c_s^2 = \frac{kT}{\mu m_H}, \tag{1.2}$$

where T is the temperature, μ is the mean molecular weight, m_H is the mass of the hydrogen atom, and k is Boltzmanns constant. From Eq. 1.1 and 1.2, it can be seen that a prestellar core of high density and low temperature is especially susceptible to gravitational collapse.

When a gravitational collapse takes place, the infalling material is kept isothermal, as the released gravitational energy from the contraction is radiated away by the dust and gas. At some point, the density becomes high enough for the region to become opaque to this radiation, causing radiative trapping, which heats up the central region. Numerical calculations by Larson (1969) show that a hydrostatic structure, called the *first hydrostatic core*, appears. This structure has a typical mass and radius of 5 Jupiter masses and 5 au, respectively, corresponding to $n_{H_2} = 1.7 \times 10^{13}\mathrm{cm}^{-3}$. As temperatures eventually reach 2000 K, high enough to dissociate H_2 in the first hydrostatic core, the energy lost to this process leads to further compression and eventual collapse. This marks the end of the first hydrostatic core.

The temperature only rises slightly during this collapse, due to most of the gravitational energy of the collapsing material being lost to the dissociation of H_2. When all the H_2 in the collapse center is dissociated, the temperature rises rapidly, and a second hydrostatic core appears. This second core remains dynamically stable for the remainder of the protostellar phase, while it accretes material. The increasing central density eventually places this second core in the protostellar regime (Larson, 1969), see Fig. 1.3.

After the collapse of the first hydrostatic core, the *main accretion phase* begins. The infalling material approaches the newly formed *protostar* at supersonic speeds, causing the entire envelope to undergo an inside-out collapse. A free-fall collapse of an isothermal sphere was described with a similarity solution by Shu (1977), where the inner envelope collapsing in free-fall was found to follow a density power-law of $\rho \propto r^{-3/2}$, while the outer static envelope follows $\rho \propto r^{-2}$.

As the material accretes onto the central protostar, shocks and impacts at the protostellar surface releases energy which is observed as the *accretion luminosity*, given by

$$L_{acc} = \frac{GM_*\dot{M}}{R_*}. \tag{1.3}$$

G is the gravitational constant, M_* is the protostellar mass, $\dot{M}$ is the accretion rate, and R_* is the protostellar radius. The protostar is, however, not the only structure expected from a collapsing dense core.

Dense cores in molecular clouds are not static objects, but have internal rotation, albeit at low levels (Goodman et al., 1993). For this reason, the dense core cannot collapse into a single point at its center, due to the conservation of angular momentum. This forces the infalling material into a flattened disk-like shape (Terebey et al., 1984), see Fig. 1.4, which will eventually become a Rotationally Supported Disk (RSD). In the hypothetical event where the dense core has uniform angular rotation, the mass closest to the rotational axis will fall close to the emerging protostar, while material farther from the rotation axis will land further from the center. This is caused by the difference in specific angular momentum, $v_{\phi,1}r_1 = v_{\phi,2}r_2$, where v_ϕ is the rotational speed around the core rotation axis and r is the distance to the rotation axis.

If no other mechanism were at play, a protostar could not emerge, as the burgeoning protostar would be torn apart by the centrifugal motions. However, angular momentum is lost from the system due to jets and winds arising from the innermost regions of the collapsing core (e.g., see Bally & Lada, 1983; Richer et al., 1992), carving large outflow cavities into the collapsing envelope of dust and gas (Fig. 1.3). Recently, the bipolar jet and the disk wind from the Class 0 protostar HH212 were found to be rotating (Lee et al., 2017a; Tabone et al., 2017), as required, in order for angular momentum to be removed. This angular momentum loss allows mass to accrete onto the central protostar.

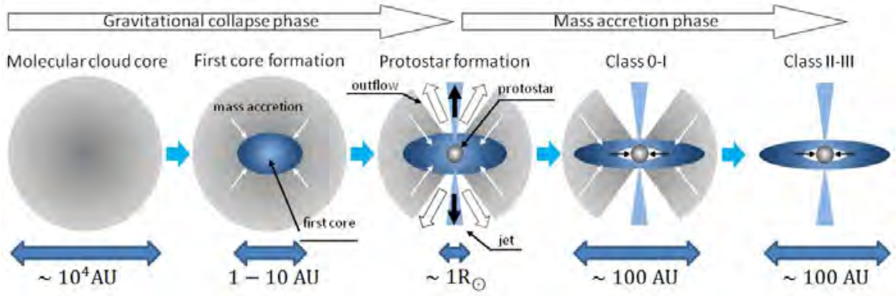

Figure 1.3: Schematic of star formation. A dense prestellar core begins a gravitational collapse, forming the first hydrostatic core. Along with the emergence of a protostar, together with jets and outflows, a disk is formed in the Class 0-I stage. After the remainder of the dusty and gaseous envelope is removed through mass loss to outflows and jets, or through accretion, and only a disk remains, the Class II stage is reached. Credit: Yusuke Tsukamoto (Kagoshima University).

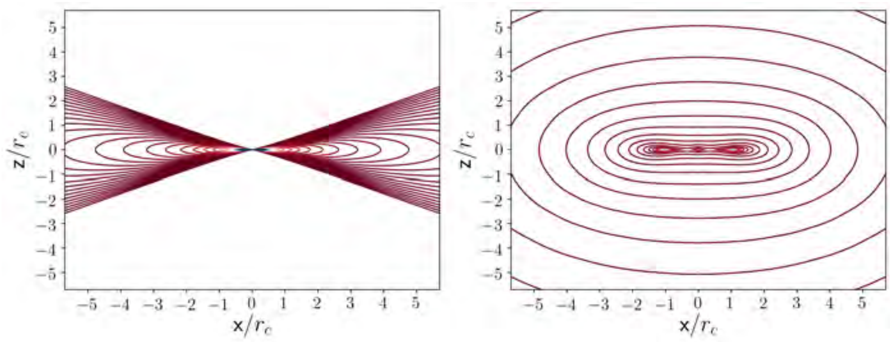

Figure 1.4: The density solution to a rotating-infalling collapse (Terebey et al., 1984) (right frame) and a flared protoplanetary disk in hydrostatic equilibrium with its host star (left frame), presented as edge-on slices through the models. The buildup of material in a rotating-collapse can be seen near $x/r_c \sim 1$. The local density contours change by a factor of $\sqrt{2}$, with the outer contours being of lowest density. The rotating-collapse model is self-similar at different values for the centrifugal radius r_c, set to r_c=20 au in order to compare to a PP-disk model in the left frame.

Furthermore, magnetic fields of the ambient environment are threaded into the rotating disk via ionized material. If these magnetic field lines are strong enough, catastrophic magnetic braking occurs, preventing an RSD from being formed (e.g., see the numerical simulations by Allen et al., 2003). Some numerical studies have shown that turbulence and Ohmic dissipation can overcome magnetic braking. However, there is still not consensus on exactly how the magnetic field is tamed enough for an RSD to be allowed to form (see review by Li et al., 2014, and references therein).

As highlighted by these examples, the formation of a protostar with a stable RSD requires a balance between the correct amount of angular momentum being removed from the system, allowing a central protostar to form, while still retaining enough to be distributed into a circumstellar disk. The presence and strength of the different angular momentum loss mechanisms are still the focus of ongoing research, and the exact formation process of stable circumstellar disks are still unknown. However, for illustrative purposes, we can investigate a simple model which follows the initial conditions set by Terebey et al. (1984). Such a model, which, however, ignores the effect of magnetic fields, can naturally explain the appearance of an RSD, i.e., a rotating disk with Keplerian motion, also called a *Kepler disk*.

1.2.1 *Protoplanetary disks*

In a collapsing, rotating envelope, with purely ballistic motions, which ignores gas pressure, the spiraling streamlines will impact the midplane of the system within a characteristic radius called the centrifugal radius r_c. Such a model is a step further than the free-fall collapse of Shu (1977) which ignored rotation. From Terebey et al. (1984),

$$r_c \approx 0.5 \frac{GM_*}{c_s^2}. \tag{1.4}$$

Within this radius, a rotationally flattened disk-like structure will emerge when r_c becomes larger than the protostellar radius R_* (Fig. 1.4). As r_c grows, the streamlines within this distance will eventually miss the protostellar surface and instead tangentially impact each other at a distance of $0.34\ r_c$, forming a ring of dense material (Stahler & Palla, 2005), see Fig. 1.5. Inside this ring, an *inner disk* is formed, where the orbital motions are nearly relaxed to a circular orbit. As r_c grows, so does the dense ring and the inner disk, where the latter will eventually become stable and rotationally supported, i.e., a Keplerian disk (Stahler & Palla, 2005). As r_c grows proportionally to the central mass M_*, there exists an early time before the formation of a Kepler disk, where the innermost regions are best described by the density solution to the infalling, rotating collapse described by Terebey et al. (1984).

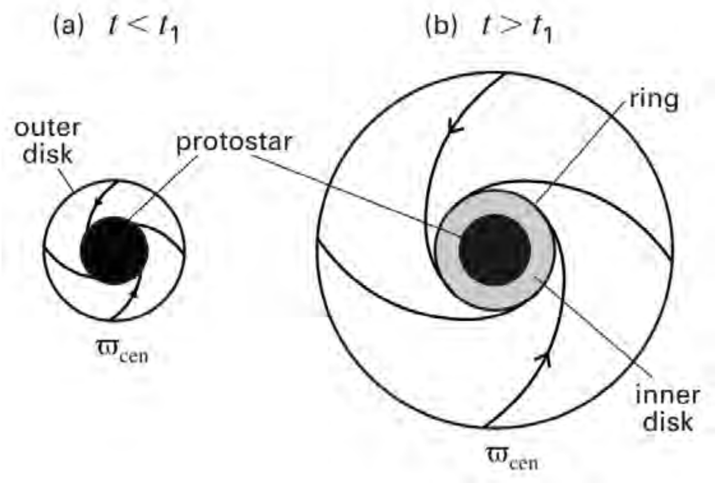

Figure 1.5: The appearance and early expansion of a circumstellar disk. The centrifugal radius ω_{cen} marks the boundary of the outer disk, where a disk-like structure begins. At a time $t < t_1$, the curved lines impact the protostellar surface, while at $t > t_1$ the streamlines impact each other, creating a dense ring of material, which grows as ω_{cen} grows. Inside this dense ring, an inner disk will form, where the material will eventually relax to the state of lowest energy; Keplerian orbital motion. Credit: Stahler & Palla (2005).

Later on, when a Keplerian disk has been established, the disk density can be described by hydrostatic equations of the equilibrium of the disk mass with the host stars gravity (e.g., see Andrews et al., 2012), see Fig. 1.4. While both the density solution to a rotating-infalling collapse within r_c and a Keplerian disk appear as circular disks of material, if the structure is poorly resolved or seen from above, there is a dramatic difference in the density distribution. The innermost regions of an infalling-rotating collapse are vertically extended and generally decreasing as $r^{-0.5}$ from the collapse center (if $r < r_c$), while Keplerian disks have an exponentially decreasing density in the vertical direction and appear flat by comparison (Fig. 1.4).

1.2.2 *Protostellar and pre-main-sequence evolutionary stages*

The emergence of a Kepler disk and the conditions of the ambient environment are related to the *evolutionary stage* of the Young Stellar Object (YSO). YSO is a term covering both the early, deeply embedded protostellar stage, as well as the later stages where the envelope is gone, and only a tenuous *protoplanetary disk* (PP-disk) remains around the central object. The name of PP-disks, which are Keplerian disks, refer to the fact that planets are expected to form in them.

The classification of the YSO stages began with the Infrared Astronomical Satellite (IRAS) survey, which covered the mid- and far-IR

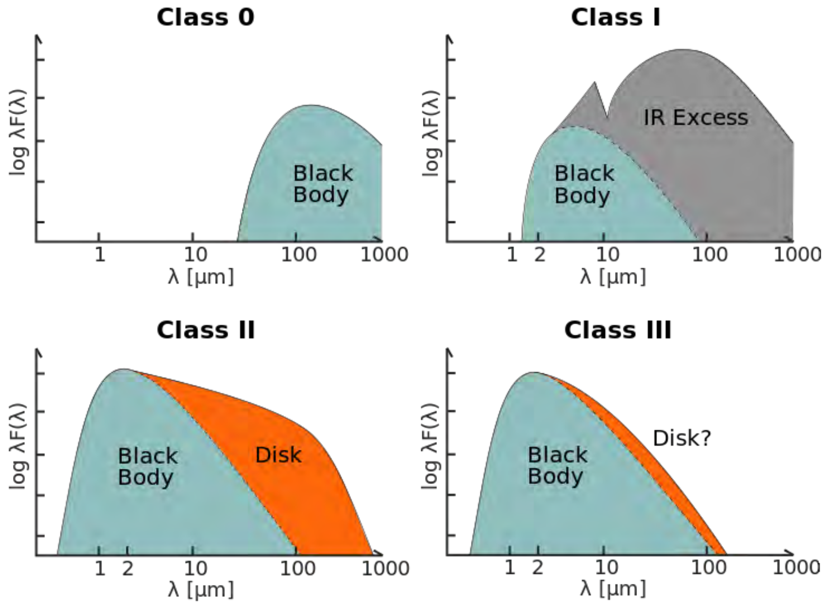

Figure 1.6: SEDs of the different YSO stages. Only the cold outer parts of the envelope are observed at the Class 0 stage, while the loss of significant amounts of dust allows the radiation of hotter dust in the inner regions to reach the observer from Class I objects. Most of the ambient material is lost by the Class II stage, where both the stellar spectrum, approximately a black-body, and the added IR- and submm emission from the surrounding PP-disk is seen. By the Class III stage the disk is reduced in mass, only weakly contributing to the SED. Credit: Magnus Persson.

emission of the Spectral Energy Distribution (SED) from YSOs. The SEDs of a range of dense cores, which showed predominantly infrared emission, were measured. This first classification scheme used the dependency of radiative flux on frequency between 2–20 μm to classify the infrared radiation source into one of three classes; Class I, Class II or Class III (Lada & Wilking, 1984; Lada, 1987). Class I and Class III peaks at the longest and shortest wavelength, respectively. These observational classes were coupled to the YSO evolutionary stage by Adams et al. (1987). Later submillimeter continuum observations revealed a large number of strong submillimeter sources, with low values of L_{bol}/L_{submm}, with emission peaks at longer wavelengths than the objects classified by Lada & Wilking (1984). This prompted the addition of another Class to the classification scheme; Class 0 (Andre et al., 1993).

The four evolutionary stages of a YSO and their physical characteristics are given below:

- After the disappearance of the first hydrostatic core, the environment of the subsequent protostar is described by infalling material. The impacts of this material on the protostellar surface releases energy, which is observed as the accretion luminosity of the deeply embedded protostar. This *Class 0* stage has weak optical and near-IR emission, due to the large amounts of cold obstructing dust in the envelope, which absorbs the protostellar radiation and re-emits it at longer wavelengths. A relatively large fraction of the observed emission is in the submillimeter regime, with $L_{submm}/L_{bol} > 0.5\%$ (Andre et al., 1993). At this point $M_{envelope} \geqslant M_*$, while the protostars gain a significant fraction of their total mass during this stage (McKee & Ostriker, 2007). Concurrently, violent ejections of mass and angular momentum occurs in outflows and jets, launched close to the central protostar (Fig 1.3). It is debated whether or not Kepler disks commonly form during this stage, though some Class 0 Kepler disks have been observed (Tobin et al., 2012; Murillo et al., 2013; Ohashi et al., 2014). The Class 0 lifetime has been estimated at 0.13–0.26 Myr by Dunham et al. (2015), based on surveys of 18 molecular clouds.

- By the *Class I* stage, a significant portion of the surrounding envelope has been lost. A protostellar core at this stage is thought to contain a relatively evolved protostar, which still accretes from the envelope. Kepler disks have been observed at this stage (Brinch et al., 2007; Jørgensen et al., 2009; Harsono et al., 2014). The reduced amount of material in the envelope allow more radiation to escape, due to the lowered optical depth. The SED will be observed to peak at lower wavelengths, as it now effectively traces hotter dust than the more embedded Class 0 stage, where the colder outer envelope dominated the SED. The lifetime of this stage has been estimated to be 0.27–0.52 Myr by Dunham et al. (2015), based on surveys of 18 molecular clouds.

- When the ambient envelope is depleted of mass, the YSO has transitioned into the *Class II stage*. The central object is now observable at optical wavelengths (unless the disk is aligned to block it), due the removal of the ambient envelope. The central object is now referred to as a pre-main-sequence (PMS) star. Consolidated, large PP-disks are observed around these objects, adding an infrared and submillimeter excess to the bolometric luminosity of the PMS star in the SED (e.g., see the case of TW Hya, Rucinski & Krautter, 1983), see Fig. 1.6. The PMS star accrete material from the disk itself at the inner boundary, which drains the disk mass. This stage was estimated to last ~ 2 Myr by Evans et al. (2009), based on previous studies of disk frequencies in clusters with known ages and mean YSO ages (e.g., see Haisch et al., 2001; Spezzi et al., 2008).

- Finally, the *Class III* stage lacks both an envelope and a large disk, causing the PMS star to have no significant accretion. A disk is still present, though much diminished from its former glory, with a significantly lower mass than in the Class II stage. Eventually, the remaining gas in the disk is lost to stellar winds and photoevaporation from the central PMS star (Alexander et al., 2006), leaving behind whatever planetesimals and planets were created in the disk lifetime. Class III objects are estimated to exist no longer than 10 Myr (Wahhaj et al., 2010).

The timeline for the appearance of Keplerian disks is debated, and while some Class 0 disks have been observed, (e.g., a 150 au Kepler disk was observed around the Class 0 protostar VLA 1623 Murillo et al., 2013), it is unknown if this is the norm or if most Kepler disks arise later in the Class I stage. While the listed evolutionary stages detail the loss of the envelope, as well as the appearance and disappearance of the PP-disk, the formation of the observed planetary systems and individual planets is also a matter of debate and an area of intense research.

1.2.3 *Planet formation*

To date, different detection techniques have found almost 4000 different exoplanets, in a wide range of planetary systems (from exoplanet.eu, see Schneider et al., 2011). Several hypotheses exist regarding planet formation in the PP-disks, with the *core accretion theory* (Safronov, 1969) being the most dominant. In this scheme, the dust grains, which agglomerate into larger sizes throughout the disk lifetime, eventually form km-sized planetesimals. Afterwards, collisions between these planetesimals form terrestrial planets and the cores of gas- and ice-giants, which then gain their atmospheres from accretion of the gas reservoir in the disk (e.g., see the numerical simulations by Pollack et al., 1996). Of special importance here, is the presence of icy dust (see Section 1.2.4), as they have a larger probability of sticking after collision, greatly enhancing grain growth compared to bare dust grains (see e.g., the numerical simulations by Okuzumi et al., 2012). As the mass of dust and gas in the disk, not locked into larger bodies, steadily drops, the disk is eventually depleted to the point where the remaining material is removed through photo-evaporation caused by the UV-field from the central PMS star (e.g., see Hartmann, 2009). As the PMS star is deprived of accreting material, the source of the luminosity is instead solely the release of gravitational energy as the protostar contracts. Eventually, the central pressure and temperature

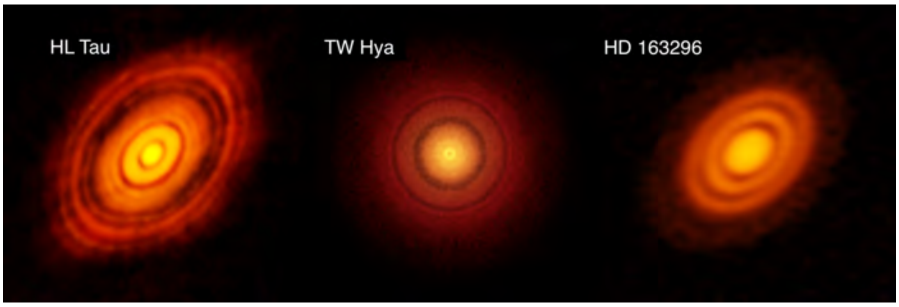

Figure 1.7: ALMA observations of HL Tau, TW Hya, and HD 163296. The gaps are thought to indicate sites of planet formation. Credit: **HL Tau**: ALMA (ESO/NAOJ/NRAO), **TW Hya**: Credit: S. Andrews (Harvard-Smithsonian CfA); B. Saxton (NRAO/AUI/NSF); ALMA (ESO/NAOJ/NRAO), **HD 163296**: ALMA (ESO/NAOJ/NRAO), Andrea Isella, B. Saxton (NRAO/AUI/NSF).

become high enough for hydrogen to fuse into helium, resulting in a main-sequence star with a complete planetary system, like our own Solar System. While these were the broad strokes of the core accretion theory, we still do not know how early or how often planets form in PP-disks.

ALMA has delivered some magnificent images of nearby PP-disks (Fig. 1.7), showcasing lanes of depressed emission. These could indicate interaction between growing planets and the PP-disk (ALMA Partnership et al., 2015; Andrews et al., 2016; Isella et al., 2016). As such, it is interesting to characterize these PP-disks as early in their evolution as possible, in order to get a better handle on how early and under what circumstances the first planets form. So far I have described the physical processes taking place in star and planet formation, but the chemistry of protostellar cores is also of great importance for both planet formation and observational techniques.

1.2.4 *Astrochemistry*

While the physical environment of the protostellar core in the early stages is evolving, the extreme conditions within it opens up several different avenues of complex chemistry, in conditions not naturally occurring on Earth. Modern astrochemistry started in 1968 when ammonia (NH_3) was detected in the ISM (Cheung et al., 1968), followed up by the detection of 200 different gas phase molecules[1], observed using rotational emission spectroscopy (see Herbst & van Dishoeck, 2009, for a review). Infrared absorption and emission studies of the ISM have revealed complex chemistry, including discrete emission spikes in the infrared regime, whose carriers have not yet been firmly identified. Some proposed originators are very large molecules called polycyclic aromatic hydrocarbons (PAHs), e.g., Pyrene

1 from the database at https://www.astro.uni-koeln.de/cdms/molecules

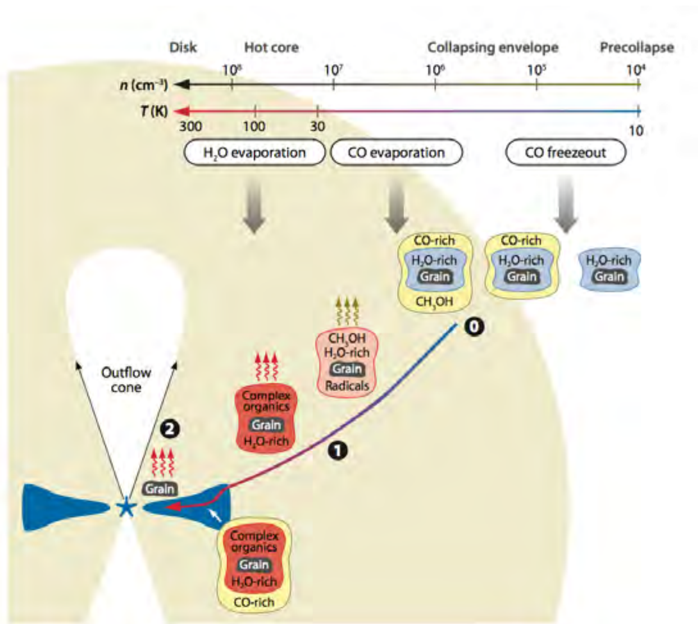

Figure 1.8: Schematic of the composition and chemical evolution of the dust ice-mantle and the sublimation into the gas phase in a collapsing 0.05 pc envelope. The formation of zeroth, first and second generation molecules are marked by 0,1 and 2 respectively, in the scheme of Charnley et al. (1992). The hot corino at (2) defines a region where the dust ice-mantle is completely sublimated, usually defined as 100 K. In the dense and cold midplane of the PP-disk, the molecules will freeze-out onto the dust grains again, allowing more grain-surface chemistry to occur. The temperature and density of the envelope is seen in the panel top. Credit:(Herbst & van Dishoeck, 2009).

($C_{16}H_{10}$) (Salama, 2008), though no firm detections have been made to date.

The different molecules found in the ISM and in protostellar cores are excellent tracers of the physical conditions therein. For example, the rotational transitions of CS trace high density regions, due to the large dipole moment of the molecule. High dipole moments result in high rates of spontaneous emission, necessitating a high local density in order to keep the molecular energy levels populated through collisional excitation (see Section 2.1.2).

Another example is that the observations of ions, such as HCO^+, naturally probe ionized regions in protostellar cores (e.g., Stahler & Palla, 2005). Also, astrochemistry has the potential to assess the overall ability of life, as we know it, to arise in other parts of the galaxy than our own Solar System. Terrestrial life is based on organic chemistry, with molecules composed of carbon, hydrogen, oxygen, nitrogen, and other elements to a lesser extent (see discussion of Ceccarelli et al., 2017, and references therein). By probing the ISM and star forming regions for prebiotic molecules, such as glycolaldehyde, and analyzing their abundances, we can estimate the potential for life, as we know it, to eventually appear on planets formed in these star forming regions.

In order to do this, we need to follow the chemistry from start to finish, in the formation of a planetary system from a prestellar core in a molecular cloud. The chemistry of the cold, outer envelope of a protostellar core is affected by cosmic rays and the UV radiation field from nearby stars, which produces ions. These ions interact with the neutral atoms and molecules in the gas phase. When the dust density becomes sufficiently high, the low temperature of the environment (10–20 K) will cause molecules to land upon the dust surface, with some interacting and sticking together, growing into an ice-mantle upon the grain (see Fig. 1.9). Due to this freeze-out of molecules upon the dust grains, only a few simple molecules exist in the gas phase of the cold envelope, (e.g., N_2H^+, HCO^+, H_2CO, see van Dishoeck, 2006, and references therein).

In contrast, the inner hot region of the envelope closest to the protostar reaches temperatures above 90–100 K, the sublimation temperature of the most strongly bound molecules, such as H_2O, in the dust ice mantle (Sandford & Allamandola, 1993). With the sublimation of ice, a multitude of molecules are released into the gas phase. This *hot corino* in a low-mass protostellar core (referred to as a *hot core* in the case of high-mass star formation) contains a unique chemistry, where Complex Organic Molecules (COMs) are observed in the gas phase (see Fig. 1.8). COMs are molecules with six atoms or more, including at least one carbon atom(Herbst & van Dishoeck, 2009).

Mid-IR spectroscopy of ices, such as the observations by Knez et al. (2005) towards stars behind the Taurus and Serpens molecular clouds,

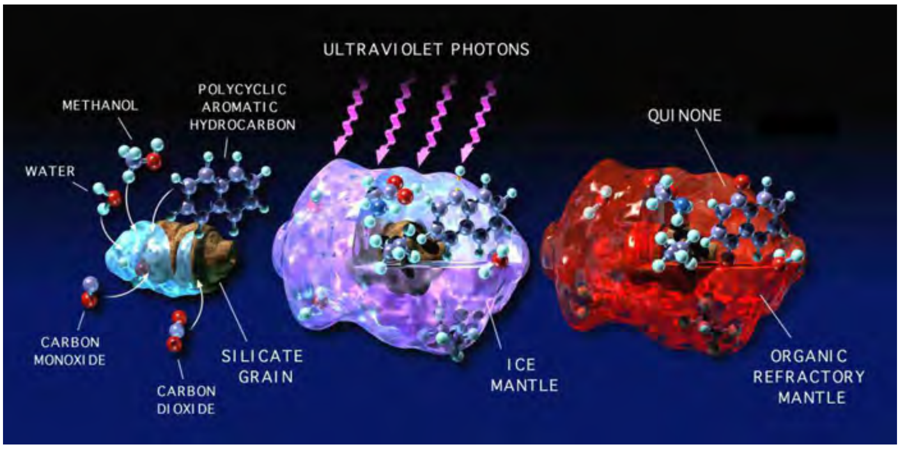

Figure 1.9: Schematic of the composition of dust. The central silicate core is covered by an ice-layer of a mixture of molecules, allowing complex dust-surface chemistry to take place, such as the formation of the organic compound Quinone ($C_6H_4O_2$) via UV-radiation formation routes. Credit: M. P. Bernstein, S. A. Sandford, and L. J. Allamandola, in Sci. Am. (July 1999), 26.

have supplied absorption spectra indicating the dust composition to be a silicate core based on the 10–20 μm features. Other studies use a mixture of silicate and carbonaceous dust grains to reproduce the interstellar extinction and infrared emission from the ISM (e.g., Weingartner & Draine, 2001). This dust grain is found to be covered with an ice-mantle of primarily H_2O, CH_3OH, NH_3, CO and CO_2 (Boogert et al., 2015) along with a range of less abundant molecules (Fig. 1.9). An important distinction between these different ice species, is whether or not they have a large dipole moment (polar ices) or not (apolar ices). Apolar ice species, such as CO and N_2, sublimate at much lower temperatures (30 K for CO, e.g., see Jørgensen et al., 2015) than polar ice species such as H_2O and COMs (90–100 K), due to differences in the binding energies of the species on the dust ice-mantle. As atoms and molecules land upon the ice-mantle they can move around and interact, which leads to a hydrogenation process upon the dust surface, which produces hydrogen-rich molecules such as H_2CO and CH_3OH, from hydrogenation of CO (Watanabe & Kouchi, 2002).

During the warm up phase of the infalling material, larger molecules such as $HCOOCH_3$ and CH_3CH_2OH can be formed through grain-surface reactions (Guélin et al., 2008). Öberg et al. (2009) performed laboratory experiments, which indicate that the UV-irradiation of CH_3OH-rich ices caused by cosmic rays, and the subsequent slow warm up phase of the ices at 20–70 K, during the protostellar collapse, can explain the observed gas phase abundances of COMs in the innermost regions of the envelope, via formation routes on the dust grain surfaces (see Fig. 1.9).

1.2.5 *Hot corino chemistry*

After the infalling dust grains have reached the hot corino region where T>100 K, the molecular layers are sublimated into the gas phase. Various observations have been made of COMs towards different Class 0 objects, with one of the most prominent objects being IRAS 16293-2422, hereafter referred to as IRAS 16293. Early, mainly single-dish, observations of IRAS 16293 have identified a dense (>10^7 cm^{-3}) and warm (>80 K) region containing organic molecules, such as CH_3OH and CH_3CN (van Dishoeck et al., 1995). Later observations with better sensitivity revealed a larger range of COMs, including $HCOOCH_3$, CH_3OCH_3, C_2H_5CN and NH_2CHO (Cazaux et al., 2003; Kahane et al., 2013).

The recent years have offered large improvements in angular resolution and sensitivity using (sub)millimeter wavelength interferometers, in particular with ALMA (Section 2.4). Such observations have revealed a very large degree of chemical richness of some of these Class 0 protostars (e.g., Jørgensen et al., 2011, 2012).

Different chemical schemes have been made to explain the presence of the COMs. While there is a broad consensus on the creation of organic molecules such as CH_3OH and H_2CO via hydrogenation on the grain surface, the origin of larger molecules such as glycolaldehyde (CH_2OHCHO) and propanal (CH_3CH_2CHO) (observed in IRAS 16293, see Jørgensen et al., 2012; Lykke et al., 2017) is debated. Charnley et al. (1992) proposed that the molecules created on the grain surface, and later released into the gas phase via sublimation, are the parents, or first generation molecules, while the larger observed COMs form in the gas phase of the hot corino from the sublimated molecules, as second generation molecules. However, this creation scheme for COMs has been called into question, as the lifetime of the infalling material in the hot corino of IRAS 16293 is not sufficient for the formation of the larger COMs (Schöier et al., 2002). Moreover, laboratory experiments and theoretical considerations by Horn et al. (2004) show that the gas phase formation of $HCOOCH_3$ in hot corino conditions is inefficient and cannot explain the observed abundances. In contrast, as noted earlier, recent laboratory experiments of Öberg et al. (2009) highlight the potential for formation routes on the dust ice-mantle alone to explain the observed COM abundances.

While the observations of COMs are usually attributed to molecule injection into the hot corino from passive heating of the dust grains from the protostar, alternative physical explanations have been found. The low-mass protostar B1-b was found to have $HCOOCH_3$ and CH_3CHO emission emanating from cold gas. This suggests a non-thermal desorption origin, such as UV photodesorption of ice, from protostellar photons traveling through the outflow cavities of B1-b

(Öberg et al., 2010). Chemical models by Drozdovskaya et al. (2015) also show that complex chemistry can take place in the outflow cavities carved into the protostellar envelope by bipolar outflows (see Fig. 1.8). This removal of material allows larger amounts of photons to penetrate the envelope, resulting in larger degrees of dust heating and irradiation.

Furthermore, observations of CH_3OH were found to be related to the interaction between the outflows and surrounding environment of the Class 0 protostar NGC 1333-IRAS4B (Jørgensen et al., 2005c). These examples showcase that COMs are not exclusively found in the gas phase due to passive heating of the dust grains.

The spatial distributions of COMs, and which structures they are affiliated with, in the innermost regions of YSOs, are also unknown, as most detections have either not resolved the hot corino structure (Imai et al., 2016) or have not characterized the physical environment where COMs are observed, as is the case for IRAS 16293 (Jørgensen et al., 2016). It is then unknown whether or not COMs reside in a hot corino around each radiation source or in an $T \geqslant 100$ K atmosphere layer of the possible PP-disks, that is, is the hot corino an inner envelope structure or is it a disk structure?

Considering theoretical dust density distributions, such as the Keplerian disk and the inner regions of a rotating-infalling collapse (see Fig. 1.4), the different physical conditions should have a large impact on the expected gas phase abundances. The early rotating-collapse environment should have higher amounts of molecules in the gas phase, since the shielded, cold dense midplane of a Kepler disk would have significant freeze-out of the molecules onto the dust grains, due to shielding from the protostellar radiation. Associating the existence of COMs with the presence or absence of disks, would be of great importance for disk and planet formation theories, as it would present an important marker for the disk formation timeline. Due to these open questions and their importance, the formation of COMs and the physical origin of their release into the gas phase is an active and debated field.

Besides the considerations of COMs and their relation to hot corinos, the ubiquitousness or rarity of hot corinos themselves, in protostellar cores, are also uncertain. A hot corino was first detected by van Dishoeck et al. (1995) in IRAS 16293, and while subsequent detections of hot corinos in other protostellar cores have been made, it is not known if all Class 0 objects harbor a hot corino. The low number of known hot corinos around low-mass Class 0 sources limits our understanding of their nature. To date, hot corinos have been detected in IRAS 16293 (van Dishoeck et al., 1995), NGC 1333 IRAS 4A (Bottinelli et al., 2004a), NGC 1333 IRAS 2A (Jørgensen et al., 2005a), NGC 1333 IRAS 4B (Sakai et al., 2006), HH212 (Codella et al., 2016), B335 (Imai et al., 2016), and L483 (Oya et al., 2017).

In order to determine the physical origin of COMs and how their presence relate to the existence or lack of an established Kepler disk, we require realistic models of the protostellar environment in terms of the dust and gas density, and temperature. This requires realistic approximations of the radiative transfer in protostellar environments, to both determine the dust temperature and the molecular energy level populations, in order to accurately interpret and assess our observations.

2 METHODS

Astronomers use almost exclusively a single natural phenomenon to investigate the universe; electromagnetic radiation. Electromagnetic radiation at optical and near-IR wavelengths appear obstructed towards the dusty and gaseous molecular clouds in the galaxy (see Fig. 1.1), but travels unhindered through the same regions at millimeter wavelengths. Transitions between discrete energy levels in rotating interstellar molecules supply rich spectra towards different star forming regions, while the dust population emits broadly across the IR and submm spectrum, approximately as black-body radiation (see Stahler & Palla, 2005, for a broad introduction).

Proper analysis of such spectra and images, of both the dust continuum and molecular line emission from star forming regions, requires a solid understanding of the physical processes behind. As the emission from the embedded, central protostar is absorbed by dust and re-emitted at longer wavelengths in the early YSO stages, it is crucial to understand the theory of *radiative transfer*, in order to assess and simulate these dusty environments. The complicated molecular line emission structures observed from the innermost regions of the protostellar environments also require detailed understanding of radiative excitation, spontaneous emission and other processes responsible for the molecular energy level populations. Molecular species can be used as effective probes of the protostellar environment, as the individual molecular gas line transitions are dependent on the ambient gas density and temperature.

In order to observe these complicated structures, we require observing instruments with high angular resolution and exquisite sensitivity, to detect the faintest emission structures. The dominant observing technique in modern radio astronomy is interferometry, where several single-dish telescopes are linked into a single array. This achieves the angular resolution of a single telescope with the same diameter as the furthest distance between two telescopes in the array. However, this technique of *aperture synthesis* come with some important assumptions and limitations. In order to obtain reliable astronomical spectra and images, it is important to understand the principles of interferometry, and how interferometric imaging comes with some intrinsic uncertainties that should not be neglected.

In Section 2.1 I present radiative transfer theory, followed by a short description in Section 2.2 of the numerical codes used during my PhD. In Section 2.3 the basics of interferometry, and how scientific images are created from interferometric data, are presented. In Section 2.4 I give a short description of the ALMA observatory, which was used to observe IRAS 16293 and L483 , and supplied the scientific data used in this thesis.

2.1 RADIATIVE TRANSFER

This Section, excluding subsection 2.1.2, is a digest of, and follows the terminology of, selected aspects of Stahler & Palla (2005) and the lecture notes for the course "Radiative transfer in astrophysics"[1] by C.P. Dullemond, University of Heidelberg.

The propagation of light through a dusty and gaseous medium is a complex process, depending on both absorption and scattering of the propagating radiation in the medium. The *specific intensity*, I_ν, is the energy per time emitted normally to a surface ΔA, through a solid angle $\Delta\Omega$, within the frequency $[\nu, \nu + \Delta\nu]$. The *flux density* is closely related and describes the monochromatic energy per time passing through a surface, with the normal vector $\hat{z}$. The projection of the emission vector $\hat{n}$ onto the surface normal vector $\hat{z}$ is the cosine of the angle θ between them, i.e., $\mu = \hat{z} \cdot \hat{n} = \cos\theta$.

The flux density is given by integrating over the emitting source solid angle Ω,

$$F_\nu = \int \mu I_\nu d\Omega. \tag{2.1}$$

If the emission is traveling through an attenuating medium, such as an interstellar cloud of gas and dust, the specific intensity will change. The dominating source of attenuation in these objects is dust, as its opacity is much greater than the molecules in the gas phase. Photons can be lost either to absorption, where the photon energy heats up the dust, or to scattering where the dust scatters the photon into a new direction, out of the beam solid angle (Fig. 2.1).

If we look at absorption first, the extinction along a path of length Δs is given by the density ρ and the opacity κ_ν. κ_ν is the frequency dependent cross-section per mass unit, i.e., how obstructing the medium is to the radiation, per mass unit.

The contribution of the medium to the radiation in the beam is given by the emission arising from a volume of dust, radiating as a black-body with a temperature of 10–30 K, the typical range of dust temperatures in the cold, outer envelope of protostellar cores, as well as dust scattering from other directions into the beam direction. The added emission is described as the emissivity j_ν, energy emitted per time per volume of dust and gas, per frequency unit, per steradian (unit of solid angle), in the beam direction $\hat{n}$. The units of emissivity are very close to those of I_ν and only differ in that j_ν is in terms

1 http://www.ita.uni-heidelberg.de/~dullemond/lectures/radtrans_2013/index.shtml

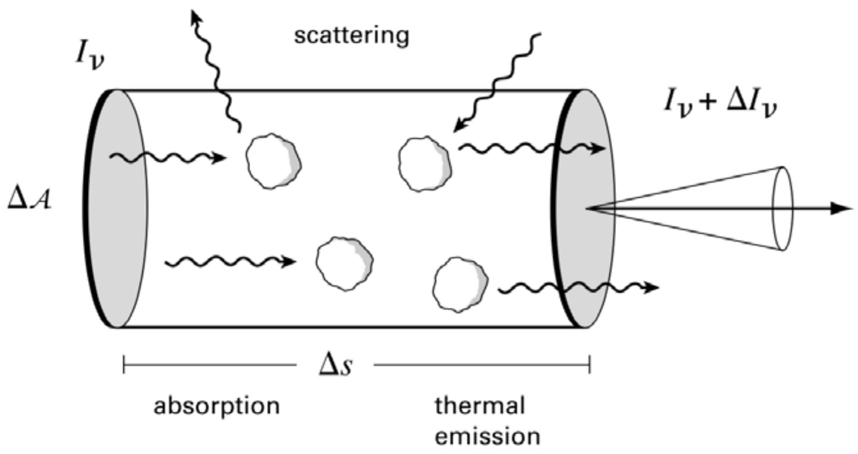

Figure 2.1: Radiative transfer of a beam of light traveling through an attenuating medium. Some radiation is lost to scattering and absorption, while the medium itself contributes to the beam of light through its emissivity. Credit: (Stahler & Palla, 2005).

of volume and I_ν is per area. The change in specific intensity after traversing a length Δs in the dusty medium is then

$$\Delta I_\nu = -\rho\kappa_\nu \Delta s I_\nu + j_\nu \Delta s, \tag{2.2}$$

which is simply calculating the net effect of radiation lost to absorption and radiation gained from the inherent emissivity of the attenuating medium (Fig. 2.1).

This equation can be rearranged to find a differential equation describing the transfer of radiation through a medium, known as the *radiative transfer equation*,

$$\frac{dI_\nu}{ds} = -\rho\kappa_\nu I_\nu + j_\nu. \tag{2.3}$$

The optical depth $\tau = \rho\kappa_\nu\Delta s$ describes the absorption strength through the medium, where a medium with $\tau \gg 1$ is said to be *optically thick* as almost no emission will escape, while $\tau \ll 1$ describes an *optically thin* medium, meaning the absorption is negligible. Note that κ_ν is frequency dependent, so the same medium can be optically thin and thick, at different wavelengths.

The heated dust grains can be approximated as black-bodies, with the isotropic specific intensity B_ν, which is only dependent on the dust temperature T_d,

$$B_\nu = \frac{2h\nu^3/c^2}{e^{h\nu/K_B T} - 1}. \tag{2.4}$$

Converting into wavelength, requires correction for frequency to wavelength space, i.e., $d\nu/d\lambda = -c/\lambda^2$,

$$B_\lambda = \frac{2hc^2/\lambda^5}{e^{hc/\lambda K_B T} - 1}. \tag{2.5}$$

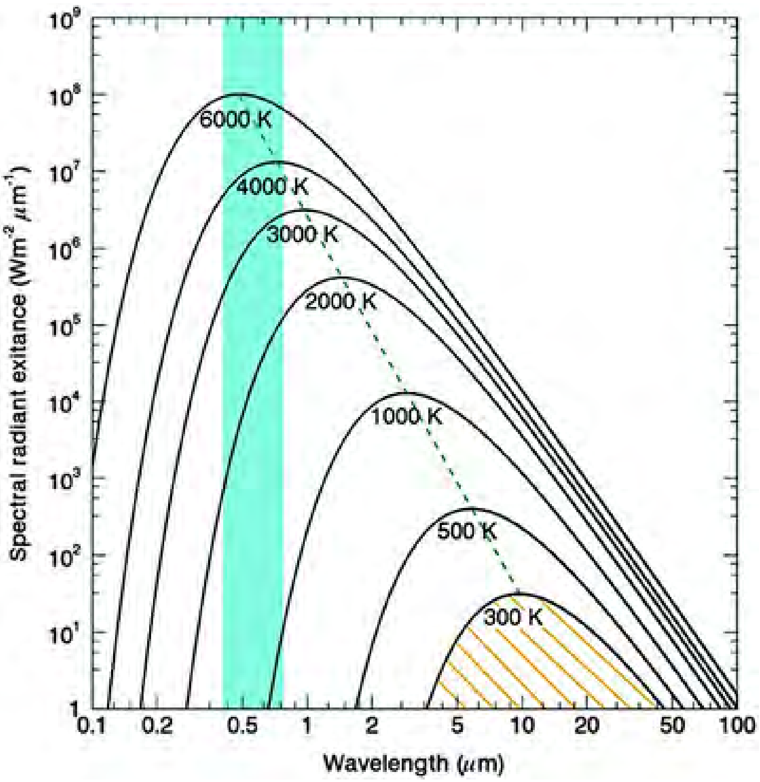

Figure 2.2: The black-body spectrum at different temperatures. As the temperature drops, the peak emission wavelength decreases according to Wien's displacement law, over-plotted as a dashed line. The spectrum of visible light is shown as a cyan bar, around the peak emission wavelength of a black-body approximation of the Sun, with a temperature of 5778 K. Credit: Claudia Kuenzer.

The negative sign is ignored, as it simply means that the graph should be inverted along the first axis, i.e., wavelength should be plotted from high to low wavelengths, in order to keep the shape of the graph. Different black-body spectra can be seen in Fig. 2.2

As T_d increases, so does the characteristic peak of the black-body spectrum, with higher temperatures peaking at lower wavelengths, following Wien's displacement law, $\lambda_{max}T = 0.29$ cm K.

Within the black-body approximation, the thermal emissivity of dust can be described as:

$$j_{\nu,therm} = \rho\kappa_{\nu,abs}B_\nu(T). \tag{2.6}$$

The added emission from a dusty medium, to a beam of radiation passing through it, is determined by the volumetric cooling rate due to emission from the dust grains, Λ_d. Using the formulation of the emissivity of matter in Eq. 2.6, and replacing $\rho\kappa_{\nu,abs}$ with $n_d\sigma_d Q_{\nu,abs}$, and integrating over all solid angles,

$$\Lambda_d = 4\pi n_d\sigma_d \int_0^\infty Q_{\nu,abs}B_\nu(T_d)d\nu, \tag{2.7}$$

where n_d is the dust number density, σ_d is the dust cross section, and $Q_{\nu,abs}$ is the frequency dependent absorption efficiency. The dust grain cross section σ_d is given by

$$\sigma_d = \sigma_{abs} + \sigma_{scat}, \tag{2.8}$$

describing the cross section as a result of both absorption and scattering. $Q_{\nu,abs}$ is related to the absorption cross section σ_{abs} by

$$\sigma_{abs} = Q_{\nu,abs}\sigma_{geo}, \tag{2.9}$$

where σ_{geo} is the geometric cross-section, πr^2. Finally, this relates to the dust *absorption opacity* $\kappa_{\nu,abs}$ by

$$\kappa_{\nu,abs} = \sigma_{abs}/m, \tag{2.10}$$

where m is the dust particle mass. The absorption efficiency is dependent on the morphology, chemical composition, and size of the dust grains. In the most simple treatment, a spherical dust grain consisting of a refractory core with an icy-mantle is used. The core is usually assumed to consist of silicates who are able to reproduce the characteristic 10 μm feature observed in SEDs of YSOs, while the icy-mantle is a mixture of H_2O, CO and other molecules (Fig. 2.3).

As can be seen in Eq. 2.6 and Fig. 2.2 + 2.3, the emissivity of dust is strongly temperature and wavelength dependent.

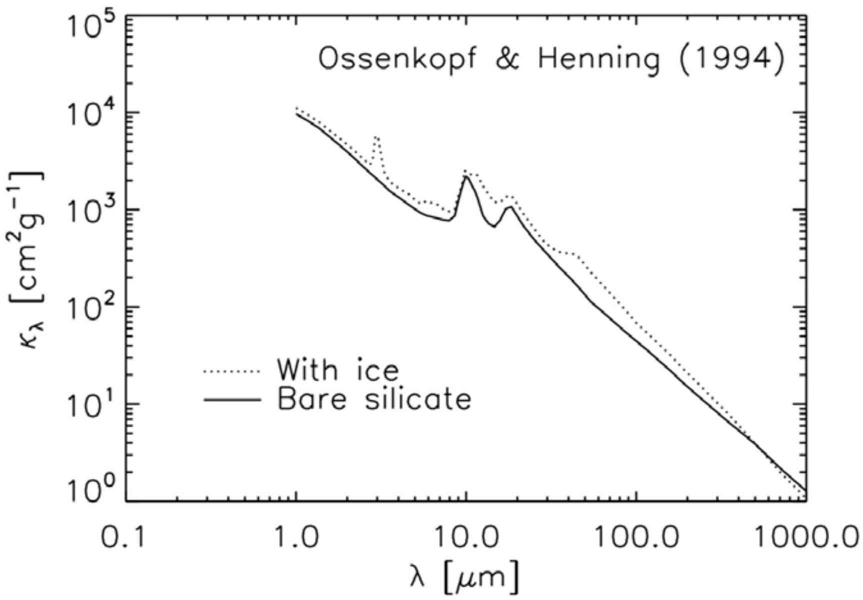

Figure 2.3: The wavelength dependent absorption opacity of dust with an ice-mantle and bare silicate grains, from Ossenkopf & Henning (1994). Credit: C.P. Dullemond.

2.1.1 *Dust thermal equilibrium*

If we wish to derive the dust density distribution in a dense envelope surrounding a protostar, based on the received light, then we have to estimate the dust temperature. Ignoring other sources of energy such as friction in viscous accretion, the dust in protoplanetary environments is heated by radiation from the protostars. The dust grains are very effective in capturing optical and IR photons (Fig. 2.3), which serves to heat the dust grains. The dust heating of a single grain depends on its opacity and the protostellar radiation $F_{\nu,*}$,

$$\Gamma_d = \int_0^\infty \kappa_{\nu,abs} F_{\nu,*} d\nu. \tag{2.11}$$

The cooling of the dust grain is given by

$$\Lambda_d = 4\pi \int_0^\infty \kappa_\nu B_\nu(T_d) d\nu. \tag{2.12}$$

These two terms must be equal in order for the dust to exist in thermal equilibrium. The dust thermal equilibrium can be solved numerically through Monte Carlo simulations of radiation from a protostar, propagating through a dusty medium, as done by the numerical code `RADMC-3D`. Using such numerical codes, astronomers can simulate the physical environment of protostellar cores and in PP-disks around young protostars. Using ray-tracing, synthetic observations can be made of these modeled environments, which can be compared with actual observations, in order to constrain the environment of protostellar cores and PP-disks.

2.1.2 *Line radiative transfer*

While dust grains emit as black-bodies, which has a smooth transitioning spectrum, gas line emission results from the transitions between different energy levels of the molecule. This emission is governed by the Einstein coefficients A_{li} (spontaneous emission, via change from energy state l to i), B_{li} (induced emission) and B_{il} (photo absorption, exciting the molecule to a higher energy state) for the transitions between two adjacent energy levels, with an energy difference of $h\nu = E_l - E_i$.

The emission and absorption coefficients are given by the equations,

$$j_{\nu,gas} = \frac{h\nu}{4\pi} n_l A_{li} \phi(\nu) \tag{2.13}$$

and

$$\alpha_{\nu,gas} = \frac{h\nu}{4\pi} (n_i B_{il} - n_l B_{li} \phi(\nu)), \tag{2.14}$$

where n_i and n_l are the fractional populations of molecules in the two molecular energy levels, h is Plancks constant, and $\phi(\nu)$ is a function of frequency, containing several line broadening mechanisms, where line broadening from local turbulence is usually dominant (Brinch & Hogerheijde, 2010).

The relevant local mean radiation field can be found by solving Eq. 2.2 and integrating the resulting intensity over all solid angles,

$$J_\nu = \frac{1}{4\pi} \int I_\nu d\Omega. \tag{2.15}$$

The gas molecule is excited either via photo-absorption or through collisions with other gas molecules (Brinch & Hogerheijde, 2010). In a gas population, the collision rate between gas molecules with the two energy levels i and l, is given by

$$C_{il} = \frac{g_l}{g_i} c_{il} \exp\left(-\frac{hc}{k_B T_{\text{gas}}}(E_l - E_i)\right), \tag{2.16}$$

where g_i is the statistical weight of the i'th level and c_{il} is the molecule dependent rate coefficients, which are usually dependent on the local gas kinetic temperature. E_i is the energy of the molecule energy level. The molecular excitation depends on J_{il}, the radiation field of photons with the exact same energy as the energy difference between the two levels i and l, and their collision rate C_{il}. Both the absorption and emission coefficients in Eq. 2.13 and 2.14 depend on the fractional population of the i'th level n_i, which is given by

$$n_i = \frac{\Sigma_{l>i} n_l A_{li} + \Sigma_{l \neq i} n_l \left(B_{li} J_{li} + C_{li}\right)}{\Sigma_{l<i} A_{il} + \Sigma_{l \neq i} \left(B_{il} J_{il} + C_{il}\right)}, \tag{2.17}$$

when statistical equilibrium is assumed between the different gas molecule energy levels in the medium. Eq. 2.17 describes the balance between level population loss to spontaneous, collisional and photon induced level transition to other levels and the gain from the same mechanisms in other energy levels. Since J_{il} depend on n_i through Eq. 2.13 and 2.14, Eqs. 2.17 and 2.15 presents a recursive problem, which has to be solved iteratively (Brinch & Hogerheijde, 2010). This can be with a line radiative transfer code, such as `LIME` (Brinch & Hogerheijde, 2010).

2.2 RADIATIVE TRANSFER CODES

This section is a digest of selected aspects of the `RADMC-3D` *v. 0.41 manual and Brinch & Hogerheijde (2010)*

In my PhD studies I have used the radiative transfer codes `RADMC-3D` and `LIME` for dust continuum and gas line emission radiative transfer modeling, respectively. `RADMC-3D` uses the Bjorkman & Wood (2001) Monte Carlo method to simulate the propagation of light through a dusty medium. `RADMC-3D` uses a predefined grid of dust cells through which discrete photon packages, from a radiation source, moves. As the photon package enters a dust cell, a fraction of the energy will be absorbed or scattered (change direction) in the cell. In the event of absorption, the dust cell will immediately re-emit the photon package in a random direction, with a new wavelength chosen according to the scheme of Bjorkman & Wood (2001), with the luminosity fraction represented by the photon package kept intact. Every time a photon package enters a cell, the dust temperature is increased, whether or not absorption has taken place. As the photon packages move and scatters around in the grid, each cell will be visited multiple times by different photon packages. Eventually, the photon packages will reach the edge of the grid at which point the radiation is regarded as having escaped the system. The dust temperature in each cell at this point is regarded as the final temperature. Due to the stochastic nature of the dust temperature assignment, it is important to have an adequate number of photon packages, to avoid a noisy and streaky dust temperature distribution in the model.

`LIME` is a non-LTE (Local Thermal Equilibrium) line radiative transfer code, which uses a random grid point distribution weighted by molecular density, in a Delaunay triangulated grid, to model protostellar environments (Brinch & Hogerheijde, 2010). The photons propagate in the Delaunay grid, which has an average grid point separation that scales with the local opacity. The local radiation field is calculated at each discrete model node which represents a parcel of dust and gas. The level population of the nodes is calculated iteratively and the synthetic spectral cubes produced using ray-tracing of the grid. `LIME` can simultaneously model multiple lines, which, together with its allowance of fully 3D models, makes it highly useful and versatile for modeling the gas line emission from young stellar environments.

2.3 APERTURE SYNTHESIS INTERFEROMETRY

In order to observe structures smaller than 1/36000th of a degree in the sky, which corresponds to a spatial scale of 20 au for a target at a 200 pc distance, we need excellent observing instruments. The instrumental journey towards this angular resolution has been a long and arduous one. Galileo was the first to fashion a telescope for astronomy use, which he utilized to discover four of Jupiter's moons in 1610. Over the following centuries optical telescopes were used to investigate the Solar System bodies nearby stars and objects of the Milky Way.
The diffraction limit of a telescope is determined by the observed wavelength, λ, and the aperture, D, of the telescope, according to Rayleigh's criterion

$$\theta \approx 2.5 \times 10^5 \frac{\lambda}{D} \mathrm{arcsec}. \tag{2.18}$$

In principle, if we desire a higher angular resolution at a specific wavelength, in order to observe very small structures on the sky, we need only build a larger telescope. The largest non-segmented optical telescope on Earth is the Large Binocular Telescope (LBT) with two 8.4 m telescopes. Reflecting telescopes larger than this, are made of segmented, usually hexagonal, mirrors on a computer controlled mount, since larger single glass-lenses start to distort under their own weight. Segmented mirrors will be implemented in the next generation of extremely large telescopes, including the 39 meter Extremely Large Telescope[2] (ELT) in the Atacama Desert in Chile and the Thirty Meter Telescope[3] (TMT) on Mauna Kea in Hawaii, both planned for first light within the next decade.

While a reflecting telescopes such as the ELT will have an angular resolution of $\sim 0.01''$ at 2 μm (Eq. 2.18), optical wavelengths and the near-IR are ill-suited for the observations of deeply embedded star forming regions, due to their opacity at these wavelengths owing to the vast amounts of opaque dust. Instead, astronomers take advantage of the fact that the dust opacity drops dramatically at (sub)mm

2 http://www.eso.org/public/teles-instr/elt/
3 https://www.tmt.org/

wavelengths (see Fig. 2.3), where we can peer directly into the heart of these regions and observe protoplanetary disks forming and evolving. However, we now face a serious issue, as the diffraction limit means that the angular resolution is inversely proportional with wavelength.

A radio telescope with the size of the ELT would only resolve 6.4″ at 1 mm (Eq. 2.18), corresponding to 1280 au at 200 pc, useful for studying large-scale envelopes around protostars, but inadequate for studying the hot corino scales (expected to be no larger than ~ 100 au scales, see Maret et al., 2004) of Class 0 objects. As such, we need subarcsecond resolution to resolve these regions. Radio telescopes use a metal dish, instead of a heavy glass lens, to concentrate the (sub)mm electromagnetic radiation into a receiver where the signal is amplified and digitized for analysis. For this reason, radio telescopes can be constructed to much larger diameters than optical telescopes, though they too are size-limited by their own weight. Steerable radio telescope dishes can be constructed up to about 100 meters, where the Green Bank telescope[4] currently holds the record. This aperture size offers us an angular resolution of ~ 2.5″ at 1 mm, still not enough to effectively investigate hot corinos or forming PP-disks. While single-dish radio telescopes, built into natural depressions of the ground, can have much larger apertures, such as the 305 m dish of the Arecibo observatory[5] and the recently constructed Five-hundred-meter Aperture Spherical radio Telescope (FAST) in Guizhou province, China, they are impaired by a limited field of vision, owing to their static nature. Moreover, these radio telescopes are only 497 m and 1000 m above sealevel, for Aricebo[6] and FAST (Nan et al., 2011), respectively, meaning that large amounts of water vapor block the emission in the (sub)mm regime (see Fig. 2.9). For this reason, these telescopes operate in the cm to meter regime.

In order to have high angular resolution in the (sub)mm regime, as well a near full field-of-view of the sky, we need more advanced technology than that of a single-dish telescope.

2.3.1 *Aperture synthesis*

Aperture synthesis is the combination of several antennae for observations of a single target, using interferometry. While interferometer arrays usually have many more antennae, the basic principle can be understood using a two-antennae interferometer as an example (Fig. 2.4).

4 urlhttp://greenbankobservatory.org/telescopes/gbt/
5 urlhttp://outreach.naic.edu/
6 http://www2.naic.edu/~astro/guide/node2.html

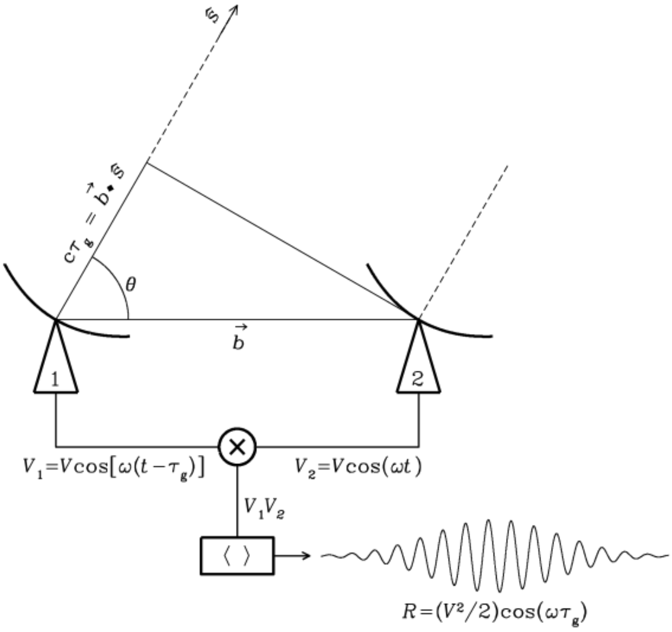

Figure 2.4: A two-telescope interferometer. $\hat{s}$ is the unit vector of the target source, $\vec{b}$ is the distance vector between the telescopes, and τ_g is the time delay. Credit: James J. Condon & Scott M. Ransom.

The two antennae in Fig. 2.4 are separated by a distance, **b**, which causes a time delay, τ_g, in the signal. The voltage of each antennae is given by

$$V_1 = V\cos\left(\omega(t-\tau_g)\right) \tag{2.19}$$
$$V_2 = V\cos\left(\omega t\right), \tag{2.20}$$

where ω is the angular frequency and t is time. The signals from the antennae are then multiplied together in a correlator,

$$< V_1V_2 > = V^2\cos\left(\omega t\right)\cos\left(\omega(t-\tau_g)\right) \tag{2.21}$$
$$R_c = \frac{V^2}{2}\cos\left(\omega\tau_g\right), \tag{2.22}$$

where R_c is the cosine response of the correlator, seen in Fig. 2.4. In order to relate the electric response of the correlator with the sky brightness distribution, which is what we desire, we need to visit the Van Cittert-Zernike theorem.

2.3.2 *Van Cittert-Zernike theorem*

This subsection is a digest of, and uses the same terminology of, the lecture notes[7] on the course 'Observational astronomy', by C. P. Dullemond, University of Heidelberg.

7 http://www.ita.uni-heidelberg.de/~dullemond/lectures/obsastro_2011/chap_interferometry.pdf

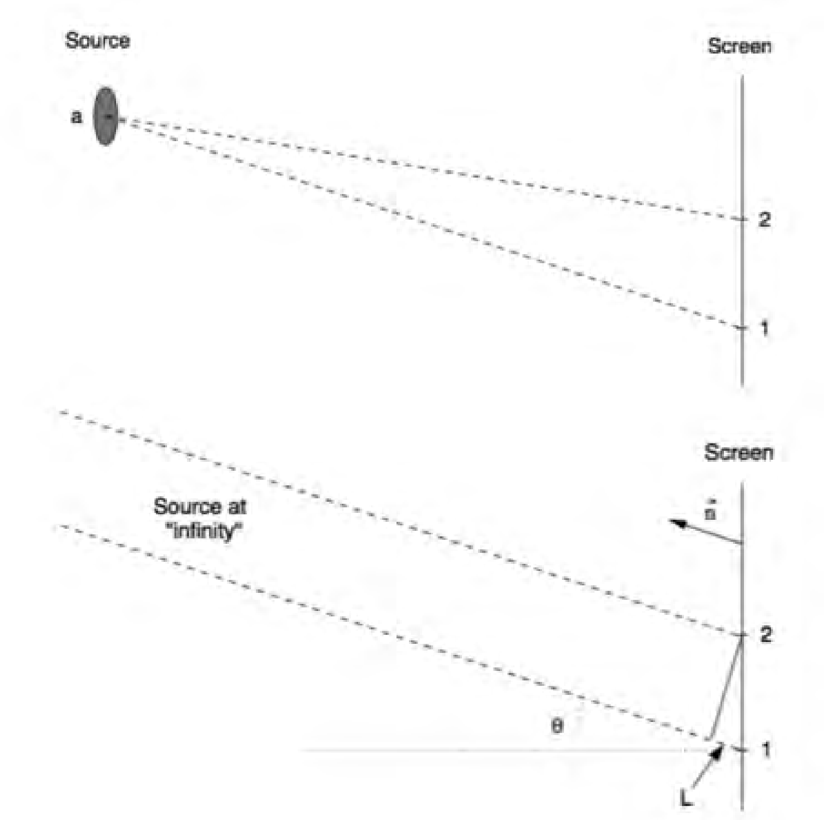

Figure 2.5: The electromagnetic radiation of a source **a** impinges on two points '1' and '2' on a screen (top panel). Moved to a great distance, the electromagnetic waves will appear parallel to each other as they encounter points '1' and '2' (bottom panel). Credit: C. P. Dullemond.

The Van Cittert-Zernike theorem (van Cittert, 1934; Zernike, 1938) details the spatial coherence of emission from a far away source, impinging on different points on a screen. If we consider a distant object **a** on the sky and two locations, '1' and '2', receiving electromagnetic radiation from **a**, the great distance will ensure that the distance to either point from the source, $d_{1,2}$, is much greater than the distance between points '1' and '2', i.e., $d_{1,2} \gg |\vec{r_2} - \vec{r_1}|$, and the average distance from the source to the two points is $d = (d_1 + d_2)/2$.

The electric field at the source itself, point **a**, is

$$E_a(t) = A_a e^{-2\pi\nu t}, \tag{2.23}$$

where A_a is a complex number, constant in time. The electric field from point **a** to to '1' will lessen in amplitude as $|E| \sim 1/d$ and have phase-shift relative to **a** as d_1/c, since the electric field from **a** reaches point '1' at a time $t + d_1/c$. The electric field at point '1' is then

$$E_1(t) \simeq \frac{\sqrt{\Delta S_a}}{d} A_a \exp\left[-2\pi i\nu\left(t - \frac{d_1}{c}\right)\right], \tag{2.24}$$

where $\Delta\ S_a$ is the source surface area, inside a square-root since we add together mutually non-coherent emitting regions, where the electric field amplitude will grow as $\sqrt{N}$ times that of a single region. We used d in the denominator of the electric field equation (Eq. 2.24), so we have d^2 in the denominator of Eq. 2.26, since $d_{1,2} \approx d$. The spatial coherence of the received light in points '1' and '2' is given by;

$$\langle E_1^*(t)E_2(t)\rangle = \frac{1}{T}\int_0^T \frac{\Delta S_a}{d^2} A_a^* A_a \exp\left[-2\pi i\nu\left(\frac{d_2 - d_1}{c}\right)\right] dt \quad (2.25)$$

$$= \frac{\Delta S_a}{d^2} A_a^* A_a \exp\left[-2\pi i\nu\left(\frac{d_2 - d_1}{c}\right)\right]. \quad (2.26)$$

Since $d_{1,2} \gg |\vec{r_1} - \vec{r_2}|$, the two light rays are essentially parallel (Fig. 2.5, bottom panel). If $\vec{n}$ is a unit vector pointing toward point **a** on the sky, then

$$d_1 - d_2 = \vec{n} \cdot (\vec{r_2} - \vec{r_1}), \quad (2.27)$$

which enables us to write the coherence as

$$\langle E_1^*(t)E_2(t)\rangle = \frac{\Delta S_a}{d^2} A_a^* A_a \exp\left[-2\pi i\nu\left(\frac{\vec{n}\cdot(\vec{r_2} - \vec{r_1})}{c}\right)\right]. \quad (2.28)$$

This is a 3D equation, but if the screen shown in Fig. 2.5 is treated as a 2D plane, and we take the z-axis to be perpendicular to the screen and define $\vec{r} = \vec{r_2} - \vec{r_1}$, then we have

$$\vec{n} \cdot (\vec{r_2} - \vec{r_1}) = \vec{n} \cdot \vec{r} = n_x r_x + n_y r_y, \quad (2.29)$$

as $r_z = 0$, since $\vec{r}$ lies in the plane of the screen. (n_x, n_y) is then a vector describing the angular position of the source **a** on the sky, while (r_x, r_y) is the 2D baseline between the points '1' and '2' on the screen. We then have

$$\langle E_1^*(t)E_2(t)\rangle = \frac{\Delta S_a}{d^2} A_a^* A_a \exp\left[-2\pi i\nu\left(\frac{n_x r_x + n_y r_y}{c}\right)\right]. \quad (2.30)$$

This shows that the radiation fields between '1' and '2' are correlated, but with a phase-shift of

$$\delta\phi(r_x, r_y) = \nu\frac{n_x r_x + n_y r_y}{c}. \quad (2.31)$$

This is the result for the single emitting region **a**. If we instead have an extended source, we can treat it as a continuous series of **a** regions. Steps in n_x and n_y are related to the sky surface area as

$$dS_a = d^2 dn_x dn_y \quad (2.32)$$

which leads to

$$\langle E_1^*(t)E_2(t)\rangle = \int A^*(n_x,n_y)A(n_x,n_y) \exp\left[-2\pi i\nu\left(\frac{n_x r_x + n_y r_y}{c}\right)\right] dn_x dn_y. \tag{2.33}$$

Since $A(n_x, n_y)$ depend on n_x and n_y, we can integrate over the desired segment of the sky. Eq. 2.33 is actually a Fourier integral with r_x/λ and r_y/λ as wavenumbers in the x- and y directions (these wavenumbers are usually given as u=r_x/λ and v=r_u/λ in interferometric equations, defining the *uv-plane*). The Fourier transformed integrand is $A^*(n_x,n_y)A(n_x,n_y)$, which is the intensity $I(n_x,n_y)$ of the source on the sky. Thus, the correlation, called the *visibility*, between points '1' and '2' is the Fourier transform of the sky brightness distribution. We can now measure the sky brightness distribution by using isolated telescopes at different positions, and analyzing the correlation of their voltage responses.

The Van Cittert-Zernike theorem is the heart of modern radio astronomy, but does come with a few assumptions. The source emission must consist of incoherent light and the target source distribution be so far away that we can approximate the incoming light as a planar wave (Fig. 2.4).

2.3.3 *Imaging*

This subsection is a digest of, and uses the terminology of, lecture notes by Dale Gary[8] (New Jersey Institute of Technology) and Jonathan Williams[9] (University of Hawaii).

The baseline vectors are given as *(u,v)* points in the plane of the array 2.7, with each baseline pair defining one unique point in *uv*-space. For an array of N telescopes, we have $N(N-1)/2$ interferometer pairs. Since we need to fill out as much of the (u,v) plane as possible, to maximize our information on $I(x,y)$, we would need to construct an impossible large number of antennae in order to fill the uv-plane, if not for a helpful physical phenomena; the rotation of the Earth. As the Earth rotates and the array is fixed on the sky target, astronomers can sample the uv-plane in paths defined by Earths rotation. The exact shape of this induced rotational pattern, depends on the latitude of the telescope array; an array perfectly at either pole will form a circle, while an array at the equator will be form a line (Fig. 2.7). This technique is called *Earth-rotation aperture synthesis.*

8 https://web.njit.edu/~gary/728/Lecture6.html
9 http://www.ifa.hawaii.edu/users/jpw/classes/alma/lectures/imaging.pdf

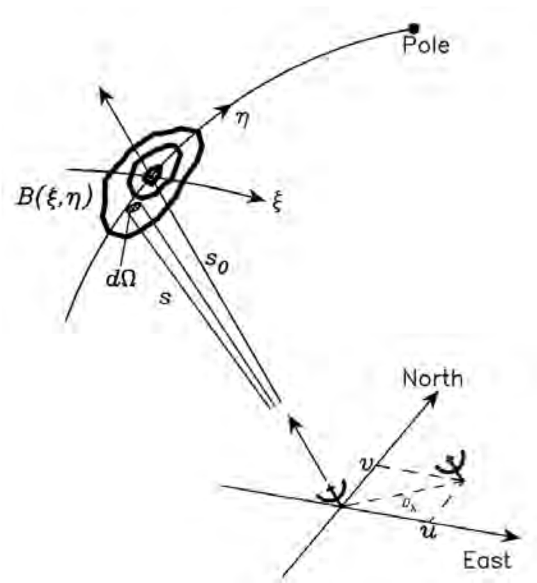

Figure 2.6: A two-telescope interferometer in an interferometer array on Earth, composing a single unique baseline in the uv-plane, centered on the bottom telescope. The source with a solid angle of dΩ, part of a larger structure B(ξ, η), and vector s is shown on the sky (ξ, η) plane, with a reference center on the sky vector S_0. D_λ is the projected distance between the telescopes, in units of wavelength. Credit: Adopted from a figure by Chin-Fei Lee, Academia Sinica, Taiwan.

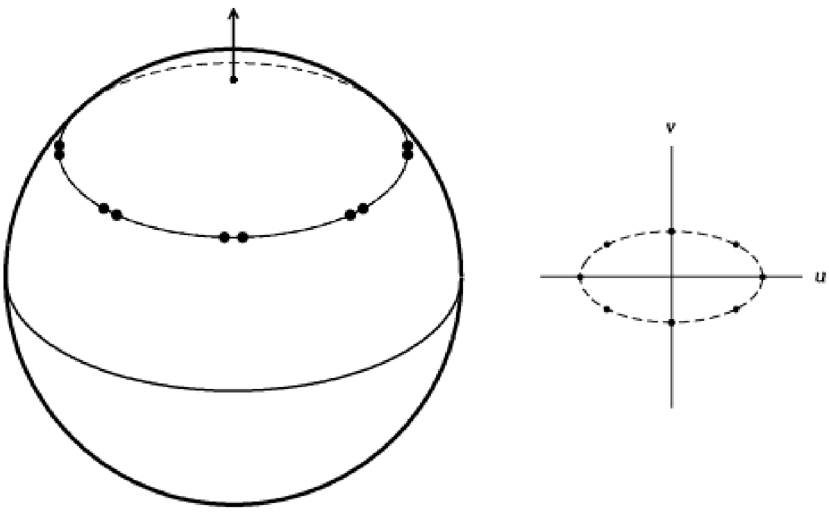

Figure 2.7: A two-telescope interferometer describing an elliptic path on the uv-plane, due to Earths rotation. Credit: J.J. Condon & S.M. Ransom.

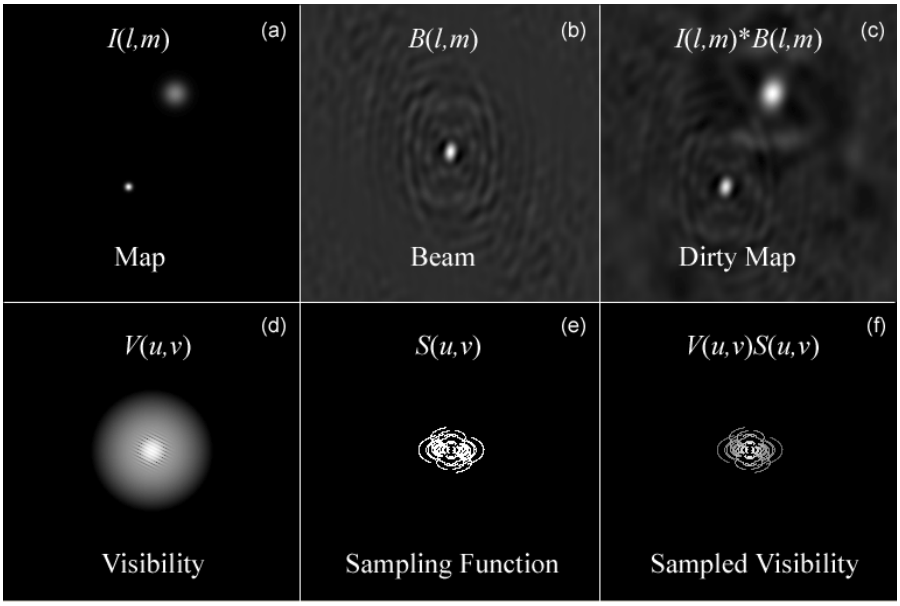

Figure 2.8: (a) The true image map with the sky coordinates (l, m), (b) the synthesized beam $B(l, m)$, (c) the dirty map, (d) the true visibility of the source, (e) the sampling function, and (f) the sampled visibility. Credit: Dale E. Gary (New Jersey Institute of Technology).

The available baselines form a sampling function $S(u, v)$ of the true visibility $V(u, v)$ in the *uv*-plane. The image we would get from using our sampled visibility, $S(u, v)V(u, v)$, is called the dirty image, I_d;

$$I_d = \mathcal{F}^{-1}[S(u, v)V(u, v)], \tag{2.34}$$

where $\mathcal{F}^{-1}$ is the inverse Fourier transform (FT). Using the convolution theorem, which states that a Fourier transform of the product of two functions is equal to the convolution of the individual Fourier transforms, we have

$$I_d = \mathcal{F}^{-1}[S(u, v)] * \mathcal{F}^{-1}[V(u, v)], \tag{2.35}$$

which means that I_d is the inverse FT of the sampling function, convolved with the true brightness distribution. $\mathcal{F}^{-1}[S(u, v)]$ is the synthesized beam of the observations (the point-spread-function (PSF) of our array). In order to retrieve the true sky brightness distribution $I(x, y)$, we need to deconvolve the dirty map $I_d(x, y)$. The artifacts seen in the dirty map is caused by the incomplete sampling of the source visibility. These sampling artifacts need to be handled in order to better estimate $I(x, y)$ (Fig. 2.8).

This is done with powerful computer algorithms, the most common being the `clean` algorithm.

2.3.3.1 `Clean` *algorithm*

The `clean` algorithm (Högbom, 1974) assumes that the true image is composed by discrete point sources, and models these point-sources iteratively;

- `Clean` finds the pixel with the peak emission in $I_d(x, y)$ and subtracts a scaled dirty beam, centered on this pixel, from the dirty map.
- A fraction of the point source is added to the `Clean` model and convolved with a restoring Gaussian beam, called the *`Clean` beam*.
- The two above steps are performed iteratively until the remaining flux in the dirty map is below a given threshold.
- The residual dirty map is added to the `Clean` model, which serves as an estimate of the noise in our final image.

This algorithm is the most widely used algorithm in radio astronomy for constructing an image from the sampled visibilities. The retrieved image resolution is dependent on the baselines of the observations. Short spacings retrieve broad sinusoids in the Fourier plane, i.e., large, extended structures on the sky, while large baselines retrieve narrow sinusoids, corresponding to small angular structures. The user must be aware that the incomplete sampling affect the `clean` model image, as the deconvolution process delivers an *approximation* of the true sky brightness distribution. As such, the image output from the `clean` algorithm is non-unique. For this reason, some researchers choose to convert their brightness source models and compare with observations directly in *uv*-space, if they have sparse *uv*-coverage. However, this is only feasible for relatively simple structures, such as a spherical envelope and disk, or a disk alone. If the source structure is complicated, such as the inner regions of IRAS 16293, comparisons should be done in image-space.

2.4 ALMA

The information in this section is from the ALMA webpage[10].

The most advanced (sub)mm interferometer array in the world is the Atacama Large Millimeter/submillimeter Array (ALMA). Situated on the Chajnantor Plateau, in the Atacama desert, at ~ 5 km above sea level, the arid climate and the height of the plateau reduces the broad absorption bands of water vapor in the atmosphere, which provides good conditions for observing submillimeter and millimeter emission (Fig. 2.9).

10 `https://almascience.eso.org/`

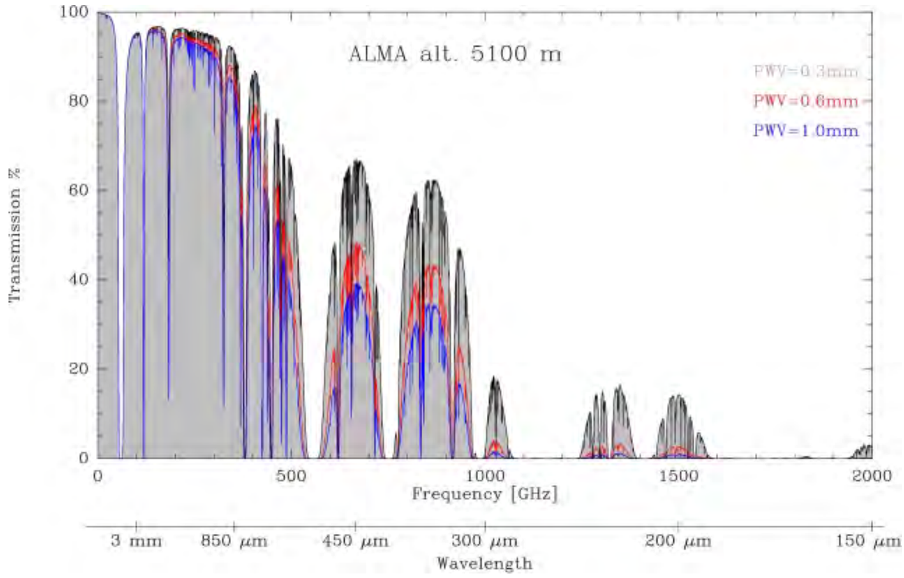

Figure 2.9: The transmission spectrum of the atmosphere above the ALMA site, at different levels of the precipitable water vapor (PWV). Higher levels of PWV rapidly decline the transmission through the atmosphere, showcasing the importance of using dry and high sites for interferometer arrays. Credit: N. Schneider.

ALMA is composed of a 12-m diameter array with 50 antennas and the Atacama Compact Array (ACA), which has twelve 7-m diameter antennas and four 12-m diameter antennas (Fig. 2.10). ALMA has a dynamic spatial configuration, allowing the individual antenna to be moved around on the plateau, enabling a variety of baselines, tailored to the observation requirements. For Cycle 6, in Band 7, the maximum baseline[11] of ALMA is ~ 8.5 km, enabling high angular resolutions of ~0.03″ at 868 μm, while ACA, which is in a tight configuration, provides the shorter baselines necessary for detecting extended structures.

ALMA has provided significant insights into star formation not only due to the unprecedented high angular resolution, but also due to the high sensitivity of the array, used to achieve a high signal-to-noise ratio (SNR) at high angular resolution. The sensitivity of ALMA is unparalleled at mm and submm wavelengths, which has offered key insights into star formation such as rings and gaps of nearby PP-disks, which are thought to indicate current planet formation, see Fig. 1.7.

11 https://almascience.eso.org/proposing/proposers-guide#section-54

Figure 2.10: ALMA array on the Chajnantor Plateau, Atacama desert, Chile. Credit:ESO/B. Tafreshi (twanight.org).

3 THE RESEARCH

3.1 SHORT DESCRIPTION

The field of star formation has taken dramatic strides in the last few decades, thanks to advances in instrumentation as well as the development of advanced algorithms and numerical codes used for simulation of the protostellar environments. Observations of the complex physics and chemistry in protostellar systems were previously hampered by poor angular resolution, which created uncertainty about which physical structures the molecules were related to. The advent of ALMA and its unprecedented high angular resolution and sensitivity, allowed complex structures in star forming regions to be resolved. Prime examples are the ring-shaped emission dips in the PP-disk of HL Tauri (ALMA Partnership et al., 2015), see Fig. 1.7, hypothesized to indicate planet formation, and the direct imaging of hot corinos (e.g., Jørgensen et al., 2016). The wealth of data and the great increase in the observed spatial complexity compared to earlier single-dish studies, require a new generation of 3D models for data interpretation, as earlier 1D models only approximate the protostellar envelope. In order to take full advantage of the high angular resolution supplied by ALMA, highly detailed 3D models of the protostellar environment are necessary.

A major issue in modern astrochemistry is the unknown physical origin of the observed COMs. It is still unknown if the observed emission lines of COMs in the innermost regions close to the protostars originate from embedded disks or from the warm inner parts of the envelope, where passive heating releases the molecules from the dust ice-mantles, i.e., a hot corino (Codella et al., 2016). In order to resolve this issue, we need radiative transfer models with sufficient details on $<$100 au scales, to rule out or confirm the different scenarios for the appearance of COMs in the gas phase, using high angular resolution ALMA observations.

In order to gauge the extent of the hot corino, and to estimate the chemistry taking place within, it is essential to have a realistic physical model of the environment, in terms of the dust and gas density, and temperature. Modeling of the sublimation of individual molecule species off the dust grains has, since the early 2000s, taken the standard approach of modeling abundances quantitatively using varying density and temperature models, with a gas phase abundance jump (e.g., Schöier et al., 2002). This jump is usually of a factor of 100, at the sublimation temperature of the given molecule, with the prototypical low-mass YSO IRAS 16293 being the target of a great part of these efforts (Schöier et al., 2002; Coutens et al., 2012). The analysis and quantification of abundances of the early discoveries of COM emission lines in IRAS 16293 was hampered by the large beamsizes, well larger than any hot corino region (van Dishoeck et al., 1995). Modeling efforts were limited to 1D envelope models due to limited angular resolution, and considerable uncertainty was associated with analysis of the COMs, since the assumed physical conditions in the innermost regions near the protostars were based on extrapolated values from the envelope of IRAS 16293 (Ceccarelli et al., 2000; Schöier et al., 2002). With the recent direct imaging of the hot corinos around the two radiation sources in IRAS 16293 (e.g., Pineda et al., 2012; Jørgensen et al., 2016), it is necessary to quantify the immediate environment of each protostar in terms of dust and gas density, and temperature, in order to analyze the COMs. This analysis of the environment can be used to constrain the abundances and column densities of the COMs within. Also, characterizing the hot regions around each protostar as either Kepler disks or rotating-collapsing material, would allow us to relate the COMs to either structure. In the last decade, a range of 3D coding tools, capable of performing non-LTE excitation and radiative transfer, became available, enabling researchers to accurately simulate complex, three-dimensional YSO environs (Brinch & Hogerheijde, 2010; Dullemond et al., 2012).

These new computational capabilities, together with the advent of sensitive, high-angular resolution interferometers such as ALMA, enables us to create a new generation of models powerful enough to take on the complicated and vast amounts of information contained in the ALMA observations of the innermost regions of low-mass YSOs.

3.2 PUBLICATIONS

The research done throughout my PhD is presented in three papers, shown in Chapters 4, 5 and 6. The research articles presented in this thesis are;

1. Jacobsen et al. 2018, in press: The ALMA-PILS survey: 3D modeling of the envelope, disks and dust filament of IRAS 16293.

2. Jacobsen et al. 2018, submitted: The organic chemistry in the innermost, infalling envelope of L483.

3. M.H.D. van der Wiel, S.K. Jacobsen, et al. 2018, in prep.: The ALMA-PILS survey: gas dynamics in IRAS 16293 and a connection between its two protostars.

3.2.1 *Paper I: The ALMA-PILS survey: 3D modeling of the envelope, disks and dust filament of IRAS* 16293 *:*

The first paper presents a complex 3D radiative transfer model of the envelope, disks and dust filament of the Class 0 object IRAS 16293. Dust and gas radiative transfer analysis were used to probe the dust density distribution closest to the two protostars, as well as the individual luminosities of the two sources for the first time. Due to the complex geometry of the inner warm envelope of IRAS 16293, it was necessary to create a complex 3D model in order to recreate the morphology of the observed 868 μm continuum emission and ^{13}CO J=3–2, C^{17}O J=3–2, and C^{18}O J=3–2 gas line emission. The first step was to find a dust density model which matched both the general 868 μm continuum emission morphology as well as the peak emission intensity towards each of the two radiation sources, IRAS 16293A and IRAS 16293B, using the radiative transfer code `RADMC-3D`. A dust density model with a filament of material joining the two protostars, and a disk- or disk-like dust distribution around each of the two protostars, was found to match the continuum morphology. Two separate dust density models for the disk regions were used; the density solution to an infalling-rotating collapse, which results in a flattened envelope structure, and a Keplerian disk in hydrostatic equilibrium with the host stars gravity. The dust density model parameters, which satisfied the constraints, were then used in an analysis of the ^{13}CO J=3–2, C^{17}O J=3–2, and C^{18}O J=3–2 gas line emission. The dust density distribution was imported into the line radiative transfer code `LIME`, and under the assumption of a gas-to-dust mass ratio of 100, the molecular abundances were varied until a reasonable match with the observed line emission intensities was found.

The exact density distribution in the disk-like domains could not be determined, as both a Kepler disk and the density solution to an infalling-rotating collapse could satisfy the constraints. However, any Kepler disk around IRAS 16293B would have to be unusually vertically extended in order to match the observations. The individual luminosities of the protostars were found to be $L_A \geqslant 18\ L_\odot$ and $L_B \leqslant 3\ L_\odot$, based on both the 868 μm continuum and C^{17}O J=3–2 gas line emission. This is the first time the individual luminosities of the two protostars have been estimated. The detailed density model and the self-consistent temperature structure we have derived, can be used in future works, for line emission analysis used to derive molecular abundances and column densities, or for chemical modeling. As such, we have taken strides, compared to earlier 1D models, in estimating the physical and chemical structure of this chemically rich Class 0 protostellar system.

3.2.2 *Paper II: The organic chemistry in the innermost, infalling envelope of L483 :*

The second paper presents high-angular resolution observations of the hot corino in the Class 0 object L483, made with ALMA Cycle 1 and 3 data. The Cycle 1 and 3 data were combined and used to image the $H^{13}CN$ *J*=4–3, HCN *J*=4–3, HCO^+ *J*=4–3, and CS *J*=7–6 emission in order to probe larger structures, while the Cycle 3 data was used to catalog and directly image the COMs present in the gas phase. The kinematics of the $H^{13}CN$ *J* =4–3 and CS *J* = 7–6 emission, from both the combined dataset and the Cycle 3 data, strongly favored the velocity profile of infall with conservation of angular momentum, and not a Keplerian velocity profile, revealing that no Keplerian disk is present in L483 down to at least 15 au. Inside this radius a Kepler disk may exist. We used the density solution to a rotating-infalling collapse to match the observed integrated 857 µm flux density and to estimate the temperature structure of the innermost regions of L483. We find a $T_{100\ K}$ radius of ~ 55 au, which matches the observed extent of the COM emission lines (40–60 au radius). This suggests that the observed COM emission lines in the gas phase arise from molecules sublimated off the dust grains in the hot inner region of the envelope, and not from a Keplerian disk.

3.2.3 *Paper III: The ALMA-PILS survey: gas dynamics in IRAS 16293 and a connection between its two protostars:*

The third paper presents an analysis of IRAS 16293 using observations of molecular gas line transitions of CO, H_2CO, HCN, CS, SiO and C_2H to trace the kinematics, density, and temperature of the protostellar binary. The transitions reveal new manifestations of the previously known outflows from source A, while kinematic analysis of the bridge of dust and gas between the two sources reveal it be quiescent and contained within a narrow velocity range close to the systemic velocity of the system. Only $C^{17}O$ *J*=3–2 and the dust continuum is found to trace the bridge of gas and dust, while all other observed gas line emission structures trace the known outflows from source A. Blue-shifted emission from H_2CO , $H^{13}CN$ and $C^{34}S$ appear to trace the interface between the dust bridge and the north-west outflow, where the outflow could be sweeping up material from the bridge in its wake. A redshifted outflow structure appears to trace the northernmost section of a known east-west outflow (Yeh et al., 2008).

Gas line emission modeling of H_2CO and $H^{13}CN$ was made with `LIME`, using the best-fitting model from Paper I, which does not include any outflow structures, but matched the observed dust continuum and $C^{17}O$ *J* = 3–2 emission well. Jumps in abundance with a factor of 100 were made in the models when the dust temperature reached 50 and 100 K, respectively for H_2CO and $H^{13}CN$, mimicking sublimation into the gas phase from the dust grain ice-mantle. While the observed $C^{17}O$ traces the bridge, and can be matched morphologically by the bridge model, the observed H_2CO emission could not be entirely matched, as clear outflow structures are present in the observations. Modeled $H^{13}CN$ emission was not seen in the bridge region, as only the disk-like regions near source A and B were dense and hot enough to produce any noticeable emission. This suggests that the observed $H^{13}CN$ is not affiliated with the bridge region through thermal release of $H^{13}CN$ from passively heated dust grains, but is likely associated with the outflows instead. None of the outflow structures are seen to be unambiguously related to source B, which leads us to conclude that source B is in an earlier evolutionary stage than source A.

3.3 OUTLOOK

The high-angular resolution and sensitivity of ALMA has enabled the research presented in the three papers, but in order to validate our interpretations of IRAS 16293, as well as investigating the protostellar binary further, we require new ALMA observations at the maximal angular resolution, such as $\sim 0.03''$ in Band 7 (868 μm). This would enable us to finally identify the disk-like structures around source A and B as either an early stage structure, such as the flattened envelope arising from a rotating-collapse, or as established Keplerian disks. At the same time, we could get a better estimation of the exact distribution of COMs and which physical structure they are affiliated with.

Regarding L483, higher angular resolution in the most extended configuration of ALMA for Band 7, would give a factor three increase in angular resolution. This would allow us to constrain the kinematics of the innermost region even further, and possibly identify the small Keplerian disk within 15 au of the central protostar, if it exists. An unbiased spectral survey of L483 over a larger bandwidth than our Cycle 3 data, similar to the ALMA-PILS survey of IRAS 16293, could be useful. It would enable the production of a molecular inventory list of L483 to be compared with other hot corinos in Class 0 objects. Such observations would increase our understanding of the chemistry at this evolutionary stage and how it ties in to the Keplerian disk below a 15 au radius, or the lack of a disk if it is found to be non-existent.

The custom software library I have developed during my time as a PhD student, which I will refer to as `radlipy` (*`RADMC-3D` -`LIME` -using-Python*) was tailored for the protostellar binary IRAS 16293. `radlipy` includes separate disk-like domains, rotatable in inclination and the azimuth, and a dust filament which can be inclined towards or away from the observer, embedded in a larger 1D envelope model with or without a central density plateau. For future modeling projects of IRAS 16293, be it with the current PILS dataset or with new, higher angular resolution observations, it would be natural to use my `radlipy` 3D model of IRAS 16293 as a starting point. This would be the case regardless of whether the interbinary region or the individual disk structures are the target(s) of the analysis. New physical structures, inside existing ones, can easily be added to the model, thanks to the code architecture. `radlipy` can also model protostellar environments with a single protostar, surrounded by a disk, a rotating collapse around the central protostar, or an 1D envelope model with a density plateau. As such, `radlipy` was also used to model the dust density structure around L483 .

The real power of `radlipy` is the interface between `RADMC-3D` and `LIME`, which allows `LIME` to calculate the gas line emission of any molecular species which would arise in the density model, with the dust temperatures estimated by `RADMC-3D`. `LIME` only requires a gas-to-dust mass ratio and a molecular abundance relative to H_2, and that the molecular data needed for excitation analysis can be supplied from databases such as the `LAMDA` database (Schöier et al., 2005a).

3.4 OWN CONTRIBUTION TO WORK

This section describes my contribution to the three papers presented in Chapters 4, 5 and 6.

PAPER I The observational data were reduced prior to this project (see Jørgensen et al., 2016). All software development and modeling was done by me. The entire manuscript was written by me, while co-authors read and commented the paper with any changes implemented by me. All tables and figures were made by me.

PAPER II While calibrated Cycle 1 and 3 data were delivered to me, I self-calibrated and combined the data. I also performed all the imaging done to produce scientific images and spectra. The line fitting and analysis presented in Section 5.3.1, excluding the last paragraph, and Section 5.3.2 was done by Jes K. Jørgensen. The rest of the manuscript was written by me. All figures and tables were made by me, except Table 5.4 and Fig. 5.1 which were made by Jes K. Jørgensen, while we both contributed to Table 5.2. Co-authors read and commented the paper with any changes, not pertaining to Section 5.3.1 and 5.3.2, implemented by me.

PAPER III I managed and ran all the `LIME` models of the H_2CO and $H^{13}CN$ gas line emission, and supplied the model emission results shown in Fig. 6.5. I co-wrote Section 6.1 with M.H.D. van der Wiel. I wrote minor parts of Section 6.4.1, while the remainder of Section 6.4.1 was written by M.H.D. van der Wiel, but in close consultation with me, as it pertained details and interpretation of my models and their results. All radiative transfer model results and extracted values were supplied by me. I read and commented the entire manuscript.

Part II

PUBLICATIONS

4

PAPER I: THE ALMA-PILS SURVEY: 3D MODELING OF THE ENVELOPE, DISKS AND DUST FILAMENT OF IRAS 16293–2422

S. K. Jacobsen[1], J. K. Jørgensen[1], M. H. D. van der Wiel[1,2], H. Calcutt[1], T. L. Bourke[3], C. Brinch[4], A. Coutens[5,6], M. N. Drozdovskaya[7], L. E. Kristensen[1], H. S. P. Müller[8], S. F. Wampfler[7]

[1] Centre for Star and Planet Formation, Niels Bohr Institute and Natural History Museum of Denmark, University of Copenhagen, Øster Voldgade 5–7, DK-1350 Copenhagen K, Denmark
[2] ASTRON, the Netherlands Institute for Radio Astronomy, Postbus 2, 7990 AA Dwingeloo, The Netherlands
[3] SKA Organization, Jodrell Bank Observatory, Lower Withington, Macclesfield, Cheshire SK11 9DL, UK
[4] Niels Bohr International Academy, Niels Bohr Institute, University of Copenhagen, Blegdamsvej 17, 2100 Copenhagen Ø, Denmark
[5] Laboratoire d'astrophysique de Bordeaux, Univ. Bordeaux, CNRS, B18N, allée Geoffroy Saint-Hilaire, 33615 Pessac, France
[6] Department of Physics and Astronomy, University College London, Gower St., London, WC1E 6BT, UK
[7] Center for Space and Habitability (CSH), Universität Bern, Sidlerstrasse 5, CH-3012 Bern, Switzerland
[8] I. Physikalisches Institut, Universität zu Köln, Zülpicher Str. 77, 50937 Köln, Germany

Accepted for publication in *Astronomy & Astrophysics* 2018, in press.

Context. The Class 0 protostellar binary IRAS 16293–2422 is an interesting target for (sub)millimeter observations due to, both, the rich chemistry toward the two main components of the binary and its complex morphology. Its proximity to Earth allows the study of its physical and chemical structure on solar system scales using high angular resolution observations. Such data reveal a complex morphology that cannot be accounted for in traditional, spherical 1D models of the envelope.

Aims. The purpose of this paper is to study the environment of the two components of the binary through 3D radiative transfer modeling and to compare with data from the Atacama Large Millimeter/submillimeter Array. Such comparisons can be used to constrain the protoplanetary disk structures, the luminosities of the two components of the binary and the chemistry of simple species.

Methods. We present ^{13}CO, C^{17}O and C^{18}O J=3–2 observations from the ALMA Protostellar Interferometric Line Survey (PILS), together with a qualitative study of the dust and gas density distribution of IRAS 16293-2422. A 3D dust and gas model including disks and a dust filament between the two protostars is constructed which qualitatively reproduces the dust continuum and gas line emission.

Results. Radiative transfer modeling in our sampled parameter space suggests that, while the disk around source A could not be constrained, the disk around source B has to be vertically extended. This puffed-up structure can be obtained with both a protoplanetary disk model with an unexpectedly high scale-height and with the density solution from an infalling, rotating collapse. Combined constraints on our 3D model, from observed dust continuum and CO isotopologue emission between the sources, corroborate that source A should be at least six times more luminous than source B. We also demonstrate that the volume of high-temperature regions where complex organic molecules arise is sensitive to whether or not the total luminosity is in a single radiation source or distributed into two sources, affecting the interpretation of earlier chemical modeling efforts of the IRAS 16293-2422 hot corino which used a single-source approximation.

Conclusions. Radiative transfer modeling of source A and B, with the density solution of an infalling, rotating collapse or a protoplanetary disk model, can match the constraints for the disk-like emission around source A and B from the observed dust continuum and CO isotopologue gas emission. If a protoplanetary disk model is used around source B, it has to have an unusually high scale-height in order to reach the dust continuum peak emission value, while fulfilling the other observational constraints. Our 3D model requires source A to be much more luminous than source B; $L_A \sim 18\ L_\odot$ and $L_B \sim 3\ L_\odot$.

4.1 INTRODUCTION

Stars form inside the dense cores of interstellar cold clouds of gas and dust. During the gravitational collapse of the dense core material, the slow rotation of the core itself will eventually cause a protoplanetary disk to appear, due to the conservation of angular momentum (Cassen & Moosman, 1981). When exactly such disks are formed and how they evolve through their early stages remain poorly understood (see, e.g., Li et al., 2014, for a review). Well established disks around T Tauri stars or Class II young stellar objects have been widely reported and studied extensively (e.g., see Andrews et al., 2009; Ricci et al., 2010). Due to the low spatial resolution of the observations used in earlier studies, the emission from the disks in Class 0 and Class I sources have been mixed with the emission from the massive amounts of dust in the ambient protostellar envelope, making detection and characterization of disks in Class 0 sources very difficult (Jørgensen et al., 2005a; Chiang et al., 2008; Jørgensen et al., 2009), with only a small number of Class 0 disks with indicated Keplerian rotation being detected so far (Tobin et al., 2012; Murillo et al., 2013; Ohashi et al., 2014; Lindberg et al., 2014; Codella et al., 2014). Jørgensen et al. (2009) detect compact mm continuum emission around several Class 0 objects, but it is unknown whether these dust components represent rotationally supported Keplerian disks. The exact transition from early density structures to a rotationally supported Keplerian disk is still uncertain, though some tentative observations of the so-called centrifugal barrier, where the infalling, rotating envelope transitions into a rotationally supported disk, have been made (Sakai et al., 2014a; Oya et al., 2016). These inner regions around embedded protostars are also particularly interesting from a chemical point of view. Observational studies of Class 0 objects have revealed complex organic molecules (e.g., Bottinelli et al., 2004b; Kuan et al., 2004; Bottinelli et al., 2004a; Jørgensen et al., 2005a; Bisschop et al., 2008a; Jørgensen et al., 2011; Maury et al., 2014), as well as active chemistry in the so-called hot corino region, where water and organic molecules are sublimated into the gas-phase from the dust grain surface (Schöier et al., 2002).

A particularly interesting source in this context is IRAS 16293–2422 (hereafter IRAS 16293), a nearby binary protostar in the ρ Ophiuchus cloud complex, composed of at least two components, IRAS 16293A and IRAS 16293B (Wootten, 1989; Mundy et al., 1992; Looney et al., 2000). IRAS 16293 is one of the most well-studied low-mass protostars, particularly in terms of astrochemistry; IRAS 16293 was the first low-mass star for which complex organics (van Dishoeck et al., 1995) and prebiotic molecules (Jørgensen et al., 2012) were detected. The source IRAS 16293A appears to be highly active with several detected outflows, while IRAS 16293B is more quiescent, with no known outflows (e.g., Chandler et al., 2005; Kristensen et al., 2013). Alves et al. (2012) find that the magnetic field strengths in IRAS 16293 are comparable to the outflow ram pressure, and thus that the magnetic field is dynamically important for this system. Both components are embedded within a larger, circumbinary envelope of dust and gas, which has been well studied in previous works using single-dish data and 1D radiative transfer modeling (Schöier et al., 2002; Jørgensen et al., 2005b; Crimier et al., 2010a). These models all use a single central radiation source, where disks or complex structures, such as a dust and gas filament, have never been included in the radiative transfer calculations. The single-star approximation is not a problem at large distances from the interbinary region as the two sources can then be approximated as a single source, especially if one source is more luminous than the other. In contrast, in the interbinary region, two sources are needed in order to estimate the temperature structure. The total luminosity is $L = 21 \pm 5\ L_\odot$ (Jørgensen et al., 2016), while the luminosity ratio of the two protostars is unknown. IRAS 16293 has been, and continues to be, under intense observational scrutiny due to its rich chemistry and any chemical modeling must assume the parameters of the physical environment in terms of dust and H_2

density, temperature structure and the local radiation field. An assessment of the individual luminosities of the sources in IRAS 16293 is crucial for chemical modeling, especially for warm gas-phase chemistry in the hot corinos.

In this paper, we construct a 3D model, including disks, a filament and two radiation sources using high angular resolution data from the ALMA Protostellar Interferometric Line Survey (PILS) as observational constraints. The impact of the binary nature of IRAS 16293 on the temperature distribution is evaluated as opposed to that of a single star. As stellar binaries are abundant, especially in the Class 0 stage (Tobin et al., 2016b), this temperature evaluation of IRAS 16293 is useful as a case study on the temperature distribution in the environment of protostellar binaries in wide orbits, found in large fractions of star-forming regions (e.g., Duchêne et al., 2004), as well as a retrospective analysis on the validity of previous works approximating a binary as a single protostar in their radiative transfer modeling, which will be useful for data-mining. This work is part of a new generation of complex 2D and 3D radiative transfer models describing Class 0 YSOs (see e.g., Yang et al., 2017), which were previously modeled with 1D envelope models.

After the observations and the general radiative transfer setup are described in Sections 4.2 and 4.3, the paper is divided into three parts: Section 4.3.5 supplies a general investigation of temperature structures in Class 0 objects and the difference between having one or two central radiation sources in a 1D model of a collapsing envelope.

Section 4.4 shows a 3D model of the dust density structure of IRAS 16293, where we used a dust continuum image at 868 μm and the spectral energy distribution (SED) as constraints. Finally, new ALMA-PILS observations of the CO isotopologues ^{13}CO, $C^{17}O$ and $C^{18}O$ are used in Section 4.5 to further constrain the physical conditions in the innermost region of IRAS 16293, ending with an evaluation of the nature of the disks, their vertical distribution and the luminosity ratio between the sources, offering a significant increase in physical complexity from earlier models as well as the first luminosity evaluation of the individual sources.

4.2 OBSERVATIONS

The PILS program (PI: Jes K. Jørgensen, project-id: 2013.1.00278.S) is an unbiased spectral survey of IRAS 16293, covering a significant part of ALMA's Band 7, corresponding to a wavelength of roughly 0.8 mm, as well as selected windows of ALMA's Bands 3 and 6, corresponding to ~3 mm and ~1.3 mm, respectively. The Band 7 data cover the frequency range from 329.15 to 362.90 GHz with ~0.2 km s^{-1} spectral resolution and $\sim 0.5''$ angular resolution (60 AU beam diameter, assuming d=120 pc). The pointing center was set between source A and

B at α_{J2000} = $16^h32^m22\overset{s}{.}72$; δ_{J2000} = $-24°28'34\overset{''}{.}3$. Further details about the survey, data reduction and an overview of the observations can be found in Jørgensen et al. (2016).

In this paper, we focused on the 868 μm continuum and CO isotopologue data, which include data from both the array of 12 m telescopes and the Atacama Compact Array (ACA), allowing both compact and extended structures to be detected. The continuum image was taken as an average of the Band 7 continuum in each channel (Jørgensen et al., 2016). The 868 μm dust continuum shows broad extended emission, enveloping both sources. Around each source, emission structures consistent with disks are observed. Source A appears to host a disk close to edge-on, while the emission around source B appears more circular, that is, suggestive of a face-on disk. The continuum is much brighter toward source B, peaking at 2.0 Jy beam^{-1}, while source A has a more extended and weaker continuum, peaking at 1.0 Jy beam^{-1} (Fig. 5.1).

The dust continuum images from Bands 3 and 6 were not used in this work due to lower spatial resolutions than the Band 7 data, which confuses the disk structures with the filament.

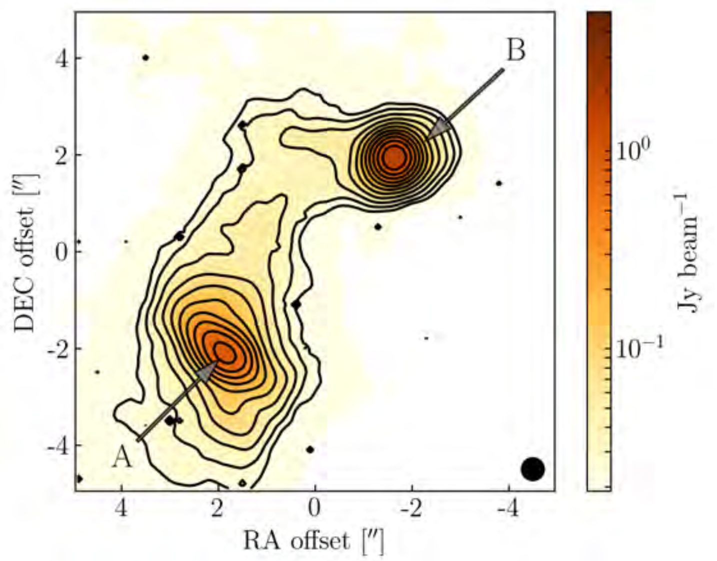

Figure 4.1: Dust continuum at 868 μm, in log-scale. Contour levels are logarithmically divided between 0.02 and 2 Jy beam^{-1}. The RA and DEC offsets are relative to the phase center of the observations. Beamsize is shown in bottom right corner.

The gas line emission from the J=3–2 transitions of three CO isotopologues, ^{13}CO (330.588 GHz, Klapper et al., 2000), C^{18}O (329.331 GHz, Klapper et al., 2001) and C^{17}O (337.061 GHz, Klapper et al., 2003) were extracted from the dataset, using the entire pixel map, after the lines were identified. The source A LSR velocity of 3.1 km s^{-1} (Jørgensen et al., 2011) was used for all lines. Channels within ± 5 km s^{-1} of each line were combined into an integrated intensity (moment zero) map for each isotopologue, using the image analysis software MIRIAD. Using this approach, the vast majority of the observed line emission was extracted, while avoiding major line-blending from other species.

Integrated emission maps

Figure 4.2 shows the integrated intensity maps of the three isotopologues. $C^{17}O$ appears to trace the dust distribution fairly well, as does the $C^{18}O$ emission. ^{13}CO, however, shows a markedly different emission structure, which is likely attributable to optical depth effects, where only the outer layer of the ^{13}CO structure is probed. Absorption toward source B is evident in all lines but to a smaller extent in $C^{17}O$, revealing that $C^{17}O$ is the line with the lowest optical depth, as expected since it has the lowest abundance (Wilson & Rood, 1994). An interesting feature is the broad emission arc between the sources, which is also present in the dust continuum emission, suggesting a common origin of both the dust and gas emission in this region. We focused on the overall structure of the emission and left a more detailed analysis of the gas kinematics to a future paper (Van der Wiel et al. in prep.).

4.3 DUST RADIATIVE TRANSFER MODELING

This Section describes the setup of the radiative transfer code RADMC-3D, including a description of the dust opacity, model grid and the envelope dust density model used. At the end of the Section, we present our investigation of the temperature structure difference between a single- and a binary protostar, where the envelope dust density model was used. We constructed 3D dust and gas line radiative transfer models consisting of a large envelope with a radius of 8×10^3 AU based on Schöier et al. (2002), two disks around the protostars, as well as a dust filament between the two protostars. The disk's dust densities were modeled with both the model protoplanetary disk (PP-disk) structure known from Class II sources (e.g., Andrews et al., 2012) and the density solution from the angular momentum conservation of an infalling, rotating collapse (Terebey et al., 1984). This infalling, rotating collapse density structure is hereafter referred to as a rotating toroid model, based on the toroidal shape appearing at the centrifugal radius (Terebey et al., 1984), which is the radius where the infalling material with the largest angular momentum impacts the midplane. In terms of luminosity, all models, whether they used one or two radiation sources, were limited to a total luminosity of 21 $L_\odot$. This luminosity is based on integration of the SED using data from *Spitzer*, ISO-LWS, *Herschel*/SPIRE and submillimeter data (Chandler et al., 2005; Correia et al., 2004; Makiwa, 2014; Schöier et al., 2002), where the luminosity is estimated to be 21 ± 5 $L_\odot$ (Jørgensen et al., 2016). This luminosity assumes a distance of 120 pc, based on recent distance estimates of the bulk of the ρ Oph cloud from extinction measurements (Knude & Hog, 1998; Lombardi et al., 2008) and VLBI parallax (Loinard et al., 2008). The interbinary distance was fixed to 636 AU for all models, based on the angular distance of $\sim 5.3''$ between the peaks of the 868 μm ALMA image, with the caveat that this distance, in reality, is only the projected, that is, the minimum distance between the sources.

4.3.1 *RADMC-3D*

To determine the dust temperature and to produce continuum images, the radiative transfer code `RADMC-3D` (Dullemond et al., 2012, v. 0.40)[1] was used. `RADMC-3D` uses the Bjorkman & Wood (2001) algorithm to perform a Monte Carlo simulation of photon propagation from one or more radiation sources, through a predefined grid of dust density cells, in order to estimate the dust equilibrium temperature. This equilibrium is a balance between the incoming radiative energy and the blackbody emission from the dust cell itself. The code setup in this work assumed that all the dust energy originated from the protostars through irradiation, and not from any internal energy source such as viscous accretion, or any external radiation source. The precision of the resulting dust equilibrium temperature depends, among other parameters, on the number of photons used in the radiation simulation (this differed between model setups, see Table 4.1).

We ignored scattering, since the absorption opacity dominates over the scattering opacity in the submillimeter regime (Dunham et al., 2010). `RADMC-3D` was also used to calculate the SED (see Appendix 4.9.1) and to produce synthetic continuum images (see Section 4.4.3).

4.3.2 *Grid*

We constructed a spherical grid of cells for use in the `RADMC-3D` radiative transfer calculations, resolved linearly in the polar and azimuthal angle ranges, while the radial dimension was divided into an inner and outer region. The inner region with constant dust density (i.e., $r \leqslant r_{\text{plat}}$, see Eq. 4.1) was resolved linearly, while $r > r_{\text{plat}}$ (containing the bulk mass of the cloud) was resolved logarithmically. In the disk components, of the global model, octree refinement was performed (splitting a grid cell into eight new grid cells), with two refinement levels, to ensure that the density gradients of the disk component models were resolved, see Table 4.1. If a PP-disk model was used, then the inner 10 AU of the disk was refined two times further, for a total of four octree refinements, to resolve the inner gap and nearby

1 http://www.ita.uni-heidelberg.de/~dullemond/software/radmc-3d/

Table 4.1: RADMC-3D model parameters

Parameter	Description	Value
Grid		
r_{out}	Envelope radius	8×10^3 AU
r_{in}	Grid start radius	5 AU
r_{plat}	Radius of the density plateau	600 AU
n_θ	Number of grid cells in the polar range	131
n_ϕ	Number of grid cells in the azimuthal range	131
Temperature analysis		
$n_{r,\,out}$	Number of grid cells in the outer radial region ($r > 600$ AU)	88
$n_{r,\,in}$	Number of grid cells in the inner radial region ($r \leqslant 600$ AU)	110
$n_{photons}$	Number of photons used in thermal Monte Carlo process	5×10^7
L_A	Luminosity of source A	3 – 20 $L_\odot$
One radiation source		
r_{oct}	Octree refinement radius around source	400 AU
$n_{octree\ levels}$	Octree refinement number	1
Two radiation sources		
r_{oct}	Octree refinement radius around each source	250 AU
$n_{octree\ levels}$	Octree refinement number	2
IRAS 16293 model		
$n_{r,\,out}$	Grid cells in the outer radial region ($r > 600$ AU)	22
$n_{r,\,in}$	Grid cells in the inner radial region ($r \leqslant 600$ AU)	110
$\rho_{0,\,env}$	Envelope reference density at $r_{0,\,env}$	2.5×10^{-14} g cm^{-3}
$r_{0,\,env}$	Envelope reference radius	1 AU
p_{env}	Envelope density power-law exponent	1.7
M_A	Source A stellar mass	1 $M_\odot$
M_B	Source B stellar mass	0.1 $M_\odot$
$^\dagger T_{eff}$	Star surface temperature	5000 K
L_A	Source A luminosity	3 – 20 $L_\odot$
$r_{0,\,disk}$	PP-disk reference radius	10 AU
$r_{inner\ disk}$	Disk inner radius	1 AU
$r_{disk,A}$	Disk A radius	150 AU
$r_{disk,B}$	Disk B radius	50 AU
Disk constraints		
$F_{peak,\,A}$	Peak flux density toward source A	1.0 Jy beam^{-1}
$F_{peak,\,B}$	Peak flux density toward source B	2.0 Jy beam^{-1}
Disk A aspect ratio	...	1.64
$N_{H_2,\,B}$	Disk B column density	$\geqslant 1.2 \times 10^{25}$ cm^{-2}
PP-disk models		
Σ_A	Parameter space for reference surface density of PP-disk A at 10 AU	0.1 – 5.0 g cm^{-2}
Σ_B	Parameter space for reference surface density of PP-disk B at 10 AU	1.0 – 12.0 g cm^{-2}
Ψ	Parameter space of the PP-disks flaring constants	0 – 0.25
p	Parameter space of the PP-disks dust density radial power-law exponents	0.5 – 1.5
$H_{0,A}$	Parameter space of PP-disk A scale-height at 10 AU	0.85 – 2.0 AU
$H_{0,B}$	Parameter space of PP-disk B scale-height at 10 AU	0.85 – 3.0 AU
i_A	Parameter space of PP-disk A inclination, 90° is edge-on	30 – 90°
$n_{lev,\,disk}$	Octree refinement level of entire disk	2
$n_{lev,\,in\ disk}$	Octree refinement level in innermost region	4
$n_{photons}$	Number of photons used in thermal Monte Carlo process	10^7
Rotating toroid models		
$r_{c,\,A}$	Parameter space of the centrifugal radius of rotating toroid A	50 – 100 AU
$r_{c,\,B}$	Parameter space of the centrifugal radius of rotating toroid A	5 – 40 AU
$\dot{M}_A$	Parameter space of the mass accretion rate into source A	1.0×10^{-6} – 5.5×10^{-6} $M_\odot$ yr^{-1}
$\dot{M}_B$	Parameter space of the mass accretion rate into source B	1.0×10^{-6} – 5.5×10^{-6} $M_\odot$ yr^{-1}
$n_{lev,\,disk}$	Octree refinement level of entire disk	2
$n_{lev,\,in\ disk}$	Octree refinement level in innermost region	2
$n_{photons}$	Number of photons used in thermal Monte Carlo process	10^6
Dust arc		
ρ_0	Reference density	2.5×10^{-17} g cm^{-3}
r_{out}	Filament radius from filament center	130 AU
Filament semi-minor axis	...	170 AU
Filament semi-major axis	...	300 AU

Notes: Model parameters for each setup. L_B is always defined as $L_B = 21.0\ L_\odot$ - L_A. †The radiation spectra of both source A and B are treated as blackbodies with a temperature of 5000 K, following Schöier et al. (2002).

structure properly, as geometric effects such as self-shadowing onto the outer disk became important.

4.3.3 *Dust opacity & temperature*

We used dust opacities from Ossenkopf & Henning (1994), which are good approximations for dense cores (van der Tak et al., 1999; Shirley et al., 2002, 2011). Opacity tables of dust with thin ice-mantles and another with bare dust grains were used, assuming coagulated dust grains with an ambient gas number density of 10^6 cm^{-3}. These dust opacity tables are generally used for models of dust around deeply embedded protostars, including IRAS 16293 (e.g., Schöier et al., 2002; Jørgensen et al., 2005b; Crimier et al., 2010a). The dust opacity was allocated in the cells in a self-consistent manner, with the first RADMC-3D thermal Monte Carlo photon propagation done in a model of purely icy-dust opacities. Grid cells with temperatures above the assumed water sublimation temperature were then allocated bare-grain dust opacities for the next photon propagation. We did not change the sublimation temperature to account for the local environment in terms of pressure but instead used a single sublimation temperature of 90 K (Sandford & Allamandola, 1993). As the cell opacities were redefined, the cell dust equilibrium temperatures after the next photon propagation will be different, with some dust cells shifting from below to above 90 K and vice versa, that is, an opacity allocation error. For both disk component model types, this error was found to be negligible after two recursions (5 and 0.1 % relative to the total bare-grain dust mass, at 1σ, for the PP-disk model and the rotating toroid model, respectively). The higher error in the PP-disk model, even with ten times more photon packages than the rotating toroid model (Table 4.1), came from the very high dust densities necessary to match the observed peak flux density, especially in disk B. In contrast, the relatively more uniform dust density distribution in a rotating toroid model ensured good photon statistics in RADMC-3D, with a much lower photon number.
Therefore, two recursions of the bare-grain opacity allocation, that is, three Monte Carlo dust temperature estimations in total were performed in RADMC-3D, for a single parameter set. The dust temperature estimated in the final photon propagation was then used for all later computations with that parameter set.

4.3.4 *Dust envelope model*

The dust envelope was modeled with a 1D radial density power-law density distribution, as the envelope has been well-fitted previously by such models (e.g., Schöier et al., 2002). More complicated circumbinary envelope structures, such as an infalling, rotating circumbinary envelope were not considered, as we focused on the innermost region of IRAS 16293 in this work. Recent observations of GG Tau (Dutrey et al., 2014), as well as simulations of the same system (Nelson & Marzari, 2016) suggest that binary star formation results in partial clearing of the material in the innermost region where the protostellar binary resides. Based on the 868 μm continuum observation, we do not expect the interior to be completely evacuated of dust between the disks, but depleted instead, due to accretion into the two protostars and dynamical effects, as described by Nelson & Marzari (2016). A dust density plateau was used to imitate the mass depletion inside a given radius r_{plat}, meaning that we used a constant, rather than a radial power-law, density distribution in this inner region, while keeping the dust density distribution in the outer envelope as a power-law:

$$\rho(r) = \begin{cases} \rho_0 \left(\frac{r}{r_0}\right)^{-p} & \text{, if } r \geqslant r_{plat} \\ \rho_0 \left(\frac{r_{plat}}{r_0}\right)^{-p} & \text{, if } r < r_{plat}. \end{cases} \tag{4.1}$$

Where ρ is dust density, r is the distance to the model center, ρ_0 is the density at distance r_0 and r_{plat} is the radius of the density plateau. r_{plat} was fixed to 600 AU in all models, a distance we chose to ensure that the entire dust filament structure resided in this density plateau. We fixed $p = 1.7$, taken from Schöier et al. (2002).

4.3.5 *Envelope temperature structure*

In order to compare the temperature structure between a single star and a binary system, we used the dust envelope model from Eq. 4.1 with one or two radiation sources in `RADMC-3D`, without including the filament and disk component models. We were interested in the volume of regions with dust above 30, 50 and 90 K, as these temperatures roughly correspond to the sublimation temperatures of CO, H_2CO and H_2O, respectively (Jørgensen et al., 2015; Ceccarelli et al., 2001; Fraser et al., 2001; Sandford & Allamandola, 1993).

These gaseous species are often used as probes of the gas and dust in observations of star-forming regions. We followed Jørgensen et al. (2015) and used the sublimation temperature of CO at 30 K, assuming that the CO is mixed with water-ice on the grain surface, which is more realistic in the protostellar environment than pure CO ice, which has a lower binding energy and thus a lower sublimation temperature of 20 K (Jørgensen et al., 2015).

A walk through the parameter space of the dust reference density ρ_0, with $p = 1.7$, was performed with r_{plat} = 600 AU, L_* = 21 $L_\odot$ (if one source) and L_1 = 10.5, 14.0 or 18.0 $L_\odot$, which means that, accordingly L_2 would be 10.5, 7.0 or 3.0 $L_\odot$, in the case of two sources. The most important value is the central density plateau, ρ_{plat}, as the 90 K region, almost all of the 50 K region and the bulk of the 30 K region resides here (Fig. 4.11 in Appendix 4.11.1). A given volume difference in two different ρ_{plat} scenarios corresponds to a higher absolute difference in the mass of dust above the given temperature threshold (Fig. 4.3).

Across the sampled parameter space, as seen in Fig. 4.3, the single star scenario has larger 90 K volumes than the binary and larger 50 K volumes for regions of higher density. The differences in 50 K go up to ~ 25 %, normalized to the volume of dust above 50 K for a single star. This is more pronounced for the 90 K volumes, where the relative difference is almost up to 40 %. In the 30 K region, the binary system generally produced a slightly larger volume than the single star, with modest differences of 2 – 5 % in the total volume. In the case of IRAS 16293, with a total model mass of ~ 4 $M_\odot$ in this work, the differences are on the order of 5 – 20 % in the 50 – 90 K volumes.

Therefore, for observations of gaseous species such as CO, H_2CO and H_2O, where the abundances in the gas-phase are expected to increase with sublimation from the dust ice-mantles, two radiation sources should be included in the modeling of IRAS 16293, and of binaries with similar separations, as the total amount of sublimated gas will otherwise be overestimated. If one star of the binary dominates the luminosity, the single-source approximation becomes more valid (Fig. 4.3) and the overestimation of the sublimated gas becomes less important. The implications of these results for previous 1D chemical models of the hot corinos in IRAS 16293 are discussed further in Section 5.5.

4.4 DUST DENSITY STRUCTURES OF IRAS 16293

In this Section we present our analysis of the ALMA dust continuum image of IRAS 16293 at 868 μm, where we investigated the presence of disks, or disk-like structures, and a dust filament, using a 3D dust density model. The disk component models were fixed to 150 and 50 AU around source A and B, respectively, based on visual inspection of the angular sizes and emission morphology of the dust continuum. The protostellar masses of source A and B are unknown. Bottinelli et al. (2004b) and Caux et al. (2011) estimate $M_A \sim 1\ M_\odot$, assuming the observed gas lines originate from infalling material, while the narrow linewidths observed by Caux et al. (2011) toward source B provide an upper limit of 0.1 $M_\odot$, under the same assumption. Pineda et al. (2012) resolve the region around source A with a $2.2'' \times 1.0''$ beam and interpret a Position-Velocity (PV) diagram of methyl formate (CH_3OCHO) and ketene (H_2CCO) as Keplerian rotation around a central object of 0.53 $M_\odot$ and a disk inclination close to edge-on, based on the linewidths (though the inclination is not constrained). Oya et al. (2016) use gas line observations toward source A of higher spatial resolution ($0.6'' \times 0.5''$ beam) to conclude that a large part of the material around source A is undergoing a rotating collapse, down to 40 – 60 AU, within which a Keplerian disk is speculated to lie. The inclination of the rotating collapse is not constrained, with best fits to their ballistic model between 30° and 70° (where 90° is edge-on). The derived mass range by Oya et al. (2016) of 0.5–1.0 $M_\odot$, is dependent on the inclination and centrifugal barrier radius. The mass of 0.53 $M_\odot$ reported by Pineda et al. (2012) assumes exactly edge-on configuration and has lower spatial resolution than Oya et al. (2016), thus arguably interpreting material undergoing a rotating collapse as part of a Keplerian disk. Also, the analysis of the velocity gradients on 50 – 400 AU scales around source A by Favre et al. (2014), shows a rotating structure which cannot be explained by simple Keplerian rotation around a point mass but needs to take the enclosed mass into account. We used $M_A = 1.0\ M_\odot$ in this work. For source B, Pineda et al. (2012) find that the narrow linewidths from the gas in this region are consistent with a face-on disk. The aspect ratio upper limit of 1.1 from the disk emission around source B (Jørgensen et al., 2016) is also consistent with a nearly face-on disk structure. Thus, the analysis by Caux et al. (2011) with a derived mass of $\leqslant 0.1\ M_\odot$ seems valid and was used in this work. There have been reports of source A itself being a binary, based on cm emission (Wootten, 1989; Pech et al., 2010) and submm emission (Chandler et al., 2005) with a projected distance of roughly $0.4''$. The PILS program, with a comparable beam (Jørgensen et al., 2016), does not find evidence of the split into separate submm sources reported by Chandler et al. (2005), but this could be due to optically thick dust emission, as the PILS continuum image (868 µm) is at a shorter wavelength than the Chandler et al. (2005) image (~ 1 mm). While it is unclear whether source A is a binary or not, we modeled it as a single radiation source.

4.4.1 *Disk component model constraints*

The PILS interferometric beam of $0.5'' \times 0.5''$ is comparatively large compared to the continuum emission at 868 µm around the two radiation sources, with the strongest continuum emission extending roughly $0.5''$ around source B and with a semi-major axis of $1''$ for the elliptical emission around source A (Fig. 5.1). Since disk A appears close to edge-on, it should be possible to investigate the vertical distribution of dust with the continuum image. The model continuum emission around source A was fitted with a 2D Gaussian in a $2'' \times 2''$ box centered on the peak flux density pixel on source A, from which the aspect ratio of the semi-major axis to the semi-minor axis was derived from the fitted FWHM in the two dimensions. The observed 868 µm continuum emission in a $2'' \times 2''$ box around source A was found to have an aspect ratio of 1.64, which we required the model to match within 10 % along with the peak central flux density of source A within 10 %. The box of 2″ × 2″ was chosen to avoid the observed warped structure around source A at larger scales (likely belonging to the dust filament, see Fig. 5.1), a disk morphology we did not attempt to recreate in this work. We only required our continuum modeling to match the peak flux density of source B within 10 %, as more detailed structures are hard to distinguish with our resolution. The column density limit toward the optically thick source B peak continuum emission, which Jørgensen et al. (2016) derive to be $N_{H_2} > 1.2 \times 10^{25}$ cm^{-2}, was used as well. Any model which satisfied these constraints also needed to reproduce the general features in both the dust continuum emission arc between the sources and the three CO isotopologue maps. Including these, six constraints were available per disk component model (the four emission maps, plus the two individual disk constraints).

4.4.2 *Dust filament*

The arc of continuum emission (Fig. 5.1) is assumed to arise from a local dust density enhancement. We modeled this dust filament as an elliptical tube, extending between and enveloping the sources. Around each source, the dust filament was extended spherically up to 130 AU. The density was modeled as a radially dependent power-law distribution of $\rho = \rho_0 (r/\mathrm{AU})^{-1/4}$ as measured from the tube center, where ρ_0 is the reference density at 1 AU. As such the filament dust mass density was made to be independent of the distance to either source. The disk components were carved out inside the dust filament model, in a sphere of 150 and 50 AU around source A and B, respectively. No attempts were made to satisfy boundary conditions, resulting in density jumps in the model filament-disk boundary regions. For simplicity, the dust filament structure was kept in the plane of the sky, as were the two protostars. We fixed the filament model with a ρ_0 value, which matched the observed central arc emission with several different luminosity ratios (Fig. 4.4), see Table 4.1. We performed a sanity check using the maximum observed emission of 0.056 Jy Beam^{-1} in the filament to calculate a column density based on Eq. 5 in Jørgensen et al. (2007), assuming a dust temperature of 30 K. The dust column density of the filament was derived to be 9.9 g cm^{-2}, while the model column density was 9.7 g cm^{-2}, assuming a gas-to-dust mass ratio of 100. This match is not surprising as we used the same opacities as Jørgensen et al. (2007) and the optical depth through the model filament is low (~ 0.2).

4.4.3 *Disk component models*

The disk components were modeled with both a PP-disk and a rotating toroid model. In the PP-disk model, the dust distribution is based on hydrostatic equilibrium with the gravity of the host star (e.g., Andrews et al., 2012).
The following equations all use cylindrical coordinates. The disk scale-height, H_d, is

$$H_d(r) = H_0(r/r_0)^{1+\Psi}, \tag{4.2}$$

where r is the radius, H_0 is the scale-height at radius r_0 and Ψ is the flaring constant, controlling the vertical distribution of the dust above the disk midplane. The disk surface density, Σ, is

$$\Sigma(r) = \Sigma_0(r/r_0)^{-p}, \tag{4.3}$$

where p is a gradient parameter. Finally the dust density is

$$\rho_d(r,z) = \frac{\Sigma(r)}{H_d\sqrt{2\pi}} e^{-z^2/(2H_d^2)}, \tag{4.4}$$

where z is the height above the disk midplane.

The disk inner radius was fixed to 1 AU for both disks, with the dust density within 1 AU set to 10^{-25} g cm^{-3} ($n_{H_2} \sim 3$ cm^{-3}), effectively assuming a dust and gas evacuated inner gap. After the dust temperature of a given model was estimated in RADMC-3D, subsequent ray tracing produced a 868 μm continuum image, which, after convolution with a $0.5'' \times 0.5''$ beam using MIRIAD, was compared with the 868 μm ALMA continuum image in Fig. 5.1. The disk orientation for source B was fixed to face-on, while the inclination of PP-disk A was a free parameter.

Due to the high number of grid cells required to resolve the relevant regions and high photon numbers required for reliable dust temperature results, but most importantly the high densities in the inner disk regions of this work, the thermal Monte Carlo calculation execution time, on the available computing facilities, for a single model was very long, sometimes on the order of days. This problem was compounded by the iterative allocation of dust opacities, which requires three separate dust temperature estimations in RADMC-3D. Thus, standard model optimization approaches such as a Markov Chain Monte Carlo (MCMC) or a χ^2 analysis of a large, uniform grid of model parameters were not feasible in this work and no parameter confidence intervals were derived. Instead, we identified parameter spaces not compatible with the current constraints and derived conclusions from these parameter space exclusions.

4.4.4 *Model analysis*

Starting with the PP-disk model, large steps were taken in the parameter space of Σ_0 and H_0 for the disk around each source, and inclination for disk A (Table 4.1), while p and Ψ were fixed to 0.5 and 0.25, respectively (see Appendix 4.10 for more details). The final number of free parameters in the PP-disk model was four for disk A (Σ, H_0, i and source A luminosity, L_A) and two for disk B (Σ and H_0), since the source B luminosity, L_B, was determined by L_A.

When only using the continuum image, the PP-disk model did not offer any meaningful constraints on disk A and B. Due to the degeneracy between H_0 and i, only models with inclinations below 55° could be excluded. The peak flux values were degenerate with different Σ_0, H_0, L_* and i values and the column density toward source B did not offer any constraints either, as almost all of our investigated parameter space satisfied the N_{H_2} column density condition. Due to previous observations of infall toward both sources (Caux et al., 2011; Chandler et al., 2005; Pineda et al., 2012; Zapata et al., 2013; Oya et al., 2016), we considered the rotating toroid model. The dust density distribution of this model can be found semi-analytically by defining discrete streamlines from the rotating envelope, which spiral inwards and impact opposing streamlines in the midplane, creating a disk structure. From Hartmann (2009),

$$\rho(r,\theta) = \frac{\dot{M}\left(1+\frac{\cos\theta}{\cos\theta_0}\right)^{-1/2}}{4\pi\sqrt{GM_* r^3}}\left(\frac{\cos\theta}{\cos\theta_0}+\frac{2\cos^2\theta_0}{r/r_c}\right)^{-1}, \tag{4.5}$$

where $\dot{M}$ is the mass accretion rate onto the central object, θ_0 is the starting polar angle of the streamline in question and r_c is the centrifugal radius. The density in each grid cell in our model was found by predefining $n_{\rm stream}$ streamlines with discrete θ_0 values and evaluating them at n_r radial points, along the streamline. A nearest-neighbor search was performed, with the dust density of the `RADMC-3D` grid cell defined to be that of the nearest defined streamline point. The rotating toroid model is effectively a 2D density model and a 3D velocity model (Hartmann, 2009).

The rotating toroid model has a radially extended dust distribution with $\rho \propto r^{-0.5}$ and a much more vertically extended dust distribution than the exponentially decreasing vertical distribution of the PP-disk model (Eq. 4.4). Consequently, the rotating toroid model has a much lower optical depth through the midplane, hence higher dust temperatures, than a PP-disk model with, for example, H_0 = 0.85 AU (this example value was taken from the range in Andrews et al., 2010).

The centrifugal radius of the collapse around source B ($r_{c,B}$) was a free parameter between 5 – 25 AU, to allow a compact toroid within the defined model disk B regime of 50 AU, fixed to face-on inclination. We fixed the inclination of the rotating toroid model around source A

Table 4.2: Example dust model parameters.

PP-disk model	L_A [$L_\odot$]	L_B [$L_\odot$]	$\Sigma_{0,A}$ [g cm^{-2}]	$\Sigma_{0,B}$ [g cm^{-2}]	$H_{0,A}$ [AU]	$H_{0,B}$ [AU]	i_A [°]
DM 1	18.0	3.0	1.0	3.0	1.25	1.5	55
DM 2	14.0	7.0	1.0	0.05	0.85	2.0	50
DM 3	10.5	10.5	1.0	0.05	1.25	2.0	60
Rotating toroid model	L_A [$L_\odot$]	L_B [$L_\odot$]	$\dot{M}_A$ [$M_\odot$ yr^{-1}]	$\dot{M}_B$ [$M_\odot$ yr^{-1}]	$r_{c,A}$ [AU]	$r_{c,B}$ [AU]	
RTM 1	18.0	3.0	3.75×10^{-6}	2.75×10^{-6}	75	20	
RTM 2	10.5	10.5	2.1×10^{-6}	2.1×10^{-6}	50	20	
RTM 3	20.0	1.0	3.8×10^{-6}	4.6×10^{-6}	75	20	
RTM 4	7.0	14.0	3.0×10^{-6}	2.0×10^{-6}	75	20	
RTM 5	3.0	18.0	3.0×10^{-6}	2.0×10^{-6}	75	20	

to edge-on and used $r_{c,A}$ = 75 AU, as it matched the aspect ratio at this inclination. The free parameters of the source A rotating toroid model were $\dot{M}_A$ and L_A, as $r_{c,A}$ and M_A were fixed (Table 4.1), while the source B rotating toroid model had $\dot{M}_B$ and $r_{c,B}$ as free parameters (since L_B was determined by L_A). We found that the observed peak flux density toward source A and B could not constrain the luminosity or the mass accretion rate of either source, as these parameters are degenerate. The minimum column density toward source B did not offer any constraint. In conclusion, the rotating toroid model can satisfy the disk constraints, but cannot constrain L_A or L_B, using continuum data alone (Table 4.1).

4.5 GAS LINE EMISSION MODELING

In order to constrain the nature of the disk-like emission further, and to obtain more constraints on the source luminosities, the *J*=3–2 line emission from ^{13}CO, $C^{17}O$ and $C^{18}O$ of select dust models were modeled in `LIME` (Brinch & Hogerheijde, 2010), a line radiative transfer code. The dust temperature output from `RADMC-3D` was imported to `LIME` (Appendix 4.9.3) and by using the standard gas-to-dust mass ratio of 100 (Bohlin et al., 1978) together with the given dust density model, the molecular hydrogen number density n_{H_2} was found. The gas line emission depends on the number density of the molecule undergoing a rotational transition, the CO isotopologue in our case, the number density of the other molecules in the gas which excite the molecule collisionally and the kinetic temperature which changes the collisional rates (Brinch & Hogerheijde, 2010) and thus the excitation of the CO isotopologue. In `LIME`, the number density of the colliders is approximated as n_{H_2}, as H_2 is by far the most abundant species in the dense molecular cores where star formation takes place (e.g., Genzel & Stutzki, 1989). `LIME` performs non-LTE (Local Thermodynamic Equilibrium) line radiative transfer modeling, where the rotational level populations are found iteratively. The CO isotopologue data files containing collisional rate coefficients (Yang et al., 2010) were downloaded from the LAMDA[2] database (Schöier et al., 2005a). The collisional rate coefficients of the CO isotopologues with H_2 in these files include collisions with both ortho- and para-H_2.

In this work, we assumed that the dust and gas temperatures are coupled, which is usually a good approximation in the dense inner environments of the envelope (Schöier et al., 2002), that were modeled here. The radius of the `LIME` model was set to 2×10^3 AU, as more distant, cold regions in the envelope will not contribute much emission due to freeze-out of CO.

Optimally, the absorption features around each source and the major features of the interbinary CO isotopologue emission seen in Fig.

2 http://home.strw.leidenuniv.nl/~moldata/

4.2 were recreated in the synthetic moment zero maps, which would imply that our dust density model is consistent with the observed gas line emission. We did not attempt to match the exact absorption level as it depends not only on the molecule abundance but also on the gas-to-dust mass ratio and dust opacity, neither of which were constrained in this work.

In the case of a PP-disk model, the velocity in the disk around each source was modeled as Keplerian rotation. Here the central stellar mass becomes important if there is any disk inclination toward the observer, as radial velocities cause spectral broadening, reducing the line optical depth. This, in turn, will result in higher integrated emission if there is any line self-absorption, which we expect around each source, based on the observations seen in Fig. 4.2. In the case of a rotating toroid model, the 3D velocity structure from Terebey et al. (1984) was used. For all regions outside the disk components, the velocity was modeled as simple free-fall,

$$v(r) = \sqrt{GM_{tot}/r}, \tag{4.6}$$

where r is the distance to the model center, G is the gravitational constant and M_{tot} is the combined mass of source A and B. This approximation is valid at kAU scales but breaks down in the innermost region. The dust in the interbinary region should arguably be drifting toward either source, in accordance with the local gravitational field. Since only one dust opacity model can be set in `LIME` (v. 1.5), bare-grain dust opacities were used in the entire model, as the dust grains in the disk regions are mostly above 90 K in the rotating toroid models, and in the PP-disk model atmosphere. If we had used icy-grain opacities in the `LIME` models instead, the reduced absorption from the dust would result in increased flux density globally in the integrated gas emission maps, with the largest difference in the disk regions.

4.5.1 *Abundance modeling*

It is assumed that the bulk of the CO isotopologue emission originates from molecules sublimated from the dust grains, represented with an abundance jump model in this work, similar to some of the previous chemical modeling of IRAS 16293 (Schöier et al., 2002, 2004; Coutens et al., 2012). The individual CO isotopologue abundances relative to H_2, the main collision partner in our modeling, were found by using the C and O isotopologue abundances given by Wilson & Rood (1994) (Table 4.3). Standard abundance values from Wilson & Rood (1994) were applied to regions with $T_{dust} \geqslant 30$ K where the CO is sublimated from the dust grains, and a drop factor of 10^{-2} was used in regions with $T < 30$ K, to imitate freeze-out. Examining the temperature complexity of a typical rotating toroid model (Fig. 4.12 in Appendix 4.11.1), when disks and the dust filament are added to the

Table 4.3: LIME model parameters

Parameter	Description	Value
Grid outer radius	...	2×10^3 AU
Grid start radius	...	30 AU
n_{nodes}	Number of grid nodes in the LIME calculations	7×10^4
CO/H_2	Standard ISM abundance of CO	10^{-4}
$^{13}CO/H_2$	Standard ISM abundance of ^{13}CO	1.30×10^{-6}
$C^{18}O/H_2$	Standard ISM abundance of $C^{18}O$	1.79×10^{-7}
$C^{17}O/H_2$	Standard ISM abundance of $C^{17}O$	5.58×10^{-8}
Freeze out factor	...	0.01
Gas-to-dust-mass ratio	Used for all conversions from dust to gas mass	100
CO isotopologues abundances of all models		
$X_{^{13}CO}$	^{13}CO abundance	2.6×10^{-7}
$X_{C^{18}O}$	$C^{18}O$ abundance	3.58×10^{-8}
$X_{C^{17}O}$	$C^{17}O$ abundance	1.12×10^{-8}

Notes. Given abundances assume that C and O atoms maximally combine into CO.

model, we can see the expected emission shape from the CO isotopologues in Fig. 4.5, based on the T = 30 K contour.

4.5.2 *Modeled CO isotopologue maps*

To constrain the luminosity ratio of the two protostars, we modeled the rotating toroid model at different luminosity values (Table 4.5), with parameter sets that satisfied the dust continuum constraints. The resulting synthetic CO isotopologue maps (Fig. 4.6) indicate that $L_A \geqslant 18\ L_\odot$ in order to reproduce the observed tendency of concentrated emission toward source A. We can deduce the luminosity dominance of source A from the observations alone, as the truncation in the observed $C^{17}O$ and $C^{18}O$ maps occurs closer to source B than source A, which requires source A to be more luminous, if we assume this truncation is due to the dust grain temperature dropping below the sublimation temperature of CO. $L_A \geqslant 18\ L_\odot$ is also consistent with the dust continuum model results (Fig. 4.4). Alternatively, the increase in continuum and gas line emission toward source A could be due to geometric effects, such as an inclination of the stellar plane so source A is closer to us than source B, or simply that more dust material exists in the filament toward source A. However, an increase in dust density would require L_A to be lowered, in order to match the observed continuum emission as well as increasing the optical depth. Both instances lower the gas temperature in the region near source A, which creates a truncated region wherein CO is sublimated closer to source A than source B. In this sense, introducing more material in our filament model toward source A should require L_A to be even higher than we currently find in order to match the observed CO isotopologue emission. The inferred low luminosity of source B implies that disk B is denser than disk A in order to dominate the dust submillimeter emission, which fits well with the observed absorption in the CO isotopologue emission around source B, compared to the vicinity of source A.

A representative rotating toroid model which satisfied the dust continuum constraints with $L_A = 18\ L_\odot$ was modeled in `LIME`, together with a representative of the best matching PP-disk model at $L_A = 14\ L_\odot$ (since $L_B < 7\ L_\odot$ could not reproduce the observed peak flux density in our H_0 parameter space, though this does not rule out $L_B < 7\ L_\odot$ by itself, see Fig. 4.10 in Appendix 4.11.1) can be seen in Fig. 4.5. The first attempt with the standard abundances described in Table 4.3, resulted in significant absorption in a region toward source B as expected, but also with some unexpected absorption toward source A. For the rotating toroid model, the $C^{18}O$ model emission in the disk A component has evident self-absorption throughout the midplane. After lowering the abundances by a factor of five, the model $C^{18}O$ emission structure was more reminiscent of the observa-

Table 4.4: LIME model parameters of Fig. 4.5.

Parameter	Description	Value
Rotating toroid model		
L_A	Luminosity of source A	18 $L_\odot$
L_B	Luminosity of source B	3 $L_\odot$
$\dot{M}_A$	Mass accretion rate	3.75×10^{-6} $M_\odot$ yr^{-1}
$\dot{M}_B$	Mass accretion rate	2.75×10^{-6} $M_\odot$ yr^{-1}
$r_{c,A}$	Centrifugal radius	75 AU
$r_{c,B}$	Centrifugal radius	20 AU
PP-disk model		
L_A	Luminosity of source A	14 $L_\odot$
L_B	Luminosity of source B	7 $L_\odot$
$\Sigma_{0,A}$	Dust surface density at 10 AU	0.6 g cm^{-2}
$\Sigma_{0,B}$	Dust surface density at 10 AU	5.0 g cm^{-2}
$H_{0,A}$	Scale-height at 10 AU	1.5 AU
$H_{0,B}$	Scale-height at 10 AU	2.0 AU
i_A	Disk A inclination	60°

tions, while $C^{17}O$ did not reproduce the observed peaked emission in the disk A component at any of the attempted abundances (Fig. 4.5).

The model emission qualitatively matches the observed ^{13}CO bimodal emission structure above and below the disk midplane, as well as the two observed $C^{18}O$ emission peaks near the corners of the disk A component, but with less absorption in $C^{18}O$ toward source A than observed. The rotating toroid model cannot, however, reproduce the $C^{17}O$ centrally concentrated emission structure, but instead results in a bimodal distribution as seen in $C^{18}O$, near $r_{c,A}$ (r_{disk} = 75 AU). The PP-disk model fails to produce the emission peaks around source A, in all isotopologues, as the PP-disk A region heavily absorbs the line emission, even when the standard abundances are lowered by a factor of five, despite the fact that we used the PP-disk model parameters with the lowest optical depth while matching continuum constraints.

When the PP-disk model standard abundances were lowered by a factor of ten or 15 instead (Fig. 4.9 in Appendix 4.11.1) the $C^{17}O$ emission from the filament became much weaker than observed, while the disk A region remained in absorption. The model absorption is then likely not due to line self-absorption, but rather originates from the optically thick dust. This suggests that the disk-like emission around

Table 4.5: LIME model parameters of Fig. 4.6.

Model	$\dot{M}_A$ [$M_\odot$ yr^{-1}]	$\dot{M}_B$ [$M_\odot$ yr^{-1}]
$L_A = 3\ L_\odot$	9.0×10^{-6}	1.3×10^{-6}
$L_A = 7\ L_\odot$	5.5×10^{-6}	1.4×10^{-6}
$L_A = 10.5\ L_\odot$	4.6×10^{-6}	1.6×10^{-6}
$L_A = 14\ L_\odot$	4.2×10^{-6}	1.85×10^{-6}
$L_A = 18\ L_\odot$	3.75×10^{-6}	2.75×10^{-6}
$L_A = 20\ L_\odot$	3.8×10^{-6}	4.6×10^{-6}

Notes. All models are rotating toroids, using $r_{c,A}$ = 75 AU and $r_{c,B}$ = 20 AU.

source A is composed of a relatively diffuse, vertically extended structure.

However, if larger amounts of CO are in front of disk A, on similar spatial scales, then it could explain the extra line emission in the observations compared to the PP-disk model emission. Since the continuum emission is consistent with a PP-disk model, we cannot exclude the possibility that the disk-like emission structure around source A could be from a flat disk, based on our model and observations alone. It is also possible that the presence of material in front of disk A could allow the rotating toroid models to use the standard ISM CO abundance and still qualitatively match the observations.

4.6 DISCUSSION

The combined constraints from the dust continuum and CO isotopologue emission, necessitate very high PP-disk model scale-heights around source B, H_0 > 3.0 AU at 10 AU, which is suggestive of a nonsettled disk with a large vertical distribution, meaning that it is indicative of a structure similar to that of the diffuse, rotating toroid model. These scale-heights are unprecedented for Class II disks, but similar to the one reported by Tobin et al. (2013), who find a best-fit PP-disk model to the Class 0 disk around L1527 with a scale-height of 48 AU at 100 AU. In comparison, when converting H_0 to the scale-height at 100 AU, the PP-disk model around source B needs a scale-height of more than 53 AU at 100 AU, when $L_B = 3\ L_\odot$, in order to reach the peak flux density value (Fig. 4.10 in Appendix 4.11.1).

This value is significantly higher than the scale-heights at 100 AU of Class I/II sources, which typically are 3 – 20 AU (Wolf et al., 2008; Andrews et al., 2009, 2010). Tobin et al. (2013) propose that the large scale-height of their best fitting PP-disk model of L1527 is approximating material from the envelope falling onto the disk and that this unusually vertically extended structure could reflect a stage before effective dust settling. The disk-like structure around source B could be similar to the L1527 disk in this regard, as infall toward source B has previously been detected.

The CO isotopologue moment maps are not entirely qualitatively matched by a rotating toroid, but the fact that the standard CO isotopologue abundances needed to be lowered by a factor of five to avoid self-absorption in $C^{18}O$ is interesting. Anderl et al. (2016) use abundances an order of magnitude lower than the standard CO isotopologue abundances in order to match their observations of regions interior to the CO snowline in a survey of nearby Class 0 protostars. In the vicinity of protostars and accretion shocks, the radiation field and chemistry is markedly different from the ISM, so deviations from the standard ISM abundances in the inner regions of a disk are not surprising (e.g., see Visser et al., 2009). However, because we base this necessity for a lower abundance on a single species, and since the self-absorption might simply reflect that the model is a poor approximation, a more thorough, quantitative investigation would be needed before making any firm conclusions on the CO abundance in the inner regions of IRAS 16293.

It has been suggested that a fraction of the CO is desorbed together with H_2O into the gas-phase at 90 K (Anderl et al., 2016), due to trapping in the water-ice, which would allow higher abundances in the gas model for regions with $T_{dust} \geqslant 90$ K than regions with 30 K $\leqslant T_{dust} < 90$ K. This should lead to an emission structure closer to that of the observed, with a more abrupt peak toward source A and should be investigated in future modeling efforts.

Considering the unusual scale-heights of the PP-disk model, necessary to produce the peak flux density around source B, a rotating toroid model is perhaps more representative of the actual dust distribution around source B than a PP-disk model, as it better approximates the infalling material, unambiguously detected toward source B (Chandler et al., 2005; Pineda et al., 2012; Zapata et al., 2013) as well as shocks (Jørgensen et al., 2011) which would be expected with a rotating collapse. It is also possible that both disks A and B are transition structures, between an early rotating toroid structure and a later Keplerian disk, perhaps similar to the structure suggested by Oya et al. (2016).

In terms of the impact of the binarity of IRAS 16293 on earlier works using a single radiation source, we can consider Schöier et al. (2002), who assume a single radiation source with a spherical density model down to scales where T_{dust} = 300 K. The inferred luminosity dominance of source A from our work makes the single source approximation more valid than a luminosity ratio closer to unity.

When looking at Fig. 4.12 in Appendix 4.11.1, it appears that the approximation of a single central source is not dramatically erroneous, as source A dominates the radiation, but rather that a spherically symmetric density model breaks down in the inner regions where the temperatures exceed 90 K. At the scales of 10″–15″ used by Schöier et al. (2002), spherically symmetrical density models are good approximations of the outer envelope of IRAS 16293 and the binary protostar is well approximated to a single source at the distances of several kAU, as well as being unresolved. However, for radiative transfer modeling of the innermost region including the two sources, their disks as well as the conjoining dust filament, subarcsec resolution data is needed together with full 3D radiative transfer modeling to capture the complexity of the temperature structure. While previous radiative transfer models of IRAS 16293 do not describe the full picture, they can arguably be useful approximations to the hot corino material around source A. If source A is indeed dominant in terms of luminosity, then previous chemical modeling using a single star focusing on hot corino chemistry (Schöier et al., 2002; Bisschop et al., 2008a; Coutens et al., 2012) will effectively have described the chemistry around source A, with the hot corino chemistry around source B acting as a "contaminant" to the signal from source A. However, for an updated model of the hot corino chemistry involving COMs in IRAS 16293, a new chemical model is needed which includes the disks, filamentary structure and radiation fields with $L_A \sim 18\ L_\odot$ and $L_B \sim 3\ L_\odot$.

4.7 CONCLUSIONS

We have constructed a 3D model of the dust and gas environment of IRAS 16293 and obtained a qualitative match to the 868 μm dust continuum and J=3–2 line emission of ^{13}CO, C^{18}O and C^{17}O from the PILS survey. This is the first model of IRAS 16293 to include multiple radiation sources as well as complex dust structures, such as disks and a dust filament. We included two different disk-like density structures; a disk structure (a true Keplerian disk) and the density solution to an infalling, rotating collapse, a disk-like structure resembling a rotating toroid. We determine that the dust density structure around source B must be vertically extended and puffed up, as a PP-disk model around source B with low to normal scale-heights cannot fulfill all the observational constraints. The disk structure around source A could not be constrained. The results from this 3D dust and gas model suggest that the source A luminosity is far higher than that of source B, based on the emission morphology of the dust and CO isotopologue line emission between the sources. This model is an important increase in complexity compared to previous works and should be followed up with higher angular resolution observations of the disks and the dust filament, for further investigation and confirmation of our results. We also performed a more generic investigation of the temperature structure differences between a single star and a binary in a simple dense envelope with a density plateau within 600 AU. The main conclusions are the following:

– The temperature distribution depends on the density structure and source luminosities. A single star will have higher volumes and masses of dust above ~50 K compared to a binary with the same combined luminosity, while the differences in dust with 30 – 50 K are negligible in a spherical 1D density model.

– Previous radiative transfer models of IRAS 16293 using a spherically symmetric density distribution and a single, central radiation source are valid at the ~kAU scales, but not in the interbinary region, where complex 3D dust structures and two radiation sources need to be included.

– A 3D model with disks or disk-like structures around source A and B in IRAS 16293 and a simple dust filament between the sources, can qualitatively match the spatial distribution of the 868 µm dust continuum and CO isotopologue line emission.

– The density structure around source A in our model is not constrained, as both a flat, inclined disk and an edge-on puffed-up disk structure (a rotating toroid model) can match the continuum peak emission and observed aspect ratio, while neither could match the observed $C^{17}O$ isotopologue emission.

– The dust density structure around source B in our model has to be vertically extended. Such a structure can be obtained with both a PP-disk model with an unusually high scale-height and with a rotating toroid model, which naturally has a puffed-up disk-like structure.

– The rotating toroid model abundances of the CO isotopologues need to be a factor of five lower than typical ISM values, in order to match the $C^{18}O$ observations, similar to the low inferred CO abundance for other embedded protostars (e.g., Anderl et al., 2016). This result needs to be investigated further, as the low abundances could be model dependent.

– Source A is likely much more luminous than source B. Our 3D density model (with coarse parameter space steps) requires the source A luminosity to be a factor of six larger; $L_A \sim 18\ L_\odot$ and $L_B \sim 3\ L_\odot$.

This work illustrates the importance of using complex, full 3D radiative transfer modeling together with subarcsecond observations of young stellar objects such as IRAS 16293 in order to constrain the physical parameters of such Class 0 disks and their environment. It also illustrates the need for even higher resolution observations of the gas and dust in the disks around source A and B in order to do a full quantitative investigation with parameter confidence intervals, to determine the exact CO isotopologue abundances and the parameters of the dust filament enveloping both sources. We also suggest that gas dynamics, including outflows and magnetic fields, are investigated in future modeling efforts. Having a detailed and robust physical model is critical for the interpretation of ALMA spectral data of the various hot corino species.

4.8 ACKNOWLEDGMENTS

The authors are grateful to Søren Frimann, Jonathan Ramsey and Attila Juhasz for useful discussions about 3D radiative transfer modeling. We would also like to thank the anonymous referee for helpful suggestions, which improved the presentation of this work. This paper makes use of the following ALMA data: ADS/JAO.ALMA#2013.1.00278.S. ALMA is a partnership of ESO (representing its member states), NSF (USA) and NINS (Japan), together with NRC (Canada) and NSC and ASIAA (Taiwan) and KASI (Republic of Korea), in cooperation with the Republic of Chile. The Joint ALMA Observatory is operated by ESO, AUI/NRAO and NAOJ. The group of J.K.J. acknowledges support from a Lundbeck Foundation Group Leader Fellowship as well as the European Research Council (ERC) under the European Union's Horizon 2020 research and innovation program (grant agreement No. 646908) through ERC Consolidator Grant "S4F". Research at the Centre for Star and Planet Formation is funded by the Danish National Research Foundation. M. N. Drozdovskaya acknowledges the financial support of the Center for Space and Habitability (CSH) Fellowship and the IAU Gruber Foundation Fellowship. A. Coutens postdoctoral grant is funded by the ERC Starting Grant 3DICE (grant agreement 336474). This research made use of Astropy, a community-developed core Python package for Astronomy (Astropy Collaboration 2013a). This research has made use of NASA's Astrophysics Data System.

4.9 APPENDIX

4.9.1 *SED*

After the dust density components were inserted into the model, the SED was used as a sanity check that our added dust components do not alter the SED too much compared to the Schöier et al. (2002) model. The envelope at $r > 10^3$ AU has temperatures of $10 - 30$ K, which dominates the submm and mm range, while deviations in the warmer dust mass will alter the near-infrared SED in the $10 - 100$ μm range. In Fig. 4.7 the final SED after including all structures, can be seen. While the SED appears reasonable, it should be noted that SEDs generally have very degenerate solutions, and one cannot exclude other structures or multidimensional solutions, based on the SED alone. The SEDs of the best rotating toroid model and PP-disk model were almost indistinguishable, as the SED is dominated by the cold dust in the envelope.

4.9.2 *CO isotopologue spectra*

While we did not attempt to fit the CO isotopologues spectral lines with our models, we provide the plots in Fig. 4.8, for completeness. A box was used around both the observations and model emission to extract the same region around the filament and two protostars, in order to avoid some of the observed extended emission south of the source A, that we did not attempt to recreate in the models.

4.9.3 *Interfacing between `RADMC-3D` and `LIME`*

A fundamental difference between `RADMC-3D` and `LIME` is the grid used. `RADMC-3D` uses a structured grid (curvilinear is chosen for this work), while `LIME` uses Delaunay triangulation to produce an unstructured grid. Custom source code changes were made to `LIME` (v. 1.5) to allow for two local logarithmically distributed grids around the center of each of the stars in order to resolve the disks, while also changing the default density weighting value of the node positions[3], to allow the global uniform grid to resolve the dust filament, with fewer nodes, as the default setting resulted in many nodes being spread in the less interesting envelope around the disks and the filament. The `RADMC-3D` grid density, temperature and velocity values (in the case of a rotating toroid) are written as arrays to a `C` header file, and a nearest-neighbor search of is done for each `LIME` node, which is then assigned the physical values of the nearest cell. Due to the size of the octree refined `RADMC-3D` grid (upward of 5 million grid cells), a brute-force search is ill-advised, as this quickly becomes a speed bottleneck. Instead, a k-d tree search algorithm[4] (e.g., Saftly et al., 2014) was inserted into our custom `LIME` code. This k-d tree is used for quick lookup of the nearest neighbor, allowing us to have very large `RADMC-3D` grids without execution time issues. The exponential mode (fastest mode)[5] as well as parallel computing was engaged in `LIME` to reduce execution time. However, due to the large number of nodes necessary to resolve the relevant disk and filament regions, the exe-

---

3 https://lime.readthedocs.io

4 The k-d tree was implemented using code modified from https://rosettacode.org/wiki/K-d_tree#C implemented in `C`.

5 https://lime.readthedocs.io/en/latest/usermanual.html#command-line-options

cution time is typically around two hours per calculation, that is, six hours to produce all spectral cubes for a single model, which compounded the issue of proper parameter sampling.

4.10 PP-DISK MODEL p AND Ψ PARAMETERS

After running the PP-disk models over a broad parameter space of p, Ψ, Σ_0 and H_0 for disk A and B (Table 4.1), it became clear that low values of p and high values of Ψ result in higher peak flux densities, both in combination and by themselves, compared to the opposite part of the parameter space. A low p value ensures larger amounts of dust at larger midplane radii, while a higher flaring coefficient Ψ raises the dust vertically. This combination results in larger amounts of dust with relatively high temperatures. Thus, p and Ψ were fixed to 0.5 and 0.25, respectively, for both disks, but neither has been constrained as optimal parameters for the two disks. However, with these fixed values, we can reproduce the maximal peak flux densities of the two disks. Another reason for these fixed values is the added computational time in `RADMC-3D` for higher p values, due to higher densities in the inner region, causing significant slowdown of the photon propagation calculation, as the photon can become trapped in high-density regions, taking hundreds or thousands of absorption and reemission events to escape the cell. Since the goal is to see if a PP-disk model type can satisfy the constraints, but not necessarily constrain the dust distribution, this approach is acceptable.

4.11 DUST OPACITY IN DISK B

A dust opacity model could possibly accommodate the peak flux density of source B, with lower scale-heights, making the PP-disk model more plausible for source B. But introducing a full investigation into the dust opacity in the disks of IRAS 16293 A and B, in terms of grain size, compositions and morphology, was beyond the scope of this work and not feasible considering our computational limitations. We note that our bare grain opacity at 850 μm is consistent with those used by Tobin et al. (2013), who uses 3.5 cm^2 g^{-1} at 850 μm, in order to fit the L1527 SED slope from 0.85 mm to 7 mm. In comparison, the bare-grain opacities that we used, which dominate the dust emission in the beam toward A and B, have a value of 3.53 cm^2 g^{-1} at 850 μm. As such, while unconstrained, the dust opacities used in this work are consistent with the independent modeling of another Class 0 disk.

4.11.1 *Auxiliary CO isotopologue maps and dust temperature contours*

Due to the absorption toward source A in the modeled CO isotopologue maps, when using both the ISM standard abundances (Table

4.4) and when dividing by a factor of five (Fig. 4.5), the standard ISM abundances were divided by 10 and 15 in two new model CO isotopologue maps (Fig. 4.9). We notice the presence of absorption in source A and B in Fig. 4.9, regardless of the CO isotopologue number density in the gas-phase, suggesting that optically thick dust is responsible for the absorption in the disk components.

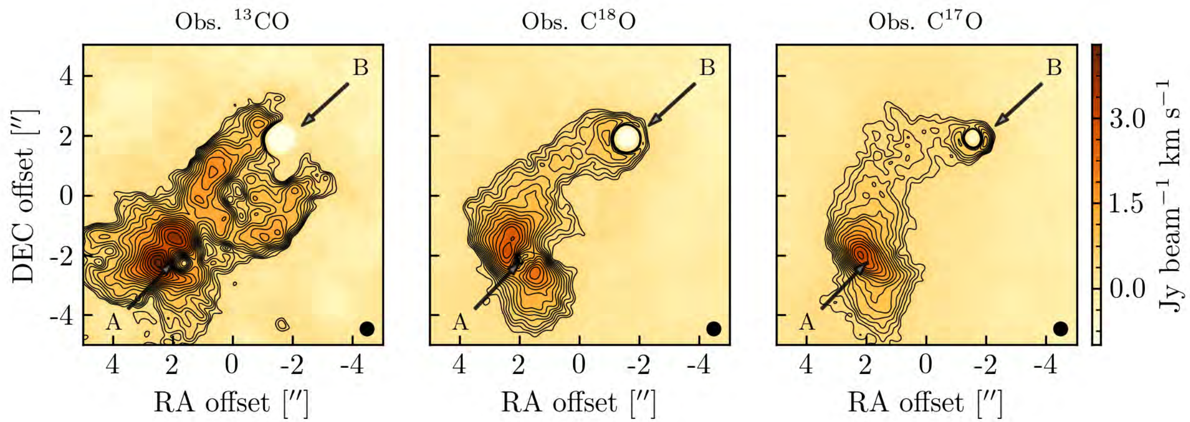

Figure 4.2: Zeroth moment maps of the ^{13}CO, C^{18}O, and C^{17}O isotopologues from the PILS observations. Contour levels are divided logarithmically from 0.5 to 7.3 Jy beam^{-1}km s^{-1}. The RA and DEC offsets are relative to the phase center of the observations.

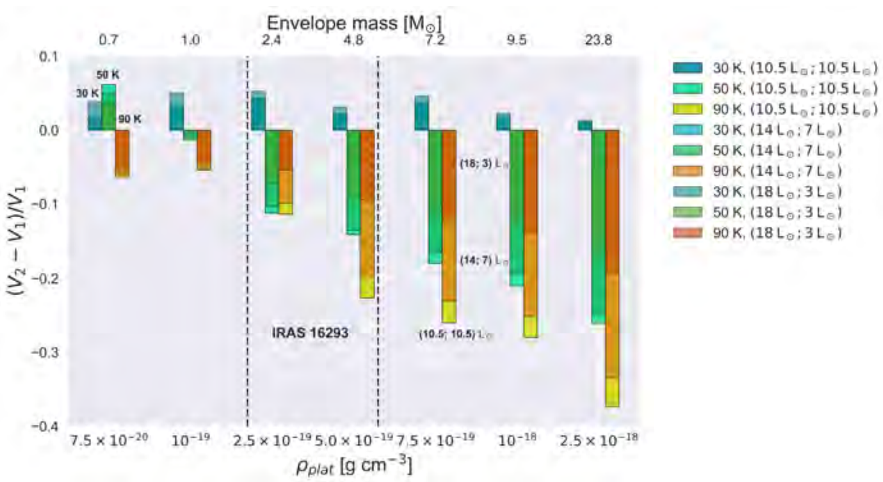

Figure 4.3: Relative differences in volumes of dust above different temperatures. The volume difference between the single star temperature volume, V_1, and binary star temperature volume, V_2, is shown, normalized to V_1, i.e. $\tau - 0.2$ means that the total temperature volume is 20 % lower if there are two stars compared to one. The envelope mass range is 0.7 – 24 $M_\odot$, consistent with the dense core mass range observed in (Alves et al., 2007). The relevant mass range for IRAS 16293 is 2.4 – 4.8 $M_\odot$, (our IRAS 16293 envelope model has a mass of ~4 $M_\odot$). There is a clear tendency for a single star to result in more dust heated above ~ 50 K.

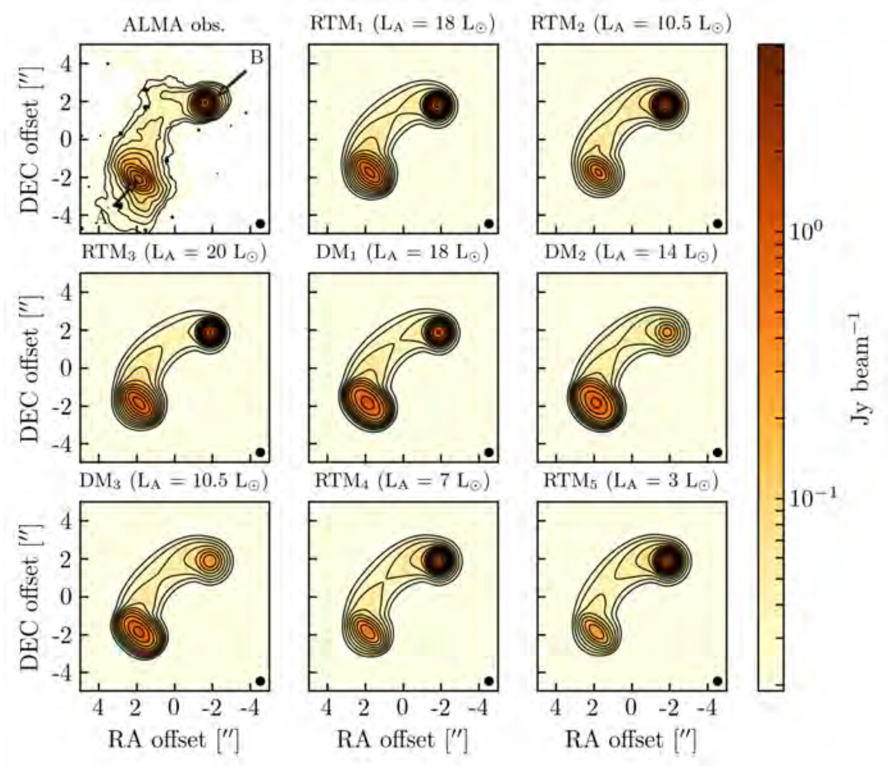

Figure 4.4: Observed and synthetic dust continuum emission at 868 μm for the different physical models summarized in 4.2. Image is in log-scale and the contours are logarithmically divided between 0.02 and 2 Jy beam^{-1}. DM denotes the PP-disk model, while RTM denotes the rotating toroid model.

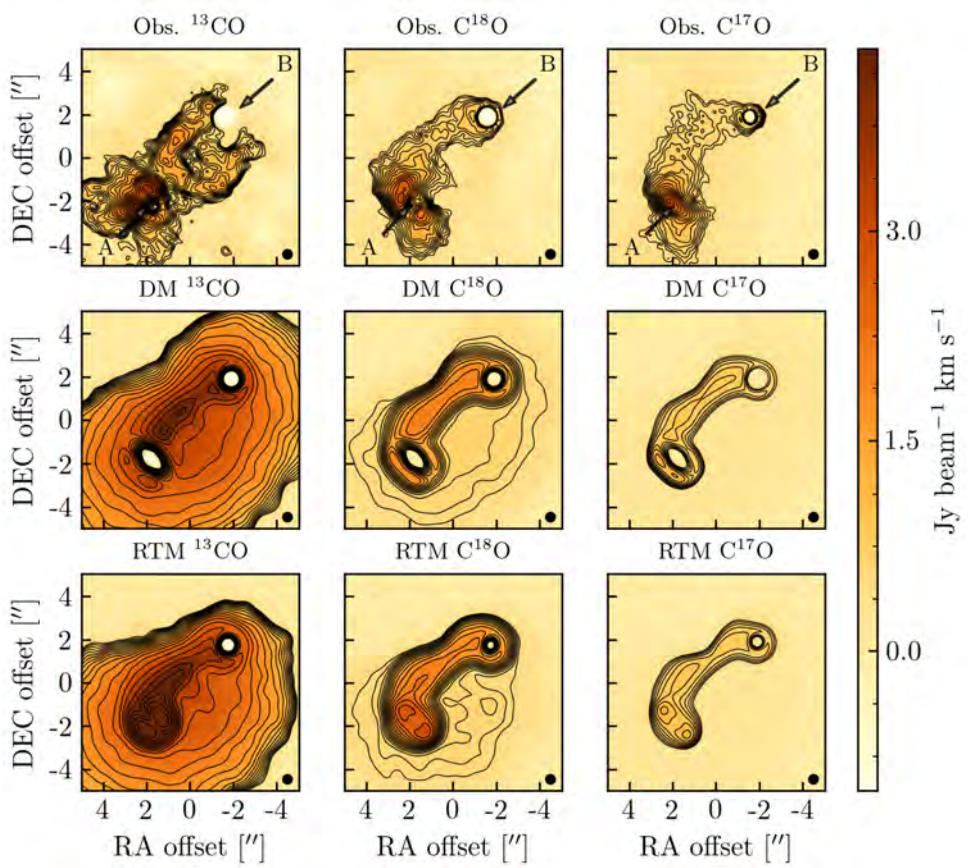

Figure 4.5: Zeroth moment maps of the observed and synthetic CO isotopologue gas line emission. Contour levels are divided logarithmically from 0.5 to 7.3 Jy beam^{-1} km s^{-1}. The RA and DEC offsets are relative to the phase center of the observations. See Table 4.4 for abundances. DM denotes the PP-disk model and RTM denotes the rotating toroid model.

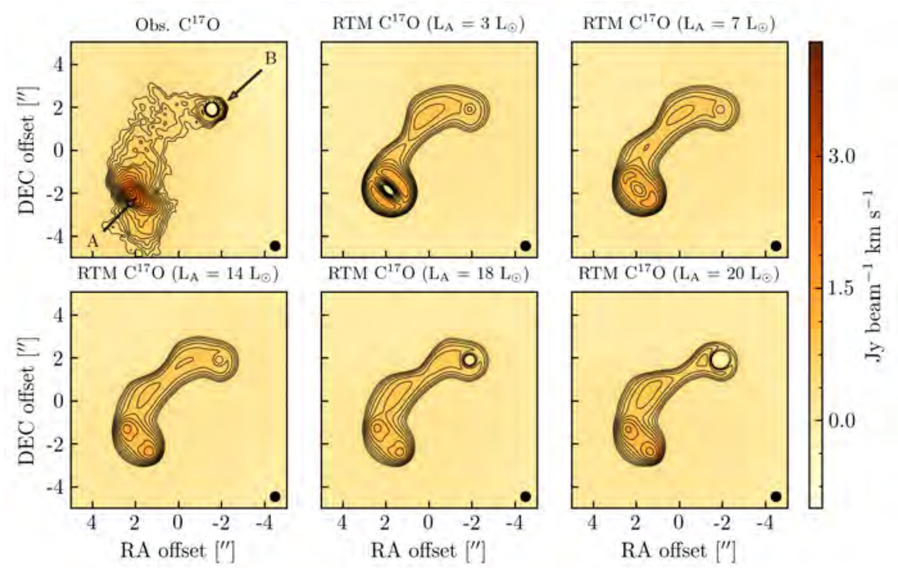

Figure 4.6: Observed and modeled $C^{17}O$ zeroth moment maps, contour levels are divided logarithmically from 0.5 to 7.3 Jy beam^{-1} km s^{-1}. All models are rotating toroid models matching the dust continuum peak flux densities for disk A and B.

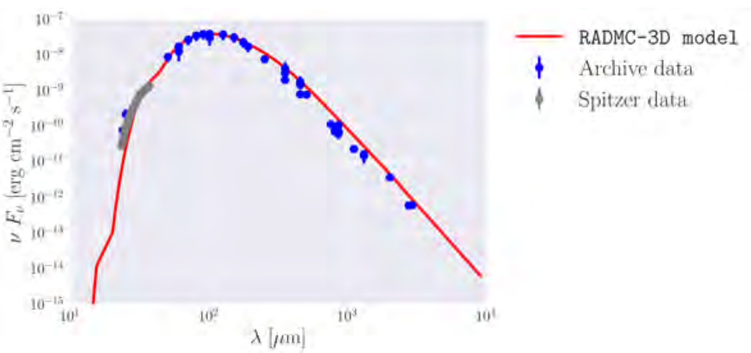

Figure 4.7: SED of the best rotating toroid model.

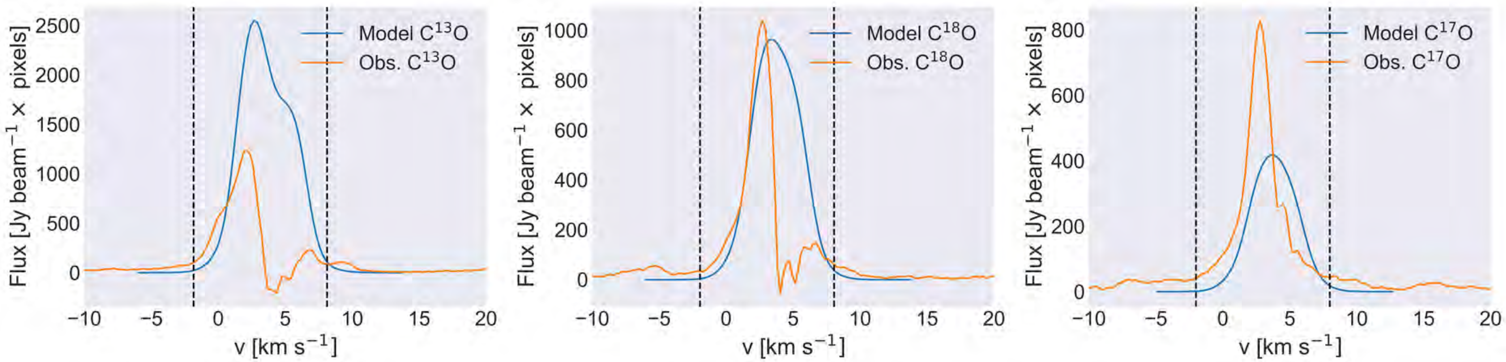

Figure 4.8: Modeled CO isotopologue spectrum and observed CO isotopologue spectrum. Vertical dashed lines show the limits of the zeroth moment maps. The model CO isotopologues are from a rotating toroid model satisfying the continuum constraints with $L_A = 14\ L_\odot$ and $L_B = 7\ L_\odot$.

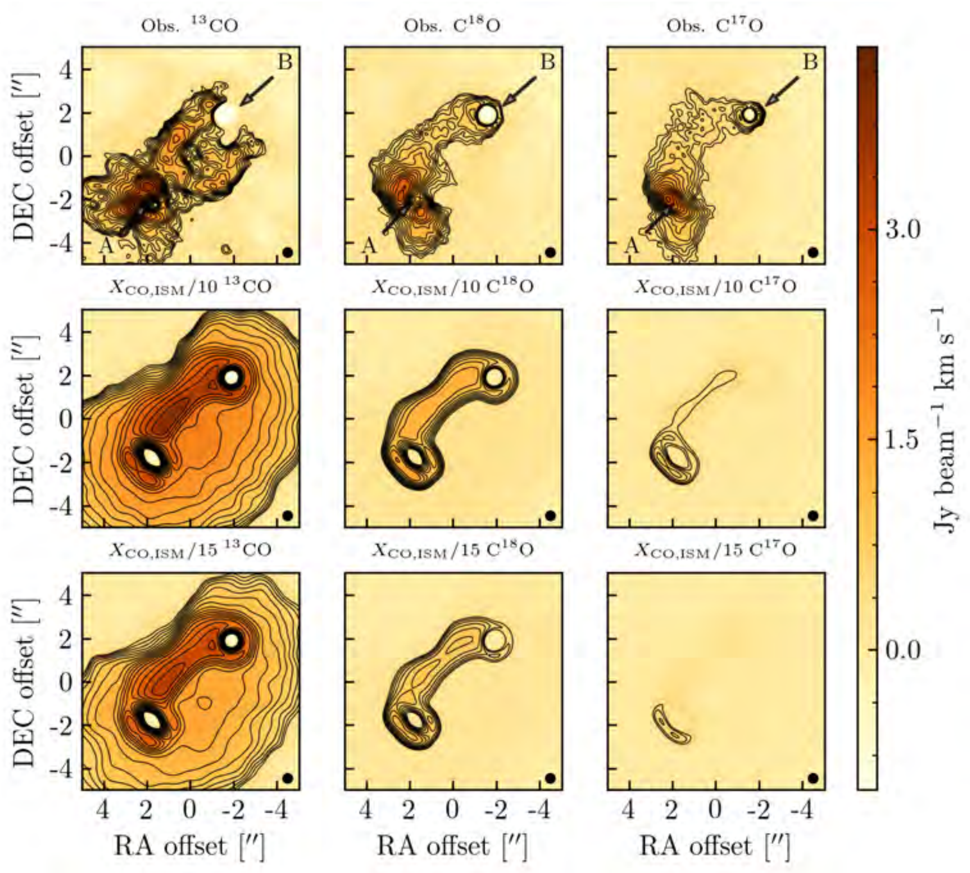

Figure 4.9: Zeroth moment maps of CO isotopologue observations and synthetic gas line emission from PP-disk models. Contour levels are divided logarithmically from 0.5 to 7.3 Jy beam^{-1} km s^{-1}. The RA and DEC offsets are relative to the phase center of the observations. Standard ISM abundances were divided by ten and 15, in the middle and lower panel rows, respectively.

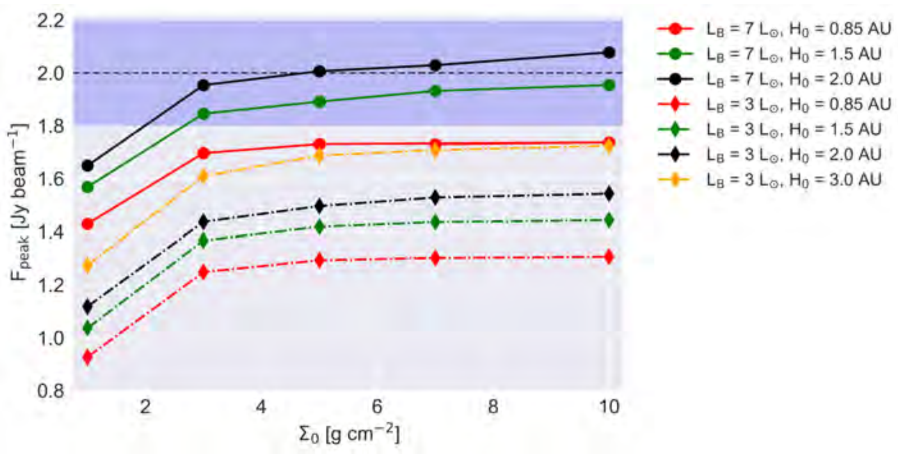

Figure 4.10: Peak flux density of disk B at 868 μm with a PP-disk model, with $L_B = 3\ L_\odot$ and $L_B = 7\ L_\odot$. The black dashed, horizontal line marks the peak continuum position of source B, while the blue area represents the uncertainty. We note that the disk mass reaches 0.35 $M_\odot$ and 0.5 $M_\odot$ at 7 g cm^{-2} and 10 g cm^{-2}, respectively. The highest Class 0 disk mass found in a mm survey by Jørgensen et al. (2009) is ~ 0.46 $M_\odot$, with typical Class 0 disk masses of 0.05 $M_\odot$.

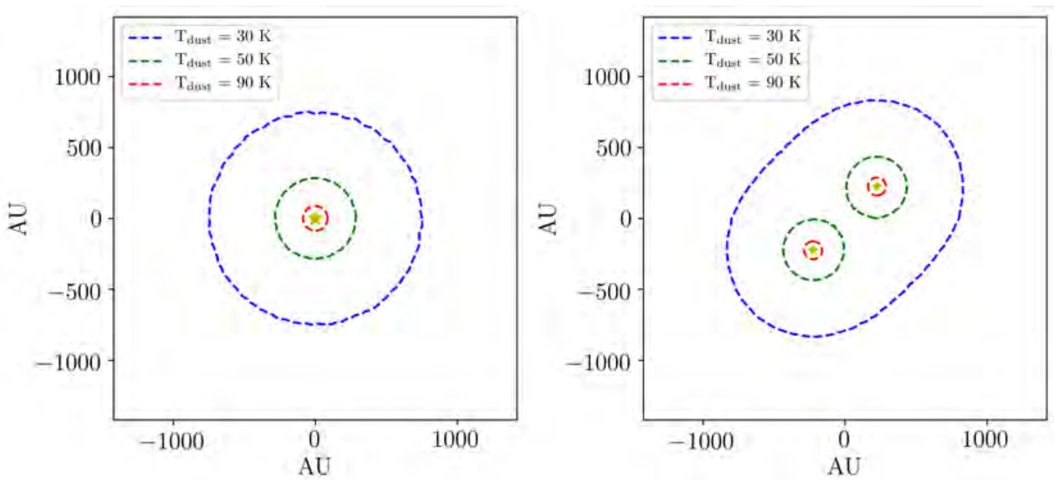

Figure 4.11: Temperature contours of a single star in the left panel with 21 $L_\odot$ in an envelope with a radial power-law density profile, $\rho_{0,\,env} = 3.1 \times 10^{-14}$ g cm^{-3}, $p_{env} = 1.7$, a central density plateau within 600 AU, and two protostars in the right panel, each with 10.5 $L_\odot$. See Table 4.1 for more details.

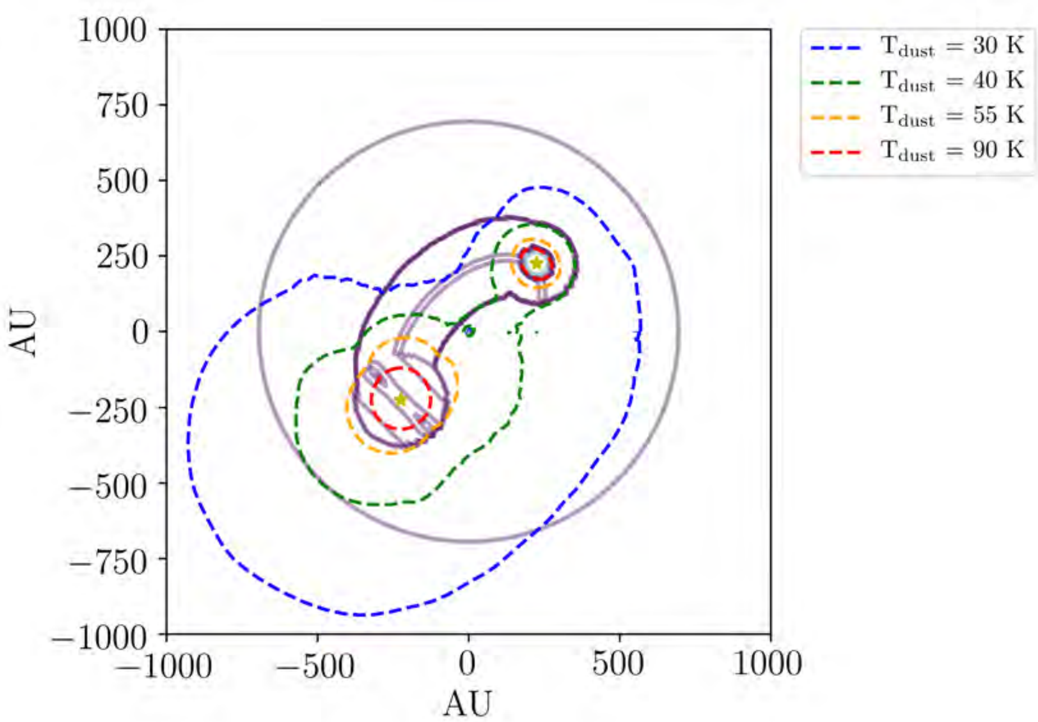

Figure 4.12: Temperature contours for a rotating toroid around each source and a dust filament between the sources in a slice through the model at z (height) = 0. Dust density contours are shown in a gray to green colormap. The radial power-law density distribution is visible along with the dust filament and rotating toroids. Here $L_A = 18\ L_\odot$ and $L_B = 3\ L_\odot$. The source A rotating toroid is edge-on while the source B rotating toroid is face-on. The 90 K contour around source B coincides with the transition from disk to dust filament. Due to the high number of grid cells, some temperature noise is visible in the plot center (due to very small cells with bad photon statistics in `RADMC-3D`). Interpolation has been performed along the temperature contours to make them appear more smooth for visual purposes, as the contours were otherwise slightly noisy in certain regions.

5

PAPER II: THE ORGANIC CHEMISTRY IN THE INNERMOST, INFALLING ENVELOPE OF THE CLASS 0 PROTOSTAR L483

Steffen K. Jacobsen[1], Jes K. Jørgensen[1], James Di Francesco[2], Neal J. Evans II[3,4,5], Minho Choi[5], Jeong-Eun Lee[6]

[1] Centre for Star and Planet Formation, Niels Bohr Institute and Natural History Museum of Denmark, University of Copenhagen, Øster Voldgade 5–7, DK-1350 Copenhagen K, Denmark
[2] NRC Herzberg Astronomy and Astrophysics, 5071 West Saanich Road, Victoria, BC, V9E 2E7, Canada.
[3] Department of Astronomy, The University of Texas at Austin, Austin, TX 78712, USA.
[4] Humanitas College, Global Campus, Kyung Hee University, Yongin-shi 17104, Korea
[5] Korea Astronomy and Space Science Institute, 776 Daedeokdae-ro, Yuseong-gu, Daejeon 34055, Republic of Korea.
[6] School of Space Research, Kyung Hee University, 1732, Deogyeong-Daero, Giheung-gu, Yongin-shi, Gyunggi-do 17104, Korea.

Submitted to *Astronomy & Astrophysics* in April 2018.

Context Observations of the innermost regions of deeply embedded protostellar cores have shown complicated physical structures as well as a rich chemistry with the existence of complex organic molecules. The protostellar envelopes, outflow and large-scale chemistry of Class 0 and Class I objects have been well-studied, but while previous works have hinted at or found a few Keplerian disks at the Class 0 stage, it remains to be seen if their presence in this early stage is the norm. Likewise, while complex organics have been detected toward some Class 0 objects, their distribution is unknown as they could reside in the hottest parts of the envelope, in the emerging disk itself or in other components of the protostellar system, such as shocked regions related to outflows.

Aims In this work, we aim to address two coupled issues about protostars: when rotationally supported disks form around deeply embedded protostars and where complex organic molecules reside in such objects. We wish to observe and constrain the velocity profile of the gas kinematics near the central protostar and determine whether Keplerian motion or an infalling-rotating collapse under angular momentum conservation best explains the observations. The distribution of the complex organic molecules will reveal with which structure they are affiliated: the hot inner envelope or a possible Keplerian disk.

Methods Using Atacama Large Millimeter/submillimeter Array (ALMA) Band 7 data from Cycles 1 and 3, we obtained spectral interferometric data, with a high angular resolution down to ~ 0.1″ (20 au) scales. We present new HCN J = 4–3, HCO^+ J = 4–3, CS J = 7–6 and $H^{13}CN$ J = 4–3 observations, along with a range of transitions that can be attributed to complex organics, including lines of CH_3OH, CH_3OCHO, C_2H_5OH, NH_2CHO, and other species.

Results We find that the kinematics of CS J = 7–6 and $H^{13}CN$ J = 4–3 are best fitted by the velocity profile from infall under conservation of angular momentum and not by a Keplerian profile. All the observed complex organics show a rotational signature consistent with CS J = 7–6 and $H^{13}CN$ J = 4–3 and the derived infall velocity profile. The spatial extents of the observed complex organics are consistent with an ice sublimation radius of the envelope at ~ 55 au, suggesting that the complex organics exists in the hot corino of L483, where the molecules sublimate off the dust grain ice-mantles and are injected into the gas phase.

Conclusions We find that L483 does not harbor a Keplerian disk down to at least 15 au in radius. Instead, the innermost regions of L483 are undergoing a rotating collapse, with the complex organics existing in a hot corino with a radius of ~ 40–60 au. This result highlights that some Class 0 objects contain only very small disks, or none at all, with the complex organic chemistry taking place on scales inside the hot corino of the envelope, in a region larger than the emerging disk.

5.1 INTRODUCTION

Low-mass stars like our Sun are formed from the gravitational collapse of a dense core within a cold molecular cloud. The inherent rotation of the cloud necessitates the presence of outflows and jets in the system to transport angular momentum away, for a central protostar to form. A protostellar disk will emerge around the growing protostar, due to the conservation of angular momentum of material not lost from the system (Terebey et al., 1984). Another angular momentum loss mechanism, strong magnetic braking, however, can prevent a disk from being formed altogether (Garcia, 2011). If a disk-like structure is able to form, it will eventually become rotationally supported, resulting in a Keplerian disk. Also, in the innermost, warmest part of the envelope, a rich chemistry should take place, with the sublimation of icy dust grain mantles leading to the presence of complex organic molecules in the gas phase: Such molecules may end up becoming part of the assembling circumstellar disk and thus incorporated into eventual planetary systems. It is therefore interesting to investigate the link between the physical and chemical structures of inner envelopes and emerging circumstellar disks, a topic where the Atacama Large Millimeter/submillimeter Array (ALMA) with its high angular resolution and sensitivity is ideally suited. This paper presents observations down to a radius of 10 au of the Class 0 protostar in the isolated core Lynds 483, with the aim of studying its chemistry and using its kinematical structure to shed light on its physical structure on these scales.

Concerted efforts have been made over some time on observing the innermost regions of deeply embedded protostars in the Class 0 and Class I stage (e.g., Hogerheijde et al., 1998; Looney et al., 2000; Jørgensen et al., 2004, 2007, 2009; Enoch et al., 2011), revealing excess compact dust emission that could be early disk-like structures or rotationally supported disks. The early evolution and exact formation time of these earliest Keplerian disks are not well-established, however, due to the difficulty of disentangling cloud and disk emission in interferometric observations, the low number of known Class 0 Keplerian disks and the unknown number of Class 0 objects lacking a rotationally supported disk. With the advent of high angular resolution interferometers such as ALMA, discovering early, relatively small disks has become feasible. Keplerian disks of $\sim$ 100 au sizes are observed around Class I objects (Brinch et al., 2007; Jørgensen et al., 2009; Harsono et al., 2014), while typically smaller Keplerian disks have been observed around some Class 0 objects. For example, the 0.3 $M_\odot$ protostar L1527 is found to have a Keplerian disk with a radius of 50–90 au (Tobin et al., 2012; Ohashi et al., 2014). Also, Murillo et al. (2013) detect a disk around the Class 0 protostar VLA1623 that is rotationally supported with a Keplerian profile out to at least 150 au, Lindberg et al. (2014) report a 50 au Keplerian disk around the Class 0/I protostar R CrA-IR7B, and Codella et al. (2014) make a tentative detection of a 90 au Keplerian disk around HH212. On the other hand, the Class 0 object B335 is shown to lack an observable Keplerian disk down to a radius of 10 au (Yen et al., 2015) and continuum emission in the innermost region of B335 is consistent with only a very small disk mass (Evans et al., 2015). Due to the uncertain nature of some of these Keplerian disk detections and the small sample size, more detections of rotationally supported disks in the earliest stages, or equivalently, non-detections and upper size-limits of disks in Class 0 objects, are needed to constrain disk formation theories.

Concurrently with the investigation of Class 0 and I disks, hot regions in the innermost parts of envelopes hosting low-mass star formation have been observed. Such regions have been linked to the formation of Complex Organic Molecules (COMs). Called a 'hot corino' in the case of a low-mass star, these regions of hot gas, T > 90–100 K, are where the icy dust mantles composed of different molecules sublimate and the molecules are released into the gas phase, in which COMs and prebiotic molecules have been discovered (e.g., Bottinelli et al., 2004b; Jørgensen et al., 2005a, 2012; Coutens et al., 2015; Taquet et al., 2015). The presence of COMs has also been linked to the transition region between the outer infalling-rotating envelope and the centrifugal barrier, i.e., the radius where the kinetic energy of the infalling material is converted into rotational energy (Sakai et al., 2014b). Accretion shocks and other heating events in this transition zone are hypothesized to induce a chemical change (e.g., Sakai et al., 2014b; Oya et al., 2016). From an astrochemical point of view, mapping the molecular inventory and distribution at this early stage of the disk, or even before the disk is formed, will set the stage for subsequent chemical evolution, all the way up to the more complex, prebiotic molecules necessary for life as we know it.

An interesting object to address these issues is the dense core, Lynds 483 (L483), constituting the envelope around the Class 0 infrared source IRAS 18148-0440. In the literature both the core and the infrared source are referred to as L483, which we follow for the remainder of the paper. Located at a distance of 200 pc in the Aquila Rift (Dame & Thaddeus, 1985), its envelope mass is 4.4 $M_\odot$ (Jørgensen, 2004), while the bolometric luminosity has been estimated to be 10–14 $L_\odot$ (Tafalla et al., 2000; Ladd et al., 1991).

L483 drives a well-collimated bipolar CO outflow (Parker et al., 1991; Parker, 1988; Fuller et al., 1995; Bontemps et al., 1996; Hatchell et al., 1999). Also, it is associated with a variable H_2O maser (Xiang & Turner, 1995) and shocked H_2 emission, which is suggested to originate from the head and edges of the jet where it interacts with ambient molecular gas (Fuller et al., 1995). Chapman et al. (2013) find the P.A. of a suggested magnetic pseudodisk to be 36° based on 4.5 μm *Spitzer* imaging, while the outflow P.A. is estimated at 105°, based on the shocked H_2 emission. Fuller et al. (1995) found the outflow inclination of L483 to be 40° based on 2.22 μm imaging. Tafalla et al. (2000) find that, using its Spectral Energy Distribution (SED), L483 is a Class 0 object, while its bipolar outflows has characteristics seen in both Class 0 and Class I objects, and therefore propose that L483 is in transition from Class 0 to Class I.

Shirley et al. (2000) made 450 μm and 850 μm continuum maps with SCUBA at the JCMT, revealing its elongated continuum emission in the outflow direction, likely the outer parts of the envelope being swept up by the outflowing material. Jørgensen (2004) find that the velocity gradients in HCN, CS, and N_2H^+ around the source are perpendicular to its outflows, indicative of a large-scale, infalling-rotating envelope, with the velocity vector being consistent with rotation around a central object of ~1 $M_\odot$. Curiously, the interferometric flux of L483 is consistent with envelope-only emission and does not require a central compact emission source (Jørgensen et al., 2007, 2009; Jørgensen, 2004). Oya et al. (2017) use a rotating collapse ballistic model and find that a 0.1–0.2 $M_\odot$ central protostar with a collapsing-rotating envelope with a centrifugal barrier radius (where the barrier radius is half of the centrifugal radius) of 30–200 au, assuming an inclination angle of 80°, can roughly explain the observed CS, SO, HNCO, NH_2CHO, and $HCOOCH_3$ lines. Oya et al. (2017) argue that some molecular species observed towards L483 are in a Keplerian disk, very near the protostar. No observations to date have confirmed the presence of a Keplerian disk in L483 or have determined the distribution of COMs on these scales. COMs could be distributed in the hot corino region or more directly linked to the disk itself, as suggested by Oya et al. (2017), tying in to the common problem of the unknown COM distribution in Class 0 objects.

In this work, we used high angular resolution from ALMA Cycles 1 and 3 to image the distribution of COMs as well as to probe the kinematics of the innermost regions down to a radius of ~ 10 au. These data enable us to improve our understanding of disk formation and the early astrochemistry of low-mass protostars. This paper is structured as follows: First, the observations are described in Section 6.2, while the results are presented in Section 6.3. An analysis of the inner region kinematics is presented, first for $H^{13}CN$ J = 4–3 and CS J = 7–6, in Section 5.4.1, and then for the observed COMs, together with an analysis of the dust temperature profile of the innermost region using a simple dust density model, in Section 5.4.2. Our results and analysis are discussed in Section 5.5 and the conclusions in Section 5.6.

5.2 OBSERVATIONS

L483 was observed on the nights of 2013 June 1, 2013 June 19, 2013 November 2, and 2013 November 3 in ALMA Band 7 as part of Cycle 1 observations (PI. N. Evans, projectid: 2012.1.00346.S) and on 2016 August 31, 2016 September 7, and 2016 September 9 in ALMA Band 7 as part of ALMA Cycle 3 observations (PI: Jes Jørgensen, projectid: 2015.1.00377.S). Both observations were centered on α_{2000}=18^{h} 17^{m}29.90^{s},δ_{2000}=-04°39′39.50″, with total integration times of 1.8 hours and 3.6 hours for Cycle 1 and Cycle 3, respectively. The Cycle 1 observations used 44 12-m antennas, with baselines in the range of 20 – 600 kλ, while the Cycle 3 observations used either 38 or 39 12-m antennas with baselines in the range of 15 – 1800 kλ.

For Cycle 1, L483 was observed on 2013 June 01 with J1733–1304 as the phase and flux calibrator and J1924-2914 as the bandpass calibrator. For 2013 June 19, J1733-1304 was the phase, flux, and bandpass calibrator. For 2013 November 2 and 3, J1733–1304 was the phase calibrator and J1924–2914 was the flux and bandpass calibrator. For Cycle 3, L483 was observed on 2016 August 31 with J1924-2914 as the bandpass and flux calibrator, and J1743-0350 as the phase calibrator. For 2016 September 7 and 9, J1751+0939 was the bandpass calib-

Table 5.1: Observational spectral windows, combined Cycle 1 and Cycle 3 observations.

ID	Frequency range [GHz]	rms [mJy]	Channelwidth [MHz]	Synthesized beam	Cycle 3 frequency range [GHz]
0	342.766 – 343.000	6	0.244	$0.36'' \times 0.26''$	342.757 – 343.000
1	345.215 – 345.450	5	0.244	$0.28'' \times 0.21''$	345.097 – 345.565
2	354.379 – 354.613	6	0.244	$0.36'' \times 0.26''$	354.261 – 354.730
3	356.611 – 356.845	7	0.244	$0.30'' \times 0.20''$	356.490 – 356.958

Frequency corresponds to $\nu_{\rm lsr} = 0$ km s^{-1}. The rms given as the typical rms in flux beam^{-1} in the channels.

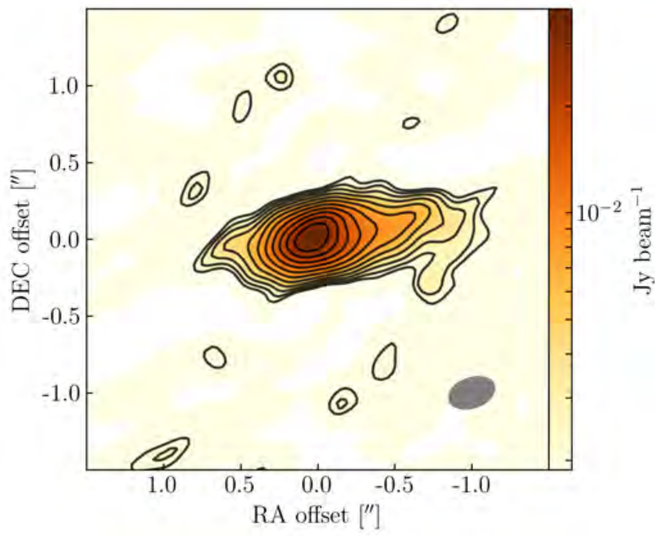

Figure 5.1: Cycles 1 and 3 combined dataset continuum emission at 857 µm in logscale. Contours are spaced logarithmically between 5–100 % of the peak emission.

rator, while J1733-1304 was the flux calibrator, and J1743-0350 was the phase calibrator. Both Cycle 1 and 3 data were calibrated using `CASA` v. 4.7. Before combination of the datasets, the Cycle 1 data were binned down with 4 channels in each bin to match the Cycle 3 channel width, as the Cycle 1 observations had higher spectral resolution than those of Cycle 3. Also, the Cycle 3 data were trimmed at the spectral window edges, to match the Cycle 1 bandwidth (see Table 5.1 for spectral window details).

Phase self-calibration was also performed on the continuum channels in each dataset before combination. After concatenation of the Cycles 1 and 3 data, the continuum was constructed using line-free channels and subtracted from the line emission cubes. After primary beam correction, both line emission channel images and the 857 µm continuum image were created with the `clean` algorithm using Briggs weighting with a robust parameter of 0.5, to get a good trade-off between sensitivity and angular resolution.

An 857 µm continuum image and line emission cubes were also constructed using phase self-calibrated Cycle 3 data alone, to investigate the spectrum of the broader bandwidth in the Cycle 3 observations, and to gauge the physical origin of COMs on the smallest scales. The Cycle 3 spectral cubes used a synthesized beam of $\sim 0.13'' \times 0.13''$ with a typical rms in each channel of ~4 mJy beam^{-1}.

5.3 RESULTS

Fig. 5.1 shows the combined dust continuum image at 857 µm, revealing concentrated emission with a deconvolved 2D Gaussian fit of

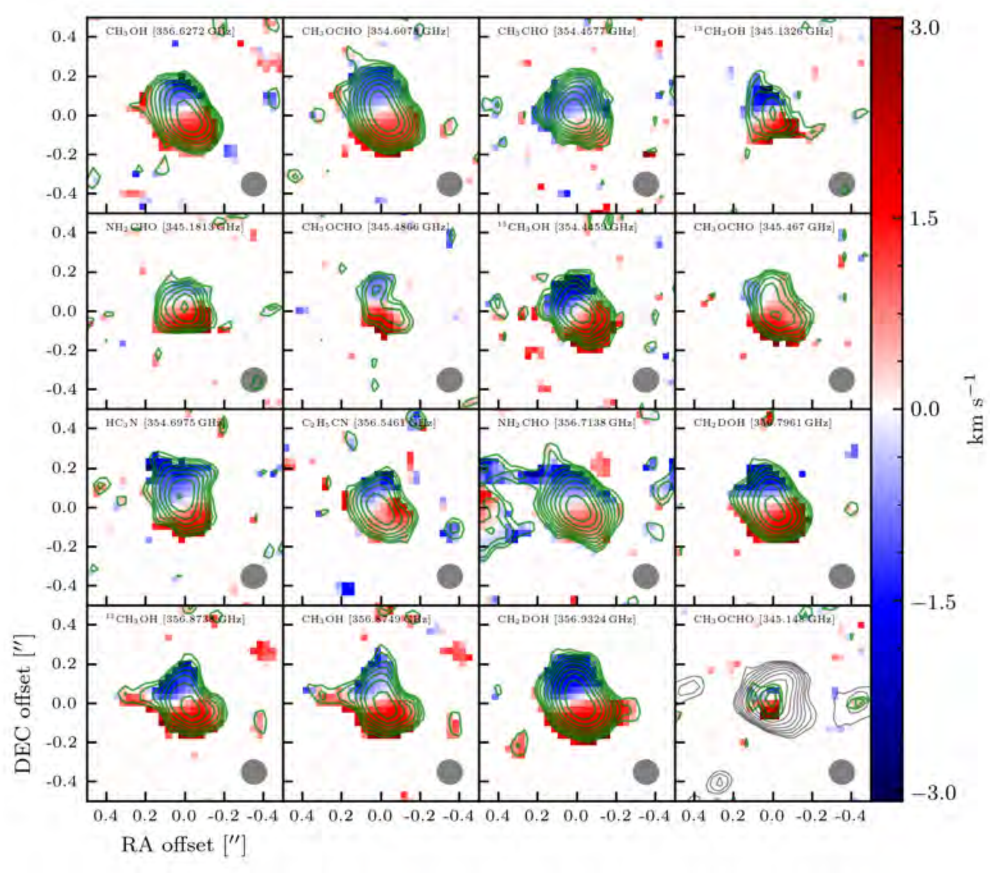

Figure 5.2: Moment 0 and 1 maps of observed COMs (Table 5.4). Moment 0 maps are in green contours, overlaid on the moment 1 map. The Cycle 3 857 μm dust continuum image is shown in the lower right frame. Both dust continuum and the moment 0 map contours are spaced logarithmically between 5–100 % of the peak emission. The first two panels show the unblended lines of CH_3OH and CH_3OCHO, while the remainder are blended to different degrees. All the data shown in this figure are from Cycle 3.

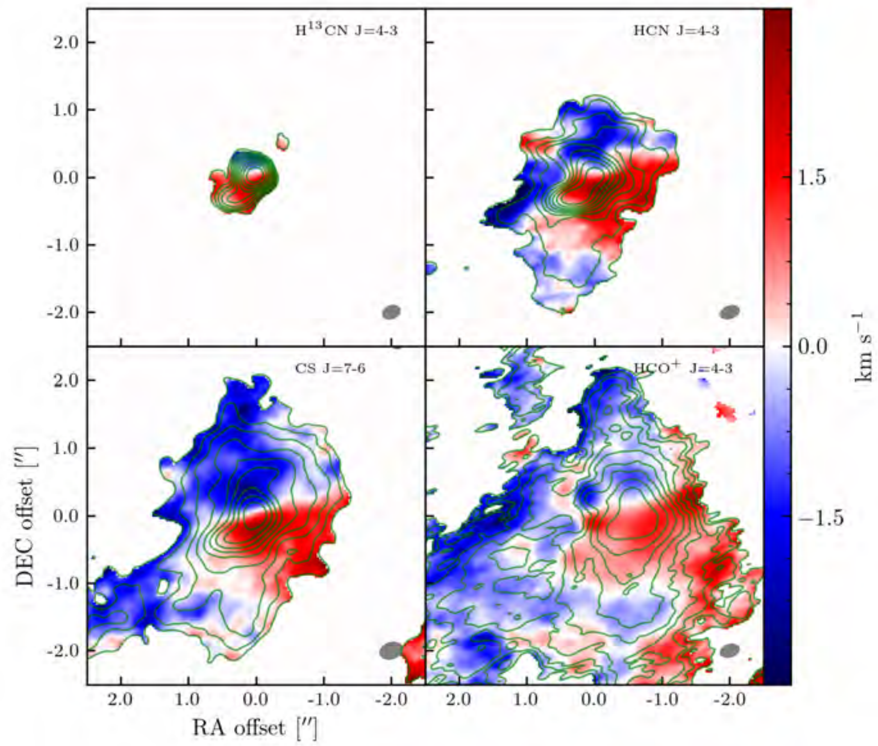

Figure 5.3: Moment 0 and 1 maps of H^{13}CN J=4–3, CS J=7–6, HCN J=4–3 and HCO^{+} J=4–3. Moment 0 maps are in green contours, overlaid on the moment 1 maps. The moment 0 map contours are spaced logarithmically between 5–100 % of the peak emission. All the data shown in this figure are from the combined dataset.

$0.38'' \times 0.19''$ at a position angle of 102°. The dust is elongated in the East-West direction, possibly caused by the outflows dragging material with it outwards. We estimate the integrated deconvolved dust continuum of the combined dataset at 857 μm (Fig. 5.1) to be 72.8 ± 5.5 mJy. This value is fairly close to the SMA 0.8 mm integrated flux density (Jørgensen et al., 2007) of 97 mJy (point source fit with baselines longer than 40 kλ), but lower than a circular fit to the SMA continuum visibility which yields an integrated flux of 0.2 Jy. Hence the combined Cycle 1 and Cycle 3 dataset does filter out some of the larger-scale emission. The Cycle 3-only continuum image has a deconvolved size of $0.16'' \times 0.13''$, with a P.A. of 156° (see Fig. 5.2), and an integrated flux density of 53.7 ± 3.5 mJy, showcasing the loss of some of extended emission detected in the combined dataset.

Fig. 5.3 shows emission from the four major molecule transitions in the observed spectral windows, $H^{13}CN$ J = 4–3, HCN J = 4–3, CS J = 7–6, and HCO^+ J = 4–3. Beyond compact emission coincident with the continuum source, each shows an extra emission component South-East of the disk itself (Fig. 5.3), which we interpret as the inner domain of the eastward part of the known bipolar outflow. A velocity gradient in the North-South direction is also observed in the four major emission lines.

Fig. 5.4 shows PV diagrams of $H^{13}CN$ J = 4–3, HCN J = 4–3, CS J = 7–6, and HCO^+ J = 4–3. Each was produced along the velocity vector using `PVEXTRACTOR`, with a path width of $0.05''$, where the offset is defined by the distance to the rotation axis (Fig. 5.5). The PV diagrams show that only $H^{13}CN$ J = 4–3 lacks extended structures and that HCN J = 4–3 and HCO^+ J = 4–3 are heavily absorbed near the rest velocity, which is also seen in the observations of the entire envelope. All molecule transitions show asymmetric lines, with redshifted emission of higher intensity than the blueshifted emission. A rest velocity of 6.0 km s^{-1} is found, based on the $H^{13}CN$ J = 4–3 emission as well as CS J = 7–6 emission within ~25 au (see Section 5.4.1). It does not apply to the vast amounts of colder, large-scale HCN J = 4–3 and HCO^+ J = 4–3 gas emission as well as the larger-scale CS J = 7–6 emission (Fig. 5.4). The previous estimate of the bulk envelope of 5.5 km s^{-1} (Hatchell et al., 1999) seems to trace the large-scale emission better, whereas our $H^{13}CN$ J = 4–3 and small-scale CS J= 7–6 observations reveal the hot gas in the innermost region of ~ 40–60 au radius, suggesting that there is a velocity shift between the outer and inner regions of L483. We apply $v_{\rm lsr}$ = 6.0 km s^{-1} to our analysis of the gas kinematics in the innermost region (Section 5.4).

Oya et al. (2017) observed a compact component with a broad velocity width of v = ± 6 km s^{-1} in CS J= 4–3, which we observe as well in our CS J=7–6 emission. While absorption against the continuum is observed near the rest velocity in HCO^+ J =4–3 and HCN J =4–3 (Fig. 5.6), it is not significantly redshifted as expected for infalling

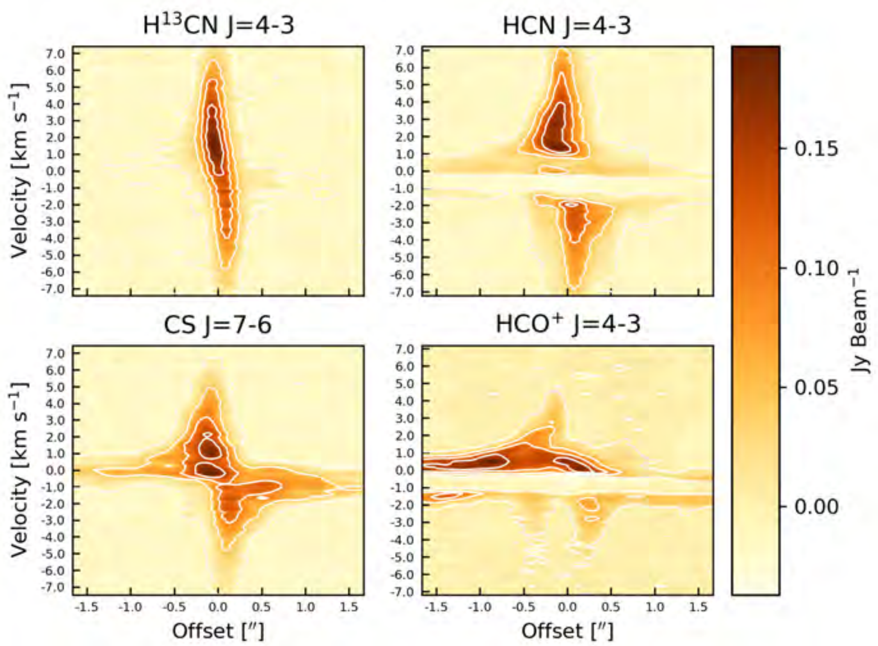

Figure 5.4: PV diagrams of $H^{13}CN$ J = 4–3, CS J = 7–6, HCN J = 4–3 and HCO^{+} J = 4–3, using v_{lsr} = 6.0 km s^{-1}. Contours are spaced linearly between 5–100 % of the peak emission. The PV diagram are made along the direction of the velocity vector and the offset is the distance to the rotation axis (Fig. 5.5). The emission center is the intersection of the rotation axis and velocity vector. v_{lsr} = 6.0 km s^{-1} matches the $H^{13}CN$ J = 4–3 emission well, while the large-scale emission seen in HCN J =4–3 , CS J =7–6 and HCO^{+} J =4–3 are better matched by 5.5 km^{-1} (Hatchell et al., 1999). All the data shown in this figure are from the combined dataset.

material. The absorption we do see is likely caused by resolving out large-scale emission, due to a lack of shorter baselines. While redshifted absorption is seen towards similar Class 0 objects, such as B335 (Evans et al., 2015), L483 has an elongated structure, with outflows at an inclination of 40° and the kinematics of the innermost region, where we have extracted our spectrum, are also dominated by rotational motion, not free-fall (Fig. 5.3). This complex geometry and the kinematics may explain why the inverse P Cygni profile with redshifted absorption against the continuum, expected for a spherical collapse, is not present in L483.

5.3.1 *Other lines and their identification*

In addition to the four main species (HCN, $H^{13}CN$, CS, and HCO^{+}) targeted as part of this program, a multitude of emission lines are found, belonging to a range of COMs, shown in Fig. 5.6 along with synthetic line spectra. Identifying these fainter transitions in the spec-

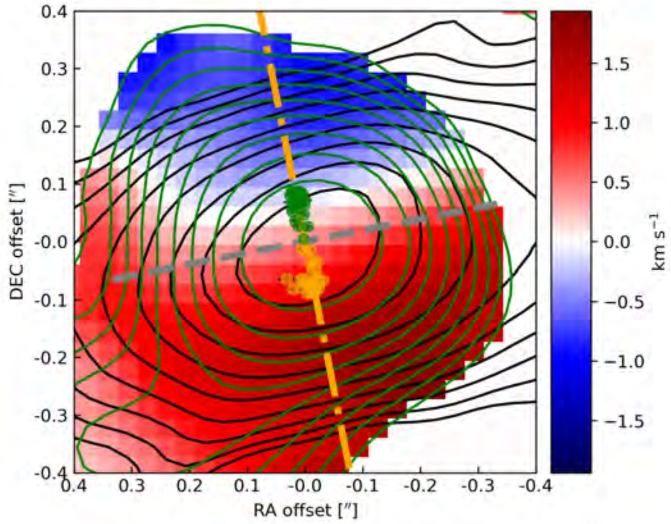

Figure 5.5: $H^{13}CN$ J = 4–3 `imfit` datapoints superimposed on the $H^{13}CN$ J = 4–3 moment 1 map, green and orange points indicating blue- and redshifted channels, respectively. Green and black contours show the $H^{13}CN$ J = 4–3 moment 0 map and 857 μm continuum emission, respectively, both spaced logarithmically between 5–100 % of the peak emission. The inferred rotation axis of $H^{13}CN$ J = 4–3 is shown as a gray dashed line and the velocity gradient vector as an orange dashed line. The emission center is the intersection between the rotation axis and the velocity vector. All the data shown in this figure are from the combined dataset.

tra requires careful comparison to spectroscopic catalogs, modeling the emission from known species, and comparison to other surveys. To do this we calculate synthetic spectra for possible molecules and compared those to the data: for a given molecule the spectra are predicted under the assumption of local thermodynamic equilibrium given assumptions of the column density, excitation temperature, systemic velocity, line width and source size. Typically besides the main (very optically thick) lines the three latter parameters can be fixed for all lines and species leaving the column densities to be constrained.

To decide which molecules to assign we compared our L483 data directly to those from the ALMA Protostellar Interfeometric Line Survey (PILS) of the low-mass Class 0 protostellar binary IRAS 16293-2422 (Jørgensen et al., 2016). Specifically, in that survey more than 10,000 separate features can be identified in a frequency range between 329 GHz and 363 GHz and modeled in a similar fashion. With the large frequency coverage in the PILS data many species can be well-identified and the column densities and excitation temperatures constrained. Given our smaller frequency coverage in the observations of L483 the assignments would in their own right only be tentative and the inferred column densities mainly a sanity check that the assignments are plausible. The general agreement with the identifications in the IRAS16293B data strengthens this case, however. Table 5.4 lists the assigned transitions, while Table 5.2 gives the inferred column densities for L483 and IRAS16293B.

Generally, the fits work well. For most species, we do not have a sufficient number of transitions to constrain the excitation temperature, except for CH_2DOH (deuterated methanol) and CH_3OCHO (methyl formate). For the former, an excitation temperature of 100 ± 25 K works well, while the fit for CH_3OCHO is driven toward a higher excitation temperature of 300 K. This excitation is similar to that of IRAS16293B where a number of species, including methyl formate, with binding energies of 5000–7000 K are better fit with a high excitation temperature of a few hundred K. Toward IRAS16293B, methanol also shows a higher excitation temperature. A colder component is also present there, however, as witnessed by extended emission in a number of lower excited transitions as well as the low temperatures of highly optically thick transitions even for the isotopologues. Toward L483, a number of the stronger lines of CH_2DOH with low upper energy levels (~ 100 K) are marginally optically thick with τ of 0.1–0.5. Thus, it is plausible that a still higher temperature component with a high column density may be present on even smaller scales, not traced by the lines identified here. Contrary, to the methanol isotopologue transitions, most of the methyl formate lines have low opacities of 0.01–0.05, and thus are very likely sampling the most compact, high column density material. Also, it should be noted that the inferred column densities are only weakly dependent on the exact excitation temperature, changing by less than 10–20% with temperatures varying from about 100 K to 300 K. For the purpose of this paper, these uncertainties are less critical.

We constructed moment 0 and 1 maps of each individual identified COM transition, integrating all emission within $\pm$ 7 km s^{-1} based on Fig. 5.7. A range of COM molecules demonstrate line emission with clear velocity gradients similar to those seen in the four main species. Deconvolved 2D Gaussian fits to the moment 0 maps of the selected COMs reveal that most molecules are extended compared to the continuum peak with deconvolved sizes of approximately 0.2–0.3″ (40–60 au). Fig. 5.2 shows the moment 0 and 1 maps for each transition.

5.3.2 *Comments about individual species/transitions*

Methanol (CH_3OH) is the most prominent organic molecule identified on small scales towards solar-type protostars with different rarer isotopologues typically possible for identification. In our frequency range, the main lines of CH_3OH are of the two isotopologues, $^{13}CH_3OH$ and CH_2DOH. CH_2DOH, in particular, has six transitions in the HCO^+ spectral window and cover two others in the $H^{13}CN$ and CS windows with three separate transitions of $^{13}CH_3OH$. In the HCO^+ window, a prominent feature is seen at 356.625 GHz. Without considering the full spectral range available, a good match in the catalogs for just this feature would be a transition of methyl mercaptan (CH_3SH) with E_u = 136 K. Unless its excitation conditions are very peculiar, one would then also expect to see its $14_{2,12} - 13_{2,11}$ transitions at 354.372 GHz and 354.643 GHz in the HCN window since they approximately have the same energies and strengths. In the PILS data, all three lines are clearly seen, though the former line (356.625 GHz) is slightly stronger and shows signs of red-shifted absorption, possibly indicating a line blend. A much better option for this line is a set of relatively highly excited transitions of the main isotopologue of methanol (CH_3OH 23_{-4}-22_{-5}). For the derived column density of $^{13}CH_3OH$, these transitions should indeed be present at a temperature of 100 K taking into account the standard ^{12}C:^{13}C ratio. A similar highly excited CH_3OH transition at 356.875 GHz is in fact blended with a transition of $^{13}CH_3OH$.

A few isolated transitions can be assigned to individual species with an assumed excitation temperature of 100 K. These include CH_3OCH_3, C_2H_5OH, NH_2CHO, SO_2, H_2CS, and HC_3N. Of these species, the relatively common gas phase molecules, H_2CS, SO_2 and HC_3N, are found to be relatively more abundant toward L483 than the complex organics. For the other species, the inferred column densities are in agreement with those toward IRAS16293B, lending credibility to their assignments.

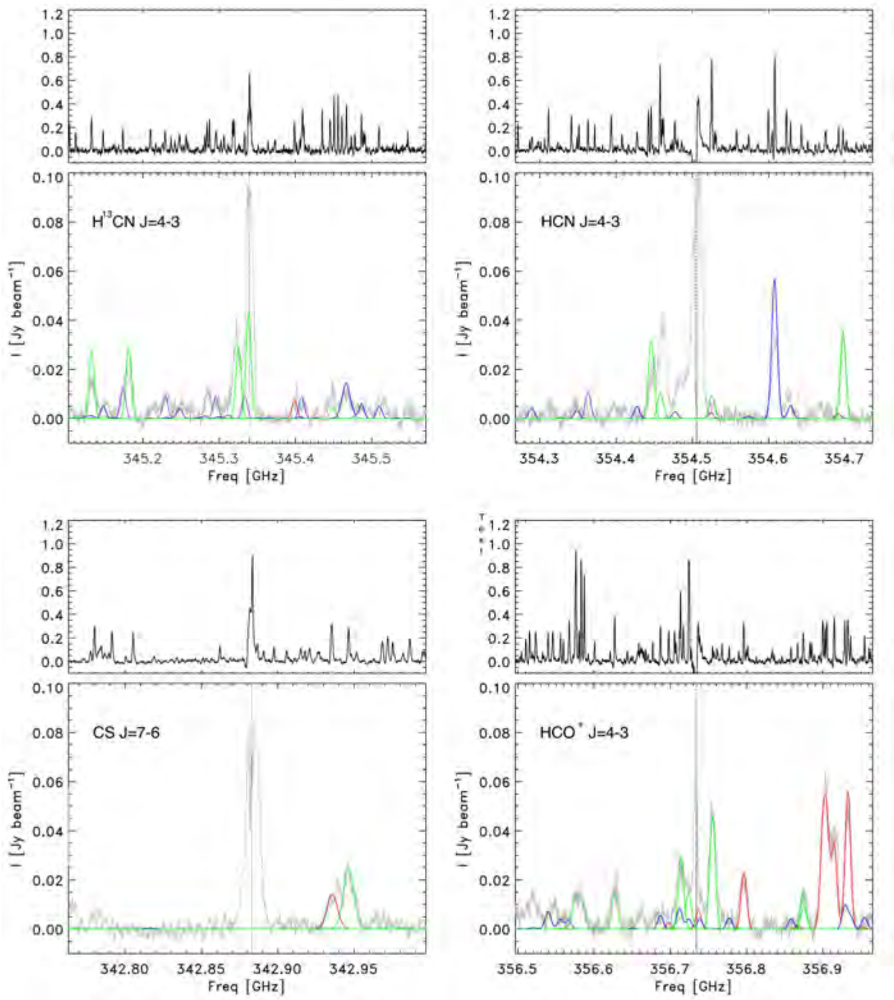

Figure 5.6: Cycle 3 spectral windows centered on $H^{13}CN$ J = 4–3, HCN J = 4–3, CS J = 7–6 and HCO^+ J = 4–3. The main transition of the spectral window is shown as a dotted line, assuming v_{lsr}=5.4 km s^{-1}. The line model fits are overlaid in colored lines (red = CH_2DOH, blue = CH_3OCHO, purple = C_2H_5OH, green = all other species), while the observed spectrum is in grey. The top frames show the corresponding IRAS16293B spectrum.

A few features remain problematic to assign. For example, one feature at 356.52 GHz in the HCO^+ window could be attributed to a few different species, including ethylene glycol and acetone, but these species would have transitions visible in other spectral windows. In the PILS data, a feature is also seen at this frequency, which is also not easily assigned to any of the tabulated species.

In the HCN window, the feature at 354.458 GHz is somewhat puzzling. By itself, it could be attributed to acetaldehyde (CH_3CHO) but this species has a similar transition at 354.525 GHz that should be equally strong and in the PILS data the two transitions in fact show up in this way. This behavior is noteworthy as acetaldehyde otherwise is considered one of the most easily identifiable of the complex organics, but in our data it can thus only be tentatively identified.

In the $H^{13}CN$ window, the feature at 345.285 GHz remains unassigned. It could be attributed to cyanamide (NH_2CN), which would be an excellent fit and was recently identified in the PILS data by Coutens et al. (2018). To reproduce the observed line strength, however, a cyanamide to formamide (NH_2CN/NH_2CHO) ratio of 20 would be required, whereas all other interferometric measurements, as well as models, have formamide being more abundant than cyanamide by an order of magnitude or more. More likely, there remains an issue with spectroscopic predictions for line intensities. For example, two transitions are seen in PILS data at the same frequencies that are unassigned: one is likely CH_2DOH (345.2842 GHz) and the other C_2H_5OH (345.2877 GHz) for which the predicted line strengths are problematic. This is a known issue for the B- and C-type transitions of deuterated methanol and previously some issues have been identified for C_2H_5OH as well (Müller et al., 2016).

For the feature at 356.546 GHz, the best assignment would be of ethyl cyanide (CH_3CH_2CN). This species does have a relatively bright transition in the HCN window at 354.477 GHz, but due to blending with the HCN transition itself it is not possible to see whether this transition is indeed present. Another CH_3CH_2CN transition is near the HCO^+ window at 356.960 GHz, but falls just outside of our frequency coverage. If the transition indeed could be solely attributed to ethyl cyanide, it would be more abundant by an order of magnitude relative to ethanol than what is seen toward IRAS16293B. Clearly, more transitions need to be observed of these species for reliable assignments and column densities.

5.4 ANALYSIS

5.4.1 *Kinematics*

To determine whether or not a Keplerian disk is present in L483, we investigated the kinematics of the gas motions in the inner 30 au of

Table 5.2: Inferred column densities for the species identified toward L483 and compared to the one beam offset position from IRAS16293B.

Species		Column density [$cm^{-}2$]	
		L483	IRAS16293B
Methanol	CH_3OH	1.7×10^{19}	1.0×10^{19}
	$^{13}CH_3OH$	2.5×10^{17}	1.5×10^{17}
	CH_2DOH	4.0×10^{17}	7.1×10^{17}
Dimethyl ether	CH_3OCH_3	8.0×10^{16}	2.4×10^{17}
Methyl formate	CH_3OCHO	1.3×10^{17}	2.6×10^{17}
Ethanol	C_2H_5OH	1.0×10^{17}	2.3×10^{17}
Acetaldehyde	CH_3CHO	8.0×10^{16}	1.2×10^{17}
Formamide	NH_2CHO	1.0×10^{16}	1.2×10^{16}
Cyanopolyyne	HC_3N	5.0×10^{17}	1.8×10^{14}
Thioformaldehyde	H_2CS	2.0×10^{16}	1.5×10^{15}
Sulfur-dioxide	SO_2	1.0×10^{17}	1.5×10^{15}

L483. For this purpose, we fit the position of the peak emission in each spectral cube channel, using the 2D Gaussian fit routine, CASA `imfit`. $H^{13}CN$ J = 4–3 and CS J = 7–6, which both show signs of a rotation profile perpendicular to the outflow direction, were fit, while we do not consider HCN J = 4–3 and HCO^+ J = 4–3 as these transitions are heavily influenced by the East-West outflow (Fig. 5.3). We further defined a box around the central emission as input to `imfit` to circumvent the large-scale emission seen in the South-East direction (Fig. 5.3) of $H^{13}CN$ J = 4–3 and CS J = 7–6.

For the two transitions, the `imfit` data points are mostly found in two clusters of blue- and redshifted `imfit` data points, which can be seen in Fig. 5.5 for $H^{13}CN$ J = 4–3. We made a weighted linear regression fit to these clusters of data, which defines the velocity vector, and took the weighted average y coordinate of each of the two data clusters as input to the inverse velocity vector function to define the average x coordinate. The midpoint between these two representative points of the data clusters was taken as the emission center, determined to be α_{2000}=$18^h17^m29.943\pm0.001^s$, δ_{2000}=-04°39′39.595 ± 0.012″.

The rotation axis was then defined as being normal to the velocity vector, intersecting the emission center, see Fig. 5.5. We defined the velocity vector, rotation axis, and emission center using $H^{13}CN$ J = 4–3 data and applied it to CS J = 7–6, as $H^{13}CN$ J = 4–3 has more datapoints. The rest velocity for L483 was estimated to be 6.0 km s^{-1}, using the $H^{13}CN$ J=4–3 and CS J=7–6 emission, under the criterion that the red- and blueshifted datapoints should be symmetric in a distance vs. velocity plot, see Fig. 5.7. This rest velocity is used as

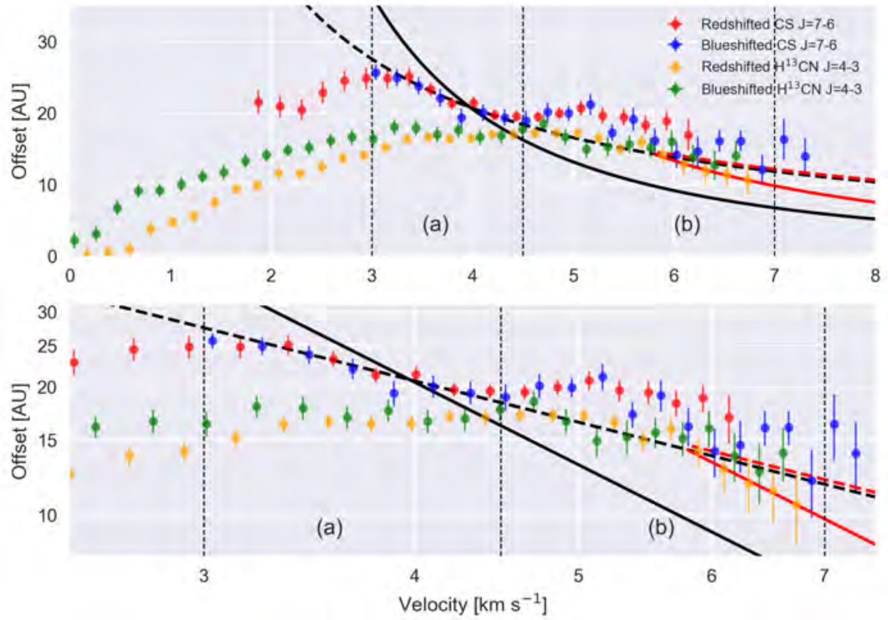

Figure 5.7: Distance vs. velocity plot of $H^{13}CN$ J = 4–3 and CS J = 7–6 `imfit` datapoints, using Cycle 3 data only (top frame) and the same data shown in logscale (bottom frame). The blue- and redshifted `imfit` datapoints of the CS J =7–6 emission are shown in blue and red, respectively, while the blue- and redshifted `imfit` datapoints of $H^{13}CN$ J =4–3 are shown in green and orange, respectively. The (a) and (b) regions, with borders marked by vertical dashed lines, show which datapoints were used for the fit. Only CS J =7–6 datapoints are used for the fit in velocity region (a), while only $H^{13}CN$ J =4–3 datapoints are used in velocity region (b). The data diverging from the model velocity profiles at low velocities, below velocity region (a), arise from the projected rotational gas motions at the edge of the emission region, and are not used in the fit. Both frames are overlaid with the best fit infall (black dashed line) and Keplerian velocity profile (black full line) to the Cycle 3 data. The red solid line and the red dashed line show the best fit to the $H^{13}CN$ J =4–3 `imfit` datapoints with absolute velocities >5.8 km s^{-1}, using a Keplerian and infall velocity profile, respectively.

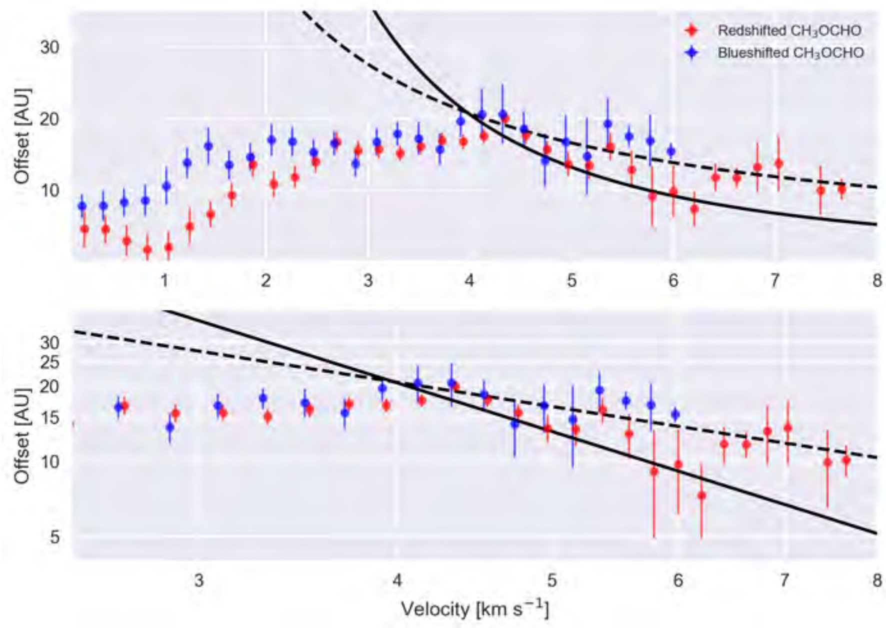

Figure 5.8: Distance vs. velocity plot of CH_3OCHO `imfit` datapoints, using Cycle 3 data only (top frame) and the same data shown in log-scale (bottom frame). The blue- and redshifted `imfit` datapoints of the CH_3OCHO emission are shown in blue and red, respectively. The data diverging from the model velocity profiles at low velocities, below ~ 4 km s^{-1}, arise from the projected rotational gas motions at the edge of the emission region. Both frames are overlaid with the best fit infall (dashed line) and Keplerian velocity profile (full line) to the Cycle 3 CS J =7–6 and $H^{13}CN$ J =4–3 data.

the reference for the velocity offset of the `imfit` data points, while the data point distance from the rotation axis was taken as the offset distance.

The `imfit` data points were then converted into (radius, velocity) points and used in a reduced χ^2 fit of two different velocity profiles, a Keplerian velocity profile, $v = \sqrt{GM_*/r}$, where G is the gravitational constant and M_* is the central mass, and the velocity profile of infall with conservation of angular momentum, $v_\phi r = v_{\phi,0} r_0$, where $v_{\phi,0}$ and r_0 is the start velocity and starting distance, respectively, of the collapsing material. Such an infall scenario will have $v_\phi \propto r^{-1}$, a velocity profile previously used to estimate the kinematics of a disk or disk-like structure around a Class 0/I object (e.g., see Lindberg et al., 2014). For the Keplerian profile, we used a central mass range 0.01-1.5 $M_\odot$ and 2.8×10^5 different constants for the infall velocity profile, to find the best fit.

We combined the $H^{13}CN$ *J*=4–3 and CS *J*=7–6 data into a single dataset, and performed a reduced χ^2 fit in the velocity regime. We excluded the lowest velocities as these are affected by the small extent of the $H^{13}CN$ gas line emission (~ 20 au radius), causing the lower velocities to be dominated by low-velocity gas toward the emission center, arising from projected gas velocities coming from the edge of the observed gas emission region. Moreover, these low velocities could include emission from the other disk-half, as thermally broadened lines from the other disk-half are convolved with the relatively large beam, drawing the `imfit` results towards a lower offset. We also excluded higher velocities, where the `imfit` results become noisy. The difference in the spatial extents of the observed CS and $H^{13}CN$ datapoints and the spatial disparity illustrated in Fig. 5.3, are likely related to the lower critical density of CS relative to HCN (Evans, 1999).

We used both the combined dataset and Cycle 3 data alone in the reduced χ^2 fit, as `imfit` is affected negatively by the larger rms and beam in the combined dataset. The Cycle 3 data have more precise `imfit` data points, due to their higher angular resolution of $\sim 0.13'' \times 0.13''$ and lower rms, while missing the shorter baselines of the combined Cycle 1 and 3 data. Fig. 5.7 shows that, using Cycle 3–only data, the infall profile is strongly favored by the reduced χ^2 fit, with $\chi^2_{\rm red}$=0.58, while the Keplerian fit has $\chi^2_{\rm red} = 14$. The combined dataset gave the same conclusion: the infall profile is heavily favored, with $\chi^2_{\rm red}$ better by more than a factor of four. This result suggests that the observed line emission is not from gas in a rotationally supported disk, but rather from gas in an infalling-rotating structure. In the event that a Keplerian disk exists, we would expect a transition between an infalling velocity profile and a Keplerian velocity profile, at the disk edge. We do see a tentative change in the $H^{13}CN$ *J* =4–3 `imfit` data near 5.8 km s^{-1}, at ~ 15 au, so we performed an independent fit to $H^{13}CN$ *J* =4–3 data above this velocity, seen in Fig. 5.7. The reduced χ^2 fit slightly favored a Keplerian velocity profile with χ^2_{red}=0.45 vs. an infall velocity profile with χ^2_{red}=0.53. However, we cannot conclude the presence of a Keplerian disk with a radius of 15 au, since the data is too noisy and sparse, and since an infall velocity profile could fit the data as well. The absence of a Keplerian disk down to at least 15 au is consistent with the analysis of the submillimeter continuum emission toward the source (Jørgensen, 2004; Jørgensen et al., 2007, 2009) where the interferometric flux of L483 was consistent with envelope-only emission and did not need a central compact emission source.

5.4.2 *Dust temperature profile and the distribution of COMs*

In order to investigate the dust temperature profile of L483 on small scales, we used the density solution to an infalling-rotating collapse (Terebey et al., 1984), with an example centrifugal radius of 60 au (consistent with the conclusions of Oya et al., 2017). For an initial total dust mass guess, we used a mass determined within a radius of 40 au, an extent based on the 857 µm emission (Fig. 5.1). While the 857 µm dust continuum traces material swept up in the outflow structure, we do not attempt to model the outflow or outflow cavities. Using the available SED data (Table 5.3), we integrated the SED and estimate the bolometric luminosity to be 10.4 $L_\odot$, comparable with previous luminosity estimations of 9 $L_\odot$ (Jørgensen et al., 2002) and 13 ± 2 $L_\odot$ Shirley et al. (2000).

The dust continuum mass was estimated from the integrated, deconvolved flux density of the 857 µm continuum image from the combined dataset (Fig. 5.1), extracted from a box around the elongated emission structure. The total dust mass is

$$M = \frac{S_\nu d^2}{\kappa_\nu B_\nu(T)}, \tag{5.1}$$

where S_ν is the total source flux, d is the distance, κ_ν is the dust opacity, and $B_\nu(T)$ is the spectral radiance. Both κ_ν and $B_\nu(T)$ depend on the temperature field as the mean dust opacity κ_ν will be a mixture of dust with and without ice-mantles due to sublimation caused by heating from the central protostar. We used bare-grain and thin-ice mantle opacities from Ossenkopf & Henning (1994), corresponding to coagulated dust grains in an environment with a gas number density of 10^6 cm^{-3}. We used initial guesses of the mean dust temperature of all dust, both with and without ice mantles, within 40 au, T_{av}, and the dust population ratio between icy-dust and bare-grain dust, also within 40 au, to get an initial estimate of the total dust mass, using Eq. 5.1, in the innermost region of L483.

With a dust mass estimate as input, we used `RADMC-3D`, a 3D Monte Carlo radiative transfer code (Dullemond et al., 2012), to determine

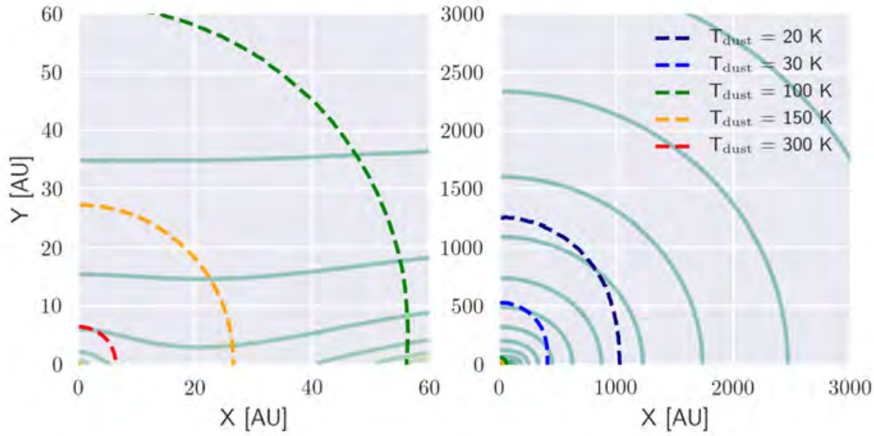

Figure 5.9: Temperature distribution in the density solution to an infalling-rotating collapse model, with r_c=60 au, M_*=0.2 $M_\odot$, and $\dot{M} = 9.0 \times 10^{-7}$ $M_\odot$ yr^{-1} using only bare-grain opacities. The density contours in solid lines are logarithmically spaced, increasing towards the x-axis, while the dust temperature contours are in dashed lines.

the dust temperature, which led to a new mass estimation, as T_{av} and κ_ν change (Eq. 5.1). The updated mass in turn led to a different temperature distribution, which again affects our estimate of κ_ν and T_{av}. After a few iterations, we had a stable estimate of all parameters, with T_{av}=150 K from visual inspection of the temperature distribution within 40 au (Fig. 5.9). All the dust within 40 au has temperatures above 90–100 K, which allows us to use bare-grain dust opacities exclusively, as the water-ice mantle sublimates at these temperatures (Sandford & Allamandola, 1993). The final temperature profile can be seen in Fig. 5.9 and we estimate the total mass (dust + gas) in the inner region to be 7.7×10^{-4} $M_\odot$. While the exact temperature distribution and derived total mass using Eq. 5.1 is dependent on the used dust density model and its parameters, we have used a dust density model consistent with both our observed kinematics (the gas kinematics of the model has a $v_\phi \propto r^{-1}$ profile) and the earlier research of Oya et al. (2017).

Fig. 5.2 shows that the spatial extent of emission from the COMs (0.2–0.3″) are within the estimated dust ice-mantle sublimation front of ~ 55 au (Fig. 5.9), implying that the COMs reside in the hot corino, which is dominated by rotational motion. The derived column densities of the COMs (Table 5.2) are in good agreement with the values found for COMs in IRAS16293B both in an absolute and relative sense. That there is a good agreement in an absolute sense, is likely because the amount of material on small scales at high temperatures is comparable toward the two sources. The envelope masses are also similar (4.4 $M_\odot$ vs. 4 $M_\odot$) and while L483 is more luminous than IRAS16293B, with 10.4 $L_\odot$, see below, vs. ~3 $L_\odot$ (Jacobsen et al., 2017), respectively, IRAS16293B is surrounded by massive amounts of disk-like material (Jacobsen et al., 2017), which may explain the comparable amount of material at high temperatures. This result suggests that a "true" hot core chemistry is present toward L483, which is counter to the argument that the presence of warm carbon-chain molecules (e.g., Oya et al., 2017; Sakai et al., 2009) in some way reflects the early evolution of the prestellar core.

Table 5.4 shows that rotation profiles are also observed for all strong COM lines, with the same North-South velocity gradient as seen for CS J = 7–6 and $H^{13}CN$ J = 4–3 (Fig. 5.3). We extracted the peak emission position in each channel for all observed COM lines in the Cycle 3 data using `imfit`, but the data were too noisy and the lines too blended for clear velocity profiles to be extracted, except for CH_3OCHO. We defined the emission center and rotation axis of CH_3OCHO based on its `imfit` data, as the CH_3OCHO emission is slightly offset compared to $H^{13}CN$ J = 4–3. This offset is, however, well within the beam. Fig. 5.7 shows that the velocity profile of CH_3OCHO is consistent with the infall profile derived from the CS J = 7–6 and $H^{13}CN$ J = 4–3 Cycle 3 data.

5.5 DISCUSSION

The lack of an observable rotationally supported disk in L483 down to ~15 au, and the presence of the COMs on scales of 40–60 au, have a number of important implications. In terms of the system geometry, the position angle of our rotation profile was 11°, virtually perpendicular to the EW outflows. Our data show that L483 is undergoing a rotating collapse, with a large-scale outflows consistent with earlier works and a small inner region dominated by rotational motion (Fig. 5.2). The infalling-rotating collapse continues down to at least 15 au in radius, with the outflows of L483 necessarily being launched very close to the central protostar, in the absence of a disk > 15 au.

L483 shows some similarities with the Class 0 object B335, as both YSOs have a lack of Keplerian disks, >15 au and > 10 au, respectively, and show very small amounts of dust in the innermost region, 7.7×10^{-4} $M_\odot$ vs. 7.5×10^{-4} $M_\odot$, for L483 and B335 (Evans et al., 2015), respectively. Both objects contain a hot corino (Imai et al., 2016), while the L483 hot corino radius of 40–60 au is likely larger than that of B335, estimated to be only a few tens of au (Imai et al., 2016), due to its relatively low luminosity of 0.72 $L_\odot$ (Evans et al., 2015). B335, however, has low levels of rotation in its infall, whereas L483 has a clear infall-rotational signature (Figs. 5.3 and 5.2).

Oya et al. (2017) invoke a chemical transition at the centrifugal barrier of L483, due to the abrupt transition in the physical environment. They also speculate that NH_2CHO and CH_3OCHO reside in an unresolved Keplerian disk, explaining the compact emission they observe. Our data of emission from the same molecules and the absence of a Keplerian disk down to a radius of at least 15 au, however, illustrate that these species also reside in the infalling envelope. Also these COMs, together with the distributions of the other COMs, can be accounted for by the release of molecules into the gas phase due to dust ice-mantle sublimation by itself. They invoked a Keplerian disk model inside the centrifugal barrier to explain the compact, high-velocity emission structure they observe out to $\pm$ 6 km s^{-1} in their PV diagrams, as their rotating-collapse model alone could not explain this emission together with the more spatially extended emission. However, they do not resolve the hot corino region (0.2″–0.3″) in their observations. We find empirically, using the peak emission position in each channel, that the compact high-velocity CS J =7–6 and H^{13}CN J =4–3 emission up to at least $\pm$ 5.8 km s^{-1}, is best matched by an infalling velocity profile, not a Keplerian one.

L483, interestingly, also exhibits a difference to some of the more evolved protostars with larger disks. For example, Lindberg et al. (2014) find very small levels of CH_3OH toward the Class 0/I protostar R CrA-IRS7B and the presence of a Keplerian disk around this source. Based on a detailed line radiative transfer analysis, they demonstrate that this lack of CH_3OH emission may reflect the low column density of the protostellar envelope at the scales where material is being assembled into the circumstellar disk. A similar situation is seen toward the Class I protostar Oph-IRS67 in Ophiuchus. For this source, Artur de la Villarmois et al. (2018) find a Keplerian disk to be present and also do not see signs of any CH_3OH down to low column densities. In contrast, acetaldehyde was found towards the Class 0 object HH212 in Orion, where a tentative detection of a $\sim$ 90 au Keplerian disk was made (Lee et al., 2014), though the abundance could not be determined due to optically thick submillimeter continuum emission Codella et al. (2016). More observations are needed to quantify the relationship between the COM column density and abundance, and the presence of Keplerian disks.

For sources with an extended disk, the mass budget is dominated by the disk plane in the inner region. If the only source of heating at these scales is the radiation by the newly formed protostar, a significant amount of the material on small scales may be relatively cold, causing molecules to freeze-out onto dust grains and thus lowering the column density of COMs. In contrast, for YSOs with smaller disks, the warm envelope will dominate the mass budget on these scales. An early stage hot corino without a sizable disk can only exist for a limited time, if a disk is forming, as pointed out by Lindberg et al. (2014), as $R_{100\ K} \propto M_*^{0.5}$, while the centrifugal radius $r_c \propto M_*$, within which rotational support is greater than the gas pressure (Terebey et al., 1984) and a stable disk can appear. Assuming a monotonically growing disk, as expected for a collapsing-rotating envelope (Terebey et al., 1984), these proportionalities define a time period within which a small Keplerian disk, or none at all, exist, where the COMs will be abundant in the gas phase in the inner hot region of the collapsing envelope, before the hot corino region becomes smaller than the growing disk. The multitude of COMs in L483 and the lack of a Keplerian disk down to at least 15 au, may therefore indicate that L483 is still in a chemical stage dominated by a warm inner envelope. In this picture, assuming that we have a protostar luminous enough to create an observable hot region, it is possible that these phenomena could be complementary, i.e., the presence of a hot corino chemistry would signify the presence of a small (young?) disk. Similarly, sources with extended disks will show small amounts of methanol and more complex species present in the gas phase.

5.6 CONCLUSION

We have presented ALMA Cycles 1 and 3 Band 7 observations of HCN J = 4–3, $H^{13}CN$ J = 4–3, CS J = 7–6, and HCO^+ J = 4–3 together with high angular resolution observations (~ 0.1″) of a series of COMs, towards the low-mass Class 0 object L483.

- We fitted combined ALMA Cycles 1 and 3 observations, as well as Cycle 3-only observations, of $H^{13}CN$ J = 4–3 and CS J = 7–6 with two velocity profiles, Keplerian orbital motion and infall following angular momentum conservation. We found that the observed kinematics strongly favors an infall velocity profile. This result excludes the presence of a Keplerian disk in L483 down to a ~ 15 au radius.
- A range of COMs was observed with the same rotational signature as $H^{13}CN$ J = 4–3 and CS J = 7–6, from which a single clear velocity profile belonging to CH_3OCHO was extracted that follow the same infall profile as $H^{13}CN$ J = 4–3 and CS J = 7–6.
- The extent of the observed COM emission go out to ~ 40–60 au radius, consistent with the derived sublimation radius of ~55 au, where the gas sublimates into the gas phase off the dust grains, suggesting that the COMs exists in the hot corino of the L483 envelope.
- The lack of a Keplerian disk down to at least a 15 au radius, and the presence of COMs in the envelope at ~ 40–60 au scales, reveal that the COMs in L483 exists in a chemical era before the expected growing disk will dominate the chemistry and possibly reduce the column densities of COMs.

The ALMA telescope has facilitated observations of unprecedented angular resolution of low-mass protostars, revealing the innermost regions of the early star-forming stages. The exact timeline for the emergence of Keplerian disks, the chemistry of saturated COMs before and during the disk era remains poorly understood due to the low number of observations of such objects. With observations of more sources, the coming years will reveal the evolution of COMs and Keplerian disks on the smallest scales in nearby star-forming regions, broadening our understanding of the formation of planetary systems.

5.7 ACKNOWLEDGEMENTS

This paper makes use of the following ALMA data: 2012.1.00346.S and 2015.1.00377.S. ALMA is a partnership of ESO (representing its member states), NSF (USA) and NINS (Japan), together with NRC (Canada) and NSC and ASIAA (Taiwan) and KASI (Republic of Korea), in cooperation with the Republic of Chile. The Joint ALMA Observatory is operated by ESO, AUI/NRAO and NAOJ. S.K.J. and J.K.J. acknowledges support from the European Research Council (ERC) under the European Union's Horizon 2020 research and innovation programme (grant agreement No. 646908) through ERC Consolidator Grant "S4F". Research at the Centre for Star and Planet Formation is funded by the Danish National Research Foundation. This research has made use of NASA's Astrophysics Data System. This research made use of Astropy, a community-developed core Python package for Astronomy Astropy Collaboration et al. (2013a). This work uses PVEXTRACTOR[1].

5.8 APPENDIX

5.8.1 *Figures and tables*

1 https://github.com/radio-astro-tools/pvextractor

Table 5.3: SED of L483. [a] 2MASS survey (Skrutskie et al., 2006), [b] Tóth et al. (2014), [c] Yamamura et al. (2010).

Wavelength [μm]	Flux [Jy]	Flux uncertainty [Jy]	Reference
1.25	5.39×10^{-4}	1.08×10^{-4}	2MASS[a]
1.63	9.14×10^{-4}	1.83×10^{-4}	2MASS[a]
2.19	3.15×10^{-2}	6.3×10^{-3}	2MASS[a]
3.35	9.34×10^{-3}	3.00×10^{-4}	WISE[b]
4.60	9.83×10^{-2}	2.10×10^{-3}	WISE[b]
11.56	3.76×10^{-2}	7.00×10^{-4}	WISE[b]
12.0	0.25	5×10^{-2}	Strauss et al. (1990)
18.39	1.05	0.06	Akari[c]
22.1	2.49	0.04	WISE[b]
23.88	6.91	0.48	WISE[b]
25.0	6.92	1.384	Strauss et al. (1990)
60.0	89.1	17.8	Helou & Walker (1988)
65	92.4	5.1	AKARI[c]
90	87.4	4.0	AKARI[c]
102	166.0	20.0	Helou & Walker (1988)
140	150.0	7.0	AKARI[c]
160	156.0	7.0	AKARI[c]
350	31.0	6.2	Dotson et al. (2010)
450	15.0	2.0	Shirley et al. (2000)
800	1.98	0.02	Shirley et al. (2000)
1100.0	0.64	0.02	Fuller et al. (1995)

Table 5.4: List of assigned transitions. * indicates that the transition is shown in Fig. 5.2.

Species	Transition	Freq [GHz]	$\log_{10} A_{ul}$ [s^{-1}]	E_u [K]
CH_3OH	$23_{-4,20}-22_{-5,17}$	356.6272*	−4.09	728
	$18_{-8,10}-19_{-7,12}$	356.8749*	−4.31	718
$^{13}CH_3OH$	$4_{0,4}-3_{-1,3}$	345.1326*	−4.08	36
	$4_{1,3}-3_{0,3}$	354.4459*	−3.89	44
	$3_{2,12}-12_{3,9}$	356.8738*	−4.10	244
CH_2DOH	$17_{2,16}-17_{1,17}$	342.9357	−3.78	343
	$16_{2,14}-15_{3,13}$	345.3989	−4.23	310
	$8_{7,1/2}-7_{7,0/1}$	356.7367	−4.39	284
	$8_{6,2/3}-7_{6,1/2}$	356.7961*	−4.07	234
	$8_{2,7}-7_{2,6}$	356.8997	−3.75	104
	$8_{5,3/4}-7_{5,2/3}$	356.9051	−3.94	193
	$8_{2,7}-7_{2,6}$	356.9147	−3.73	113
	$8_{4,4/5}-7_{4,3/4}$	356.9324*	−3.85	149
CH_3OCH_3	$8_{4,5}-7_{3,4}$ (AE/EE)	356.5753	−3.68	55
	$8_{4,5}-7_{3,4}$ (AA)	356.5829	−3.68	55
	$8_{4,4}-7_{3,4}$ (EE/EA)	356.5868	−4.20	55
	$8_{4,5}-7_{3,5}$ (EE)	356.7130	−4.20	55
	$8_{4,4}-7_{3,5}$ (EE)	356.7237	−3.83	55
	$8_{4,4}-7_{3,5}$ (AA)	356.7245	−3.68	55
CH_3OCHO	$28_{6,23}-27_{6,22}$ (A)	345.1480*	−2.31	452
	$28_{10,19}-27_{10,18}$ (E)	345.2482	−2.35	493
	$28_{13,15}-27_{13,14}$ (E)	345.4610	−2.40	352
	$28_{13,15}-27_{13,14}$ (A)	345.4670*	−3.31	352
	$28_{9,19}-27_{9,18}$ (E)	345.4732	−2.34	481
	$28_{13,16}-27_{13,15}$ (E)	345.4866*	−2.40	352
	$28_{9,20}-27_{9,19}$ (A)	345.5100	−2.34	481
	$29_{13,16}-28_{13,15}$ (E)	354.3487	−2.45	556
	$33_{0/1,33}-32_{0/1,32}$ (E/A)	354.6078*	−2.55	293
	$28_{7,21}-27_{7,20}$ (E)	354.6287	−2.29	461
	$29_{18,12}-28_{18,11}$ (A)	356.5398	−2.55	471
	$29_{18,11}-28_{18,10}$ (E)	356.5559	−2.55	471
	$29_{18,12}-28_{18,11}$ (E)	356.5663	−2.55	471
	$29_{6,24}-28_{6,23}$ (A)	356.6869	−2.36	469
	$29_{17,13/12}-28_{17,12/11}$ (A)	356.7118	−3.34	448
	$29_{17,12}-28_{17,11}$ (E)	356.7239	−2.52	448
	$29_{17,13}-28_{17,12}$ (E)	356.7384	−2.52	448
	$29_{10,19}-28_{10,18}$ (E)	356.7770	−2.41	510
	$29_{11,19}-28_{11,18}$ (E)	356.8582	−2.41	524
	$29_{16,14/13}-28_{16,13/12}$ (A)	356.9287	−3.32	426
	$29_{16,13}-28_{16,12}$ (E)	356.9363	−2.50	426
	$29_{16,14}-28_{16,13}$ (E)	356.9545	−2.50	426
C_2H_5OH	$7_{7,0/1}-6_{6,0/1}, vt=0-1$	345.1739	−3.60	140
	$21_{1,21}-20_{1,20}, vt=0-0$	345.2293	−3.43	242
	$21_{1,21}-20_{1,20}, vt=1-1$	345.2954	−3.44	246
	$21_{0,21}-20_{0,20}, vt=0-0$	345.3334	−3.43	242
	$21_{0,21}-20_{0,20}, vt=1-1$	345.4082	−3.44	246
	$20_{3,17}-19_{2,17}, vt=0-1$	354.3632	−3.31	245
CH_3CHO	$18_{2,16}-17_{2,15}$	354.4577*	−2.80	375
	$19_{0,19}-18_{0,18}$	354.5254	−2.80	377
NH_2CHO	$17_{0,17}-16_{0,16}$	345.1813*	−2.52	152
	$16_{1,15}-15_{1,14}$	345.3254	−2.52	145
	$17_{2,16}-16_{2,15}$	356.7138*	−2.48	167
H_2CS	$10_{0,10}-9_{0,9}$	342.9464	−3.22	91
HC_3N	$39-38$	354.6975*	−2.45	341
SO_2	$13_{2,12}-12_{1,11}$	345.3385	−3.62	93
	$26_{9,17}-27_{8,20}$	345.4490	−4.12	521
	$10_{4,6}-10_{3,7}$	356.7552	−3.48	90
C_2H_5CN	$40_{3,38}-39_{3,37}$	354.4767	−2.42	361
	$40_{2,38}-39_{2,37}$	356.5461*	−2.42	361
	$41_{2,40}-40_{2,39}$	356.7896	−2.41	368
	$41_{1,40}-40_{1,39}$	356.9604	−2.41	368

6

PAPER III: THE ALMA-PILS SURVEY: GAS DYNAMICS IN IRAS 16293–2422 AND A CONNECTION BETWEEN ITS TWO PROTOSTARS

M. H. D. van der Wiel[1,2], S. K. Jacobsen[1], J. K. Jørgensen[1], T. L. Bourke[3], L. E. Kristensen[1], P. Bjerkeli[4,1], N. M. Murillo[5], H. Calcutt[1], H. S. P. Müller[7], M. N. Drozdovskaya[8], and the PILS team

[1] Centre for Star and Planet Formation, Niels Bohr Institute and Natural History Museum of Denmark, University of Copenhagen, Øster Voldgade 5–7, DK-1350 Copenhagen K, Denmark
[2] ASTRON, the Netherlands Institute for Radio Astronomy, Postbus 2, 7990 AA Dwingeloo, The Netherlands
[3] SKA Organization, Jodrell Bank Observatory, Lower Withington, Macclesfield, Cheshire SK11 9DL, UK
[4] Department of Space, Earth and Environment, Chalmers University of Technology, Onsala Space Observatory, 43992 Onsala, Sweden
[5]Leiden Observatory, Leiden University, P.O. Box 9513, 2300 RA, Leiden, The Netherlands
[7]I. Physikalisches Institut, Universität zu Köln, Zülpicher Str. 77, 50937 Köln, Germany
[8]Center for Space and Habitability (CSH), Universität Bern, Sidlerstrasse 5, CH-3012 Bern, Switzerland

In preparation for submission to *Astronomy & Astrophysics*.

Context: The majority of stars form in binary or higher order systems. The Class 0 protostellar system IRAS 16293-2422 contains two emission sources, 'A' and 'B', separated by ~600 au and embedded in a single, 10^4 au scale envelope. It is unknown whether the two components formed simultaneously.

Aims: We aim to study the relation and interplay between the two protostars A and B at spatial scales of 60 au.

Methods: We select several molecular gas line transitions of CO, H_2CO, HCN, CS, SiO, and C_2H from the ALMA-PILS spectral imaging survey (329–363 GHz) and use them as tracers of kinematics, density, and temperature in the IRAS 16293-2422 system. The angular resolution of the PILS data set allows us to study these quantities at a resolution of 0.5″ (60 au).

Results: Line-of-sight velocity maps of both optically thick and optically thin molecular lines reveal (1) new manifestations of previously known outflows emanating from core A, (2) a kinematically quiescent bridge of dust and gas spanning between the two protostars, with a density between ~10^5 and ~10^7 cm^{-3}. Signs of various outflows, all emanating from core A, are evidence of high-density and

warmer gas; none of them coincide spatially and kinematically with the bridge.

Conclusions: We hypothesize that the bridge arc is a remnant of filamentary substructure in the protostellar envelope material from which protostellar sources A and B have formed. One particular morphological structure appears to be due to outflowing particles impacting the quiescent bridge material. The continuing lack of clear outflow signatures unambiguously associated to core B and the vertically thick structure derived for its pseudo-disk lead us to conclude that core B may be in an earlier evolutionary stage than core A.

6.1 INTRODUCTION

The majority of stars currently forming are part of multiple systems (Tobin et al., 2016b). Stellar systems of binary and higher order are formed according to two scenarios: through disk fragmentation (Adams et al., 1989; Bonnell & Bate, 1994), leading to close binaries (up to a few hundred au separation), and through turbulent fragmentation of a natal protostellar envelope (Offner et al., 2010), leading to wide separation binaries ($\gtrsim$1000 au). The difference in initial separation is often obfuscated at later stages by the effects of tidal interactions after the initial formation of protostars. There is another observable difference that can help to distinguish between formation scenarios: binaries formed through disk instability may be more prone to exhibit aligned rotation axes, whereas rotation axes of those formed from turbulent fragmentation should be randomly distributed. The rotation axis of a protostar can be inferred through studying the morphology and kinematics of its disk-outflow system (e.g., K. I. Lee et al. 2016). High angular resolution observations of embedded protostellar systems have now convincingly shown that both mechanisms of multiple star formation occur in nature (e.g., Tobin et al. 2016a; Brinch et al. 2016; J.-E. Lee et al. 2017).

IRAS 16293-2422 (hereafter IRAS 16293) is a nearby, young, Class 0 protostellar system in the Ophiuchus cloud complex (see Sect. 2 of Jørgensen et al. (2016) for a review of the source). The distance to three other young stellar objects in the same cloud complex has recently been determined at 147±3 pc (Ortiz-León et al., 2017), and trigonometric parallax measurements of water maser spots in IRAS 16293 itself put it at a distance of 141^{+30}_{-21} pc (Dzib et al., 2018). However, to be consistent with earlier work and with detailed numerical modeling of the IRAS 16293 system conducted by our team, we adopt a distance estimation of 120 pc based on extinction measurements and VLBI parallax measurements of two stars in the core of the complex (Loinard et al., 2008). This value is within the 1σ uncertainty margin of Dzib et al. (2018). In general, the ~18% uncertainty in the distance estimate translates into differences in projected linear scales of a factor 1.18, while quantities such as volume, mass, and luminosity would scale by a factor 1.6. With d=120 pc, the angular distance of 5.3″ between the two submillimeter sources A and B corresponds to a projected distance of 636 au. The exact three-dimensional geometry of the two sources, their potential disks and the filament structure is unknown. Based on a total of 515 spectral lines from 54 molecular species detected in a Submillimeter Array (SMA) spectral survey, Jørgensen et al. (2011) derived LSR velocities of cores A and B of +3.2 and +2.7 km s^{-1}, respectively (throughout this work, IRAS 16293A will be abbreviated as 'core A' and IRAS 16293B as 'core B'). Different centroid velocities have been reported based on individual molecular lines: for core A, +3.8 km s^{-1} from $C^{17}O$, $C^{34}S$ (Favre et al., 2014), +3.6 km s^{-1} from HCN (Takakuwa et al., 2007); for core B, +3.4 km s^{-1} (Pineda et al., 2012). All of these published centroid velocities fall well within the ~ 3–4 km s^{-1} wide distributions of V_{lsr} values fitted by Jørgensen et al. (2011). In this work, we adopt the statistically averaged systemic velocities for each of the two cores based on the multi-line analysis by Jørgensen et al. (2011).

Caux et al. (2011) used single-dish observations to estimate the masses of the two protostellar cores. Assuming that the line broadening of the profiles is due to infalling motions, these authors arrive at ~ 0.8 $M_\odot$ for core A and 0.1 $M_\odot$ for core B. The same mass of core A was found by Bottinelli et al. (2004b), also assuming infalling motion to explain the observed line broadening, but using interferometric observations in which core A is spatially separated from core B. Alternatively, the line broadening could be caused by rotating motion instead of infall, as assumed for core A by Pineda et al. (2012), who used observations of methyl formate (CH_3OCHO) and ketene (H_2CCO) with a 2.2″ ×1.0″ beam to derive Keplerian rotation around a central object of 0.53 $M_\odot$. Oya et al. (2016) found a mass varying between 0.5 and 1.0 $M_\odot$, depending on the assumed inclination and centrifugal barrier radius. These studies show that the core masses are in the regime of low-mass protostars, but the various methods yield masses differing by up to a factor of two.

The binary protostellar system IRAS 16293 is embedded in an envelope with a radius of 6–8 10^3 au (e.g., Schöier et al., 2002; Crimier et al., 2010b). Rotating, infalling motions of this envelope have been inferred from spectral line profiles (e.g., Menten et al., 1987; Zhou, 1995; Schöier et al., 2002; Takakuwa et al., 2007; Ceccarelli et al., 2000). In a detailed velocity model posited by Oya et al. (2016), the large-scale envelope could transition into a Keplerian disk within the centrifugal barrier around core A, as indicated by observations presented in Favre et al. (2014). The latter study found rotation on 50–400 au scales, which could not be explained by simple Keplerian rotation around a point-mass, but needed to take into account the extra material of the enclosed mass at these scales.

At least two major outflows have been observed from core A: an east-west bipolar outflow (Yeh et al., 2008) and a northwest outflow (Kristensen et al., 2013; Girart et al., 2014). On larger scales of > 5000 au, a northeast outflow has also been observed (Mizuno et al., 1990; Stark et al., 2004), the origin of which is speculated to be core A, based on high-resolution CO images revealing a collimated structure near core A (see Fig. 6.1). In contrast, any signs of outflows associated with IRAS–16293B have long escaped detection. Loinard et al. (2013) argued that the blueshifted emission found southeast of source B is from a young monopolar outflow from source B, but Kristensen et al. (2013) demonstrated with the same data that it could be a bow-shock from the northwest-southeast outflow from IRAS 16293A. Oya et al. (2018) presented SiO velocity maps indicative of a pole-on pair of outflows from core B, but these authors also recognize that interaction with the outflow from core A is not ruled out as a possible scenario.

The quadruple outflow structure from core A has led to speculations that core A itself is a multiple system. Indeed, continuum observations at centimeter waves resolved IRAS 16293A into two (Wootten, 1989; Chandler et al., 2005) or even three components (Loinard et al., 2007; Pech et al., 2010), with a separation of up to ~0.5″ . The 0.5″ resolution maps from the ALMA PILS program appear to indicate a singularly peaked source at the position of core A, both in continuum (Jørgensen et al., 2016) and in optically thin $C^{17}O$ (Jacobsen et al., 2018). However, the integrated $C^{17}O$ 3–2 intensity is affected by contamination from more complex molecules in the dense, warm regions close to the two cores, which modifies the apparent morphology of emission integrated over channels bracketing the $C^{17}O$ line frequency. Moreover, the 868 μm dust continuum is optically thick in the disk domains, which could hide any intrinsically multi-peaked structure (Calcutt et al., submitted). The PILS maps of various isotopologues of methyl cyanide in Calcutt et al. (submitted), for example, for which the emission is integrated over a moving velocity interval to avoid incorporating contributions from other species, do show two clearly separated emission peaks.

Material spanning the interbinary region between IRAS 16293A and B was first identified in millimeter observations from the BIMA array[1] by Looney et al. (2000), who interpreted it as a circumbinary envelope. The same bridge material is also clearly detected in sensitive Atacama Large Millimeter/Submillimeter Array (ALMA) observations (Pineda et al., 2012; Jørgensen et al., 2016). Jacobsen et al. (2018) (hereafter J2018) show that a dust filament model can match the observed spatial emission from high-resolution submillimeter continuum emission and $C^{17}O$ 3–2 gas line emission. Similar structures

1 BIMA stands for Berkeley-Illinois-Maryland Association, which operated and funded the nine-telescope array at Hat Creek in California until 2004, when its hardware was relocated and merged into the Combined Array for Research in Millimeter-wave Astronomy (CARMA).

observed in other multiple protostellar systems are interpreted as fragmentation of large-scale circum-multiple envelopes (J.-E. Lee et al. 2017) or (Keplerian) rotating disks that have become locally gravitationally unstable (Tobin et al., 2016a; Fernández-López et al., 2017; Dutrey et al., 2014, 2016).

The exact evolutionary stage of the two protostars is unknown, partly due to age determination being hampered by the different inclination angles of cores A (edge on; Pineda et al. 2012; Oya et al. 2016) and B (face on; Oya et al. 2018). Given the outflow and infall signatures near core A, its status as a protostar is firmly established. In contrast, the apparent quiescence of core B has led to speculations that it is not a young protostar, but rather harbors a late-stage T Tauri disk (Stark et al., 2004). This was later called into question when spectral line signatures of infalling material were observed towards core B (Chandler et al., 2005; Pineda et al., 2012; Jørgensen et al., 2012). Since ages are not known for either core A or B, it is consequently unknown if they formed at the same time.

The outflows from core A, along with the striking arch of dust and gas connecting sources A and B, make IRAS 16293 a very complex system, where the observed gas line emission can only be explained by a combination of multiple physical components. We aim to disentangle these structures in our new observations and to map the physical origins of the observed molecular emission lines.

This paper is based on observations from the ALMA Band 7 segment of the Protostellar Interferometric Line Survey (PILS[2]) targeting IRAS 16293. The many thousands of line detections in the PILS data set facilitate the discovery of complex organic molecules (>6 atoms, including carbon; Herbst & van Dishoeck 2009) and the study of their interstellar chemistry. Relatively weak lines of complex molecules are most easily separable in spectra extracted toward spatial positions near the kinematically simple and spatially compact core B, with narrow ($\sim 1\ \mathrm{km\,s^{-1}}$), single-moded spectral line shapes. Most analysis based on the PILS data cubes has therefore been restricted to spatial positions close to the two protostars (Jørgensen et al., 2016; Coutens et al., 2016; Lykke et al., 2017; Ligterink et al., 2017; Fayolle et al., 2017). In contrast, in this work, we fully exploit the spatial dimensions of the PILS data set, but focus on a few restricted frequency ranges containing lines of well-known, simple molecular species. The aim is to study the kinematic structure of the binary system and the intervening and surrounding gaseous material.

We summarize the characteristics of the observational data in Sect. 6.2, and describe the selection of molecular tracers and the morphology and dynamics observed in each of them in Sect. 6.3. Section 6.4 presents analysis of the physical characteristics of the bridge filament between the two protostars and the kinematics of outflow motions.

2 http://youngstars.nbi.dk/PILS

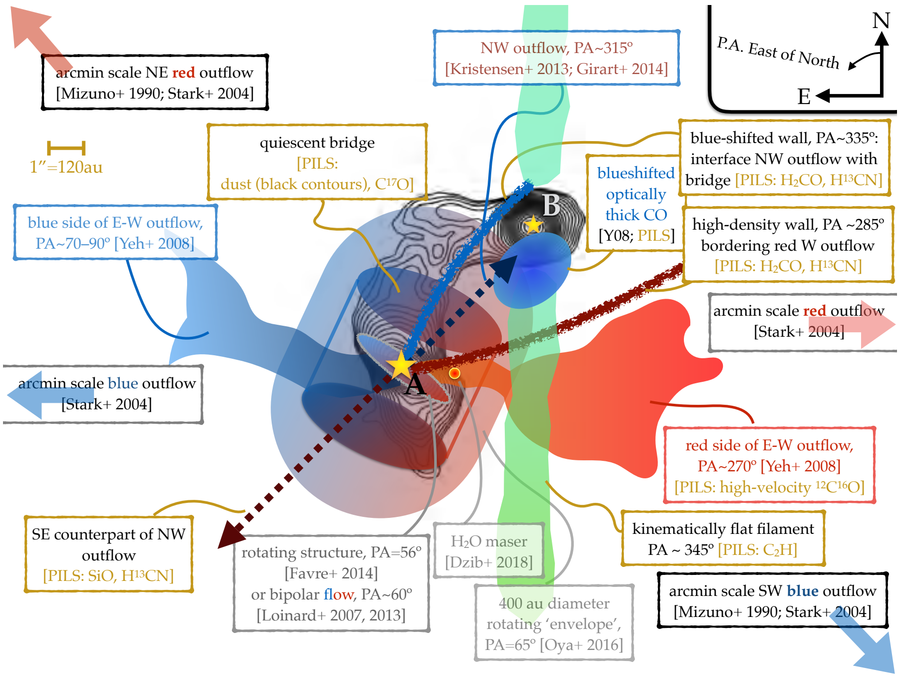

Figure 6.1: Illustration of physical components surrounding and bridging protostars A and B in the IRAS 16293 system, and outflows emanating from IRAS 16293A. Thick, solid arrows at the edges of the panel point to scales beyond the ~ 20″ depicted in this illustration. Position angle (P.A.) is defined from north to east, as indicated in the top right. Each component is labeled by a rectangular box, with literature sources listed in square brackets or 'PILS' for a reference to this work. In all references given in square brackets in the illustration, 'et al.' is abbreviated as '+': Dzib et al. (2018), Girart et al. (2014), Kristensen et al. (2013), Loinard et al. (2007, 2013), Mizuno et al. (1990), Oya et al. (2016), Stark et al. (2004), Yeh et al. (2008) [further abbreviated as 'Y08' where needed]; 'PILS' refers to structures observed in ALMA PILS observations (Jørgensen et al. 2016, J2018, and this work).

Discussion of the results is given in Sect. 6.5, and Sect. 6.6 summarizes the main conclusions.

6.2 OBSERVATIONS

The PILS program was conducted with ALMA between June 2014 and May 2015, using both the main array of 12-m dishes and the shorter baselines available in the array of 7-m dishes in the Atacama Compact Array (ACA). Its end product comprises a three-dimensional data set covering the uninterrupted spectral range 329–363 GHz (all in ALMA Band 7) in spectral channels of 0.244 MHz in width, and a sky area of ~ 15″ in diameter sampling the two binary components of IRAS 16293 and their surroundings with a synthesized beam FWHM of 0.5″ . While the main array provides the unprecedented sensitivity,

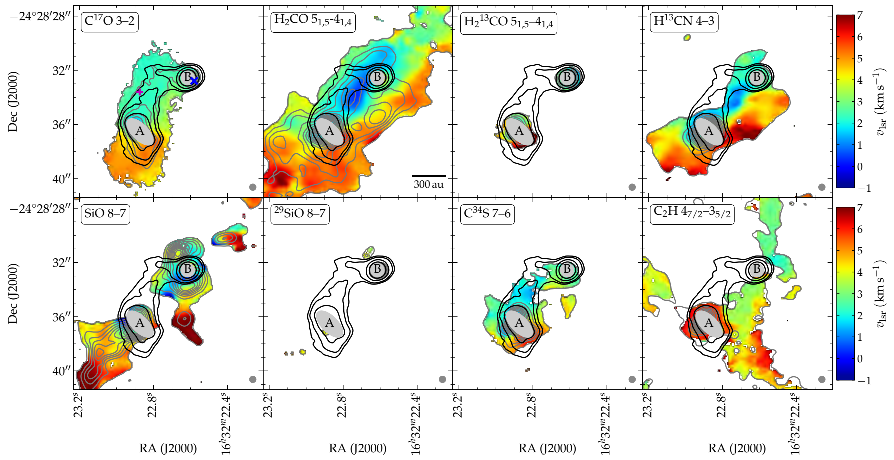

Figure 6.2: Velocity maps of molecular species listed in Table 6.2 (except $^{12}C^{16}O$, see Fig. 6.4). Black contours represent 868 μm dust continuum at levels of 30, 45, 100, 250 mJy beam^{-1}. Gray contours for integrated spectral line intensity start at 0.35 Jy beam^{-1} km s^{-1}, and velocity values are only shown where the integrated intensity is above this threshold. The threshold for C_2H is 0.07 Jy beam^{-1} km s^{-1}, to reflect its narrower integration range ([−1, +7] instead of [−4,+11] km s^{-1}); it is 0.20 Jy beam^{-1} km s^{-1} for ^{29}SiO. Higher level integrated line intensity contours (also in gray) cover 14 linear steps up to the maximum intensity in each map (in units of Jy beam^{-1} km s^{-1}): 5.62 for $C^{17}O$, 21.67 for H_2CO, 8.10 for $H_2{}^{13}CO$, 32.55 for $H^{13}CN$, 13.23 for SiO, 2.91 for ^{29}SiO, 6.54 for $C^{34}S$, and 6.02 for C_2H. Velocities between +7 and +11 km s^{-1} are represented by the darkest red color, and velocities between −4 and −1 km s^{-1} by the darkest blue color. The circular synthesized beam of 0.5″ in FWHM is indicated in the bottom right of all panels, except the H_2CO panel, which features a scale bar representative of 300 au at the source distance of 120 pc. The blue '×' sign in the top left panel marks the position 0.5″ southwest of the continuum peak of core B, often used to extract signals of complex organic molecules (e.g., Coutens et al., 2016; Lykke et al., 2017; Ligterink et al., 2017). The magenta '+' sign marks the position at which the representative bridge filament spectral profiles are extracted (see Appendix 6.9).

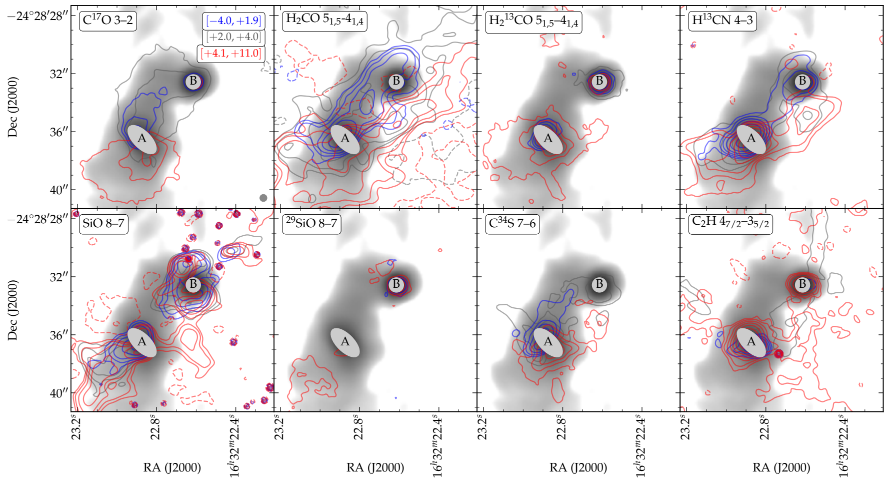

Figure 6.3: Integrated velocity ranges (blue, gray, and red contours) for each molecular line tracer. Contour levels start from 0.2 Jy beam^{-1} km s^{-1}, except for H_2CO (0.4 Jy beam^{-1} km s^{-1}), $H_2{}^{13}CO$ (0.1 Jy beam^{-1} km s^{-1}), ^{29}SiO and C_2H (both 0.07 Jy beam^{-1} km s^{-1}), and increase by a factor of two to the next level. Equivalent negative contours are plotted in dashed style. The 868 μm continuum emission is shown in grayscale, stretching from 0.002 to 2.0 Jy beam^{-1}.

which is roughly uniform at ~ 8 mJy beam^{-1} channel^{-1} across the full spectral range, the addition of ACA baselines ensures that large scale emission up to ~ 13″ is recovered. We refer to Jørgensen et al. (2016) for additional details of observing conditions, data characteristics, and the data processing strategy.

6.3 RESULTS: OBSERVED DYNAMICS AND MORPHOLOGY

The morphology of the dust continuum emission in IRAS 16293 as observed with ALMA at 0.5″ resolution at 868 μm (Jørgensen et al. 2016; J2018) can be broken up into three distinct components: a nearly circular structure that hints at a face-on disk surrounding core B; an elliptically shaped structure related to the inclined disk-like structure around core A; and a ridge of material stretching from B to A and even beyond, to the southeast of A. The centroid coordinates of the continuum peaks of components A and B, measured using two-dimensional Gaussian fits on the PILS 826–912 μm continuum image, are listed in Table 6.1. These positions of the 868 μm continuum measured from our PILS data products are consistent with the 1.15–1.30 mm continuum peak locations reported by Oya et al. (2018) to within 0.05″, i.e., one tenth of the synthesized beam size of either observation.

We select spectral signatures of $C^{17}O$, $H^{13}CN$, H_2CO, $H_2{}^{13}CO$, $C^{34}S$, SiO, ^{29}SiO, and C_2H. The motivation for selecting these tracer

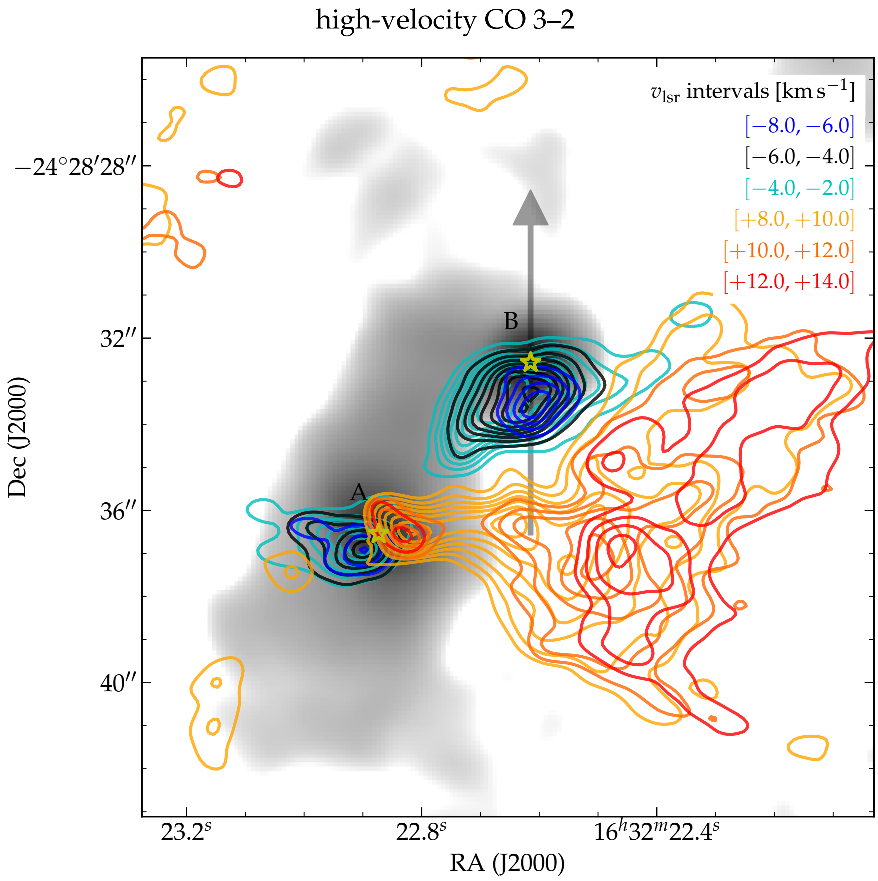

Figure 6.4: Map of six different velocity bins of the main CO isotopologue, highlighting high-velocity gas at > 5 km s^{-1} from the systemic velocity ($V_{lsr}\approx+3$ km s^{-1}) of the protostars: absolute velocity difference [5,7] km s^{-1} in cyan and orange contours, [7,9] km s^{-1} in black and darker orange, [9,11] km s^{-1} in blue and red. The lowest contour level and step to the next contour is 1.0 Jy beam^{-1} km s^{-1}. The 868 μm dust continuum is shown in grayscale. The arrow indicates the slice for the position-velocity diagram shown in Fig. 6.6.

Table 6.1: Coordinates of submillimeter continuum peaks in IRAS 16293-2422.

Component	Right Ascension (J2000)	Declination (J2000)
core A	16^{h}32^{m}22^s.873	−24°28′36″.54
core B	16^{h}32^{m}22^s.6147	−24°28′32″.566

Notes. The uncertainties on fitted positions are 0.03″ for both coordinates of component A, and 0.005″ for component B.

Table 6.2: Selected line transitions.

Molecule	Transition	Rest frequency[a] (GHz)	E_{up}/k (K)	n_{crit}[b] (cm^{-3})	Traced component[e]
Dust	(continuum)	868 μm	-	-	Quiescent bridge between A and B.
$C^{17}O$	$J = 3–2$	337.061	32.5	4.1×10^4	Quiescent bridge between A and B.
$^{12}C^{16}O$ [c]	$J = 3–2$	345.796	33.2	4.1×10^4	Redshifted, outflow cone accelerating westward from A; onset of eastern counterpart of westward outflow; blueshifted knot south of B.
$H^{13}CN$	$J = 4–3$	345.33977	41.4	1.2×10^8	Redshifted northern wall of PA 270° outflow; Redshifted outflow southeast (PA 135°) from A.
o-H_2CO	$J_{K_a,K_c} = 5_{1,5} - 4_{1,4}$	351.76864	62.5	7.5×10^7	Redshifted northern wall of PA 270° outflow; Blueshifted interface wall with bridge. Redshifted outflow southeast (PA 135°) from A.
o-$H_2{}^{13}CO$	$J_{K_a,K_c} = 5_{1,5} - 4_{1,4}$	343.32571	61.3	"	Redshifted northern wall of PA 270° outflow;
$C^{34}S$	$J = 7–6$	337.39646	50.2	1.5×10^8	Blueshifted gas in same direction as 'axis' of bridge.
SiO	$J = 8–7$	347.33058	75.0	6.1×10^7	Axes of of redshifted (PA 135°) and blueshifted (315°) blue outflows from A; Mixed-velocity pockets north and south of B;
^{29}SiO	$J = 8–7$	342.98084	74.1	5.9×10^7	Redshifted outflow southeast (PA 135°) from A. Mixed-velocity pockets north and south of B;
C_2H	$N_J = 4_{7/2} - 3_{5/2}$	349.39997[d]	41.9	1.4×10^7	Quiescent, narrow filament across B.

Notes. [a] Rest frequencies taken from the Cologne Database for Molecular Spectroscopy, CDMS (Müller et al., 2005; Endres et al., 2016). Original sources of spectroscopic data: $C^{17}O$, Klapper et al. (2003); CO, Winnewisser et al. (1997); $H^{13}CN$, Cazzoli & Puzzarini (2005); H_2CO and $H_2{}^{13}CO$, Cornet & Winnewisser (1980); $C^{34}S$ Gottlieb et al. (2003); SiO and ^{29}SiO, Müller et al. (2013); C_2H, Padovani et al. (2009).
[b] Critical density is calculated as the ratio of the Einstein A coefficient and the collision rate at a temperature of 100 K, which are accessed through the LAMDA database (Schöier et al., 2005b), with the following original sources: CO (adopting o-H_2 as dominant collision partner), Yang et al. (2010); $H^{13}CN$, Dumouchel et al. (2010) for main isotopologue; H_2CO and adopting identical rates for $H_2{}^{13}CO$, Wiesenfeld & Faure (2013); $C^{34}S$ adopting rates for the main isotopologue $C^{32}S$, Lique et al. (2006); SiO and adopting identical rates for ^{29}SiO, Dayou & Balança (2006); C_2H, Spielfiedel et al. (2012).
[c] For $^{12}C^{16}O$, we study morphological features using only velocity channels at $| V_{lsr} - v_{systemic} | > 5$ km s^{-1}, as shown in Fig. 6.4.
[d] The rest frequency for C_2H $4_{7/2} - 3_{5/2}$ is the average of the tabulated rest frequencies for the individual hyperfine components, F=4–3 at 349.39928 GHz and F=3–2 at 349.40067 GHz. [e] Core A and core B are abbreviated as 'A' and 'B'; 'PA' denotes position angle east of north, following Fig. 6.1.

transitions is that their emission is spatially extended across the inter- and circumbinary region, the molecules are chemically simple, and represent a range of densities, temperatures (see E_{up} and n_{crit} in Table 6.2) and physical processes such as grain sputtering. Although we recognize the additional value of studying other tracer molecules also covered in the 329–363 GHz PILS data, the selection in this paper is deliberately restricted to its current scope. The rest frequencies for the relevant transitions of these species are listed in Table 6.2. Velocity channel maps of each of these species are shown in Figs. 6.15–6.22, with a velocity range in V_{lsr} between 0.0 and +6.5 km s^{-1}, bracketing the systemic velocities of +3.2 and +2.7 km s^{-1} for sources A and B in the IRAS16293 binary (Jørgensen et al., 2011). As our aim is to study material nearby, but not in the dense protostellar cores, two masks are placed on the disks of each source in all maps presented in this work. This procedure ensures that high-intensity, partially (self)-absorbed spectral line signals do not skew the intensity scaling on the integrated intensity maps and the calculation of the weighted velocity (moment 1) maps. Contamination of the selected molecular line transitions by nearby transition of other species are discussed in detail in Appendix 6.9.

We construct velocity maps of the selected species by considering only channels with V_{lsr} in the range [−4,+11] km s^{-1} (except for C_2H, where we choose [−1,+7] km s^{-1} to limit contamination by other species), and calculating a intensity-weighted mean velocity for each pixel, excluding all flux density values below 40 mJy beam^{-1}. As seen in Fig. 6.2, the $C^{17}O$ gas has an intensity-weighted mean velocity restricted to ± 1 km s^{-1} of the systemic velocity in the bridge region between core A and B. The bridge is therefore kinematically quiescent. The spatial distribution of $C^{17}O$ coincides with the dust bridge traced by submillimeter continuum, while none of the other (higher density) tracers in this study have intensity peaks that are cospatial with the bridge, at 0.5″ resolution (60 au in projection). A tentatively axisymmetric structure is seen in the channel maps of H_2CO and $H^{13}CN$ (Figs. 6.2, 6.17, 6.16): two arcs emanating from core A, one on the NE side at velocities between +2 and +3.5 km s^{-1}, and its counterpart on the SW side at velocities between +4 and +5.5 km s^{-1} (e.g., Fig. 6.16). These arcs bracket the axis defined by the NW outflow as seen in CO 6–5 by Kristensen et al. (2013), and are kinematically symmetric around V_{lsr} = +3 km s^{-1}. Examining the other molecular tracers considered in this work: this velocity gradient (roughly perpendicular to the bridge) is also seen in $H^{13}CN$, but the structure appears spatially more compact; there may be evidence of it in $C^{34}S$; but it is absent in $C^{17}O$, SiO, and C_2H (Fig. 6.2, Fig. 6.3). We therefore conclude that the striking symmetry observed in H_2CO is not the result of a bulk rotation of the gas about the axis of the bridge or the axis of the northwest outflow from core A.

While none of the tracer molecules listed above have signals bright enough to study faint line wings at velocity offsets more than 4 km s^{-1}, the main isotopologue of CO provides sufficiently bright signal to probe higher line-of-sight velocities. In fact, in Fig. 6.4 we use only high-velocity (>5 km s^{-1}) channels of CO 3–2 emission, thereby avoiding complications in interpreting extremely optically thick emission at lower velocities. The western lobe of the east-west outflow pair is prominently visible in CO 3–2 in a cone-shaped distribution, with a much smaller region of blueshifted counterpart appearing on the eastern side of core A. At somewhat coarser angular resolution (1.5″ beam, using the SMA), Yeh et al. (2008) have previously studied the east-west outflow from core A in CO 2–1 and 3–2. Compared with their work, our 0.5″ resolution map in CO 3–2 reveals a more cone-like shape of the westward, redshifted outflow lobe, and there is an apparent acceleration taking place with increased distance from core A. There is also bright CO 3–2 emission with an emission peak 1″ south of core B, with velocities ranging up to 10 km s^{-1} blueshifted with respect to core B. Its location is consistent with the position 'b2' described in Yeh et al. (2008). In our map (Fig. 6.4), this blueshifted knot is clearly morphologically connected to core B.

We observe that the SiO velocity map in Fig. 6.2 traces both sides of the NW-SE outflow pair extending up to ~ 8″ from core A, blueshifted on the northwest side and redshifted on the southeast side. The lower optical depth line of ^{29}SiO only shows emission on the redshifted side southeast of core A. In contrast, a redshifted southeast outflow appears absent in the high-temperature tracer CO 6–5 (Kristensen et al., 2013), but it was previously seen in colder gas (CO 2–1; Girart et al. 2014). Likewise, the PILS CO 3–2 data (Fig. 6.4) do show redshifted emission about 6″ southeast of core A, and it is very prominent in the SiO velocity map (Fig. 6.2) at $V_{lsr} \geqslant +5$ km s^{-1}, as well as in H_2CO and $H^{13}CN$. In addition, a significantly redshifted patch of emission is observed in SiO about 3.″5 due west of A (and 4″ south of B).

Finally, a filamentary structure connected to core B with a position angle of ~ 170° is visible in C_2H, but not in any other tracer. Its velocity structure is flat, restricted to V_{lsr} values between +2 and +4 km s^{-1} (see Sect. 6.4.3 for further discussion). The redshifted (>+5 km s^{-1}) emission in the velocity map of C_2H (Fig. 6.2) is due to a bright CH_3CN transition at 349.393 GHz. In positions near core A, the CH_3CN line also contaminates channels closer to the systemic velocity of C_2H (see Appendix 6.9). In other positions in the map with integrated intensity of C_2H above 0.07 Jy beam^{-1} km s^{-1}, the spectral profile shows a characteristic double peak spaced by 1.4 MHz and with roughly equal intensities of both peaks (cf. Fig. 6.14).

The interpretation of the observed morphology and velocity structure is addressed in Sect. 6.4.3 and Sect. 6.5.

6.4 ANALYSIS

6.4.1 *Radiative transfer modeling of the interbinary bridge*

The bridge between protostars A and B, as traced by the submillimeter dust continuum and cold $C^{17}O$ gas (Sect. 6.3), is kinematically quiescent (Sect. 6.3) and its central velocity at V_{lsr}=+3 km s^{-1} is consistent with the velocities of the individual protostars (+2.7 and +3.1 km s^{-1}). It is therefore unlikely to be associated with any of the outflows, and it is treated as a separate entity in this work. Besides $C^{17}O$, none of the other selected molecules match, simultaneously, the morphology of the dust bridge filament and the narrow line-of-sight velocity distribution of $C^{17}O$.

In principle, an assessment of density and temperature conditions throughout the inter- and circumbinary region of IRAS 16293 could be set up using spectral line intensity ratios of various molecules and transitions highlighted in this work (see Table 6.2). However, given the multitude of partially resolved dynamical components, it is not at all certain that line intensities measured toward a particular position emanate in the same gas for one transition of a species and another transition of another species. We therefore refrain from embarking on such an analysis.

To study the quiescent interbinary bridge, we use a curved cylinder filament model, spanning 636 au between and enveloping the two sources in an arc-like structure. This is the same filament model used in J2018, who show that, when using source luminosities of 18 $L_\odot$ and 3 $L_\odot$ for core A and B, respectively, the model yields a qualitative match with the morphology and peak emission levels seen in the 868 μm dust continuum emission and $C^{18}O/C^{17}O$ gas line emission. The fiducial model adopted in this paper is equivalent to 'Rotating Toroid model 1' in J2018. The temperature structure of each cell in the model is derived self-consistently, based on the adopted luminosities of both sources A and B (Fig. F.4 of J2018).

The line radiative transfer code `LIME` (Brinch & Hogerheijde, 2010) is used to obtain synthetic line emission cubes of the H_2CO $5_{1,5}$–$4_{1,4}$ and $H^{13}CN$ 4–3 gas line emission. We use an abundance jump model to emulate freeze-out onto the dust grains. When the dust temperature is below the sublimation temperature, the gas phase abundance is decreased by a depletion factor. See Table 6.3 for more information on the individual molecules. The number density of H_2 is above 10^8 cm^{-3} in the modeled bridge filament, sufficiently high to validate the occurrence of depletion of gas-phase particles onto dust grain surfaces. Since we are investigating the appropriateness of a static filament structure to the observation of the quiescent bridge only, we keep the velocity structure of the model static, with only random velocity dispersions included, such as from turbulence. We fix the velocity

Table 6.3: LIME model parameters.

Molecule	X/H_2 range	T_{subl} [a] [K]	Depletion factor	b [b] [$km\,s^{-1}$]
$C^{17}O$	5.58×10^{-8}	30	100	1
o-H_2CO	$[1 \times 10^{-8}, 3 \times 10^{-6}]$	50	100	1
$H^{13}CN$	$[2 \times 10^{-12}, 2 \times 10^{-10}]$	100	100	1

Notes. All parameters for $C^{17}O$ are identical to those in J2018 (see their Table 3). [(a)] Ice mantle sublimation temperature for HCN follows those of other CN-bearing species (e.g. Noble et al., 2013). That of H_2CO follows Aikawa et al. (1997), Ceccarelli et al. (2001) and Rodgers & Charnley (2003). [(b)] Doppler parameter as defined in LIME, i.e., the 1/e halfwidth of a thermally broadened line.

dispersion parameter in LIME to 1 $km\,s^{-1}$. The only free parameter is the molecular abundance. Twenty different abundance values are run for each molecule in the range given in Table 6.3. After LIME produces a synthetic line emission cube, it is convolved with a $0.5'' \times 0.5''$ beam in the image analysis software package MIRIAD. We refer to J2018 for further details of the model definition and the radiative transfer approach.

In Fig. 6.5, integrated intensity maps of the radiative transfer calculations described above are juxtaposed with their observed counterparts. The latter are produced by integrating over the narrow velocity range V_{lsr}=[+2.0,+4.0] $km\,s^{-1}$ (i.e., all channels with contours in black in Figs. 6.15–6.17 in the Appendix), with the aim of filtering out dynamically active gas associated to the various outflow components which are not included in the density distribution of the model (J2018). As already concluded by J2018, the model in $C^{17}O$ provides a qualitative match to the morphology of the bridge connecting the two protostars, although the observed $C^{17}O$ filament is laterally ~ 3 times wider than the modeled arch. Absolute flux values produced by the model are a factor ~ 2 higher than observed. H_2CO is also present and detected in its $5_{1,5}$–$4_{1,4}$ transition across the bridge area outlined by the continuum contours, but its observed morphological shape is different from that of $C^{17}O$ and the continuum. The difference is partly due to the inclusion of outflow-impacted gas, despite the attempt to exclude this by using a narrow velocity integration range. The modeled H_2CO emission extends radially over many hundreds of au surrounding the binary, an effect of H_2CO molecules being present in the gas phase in the spherical envelope component of the model. The superposed density structure of the disks-bridge-envelope model is dominated by that of the spherical envelope model at such large radii of ~ 700 au (from the midpoint between A and

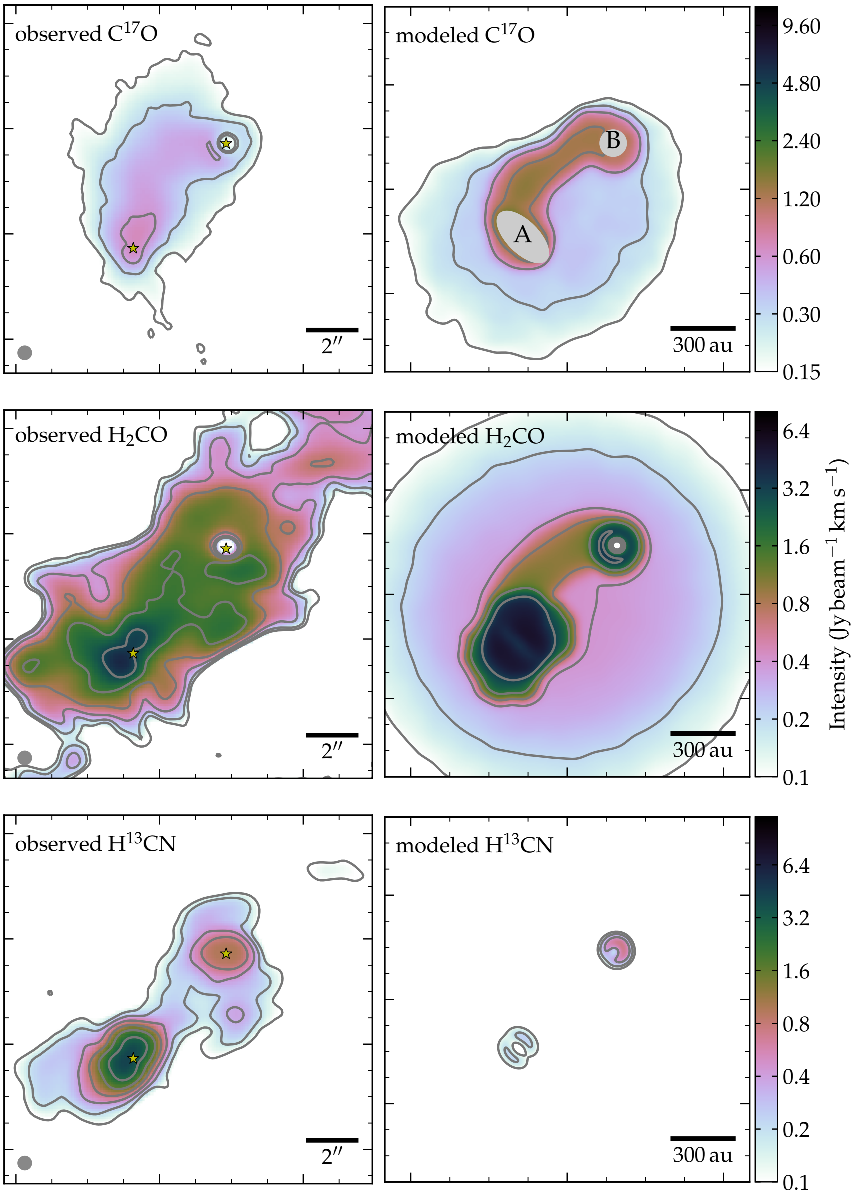

Figure 6.5: Comparison of observed (left) and modeled (right) morphology of spectral line emission from $C^{17}O$, H_2CO, and $H^{13}CN$. In the $C^{17}O$ model panel, the disk domains are masked (as in Fig. 6.2). Total intensity from the observed cubes is calculated by integrating over V_{lsr} range [+2,+4] km s^{-1}. The continuum peak locations are marked by star symbols, the ALMA interferometric beam size is indicated in the bottom left of each 'observed' panel. The modeled line intensity maps are convolved with the observational beam size, to aid direct comparison. Line intensity is represented by the color scale and gray contours (identical for observed and modeled panels: lowest level at 0.15 for $C^{17}O$, 0.10 Jy/beam km s^{-1} for H_2CO and $H^{13}CN$, and increasing by a factor 2 each level). Black contours indicate the 868 μm dust continuum.

B). Outside this radial distance of 700 au, the number density of the modeled envelope component drops below 10^7 cm^{-3} (the outermost gray, circular contour in Fig. F.4 of J2018). Along with radially decreasing temperatures, this leaves conditions insufficient to excite o-H_2CO $5_{1,5}$, with a critical density of 7.5×10^7 cm^{-3} and an upper energy level of E_{up}/k=62.5 K (Table 6.2). In addition to tracing the bridge filament, the H_2CO model map shows enhanced H_2CO emission up to $\sim 2''$ above the disk of core A (northwest and southeast of A), where the temperature is sufficiently high to sublimate H_2CO from dust grains (cf. 55 K contour in Fig. F.4 of J2018). Finally, the observed morphology of $H^{13}CN$ in the inter-binary region does not follow the shape of the bridge filament. As expected from its high critical density, the radiative transfer model does not populate the J=4 level of HCN species beyond the disk domains. The exception is a small region immediately above the disk plane, where $T_{kin} > 100$ K (again, see Fig. F.4 of J2018), where the observed enhancement in $H^{13}CN$ emission is reproduced by the model.

In conclusion, the bridge morphology is observed in dust, $C^{17}O$, and partly also in o-H_2CO, and the physical model constructed by J2018 roughly reproduces the morphology of the dust continuum and $C^{17}O$ emission. The apparent match between the observed H_2CO emission and that produced by the model (Fig. 6.5, middle panels) should not be overinterpreted. As shown in Figs. 6.2 and 6.17, the H_2CO observed in the direction of the bridge filament domain is largely at line-of-sight velocities that are offset from the quiescent $C^{17}O$ bridge filament at the systemic velocity. In fact, the lower optical depth tracer $H_2{}^{13}CO$ in the same transition (Fig. 6.18) shows no detectable emission in the bridge domain in the V_{lsr} range from +2.0 to +4.0 km s^{-1}. This means that the observed H_2CO emission is not tracing the bulk gas in the quiescent bridge filament, but rather surface layers of dynamically stirred components. In our interpretation, this indicates that the number densities in the modeled bridge component are higher than in reality. A more realistic model would not produce any H_2CO emission from the bridge component. $H^{13}CN$ 4–3 emission is not seen outside of the disk domains in the modeled map, and does not trace the bridge morphology in the observed map (Fig. 6.5, bottom panels). The explanation for the lack of H_2CO and $H^{13}CN$ emission in the bridge filament is provided by the excitation balance governed by density and temperature. Looking at the critical densities and E_{up} values in Table 6.2, the upper levels of the relevant $H^{13}CN$ and H_2CO transitions do not get populated sufficiently. The freeze-out abundance drop in the model (Table 6.3) is not the cause, which we confirm with a separate radiative transfer model run in which freeze-out is neglected completely, keeping all molecules in the gas phase. In the resulting emission maps, there is still no $H^{13}CN$ 4–3 emission outside of the disk regions. The model o-H_2CO $5_{1,5}$–

$4_{1,4}$ emission map without freeze-out does show a small intensity enhancement in part of the bridge arc region, probably reflecting its slightly lower critical density when compared with HCN 4–3.

The fiducial model (RT1 from J2018) is not necessarily the only and best fit to the data (and the only data that were taken into account were CO 3–2 isotopologues, submillimeter dust morphology, and multiwavelength SED). The number density at the axis of the modeled bridge arc is $7.5 \times 10^8\ \mathrm{cm^{-3}}$. The density structure that was adopted by J2018 was mainly driven by the wish to reproduce the dust emission morphology. However, dust emission strength depends on several factors which are all assumed to be fixed in the model setup: dust opacity, gas-to-dust ratio, and a dust temperature being coupled rigidly to that of the gas. For example, if a different grain size distribution is assumed, higher submillimeter grain opacities could arise, lowering the peak (column) density required to match the observed dust emission. Similar arguments hold for a lower gas-to-dust ratio and a higher dust temperature. A combination of these effects can easily bring the model peak number density down by a factor of 10–100 to well below the critical densities of the CS, H_2CO and HCN transitions selected in this work (Table 6.2). In this work, the observed maps of the suite of molecular tracers with different critical densities and energy levels indicate that, indeed, the real density of the bridge is likely between the critical density of CO 3–2 ($4 \times 10^4\ \mathrm{cm^{-3}}$) and those of o-$H_2CO$ $5_{1,5}$–$4_{1,4}$ and $H^{13}CN$ 4–3 ($\sim 10^8\ \mathrm{cm^{-3}}$).

Besides the low-density tracers $C^{17}O$ 3–2 and 868 µm dust, all emission observed from other molecular species in the vicinity of the bridge domain can be ascribed to dynamically active components, or their impact on more quiescent regions (see Sect. 6.4.3).

6.4.2 *Fragmentation of the bridge*

It is conceivable that both cores A and B formed from the bridge filament through gravitational instability. In this context, we follow the analytic approach by Ostriker (1964) and treat the bridge as an isothermal cylinder. In this idealized scenario (far more simplified than the self-consistently derived temperature structure modeled by J2018 and used in our Sect. 6.4.1), the thermal pressure in the cylinder keeps it from collapsing radially if the mass per unit length is below a certain threshold, depending only on kinetic temperature and the mean molecular weight (the equivalent of Jeans mass in cylindrical geometry). Using the mean molecular weight of H_2 and a temperature value of 30 K, we arrive at a stability threshold of 0.17 $M_\odot$ per 600 au (the approximate projected length of the bridge).

We compare the mass per length stability criterion derived above with an observationally derived mass of bridge material, calculated as follows. We take the average $C^{17}O$ 3–2 intensity of 600 $\mathrm{mJy\,beam^{-1}}$

(integrated over the [+2,+4] $km\,s^{-1}$ velocity range), and use RADEX (Van der Tak et al., 2007) non-LTE radiative transfer calculations to convert to a $C^{17}O$ column density. Such a calculation requires a kinetic temperature and a number density of collision partners as input. To represent a natal, isothermal, cylindrical filament, we choose a temperature between the minimum temperature of the modeled bridge arc (24 K) and the average temperature in the bridge domain (41 K) (see Sect. 6.4.1 and J2018). For number density, n_{H_2}, we adopt 10^4 cm^{-3}, which is of the same order as the critical density of $C^{17}O$, and well below those of HCN, H_2CO and CS (Table 6.2). With T_{kin}=30 K, n_{H_2}=10^4 cm^{-3}, we obtain a $C^{17}O$ column density of 6.7×10^{15} cm^{-2}, which corresponds to $N(H_2)$=1.3×10^{23} cm^{-2} (using canonical isotopic ratios[3] and CO/H_2=10^{-4}). The total mass enclosed in the 250×600 au area encompassed by the bridge 'cylinder' between sources A and B is 0.007 $M_\odot$. On the other hand, integrating the mass of all particles in the bridge component of the model described in Sect. 6.4.1 yields a total mass of 0.055 $M_\odot$. Both of these total mass values are below the stability threshold at the assumed temperature of 30 K.

The discrepancy between these two bridge mass calculations is not surprising, given the assumptions in the dust model from J2018. The dust opacity model, from Ossenkopf & Henning (1994), uses a micron-sized dust distribution, but grain growth may already have taken place. Using too small grains in the radiative transfer calculations will lead to an overestimation of the mass in the filament. Moreover, the canonical gas-to-dust mass ratio of 100 was used, and any deviation from this value would change the total mass estimate of the modeled filament.

In the case presented above in which the filament mass is below the Ostriker stability criterion, the filament would be supported against radial collapse, providing an opportunity for the young filament to fragment along its vertical (length) direction (Inutsuka & Miyama, 1992). Again, in an idealized nearly isothermal scenario, Inutsuka & Miyama (1997) have shown that separation between fragmented cores within a radially stable filament are of the order of four times its width. This ratio is not inconsistent with the bridge observed in IRAS 16293, with an observed diameter of ~250 au, and separation between the cores of at least 600 au, knowing that the vector connecting cores A and B may be inclined with respect to the plane of the sky.

Finally, we emphasize that, if indeed the bridge filament has been host to cores A and B, the filament must have been considerably more massive in the past. After adding even half of the current mass of cores A and B (0.5 $M_\odot$) to the current bridge filament mass calculated above, it is lifted well above the gravitational instability threshold. In

3 Adopted $^{16}O/^{17}O$ ratio is 1.8×10^3 from the local ISM values by Wilson & Rood (1994).

general, the observed filament is obviously more complex in nature than a static, cylindrically symmetric shape characterized by a single temperature. A true assessment of its gravitational stability would therefore require a much more elaborate treatment than the thought experiment described in this section.

6.4.3 *Kinematics*

Besides the bridge filament (Sects. 6.4.1, 6.4.2), almost all other morphological components discussed in this paper are dynamic and can be attributed to protostellar outflow activity. Distinct components are discussed in this subsection and are summarized in Fig. 6.1 and Table 6.2.

The CO 3–2 velocity map in Fig. 6.4 clearly traces the western lobe of the known east-west outflow pair, while its eastern counterpart and the separate southeast-northwest pair are all much less visible. In addition to the velocity bins shown in Fig. 6.4, the southeast outflow lobe from core A is detected in larger spatial extent at more modestly redshifted velocities (V_{lsr}=[+6,+8] km s^{-1}). The line-of-sight velocity in the western lobe increases with distance from core A, implying an acceleration with time. This is consistent with a centrally driven outflow that would naturally accelerate as the density of the ambient envelope, and therefore the pressure, decreases with radius (e.g., Moriarty-Schieven & Snell, 1988) In addition, the CO outflow in Fig. 6.4 exhibits a relatively collimated morphology up to $\sim 3''$ (~350 au in projection) from core A, at which point it abruptly fans out into a cone-like structure. This kink may be related to the radial extent of the rotating 'inner envelope' described by Oya et al. (2016). However, these authors infer a radius of the inner envelope of 200 au, whereas a density drop would be needed beyond 300 au to explain the location of the kink in the CO outflow morphology described above. Alternatively, the opening angle of the western outflow may be restricted by higher pressure inside the quiescent interbinary bridge described in Sect. 6.4.1 of this work. Its radius (Fig. 6.2, top left; Fig. 6.5, top left) appears to be more congruent with the 350 au radial separation from core A.

In contrast to $^{12}C^{16}O$, the other molecular tracers selected from the PILS data set mainly highlight the collimated northwest-southeast pair. Kristensen et al. (2013) detected only the northwest side of this outflow in CO 6–5, while Girart et al. (2014) detected both sides in CO 3–2 and SiO 8–7. In addition to previously detected tracers, in this work, we also detect both symmetric counterparts in H_2CO, $H^{13}CN$: redshifted with respect to core A to the southeast, blueshifted to the northwest (Fig. 6.2). Blueshifted emission in H_2CO, $H_2{}^{13}CO$, and $H^{13}CN$ appears to trace the interface of the northwest outflow with the dust bridge. This observed blueshifted emission at the southwestern edge ('inside bend') of the bridge could be an indication of the outflow impacting the quiescent bridge and sweeping up material in its wake. Pockets of enhanced H_2CO emission may be the result of molecules sputtering from the mantles of mildly shocked grains associated to one of the outflow lobes. However, sputtering would also produce increased amounts of SiO in the gas phase, and the lack of correlation between the spatial extent of observed SiO and H_2CO suggests that sputtering is not solely responsible and that other aspects, such as local density and temperature, also play a role in determining the morphology of the H_2CO emission map. The morphology of SiO emission, particularly on the southeast side of core A, outlines a more collimated, redshifted outflow (jet) structure than the maps of H_2CO and $H^{13}CN$ do (Fig. 6.2).

The blueshifted structure of $C^{34}S$ is seen deeper into the bridge than H_2CO and $H^{13}CN$, closer to the central axis of the bridge. Despite the overlap between the bridge and the $C^{34}S$, the blueshifted velocities of the latter suggest that it is not part of the quiescent bridge. The redshifted emission component seen in H_2CO, $H^{13}CN$ and $C^{34}S$ appears to be at the northernmost section of the redshifted outflow at position angle $\sim 270°$ (Yeh et al., 2008). In contrast with $C^{34}S$, another ^{34}S-bearing molecule detected in the PILS survey, $^{34}SO_2$ has a distribution confined to the disk domains of the two cores (Drozdovskaya et al., 2018). In summary, the two outflow-like emission shapes at position angles 335° and 315° (Fig. 6.1) are interpreted as two unrelated features. There is insufficient symmetry and alignment to assign them to the rotating structures around core A at position angle (rotation axis) 326–360° (Favre et al., 2014; Oya et al., 2016). We refer to Fig. 6.1 for an illustration of the misalignment.

The picture drawn in Fig. 6.1 also addresses the coupling of small scales (60–1500 au), as seen in interferometric observations, with larger scales (~2000–30 000 au) measured in single-dish observations. Firstly, we confirm the finding by Yeh et al. (2008) that the east-west outflow pair at a few-hundred au scales is consistent with the much larger outflow lobes extending out to thousands of au in the same direction, likely both driven by component A in the IRAS 16293 system. Secondly, the arcminute-scale outflow pair which is redshifted to the northeast and blueshifted to the southwest (Mizuno et al., 1990; Stark et al., 2004) does not appear to have any counterpart at scales below ~1000 au. This points to an outflow driven by IRAS 16293A at some time in the past, but which has been quenched in recent times. Adopting an inclination angle of 65° for the northeast-southwest outflow lobes and a line-of-sight velocity offset of 10 km s^{-1} (Stark et al., 2004), the absence of a northeast-southwest flow at scales $\lesssim$1000 au translates into a timeframe for the quenching of a few hundred years.

Finally, the strongly blueshifted components apparent in CO 3–2 (Fig. 6.4) near core B are interpreted using the position-velocity dia-

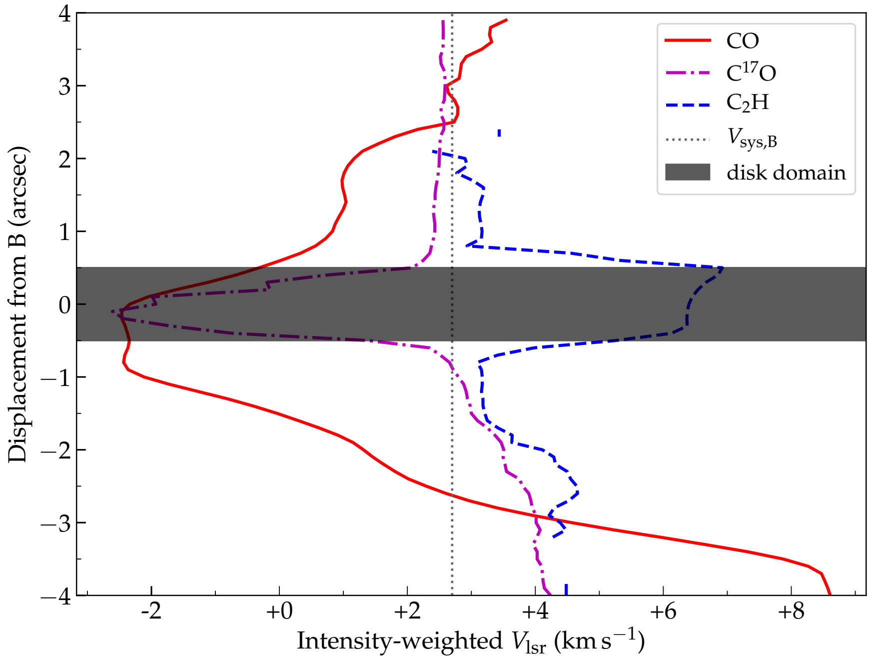

Figure 6.6: Position-velocity diagram along the slice indicated by the arrow in Fig. 6.4, with displacement defined to be positive to the north of core B. The 'disk domain', inside which intensity-weighted velocity values are not meaningful, is marked with a partly transparent gray box.

gram in Fig. 6.6. In this diagram, displacement values below -3″ correspond to the regime of the northern edge of the outflow cone emanating westward from core A, where redshifted velocities are observed. All weighted velocity values for the main CO isotopologue within 3″ on either side of core B, however, are significantly blueshifted with respect to the systemic velocity of core B (vertical dotted black line in Fig. 6.6). This must mean that surface layers on the front side (facing the observer), probed by optically thick CO emission, are moving away from the center of mass of protostellar core B. Already noted in the 2008 publication by Yeh et al. (their position 'b2'), the origin of this kinematic structure is still under debate. It may be a compact (and therefore young) outflow feature driven by core B (Loinard et al., 2013; Oya et al., 2018), or alternatively, a bow shock feature related to the northwest outflow driven by A (Kristensen et al., 2013). If driven by B, it remains to be explained why the symmetrical counterpart is hidden from sight, even at displacements 2–3″ north of core B, where dust optical depth would not be sufficient to absorb line emission from the background. If driven by A, it is unclear how the relatively modest velocity of the NW outflow axis, $\lesssim 5$ km s^{-1} with respect to either core (H^{13}CN and SiO panels in Fig. 6.2) could lead to line-of-sight velocities for the dense material in the outskirts of core B as high as 10 km s^{-1} with respect to the core. It is therefore plausible that some additional dynamic process is contributing. In the same region where ^{12}CO is blueshifted, the bulk mass traced by optically thin C^{17}O has velocities consistent with the systemic velocity of core B. In the disk domain, masked in Fig. 6.6 with a box spanning a width identical to the diameter of the masks in Fig. 6.2, even C^{17}O is affected by the high optical depth of line and continuum photons. The C_2H emission, which also stretches north-south across core B (Figs. 6.2, 6.22), shows a velocity trend in Fig. 6.6 overlapping that of C^{17}O. These two species show a modest velocity gradient across core B,: V_{lsr} is +1.8 to +2.7 km s^{-1} north of core B, and +2.6 to +4.1 km s^{-1} south of B, whichever physical component it traces.

Two pockets of SiO 8–7 emission are seen $\sim 1''$ north and south of core B, at position angle 15° east of north (Fig. 6.20), not overlapping with the C_2H filament (Sect. 6.5.3) at position angle −15°. Line of sight velocities of SiO in these pockets are shifted towards both blue and red sides of the systemic velocity, which makes their association to either outflow or inflow motions ambiguous. The much weaker, but optically thin emission from ^{29}SiO (Fig. 6.21) shows the same morphology, again with mixed blue and red velocities. The morphology and kinematics of SiO 8–7 in our map is consistent with that observed in SiO 7–6 by Oya et al. (2018), who interpret this structure as a signature of a pole-on pair of outflows.

6.5 DISCUSSION

To highlight the different physical and dynamical components studied in this work, the molecular gas observed between and around the binary protostellar system IRAS 16293 at 60–1500 au scales is divided into three distinct domains: (i) dense and hot (> 100 K) gas in the disk or disk-like regions around sources A and B; (ii) more tenuous and colder gas residing in the dust bridge between the protostars; and (iii) kinematically active gas within or on the borders of outflow lobes driven by core A. Domain (i) is not examined in this work, but its kinematics and temperature structure was extensively studied, using a different set of molecular tracers, by Oya et al. (2016) for core A and by Oya et al. (2018) for core B. Domains (ii) and (iii) are discussed in Sects. 6.5.1 and 6.5.2. A structure seen in C_2H, seemingly unrelated to outflow or infall dynamics, is addressed in Sect. 6.5.3. Finally, the possible age difference between the two cores in IRAS 16293 is addressed in Sect. 6.5.4.

6.5.1 *The quiescent bridge*

The arc-like bridge structure between protostars A and B is made up of material of low density (4×10^4 cm^{-3}– $\sim 10^8$ cm^{-3}), low temperature (< 50 K), or both. Evidence is provided by the observation that the only molecular species clearly tracing the morphology of the dust arc is $C^{17}O$, while all tracers of higher density (see Table 6.2) follow outflow structures and have line-of-sight velocity structures that deviate significantly from that of $C^{17}O$. This interpretation is supported when our observations are compared with three-dimensional models from J2018, yielding a qualitative match in morphology of the observed bridge structure (Sect. 6.4.1). We hypothesize that the bridge is a remnant substructure of the circumbinary envelope (Schöier et al., 2002) or a filamentary core, from which both protostellar cores have formed in the past. With its current mass budget and temperature conditions, the bridge filament is stable against further gravitational collapse (Sect. 6.4.2). In addition, the bridge arc is kinematically quiescent, lying at a flat V_{lsr} within 0.5 km s^{-1} of the systemic velocities of both protostars (Fig. 6.2, top left). This straightforward observational fact rules out a scenario in which the bridge arc is one segment of a large, circumbinary disk (or torus) in which both protostars would be embedded. In such a scenario, the bridge gas would have shown a line-of-sight velocity gradient following the kinematic signatures of sources A (+3.1 km s^{-1}) and B (+2.7 km s^{-1}), i.e., a blue-to-red gradient in the southeast-to-northwest direction. This would only comply with the observed flat velocity distribution if the 'disk' would rotate entirely in the plane of the sky, which is inconsistent with the line of sight velocity difference of the two protostars. Compared to other, tighter protostellar binary systems such as GG Tau (Dutrey et al., 2014, 2016) and IRS 43 (Brinch et al., 2016), the bridge that we observe between the components of IRAS 16293 lacks a symmetric complement to close a full circumbinary disk or torus, and its velocity structure is inconsistent with disk-like rotation. If there is any velocity gradient across the bridge, it is in the transverse direction rather than along the length of the arc.

Although the 600 au separation between the two components in IRAS 16293 is somewhere in the mid-field between close and wide binaries (see Sect. 6.1), we conclude that the formation of protostars A and B must have occurred through turbulent fragmentation. The reason is that the competing scenario, disk fragmentation (Adams et al., 1989), is unlikely due to the lack of evidence for a remnant of a circumbinary disk and the stark misalignment between the two disk-like structures, face-on for core B (Jørgensen et al., 2016; Oya et al., 2018), and roughly edge-on for core A (Pineda et al., 2012; Girart et al., 2014).

Like IRAS 16293, the more evolved Class I binary protostellar system IRAS 04191 + 1523, with two components separated by 860 au, also shows a bridge of gas connecting the two protostellar cores (J.-E. Lee et al. 2017). Based on the velocity structure of the $C^{18}O$ bridge, J.-E. Lee et al. 2017 conclude that the two cores and the bridge are a substructure of the same natal envelope, which has given rise to protostar formation through turbulent fragmentation. In contrast, the Class 0 L1448 IRS3B triple protostellar system hosts a heavily curved connecting filament seen in $C^{18}O$, and its kinematics are consistent with being a remnant of a 254 au diameter disk that is hypothesized to have spawned all three cores through disk fragmentation (Tobin et al., 2016a). A connecting bridge was also found in the triple system SR24, with a $\sim$ 700 au size, by Fernández-López et al. (2017), who hint that it, too, may be interpreted as a remnant of a disk spiral arm. In each of these case studies, the bridging filaments appear to have a relation to the nursery of the protostellar cores, either in the form of a protostellar disk undergoing fragmentation or a substructure of a larger-scale envelope. IRAS 16293 appears to belong in the latter category.

6.5.2 *Outflow signatures*

The SiO gas surrounding IRAS 16293B at projected radii up to 250 au (J=8–7, Sect. 6.4.3 of this work; J=7–6, Oya et al. 2018) is of mixed blue- and red-shifted velocity up to $\pm 3\,\mathrm{km\,s^{-1}}$ from the systemic velocity of core B. The presence of SiO in the gas phase is often used as a tracer of grain sputtering due to outflow shocks (e.g., Flower et al., 1996; Caselli et al., 1997; Jiménez-Serra et al., 2008). While the overlapping blueshifted and redshifted SiO emission is suggestive of a geometry with approaching and receding outflows superposed in projection (Oya et al., 2018), the relatively low velocities would not be expected to lead to sputtering. Correcting the observed velocity for projection effects has a marginal effect, since the V_{lsr} offset is necessarily almost completely parallel with the true velocity vectors in case of a face-on disk launching an outflow along the line of sight. However, in the scenario that the SiO pockets near core B are due to impact of the northwest outflow from core A, it is also questionable whether velocities of $< 10\,\mathrm{km\,s^{-1}}$ would be sufficient to lead to shocks. This leaves neither the pole-on outflow from core B nor the impact of the outflow from A onto core B as a fully viable scenario.

The morphology of two molecular lines that are sensitive to densities above 10^7 $\mathrm{cm^{-3}}$, o-H_2CO $5_{1,5}$–$4_{1,4}$ and $H^{13}CN$ 4–3 (Table 6.2), are compared with a three-dimensional model in Sect. 6.4.1. In the observed maps (Fig. 6.2), these high-density tracers do not coincide with the axis of the dust/$C^{17}O$ bridge. The modeled structure (J2018; Sect. 6.4.1 of this work) does not produce emission in H_2CO or $H^{13}CN$ from its bridge domain, consistent with the observations. Instead, the modeled emission is concentrated in the disk domains (and is extremely optically thick for o-H_2CO), with an extended hour-glass at positions above the disk plane of core A, qualitatively consistent with enhanced pockets of emission seen in the observed maps southeast and northwest of the edge-on core A. This is caused by self-absorption in the high-density midplane of the disk or disk-like structure, whereas its atmosphere is less opaque, but still sufficiently dense and hot to excite the $H^{13}CN$ into J=4. The absence of $H^{13}CN$ in the bridge in the models is due to the chosen ice sublimation temperature of 100 K, which is only exceeded in the innermost regions close to the protostars.

The high-density molecular gas observed in emission near the bridge filament is interpreted as being the effect of two outflows at position angles 315° and 270°, impacting patches of higher density in the ambient envelope. The northernmost of the two is blueshifted, and is posited to be material on the southwestern edge of the bridge, swept up by the blueshifted side of the northwest-southeast outflow pair (Sect. 6.4.3, Fig. 6.1). The southern, redshifted component at position angle 335°, coincides with the northern border of the redshifted western outflow cone (Yeh et al. 2008; Fig. 6.4 in this work). The same molecules are not observed at the southern edge of the western outflow; we speculate that this is due to a density contrast in the ambient medium, with higher density at the northern side, toward the bridge filament. H_2CO in particular is known to sublimate efficiently from dust grain surfaces not just by thermal desorption, but also by photodesorption such as occurs in classical photodissociation regions (Van der Wiel et al., 2009; Guzmán et al., 2011). It is therefore natural to expect enhanced gas-phase H_2CO abundances in directly irradiated walls of outflow cavities in protostellar systems such as IRAS 16293.

6.5.3 *The C_2H filament*

A narrow filament of material stretching across core B in the south-north direction is visible in C_2H, and a similar but slightly offset patch of high-velocity ($V_{lsr}<-6$ km s^{-1}) ^{12}CO up to 1.″5 south of core B. Compared with the C_2H emission observed in single-dish IRAM 30m observation (Caux et al., 2011), it is evident that the majority of C_2H flux is filtered out in our interferometric ALMA observations, much more than for spectral lines of other species. However, regardless of missing flux from a smooth, large-scale component, our ALMA C_2H map reveals compact substructures at scales $\sim10^2$-10^3 au. The velocity profiles of ^{12}CO, $C^{17}O$ and C_2H along this feature are shown in Fig. 6.6. C_2H, as already apparent from its intensity-weighted velocity map in Fig. 6.2, has a rather flat velocity structure along the length of the filament, at V_{lsr} within $\sim$ 1 km s^{-1} of that of core B itself. The morphology of this feature, combined with its small line of sight velocity gradient, would be more consistent with a symmetric (outflow or infall) motion almost exactly in the plane of the sky, than with an outflow emanating perpendicularly from the face-on disk of core B. The morphology of C_2H is also studied in Murillo et al. (submitted), who find that it anti-correlates with that of cyclic C_3H_2. While non-overlapping distributions of these two chemically related species (Gerin et al., 2011) may seem surprising, there are also models and observations that indicate somewhat different physical conditions being needed for C_2H and c-C_3H_2 emission lines to occur (Cuadrado et al., 2015). Lacking an obvious connection to any of the other features connected to core A, the physical, dynamical and chemical origin of the C_2H emission remains an open question.

6.5.4 *An age difference between cores A and B*

Based on the conclusions drawn in this paper and accompanying PILS papers (J2018; Calcutt et al. submitted), it remains unclear if sources A and B in the IRAS 16293 system are coeval. Their rotation axes are not aligned and a formation scenario from a giant circumbinary disk is therefore unlikely (see Sect. 6.5.1). Sources A and B differ in various aspects. Here we list those of relevance to the matter of evolutionary stage. (i) core A is known to drive at least two sets of bipolar outflows, and an additional one in the past, whereas core B shows signs of infall, but exhibits no unambiguous proof of outflow activity (Pineda et al. 2012; Loinard et al. 2013; Kristensen et al. 2013; Sect. 6.4.3 of this work). (ii) J2018 find that the observed dust emission of the face-on disk of core B can only be explained with a vertically extended disk or disk-like model (i.e., one that has not yet undergone significant settling), while the vertical structure of the disk of core A is not constrained by their model. (iii) Chemical differentiation is seen between both sources particularly when analysing CN-bearing species. Such species have time dependent formation pathways (Garrod et al., 2017) with some, such as vinyl cyanide (C_2H_3CN), being formed later during the warm-up phase, as a result of the destruction of ethyl cyanide (C_2H_5CN). Calcutt et al. (submitted) find vinyl cyanide to be nine times more abundant toward the B source. However, these authors stress that although this could indicate that core A is younger, it could also imply that the warm-up timescales for core A were very short, limiting the amount of vinyl cyanide that could be formed. Collecting the above information elements, (i) and (ii) are consistent with a view that core B is at an earlier stage of evolution than core A, whereas (iii) could be explained either way, appreciating that the temperature history of each core is not necessarily monotonous and smooth. We thus pose that core B is at least as young and probably younger than core A.

If there is an age difference between cores A and B, outflowing material from core A may have provided a trigger for gravitational collapse to set in, some six hundred au (projected) further down its own natal filament. Alternatively, even if the initial collapse of core B started spontaneously, the northwest outflow from core A could now be feeding gas and dust originating in protostar A onto the disk of core B. Such a scenario would add a new element to the investigation of the different levels of various groups of chemical compounds found in cores A and B (Bisschop et al., 2008b; Calcutt et al., submitted).

6.6 SUMMARY AND CONCLUSIONS

We have presented an analysis of the distribution and kinematics of molecular gas in the protostellar binary system IRAS 16293 at scales of 60–2000 au, using ALMA-PILS observational data and three - dimensional line radiative transfer modeling. The selected tracers are 868 µm dust continuum, CO 3–2, $C^{17}O$ 3–2, $H^{13}CN$ 4–3, o-$H_2CO5_{1,5}$–$4_{1,4}$, $H_2{}^{13}CO5_{1,5}$–$4_{1,4}$, $C^{34}S$ 7–6, SiO 8–7, ^{29}SiO 8–7, and C_2H $4_{7/2}$–$3_{5/2}$, together highlighting different aspect of the morphology and dynamics of the system. The main conclusions are summarized here.

1. The arc-shaped filament connecting the two protostellar cores is clearly seen in dust continuum and $C^{17}O$ 3–2 emission. The kinematic pattern of $C^{17}O$ indicates that is quiescent, and consistent with the systemic velocities of both cores. Other molecular tracers considered in this work show a different spatial distribution, different kinematics, or both (Sect. 6.3). The true density of the bridge filament is likely to be between 4×10^4 cm^{-3} and ~10^8 cm^{-3} (Sect. 6.4.1). A three-dimensional radiative transfer model qualitatively matches the observed structure in dust and $C^{17}O$, but not those in $H^{13}CN$ and H_2CO emission (Sect. 6.4.1).

2. Using a simplified description of the bridge filament, balancing thermal pressure and gravity, the bridge is inferred to be stable against radial collapse, in principle allowing time for it to fragment along the direction of its axis (Sect. 6.4.2).

3. Given the physical nature of the bridge filament, we pose that it is a remnant substructure of a filamentary circumbinary envelope that has undergone turbulent fragmentation to form both protostellar cores (Sect. 6.5.1).

4. The western side of the east-west outflow pair is clearly traced in CO 3–2 in our observations, shown to be accelerating with distance from the launching core A. In addition, it is seen to change from a collimated to a more wide-angle structure at a projected distance of ~350 au from core A, possibly related to a density and pressure gradient of one of the more or less cylindrical structures observed in this system (Sect. 6.4.3).

5. Molecular lines of (isotopologues of) H_2CO, HCN, SiO, and CS trace outflow motions or the impact of outflows onto more quiescent components. Dynamic structures near core B might be

due to nearly pole-on outflow from core B itself, or impact of the northwest outflow from core A onto dense material in core B (Sect. 6.4.3). In our observations, we find no counterpart for the large scale (thousands of au) northeast-southwest outflow pair, indicating that its launching engine must have been quenched a few hundred years ago (Sect. 6.4.3).

6. A striking, previously unknown structure stretches straight across core B at position angle ~ 15° from north-south. It is only seen in C_2H and is kinematically flat, which rules out an origin in outflow activity of core B (Sect. 6.5.3).

7. Combining evidence from this work and other studies, we suggest that core B is not more evolved than its sister core A (Sect. 6.5.4).

8. When used as a target to search for complex (organic) molecules, as is often done, the physical and dynamical complexity of the IRAS 16293 protostellar binary system should be taken into account. While searches for complex molecules generally avoid the broad line regions near core A, even the often-used positions on or near the blue '×' mark in Fig. 6.2, 0.5″ offset from core B, may exhibit spectral line shapes with evidence of line-of-sight motions, which will manifest differently in different molecules.

By abandoning spherically symmetric model descriptions of the envelopes of IRAS 16293 (e.g., Jørgensen et al., 2002; Schöier et al., 2002; Crimier et al., 2010a) and other protostellar systems, J2018 have now taken a significant leap by developing a three-dimensional density model that includes an envelope hosting two individual energy sources, cores A and B, disk-like structures around each, an inter-binary bridge filament, and a self-consistently derived temperature structure of the ensemble. While the radiative transfer scheme initially included dust and CO isotopologues, it was further expanded in this work to include two additional molecular species. There are still steps to be made, however, to make such a model more realistic. For example, chemistry and freezing and sublimation of molecules could be included, beyond the currently implementation using gas-phase abundance jumps at certain threshold temperatures. In addition, various dynamic components should be added, such as the outflows, but also the rotating, disk-like structure around core A. In addition, future observational work could answer currently open questions about, for example, (i) the the evolutionary state of core B, (ii) the debated small-scale multiplicity of core A, or (iii) the connection between the relatively young, small-scale outflow signatures (a few hundred to a few thousands au) observed in interferometric observations such as in this paper, and the older outflows seen at tens of thousands of au distance from the protostellar cores.

Considering the already known level of complexity of the system, and the additional aspects yet to be uncovered, adding all these elements to a (self-consistent) physical model would further increase the number of degrees of freedom, which may result in challenges when attempting to sensibly constrain the model parameters.

In a bigger context, the protostellar stages of this and other binary systems should be studied further in order to understand how interactions with binary companions (through direct illumination or even mass transfer through an outflow) affect the time evolution of the inner few tens of au, where planet formation is expected to take place. After all, in the hunt for an explanation of the formation scenario of sun-like stars and of the ubiquity of planetary systems, those in multiple star systems, given their occurrence rate, deserve at least as much attention as singular systems.

6.7 ACKNOWLEDGEMENTS

MHDvdW, SKJ, JKJ, LEK and HC acknowledge support from the European Research Council (ERC) under the European Union's Horizon 2020 research and innovation programme (grant agreement No. 646908) through ERC Consolidator Grant "S4F", as well as from a Lundbeck Foundation Group Leader Fellowship. PB acknowledges support from the Swedish Research Council through contract 637-2013-472. Research at the Centre for Star and Planet Formation is funded by the Danish National Research Foundation. MND acknowledges the financial support of the Center for Space and Habitability (CSH) Fellowship and the IAU Gruber Foundation Fellowship.
This paper makes use of the following ALMA data: ADS/JAO.ALMA #2013.1.00278.S. ALMA is a partnership of ESO (representing its member states), NSF (USA) and NINS (Japan), together with NRC (Canada), NSC and ASIAA (Taiwan), and KASI (Republic of Korea), in co - operation with the Republic of Chile. The Joint ALMA Observatory is operated by ESO, AUI/NRAO and NAOJ.
This research has made use of NASA's Astrophysics Data System Bibliographic Services. This research has made use of APLpy, an open-source plotting package for Python (Robitaille & Bressert, 2012); Astropy, a community-developed core Python package for Astronomy (Astropy Collaboration 2013b), the matplotlib plotting library (Hunter, 2007), and the CASA data processing package (McMullin et al., 2007).

6.8 APPENDIX

6.9 LINE CONTAMINATION

Since the PILS data set, covering 329.15–362.90 GHz, has a line density of about one line every 3 MHz (Jørgensen et al., 2016), it is important to consider the effect of contamination of other species contributing to the observed signal of a selected tracer. The potential contributions from species and transitions other than those listed in Table 2 are visualized in the spectral profiles in Figs. 6.7–6.14 below.

In general, while various contaminating contributions are identified in the spectrum extracted toward the position one beam west-southwest of core B, this signal is exclusively due to relatively complex molecular species, with the exception of SO_2 (near $H^{13}CN$, Fig. 6.8) and $N^{17}O$ (near ^{29}SiO, Fig. 6.13), which are known to have spatial distributions confined to the regions in the central 1–2″ of cores A and/or B (e.g., Baryshev et al., 2015; Lykke et al., 2017; Ligterink et al., 2017), domains explicitly not under study in the current work. Particular cases that require a more detailed description are addressed in the following paragraphs.

$H^{13}CN$ 4–3. There is potential contamination of the $H^{13}CN$ 4–3 signal by the SO_2 $13_{2,12}$–$12_{1,11}$ transition (345.3385377 GHz), with a modest upper level energy of 92 K, at only 1.2 MHz from the rest frequency of $H^{13}CN$. At the position 0.5″ southwest of core B ('×' mark in Fig. 6.2), preferred for identifying spectral signatures of rare, complex molecules in previous PILS papers (e.g., Coutens et al., 2016; Lykke et al., 2017; Ligterink et al., 2017), lines are narrow and spectrally resolved, and we do not see evidence of SO_2 contribution to the $H^{13}CN$ total intensity beyond a few percent. At other positions, for example in the western outflow from core A or close to core A itself, contamination cannot be ruled out.

^{29}SiO 8–7. The signal of the ^{29}SiO 8–7 itself is weak and somewhat blueshifted (~1 km s^{-1}) toward the position 0.5″ offset from core B (Fig. 6.13). We are confident, however, that the signal ascribed to ^{29}SiO in the channel maps (Fig. 6.21) and velocity map (Fig. 6.2), because the morphology of the redshifted ^{29}SiO channel maps follows that of the brightest patches of SiO (Fig. 6.20) and the spectral line shape toward those positions (for example the extension southeast of core A) is single-peaked. On the redshifted side, ^{29}SiO may be contaminated by at least one of the three nitric oxide ($N^{17}O$) lines, but only near the '0.5″ offset from core B' position. The characteristic tripple-peaked spectral profile is not seen elsewhere in the map.

C_2H $4_{7/2}$–$3_{5/2}$. For the C_2H N_J=$4_{7/2}$–$3_{5/2}$ transition, there are two finestructure components (F=4–3 and 3–2), separated by 1.4 MHz. Such a small separation means that they lie within 1.2 km s^{-1} of one another in the spectral dimension, but are resolved in our 0.2 km s^{-1} spectral resolution data cubes, which complicates the interpretation of its velocity structure. In this work, the reference frequency (zero-point for V_{lsr}) is taken as the mid-point between the two finestructure lines, F=4–3 at 349.39928 GHz and F=3–2 at 349.40067 GHz (Padovani et al., 2009). In addition, most of the redshifted (>+5 km s^{-1}) emission in the velocity map of C_2H (Fig. 6.2, Fig. 6.22) is due to the bright CH_3CN 19_3–18_3 transition at 349.39329 GHz. For this reason, we have adopted a narrower integration for C_2H than for the other lines (cf. Fig. 6.14 vs. Fig. 6.7–6.13). In positions near sources A and B, the CH_3CN line also contaminates channels closer to the systemic velocity of C_2H.

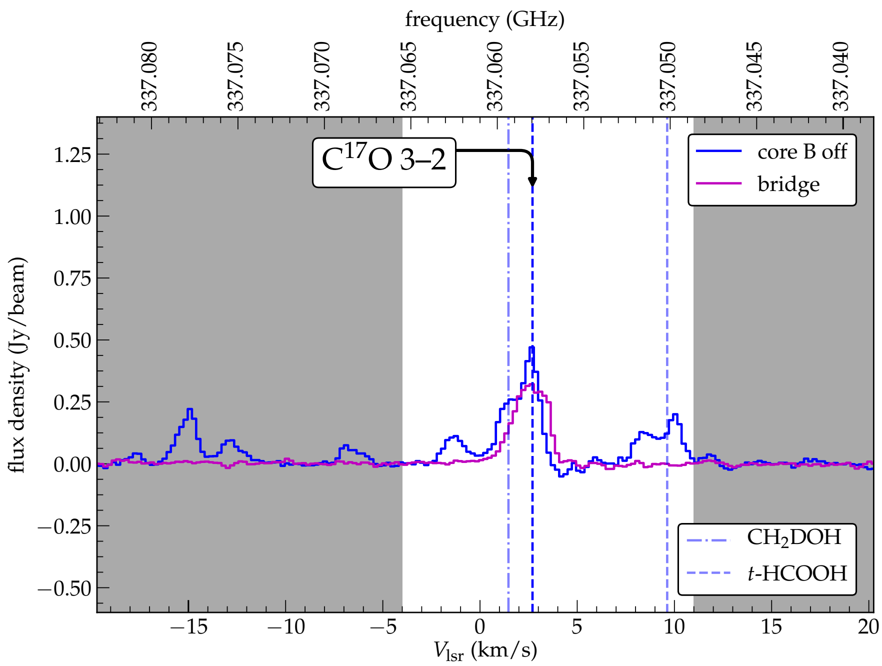

Figure 6.7: Spectral profiles of $C^{17}O$ 3–2 at two spatial positions: one beam west-southwest of core B (blue '×' mark in Fig. 6.2) and within the bridge filament (magenta '+' mark in the same figure). The frequency of the species of interest is marked by the blue, vertical dashed line; other lines identified in the frequency range are marked with dotted, dash-dotted, or solid lines. All rest frequencies are shifted by +2.7 km s^{-1} to account for the systemic velocity of core B. The section of the velocity axis with white background denotes the maximum range over which velocities are integrated.

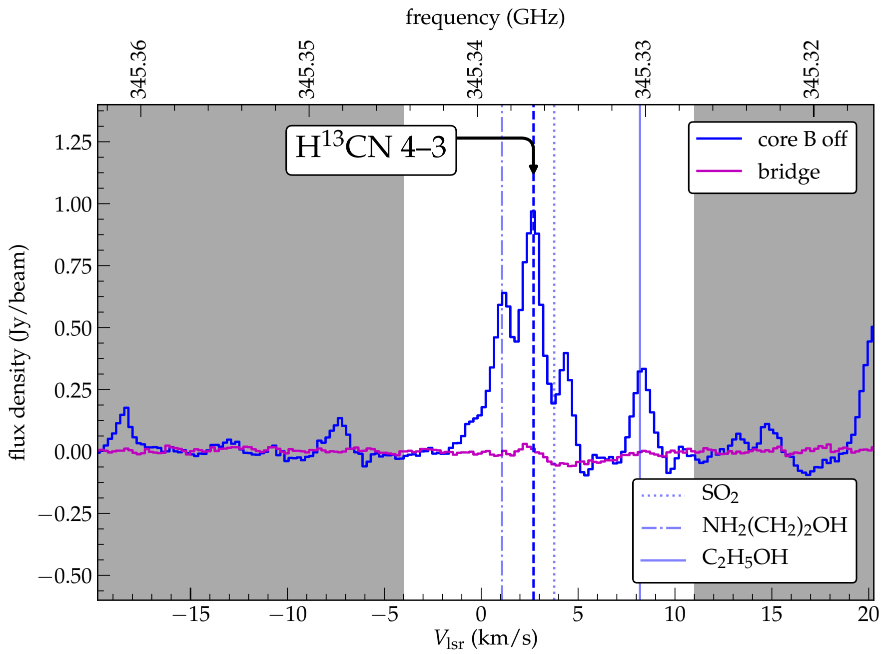

Figure 6.8: As Fig. 6.7, but for $H^{13}CN$.

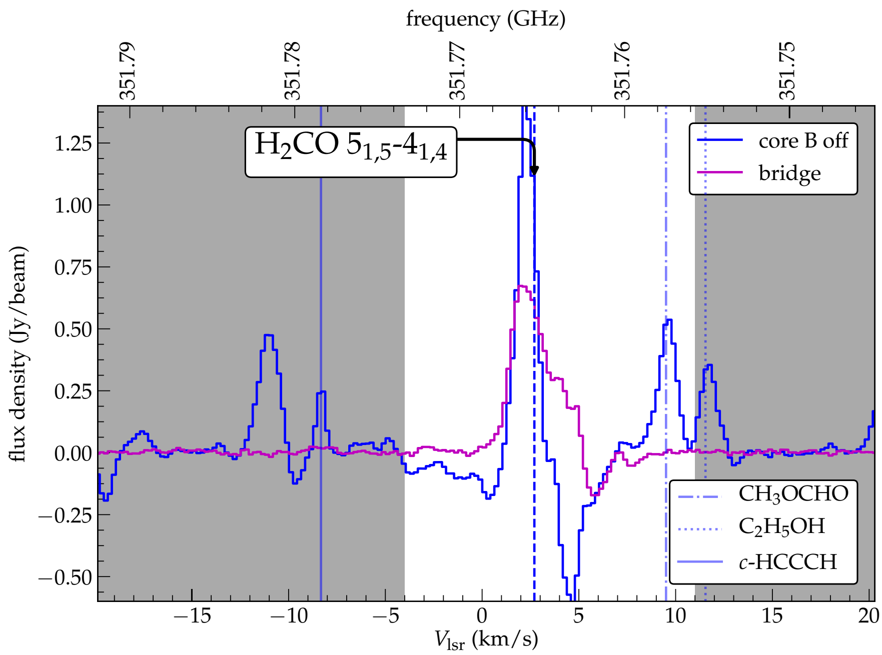

Figure 6.9: As Fig. 6.7, but for H_2CO.

6.10 CHANNEL MAP FIGURES

Channel maps of the molecular lines listed in Table 6.2 are shown in Fig. 6.15–6.22.

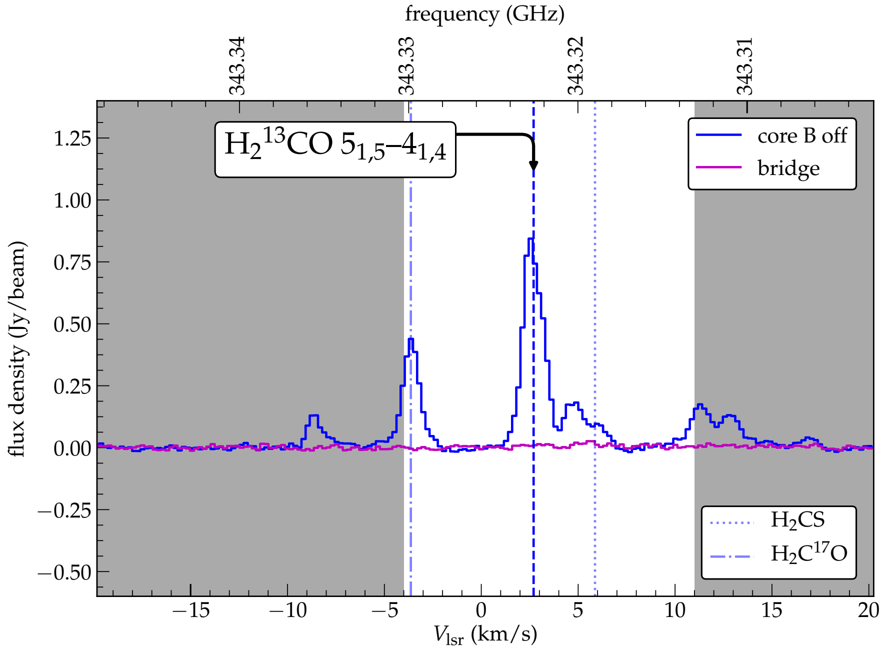

Figure 6.10: As Fig. 6.7, but for $H_2{}^{13}CO$.

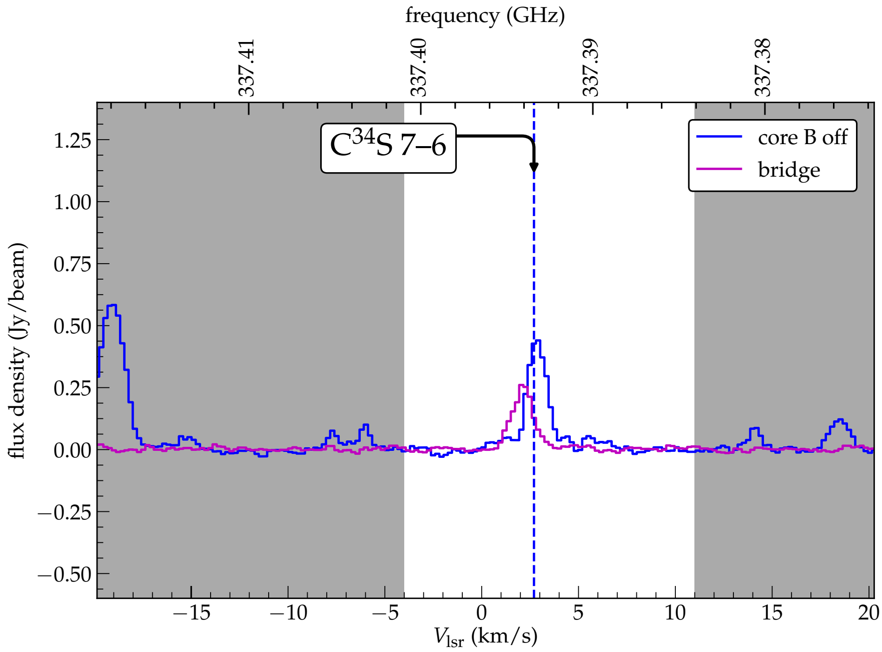

Figure 6.11: As Fig. 6.7, but for $C^{34}S$.

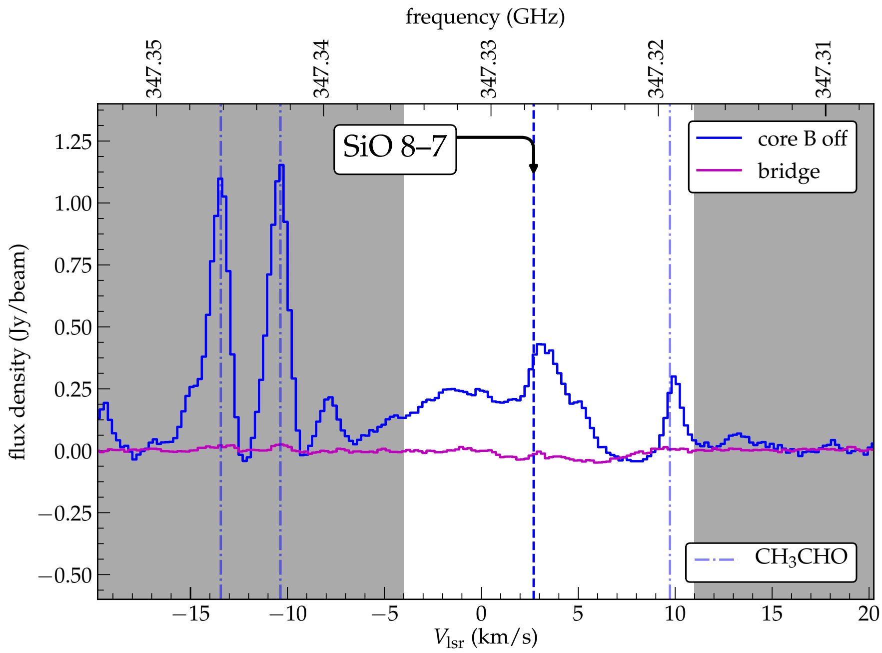

Figure 6.12: As Fig. 6.7, but for SiO.

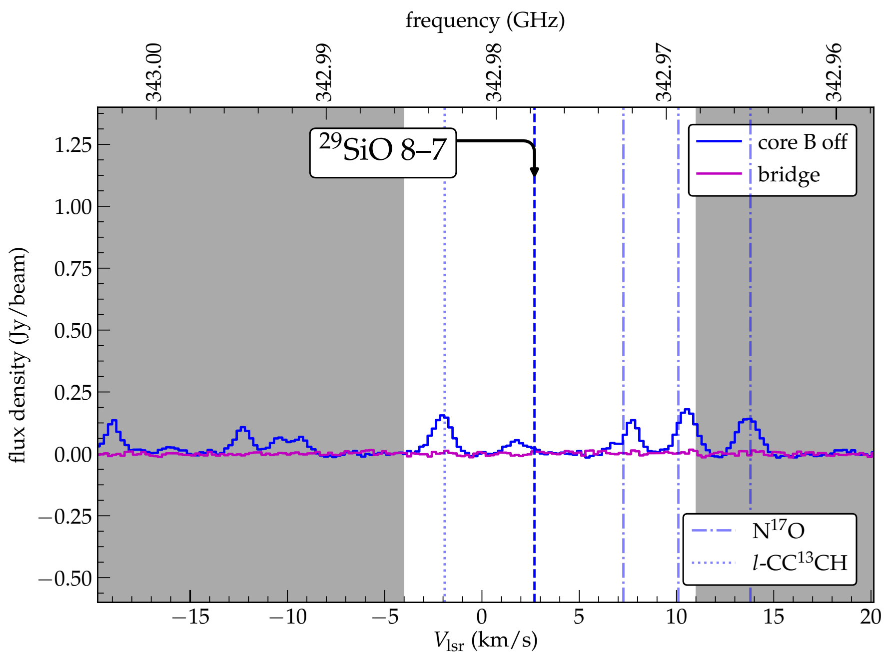

Figure 6.13: As Fig. 6.7, but for ^{29}SiO.

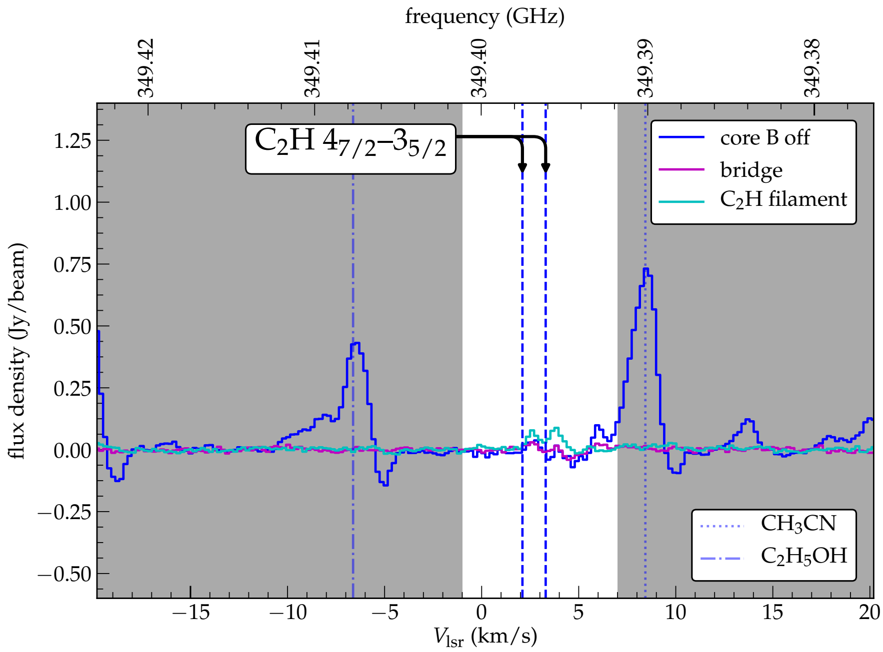

Figure 6.14: As Fig. 6.7, but for C_2H.

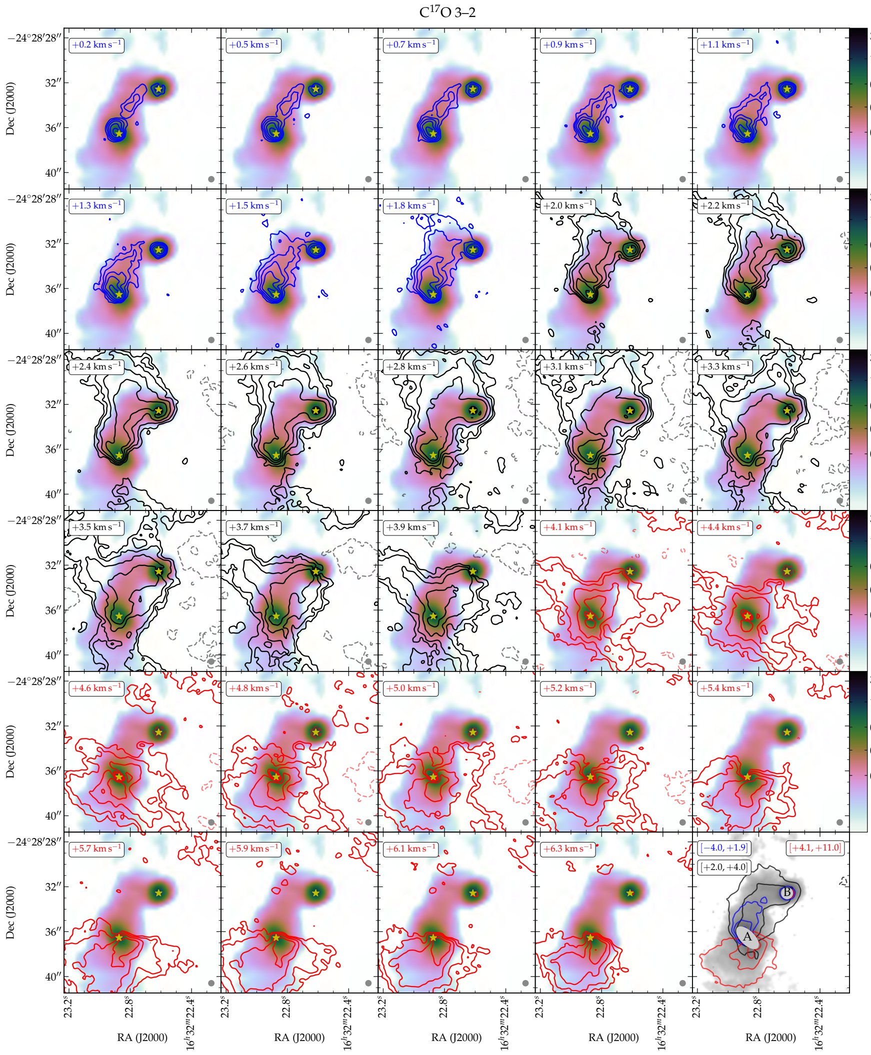

Figure 6.15: $C^{17}O$ 3–2 channel maps with contours representing logarithmically spaced line intensity in each channel. The first positive contour (solid blue, black, or red) is at 0.03 Jy beam^{-1}, the first negative contour (lighter, dashed) is at −0.06 Jy beam^{-1}, with every next contour level spaced by a factor of two. The bottom right panel displays three integrated velocity ranges in colored contours: all 'blue' channels, [−4.0, +2.0⟩ km s^{-1}; all 'systemic velocity' channels, [+2.0, +4.0] km s^{-1}; and all 'red' channels, ⟨+4.0, +11.0] km s^{-1}. For each of these three, the first contour level is at 0.2 Jy beam^{-1} km s^{-1} and levels increase by factors of two, and equivalently for negative contours displayed in dashed line format. Gray scale in bottom right panel (logarithmic stretch from 0.002 to 2.0 Jy beam^{-1}), color scale in all other panels (logarithmic stretch indicated in color bar): 868 µm continuum. Star symbols mark the continuum peak locations of protostars A and B (see Table 6.1).

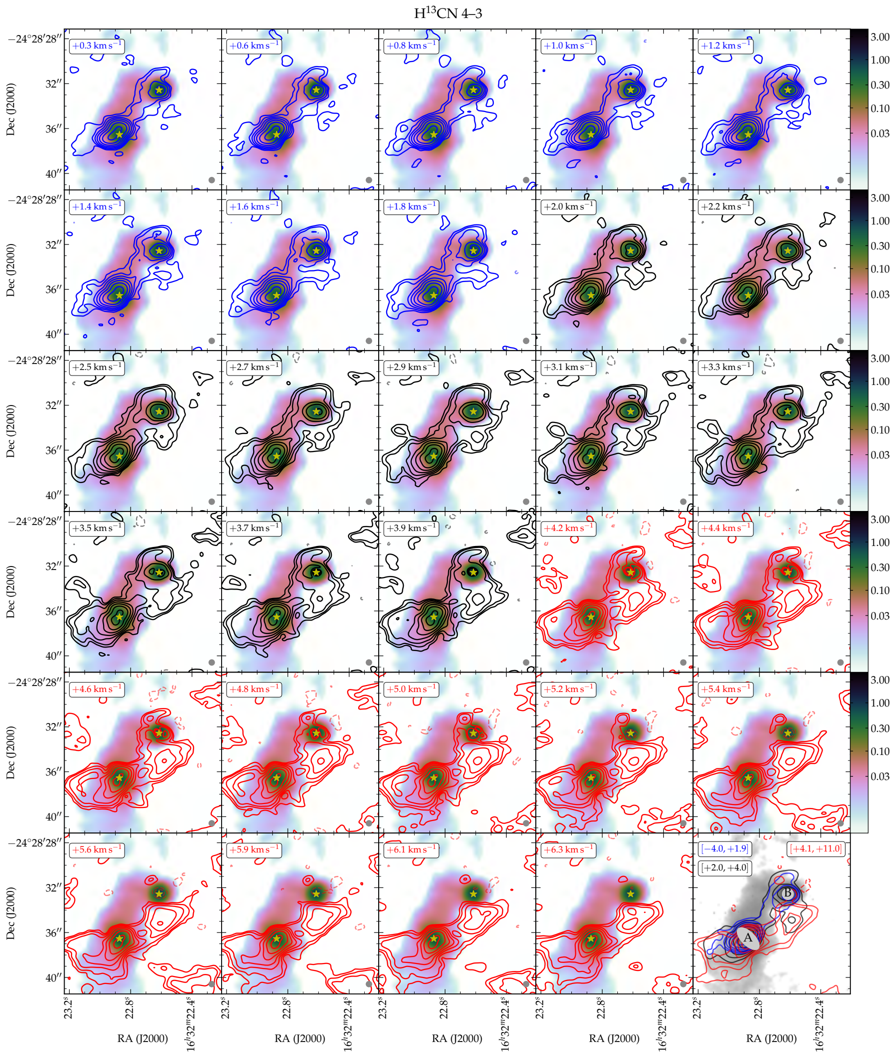

Figure 6.16: H^{13}CN 4–3 channel maps. As Fig. 6.15. First positive (negative) contour level in individual channel maps: 0.03 (−0.06) Jy beam^{-1}; first contour levels in the bottom right integrated ranges panel: 0.2 Jy beam^{-1} km s^{-1}.

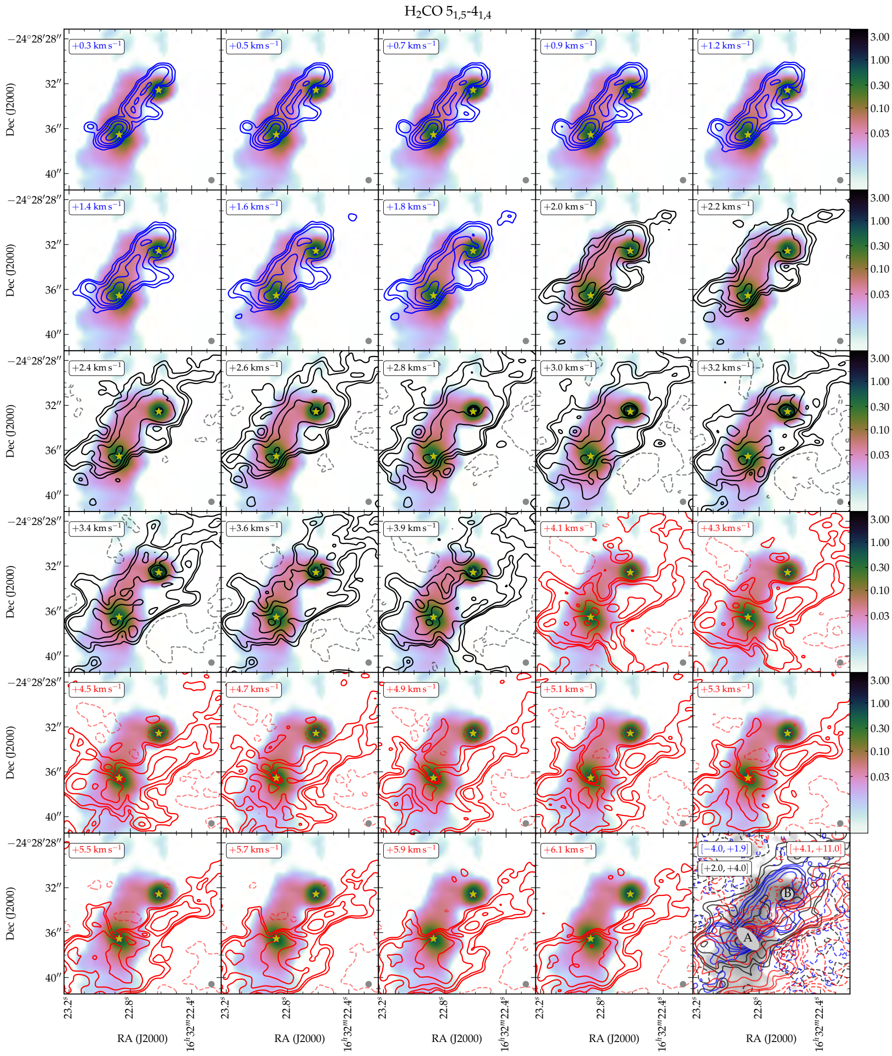

Figure 6.17: H_2CO $5_{1,5}$–$4_{1,4}$ channel maps. As Fig. 6.15. First positive (negative) contour level in individual channel maps: 0.12 (−0.24) Jy beam^{-1}; first contour levels in the bottom right integrated ranges panel: 0.2 Jy beam^{-1} km s^{-1}.

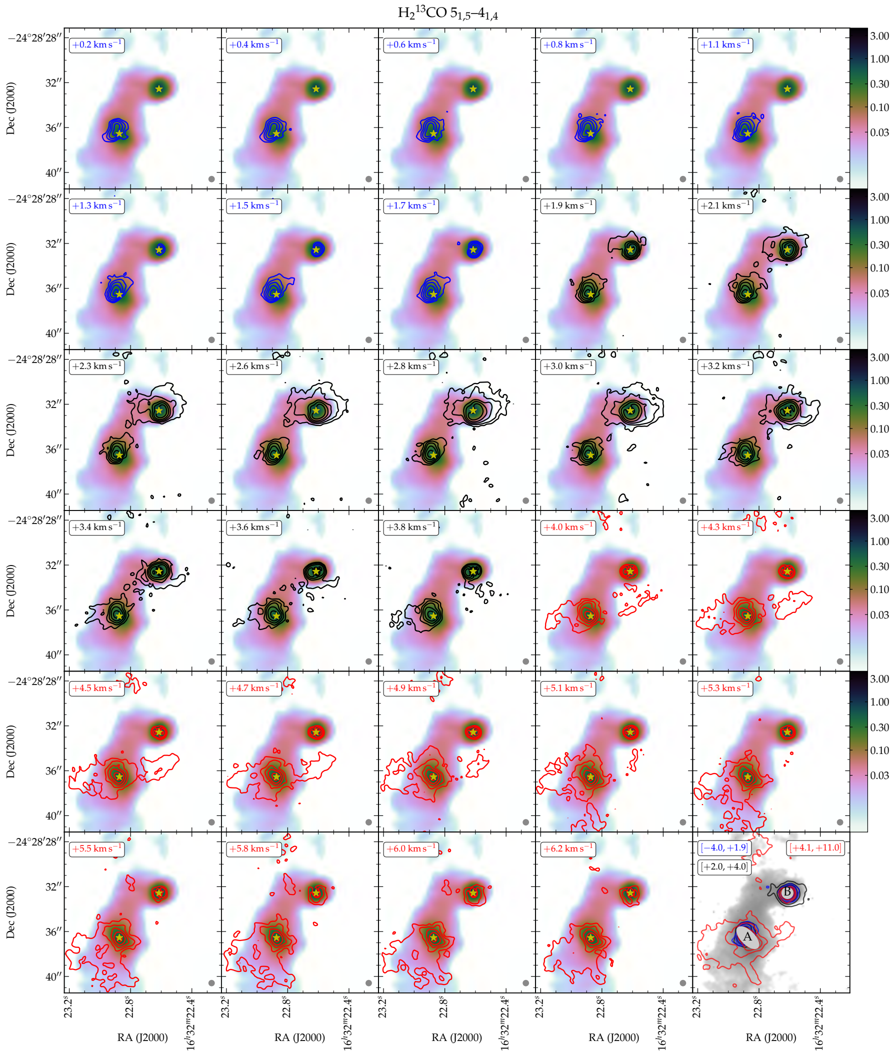

Figure 6.18: $H_2{}^{13}CO$ $5_{1,5}$–$4_{1,4}$ channel maps. As Fig. 6.15. First positive (negative) contour level in individual channel maps: 0.03 (−0.06) Jy beam^{-1}; first contour levels in the bottom right integrated ranges panel: 0.1 Jy beam^{-1} km s^{-1}.

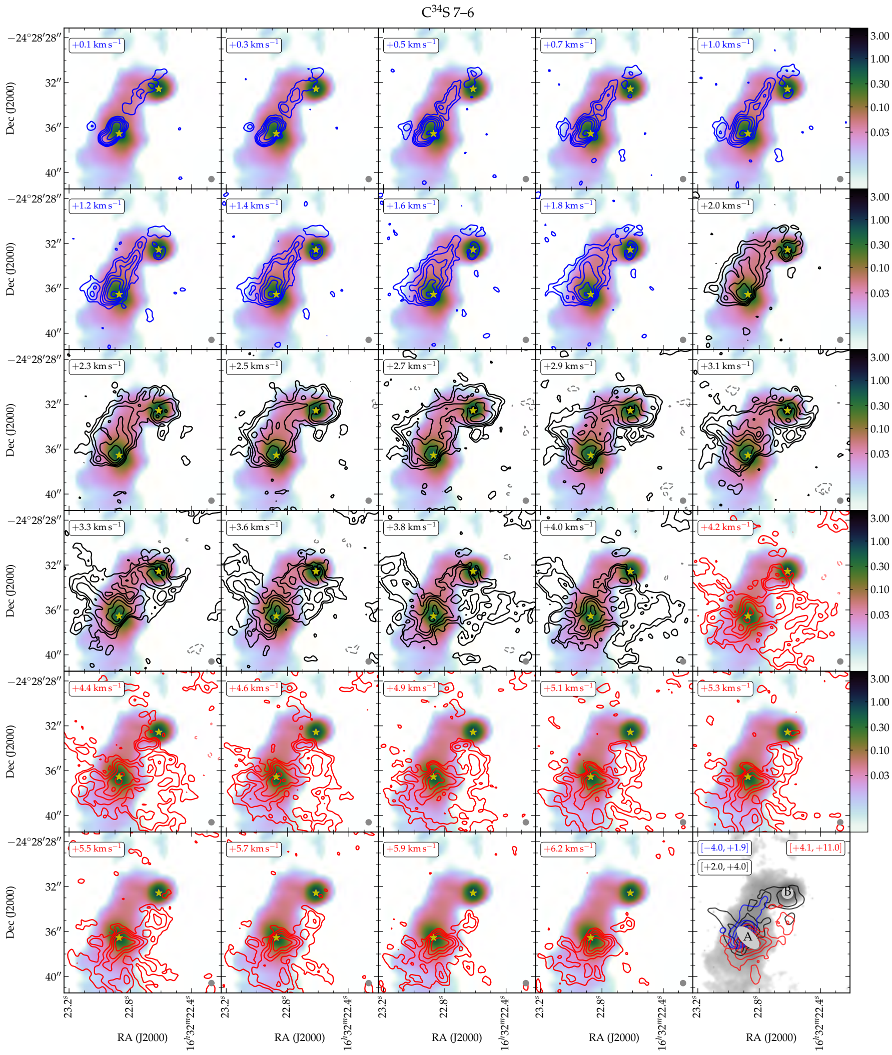

Figure 6.19: $C^{34}S$ channel maps. As Fig. 6.15. First positive (negative) contour level in individual channel maps: 0.03 (−0.06) Jy beam^{-1}; first contour levels in the bottom right integrated ranges panel: 0.2 Jy beam^{-1} km s^{-1}.

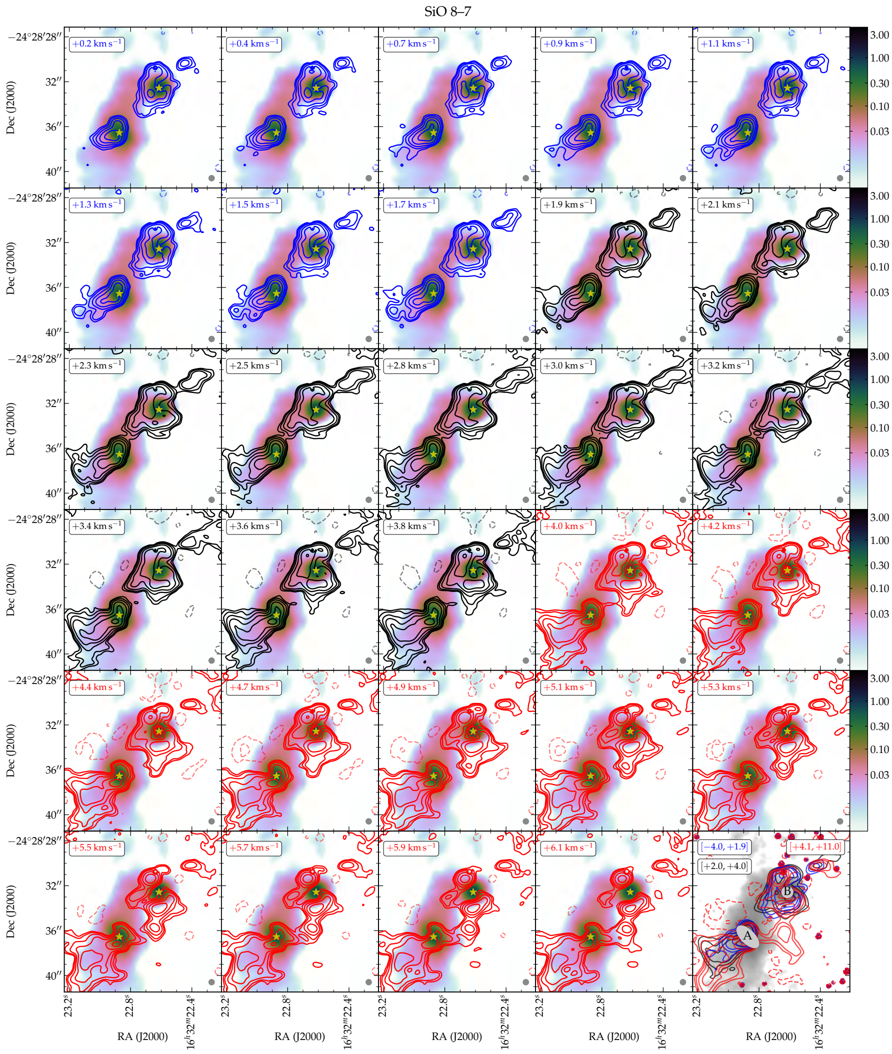

Figure 6.20: SiO (main isotopologue) 8–7 channel maps. As Fig. 6.15. First positive (negative) contour level in individual channel maps: 0.03 (−0.06) Jy beam^{-1}; first contour levels in the bottom right integrated ranges panel: 0.2 Jy beam^{-1} km s^{-1}.

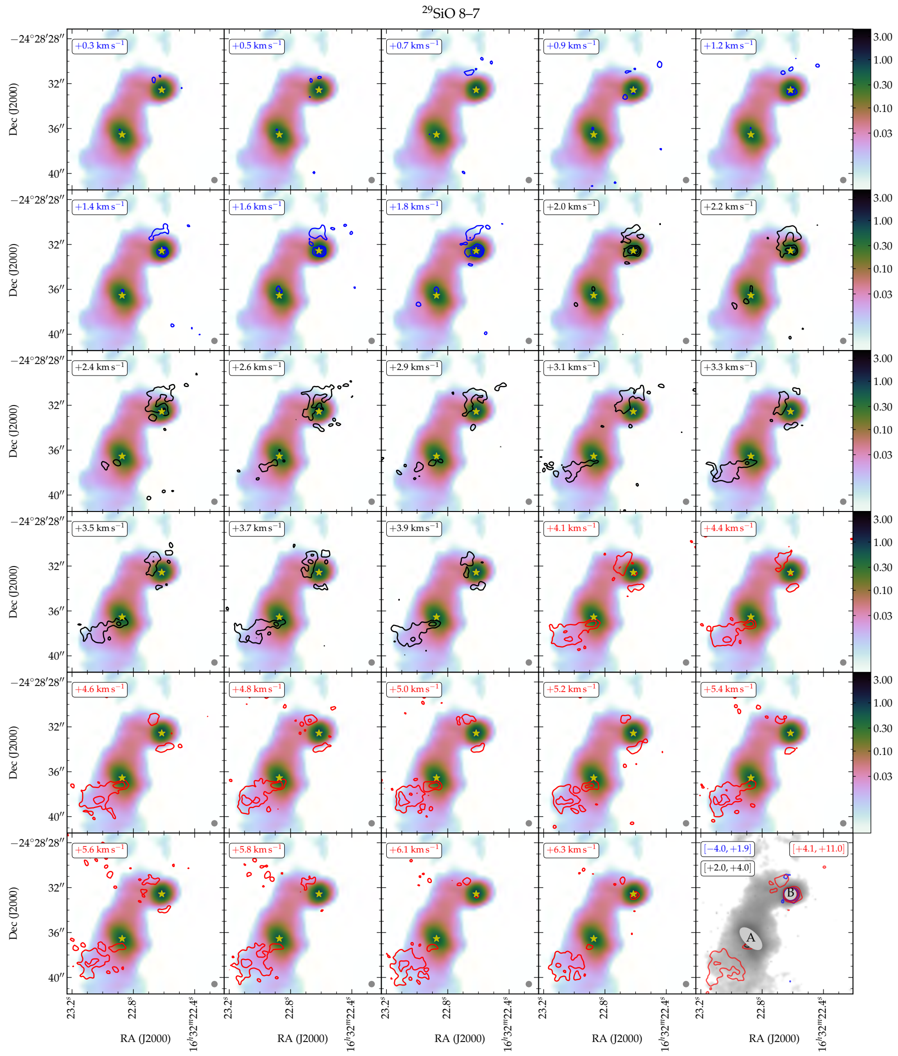

Figure 6.21: ^{29}SiO 8–7 channel maps. As Fig. 6.15. First positive (negative) contour level in individual channel maps: 0.02 (−0.04) Jy beam^{-1}; first contour levels in the bottom right integrated ranges panel: 0.07 Jy beam^{-1} km s^{-1}.

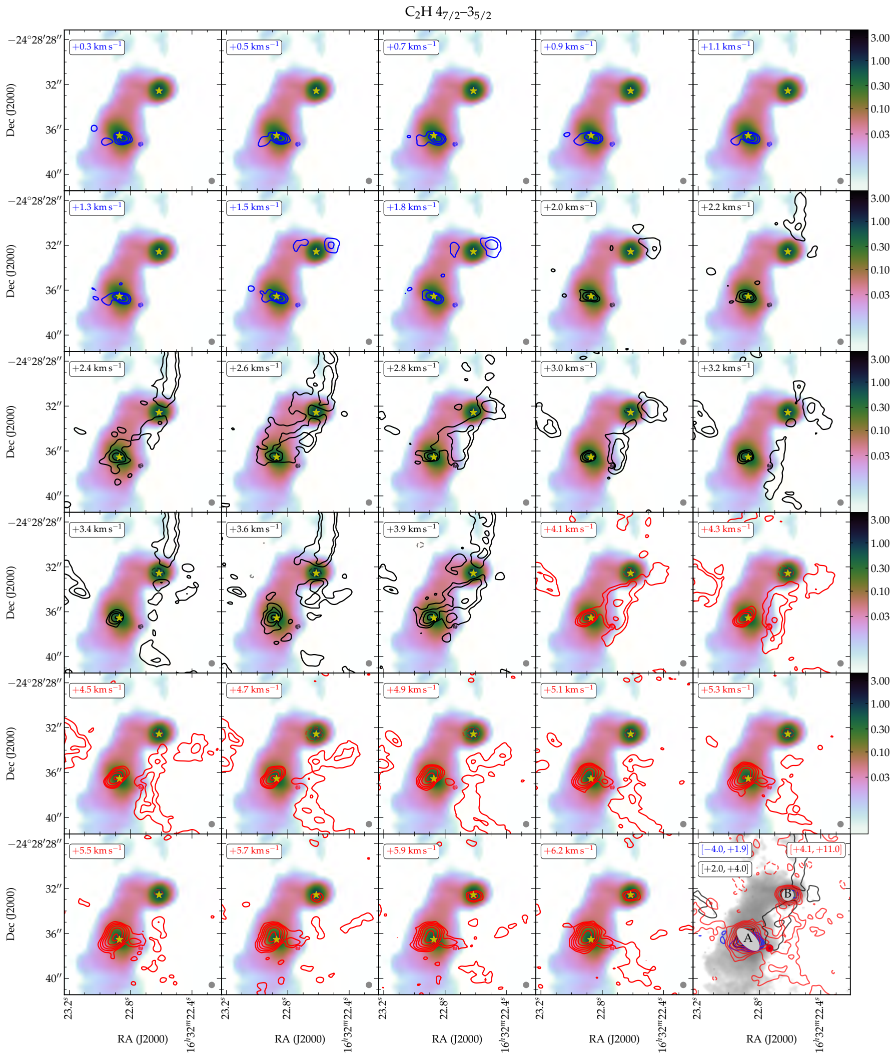

Figure 6.22: C_2H channel maps. As Fig. 6.15. First positive (negative) contour level in individual channel maps: 0.03 (−0.06) Jy beam^{-1}; first contour levels in the bottom right integrated ranges panel: 0.07 Jy beam^{-1} km s^{-1}. Note that emission in channels above +5 km s^{-1} is due to CH_3CN 19(3)–18(3) and not C_2H.

Adams, F. C., Lada, C. J., & Shu, F. H. 1987, ApJ, 312, 788

Adams, F. C., Ruden, S. P., & Shu, F. H. 1989, ApJ, 347, 959

Aikawa, Y., Umebayashi, T., Nakano, T., & Miyama, S. M. 1997, ApJ, 486, L51

Alexander, R. D., Clarke, C. J., & Pringle, J. E. 2006, MNRAS, 369, 229

Allen, A., Li, Z.-Y., & Shu, F. H. 2003, ApJ, 599, 363

ALMA Partnership, Brogan, C. L., Pérez, L. M., et al. 2015, ApJ, 808, L3

Alves, F. O., Vlemmings, W. H. T., Girart, J. M., & Torrelles, J. M. 2012, A&A, 542, A14

Alves, J., Lombardi, M., & Lada, C. J. 2007, A&A, 462, L17

Anderl, S., Maret, S., Cabrit, S., et al. 2016, A&A, 591, A3

Andre, P., Ward-Thompson, D., & Barsony, M. 1993, ApJ, 406, 122

Andrews, S. M., Wilner, D. J., Hughes, A. M., Qi, C., & Dullemond, C. P. 2009, ApJ, 700, 1502

Andrews, S. M., Wilner, D. J., Hughes, A. M., Qi, C., & Dullemond, C. P. 2010, ApJ, 723, 1241

Andrews, S. M., Wilner, D. J., Hughes, A. M., et al. 2012, ApJ, 744, 162

Andrews, S. M., Wilner, D. J., Zhu, Z., et al. 2016, ApJ, 820, L40

Artur de la Villarmois, E., Kristensen, L. E., Jørgensen, J. K., et al. 2018, ArXiv e-prints

Astropy Collaboration, Robitaille, T. P., Tollerud, E. J., et al. 2013a, A&A, 558, A33

Astropy Collaboration, Robitaille, T. P., Tollerud, E. J., et al. 2013b, A&A, 558, A33

Bally, J. & Lada, C. J. 1983, ApJ, 265, 824

Baryshev, A. M., Hesper, R., Mena, F. P., et al. 2015, A&A, 577, A129

Bisschop, S. E., Jørgensen, J. K., Bourke, T. L., Bottinelli, S., & van Dishoeck, E. F. 2008a, A&A, 488, 959

Bisschop, S. E., Jørgensen, J. K., Bourke, T. L., Bottinelli, S., & Van Dishoeck, E. F. 2008b, A&A, 488, 959

Bjorkman, J. E. & Wood, K. 2001, ApJ, 554, 615

Bohlin, R. C., Savage, B. D., & Drake, J. F. 1978, ApJ, 224, 132

Bonnell, I. A. & Bate, M. R. 1994, MNRAS, 269

Bontemps, S., Andre, P., Terebey, S., & Cabrit, S. 1996, A&A, 311, 858

Boogert, A. C. A., Gerakines, P. A., & Whittet, D. C. B. 2015, ARA&A, 53, 541

Bottinelli, S., Ceccarelli, C., Lefloch, B., et al. 2004a, ApJ, 615, 354

Bottinelli, S., Ceccarelli, C., Neri, R., et al. 2004b, ApJ, 617, L69

Brinch, C., Crapsi, A., Jørgensen, J. K., Hogerheijde, M. R., & Hill, T. 2007, A&A, 475, 915

Brinch, C. & Hogerheijde, M. R. 2010, A&A, 523, A25

Brinch, C., Jørgensen, J. K., Hogerheijde, M. R., Nelson, R. P., & Gressel, O. 2016, ApJ, 830, L16

Calcutt, H., Jørgensen, J. K., Müller, H. S. P., et al. submitted, A&A, (subm. Nov. 2017; in revision)

Caselli, P., Hartquist, T. W., & Havnes, O. 1997, A&A, 322, 296

Cassen, P. & Moosman, A. 1981, Icarus, 48, 353

Caux, E., Kahane, C., Castets, A., et al. 2011, A&A, 532, A23

Cazaux, S., Tielens, A. G. G. M., Ceccarelli, C., et al. 2003, ApJ, 593, L51

Cazzoli, G. & Puzzarini, C. 2005, Journal of Molecular Spectroscopy, 233, 280

Ceccarelli, C., Caselli, P., Fontani, F., et al. 2017, ApJ, 850, 176

Ceccarelli, C., Castets, A., Caux, E., et al. 2000, A&A, 355, 1129

Ceccarelli, C., Loinard, L., Castets, A., et al. 2001, A&A, 372, 998

Chandler, C. J., Brogan, C. L., Shirley, Y. L., & Loinard, L. 2005, ApJ, 632, 371

Chapman, N. L., Davidson, J. A., Goldsmith, P. F., et al. 2013, ApJ, 770, 151

Charnley, S. B., Tielens, A. G. G. M., & Millar, T. J. 1992, ApJ, 399, L71

Cheung, A. C., Rank, D. M., Townes, C. H., Thornton, D. D., & Welch, W. J. 1968, Physical Review Letters, 21, 1701

Chiang, H.-F., Looney, L. W., Tassis, K., Mundy, L. G., & Mouschovias, T. C. 2008, ApJ, 680, 474

Codella, C., Cabrit, S., Gueth, F., et al. 2014, A&A, 568, L5

Codella, C., Ceccarelli, C., Cabrit, S., et al. 2016, A&A, 586, L3

Cornet, R. A. & Winnewisser, G. 1980, Journal of Molecular Spectroscopy, 80, 438

Correia, J. C., Griffin, M., & Saraceno, P. 2004, A&A, 418, 607

Coutens, A., Jørgensen, J. K., Van der Wiel, M. H. D., et al. 2016, A&A, 590, L6

Coutens, A., Persson, M. V., Jørgensen, J. K., Wampfler, S. F., & Lykke, J. M. 2015, A&A, 576, A5

Coutens, A., Vastel, C., Caux, E., et al. 2012, A&A, 539, A132

Coutens, A., Viti, S., Rawlings, J. M. C., et al. 2018, MNRAS, 475, 2016

Crimier, N., Ceccarelli, C., Maret, S., et al. 2010a, A&A, 519, A65

Crimier, N., Ceccarelli, C., Maret, S., et al. 2010b, A&A, 519, A65

Cuadrado, S., Goicoechea, J. R., Pilleri, P., et al. 2015, A&A, 575, A82

Dame, T. M. & Thaddeus, P. 1985, ApJ, 297, 751

Dayou, F. & Balança, C. 2006, A&A, 459, 297

Dotson, J. L., Vaillancourt, J. E., Kirby, L., et al. 2010, ApJS, 186, 406

Drozdovskaya, M. N., Van Dishoeck, E. F., Jørgensen, J. K., et al. 2018, accepted by MNRAS (arXiv: 1802.02977)

Drozdovskaya, M. N., Walsh, C., Visser, R., Harsono, D., & van Dishoeck, E. F. 2015, MNRAS, 451, 3836

Duchêne, G., Bouvier, J., Bontemps, S., André, P., & Motte, F. 2004, A&A, 427, 651

Dullemond, C. P., Juhasz, A., Pohl, A., et al. 2012, RADMC-3D: A multi-purpose radiative transfer tool, Astrophysics Source Code Library

Dumouchel, F., Faure, A., & Lique, F. 2010, MNRAS, 406, 2488

Dunham, M. M., Allen, L. E., Evans, II, N. J., et al. 2015, ApJS, 220, 11

Dunham, M. M., Evans, II, N. J., Terebey, S., Dullemond, C. P., & Young, C. H. 2010, ApJ, 710, 470

Dutrey, A., Di Folco, E., Beck, T., & Guilloteau, S. 2016, A&A Rev., 24, 5

Dutrey, A., di Folco, E., Guilloteau, S., et al. 2014, Nature, 514, 600

Dzib, S. A., Ortiz-León, G. N., Hernández-Gómez, A., et al. 2018, accepted by A&A (arXiv:1802.03234)

Endres, C. P., Schlemmer, S., Schilke, P., Stutzki, J., & Müller, H. S. P. 2016, J. Mol. Spectrosc., 327, 95

Enoch, M. L., Corder, S., Duchêne, G., et al. 2011, ApJS, 195, 21

Evans, II, N. J. 1999, ARA&A, 37, 311

Evans, II, N. J., Di Francesco, J., Lee, J.-E., et al. 2015, ApJ, 814, 22

Evans, II, N. J., Dunham, M. M., Jørgensen, J. K., et al. 2009, ApJS, 181, 321

Favre, C., Jørgensen, J. K., Field, D., et al. 2014, ApJ, 790, 55

Fayolle, E. C., Öberg, K. I., Jørgensen, J. K., et al. 2017, Nature Astronomy, 1, 703

Fernández-López, M., Zapata, L. A., & Gabbasov, R. 2017, ApJ, 845, 10

Flower, D. R., Pineau des Forets, G., Field, D., & May, P. W. 1996, MNRAS, 280, 447

Fraser, H. J., Collings, M. P., McCoustra, M. R. S., & Williams, D. A. 2001, MNRAS, 327, 1165

Fuller, G. A., Lada, E. A., Masson, C. R., & Myers, P. C. 1995, ApJ, 453, 754

Garcia, P. J. V. 2011, Physical Processes in Circumstellar Disks around Young Stars

Garrod, R. T., Belloche, A., Müller, H. S. P., & Menten, K. M. 2017, A&A, 601, A48

Genzel, R. & Stutzki, J. 1989, ARA&A, 27, 41

Gerin, M., Kaźmierczak, M., Jastrzebska, M., et al. 2011, A&A, 525, A116

Girart, J. M., Estalella, R., Palau, A., Torrelles, J. M., & Rao, R. 2014, ApJ, 780, L11

Goodman, A. A., Benson, P. J., Fuller, G. A., & Myers, P. C. 1993, ApJ, 406, 528

Gottlieb, C. A., Myers, P. C., & Thaddeus, P. 2003, ApJ, 588, 655

Guélin, M., Brouillet, N., Cernicharo, J., Combes, F., & Wootten, A. 2008, Ap&SS, 313, 45

Guzmán, V., Pety, J., Goicoechea, J. R., Gerin, M., & Roueff, E. 2011, A&A, 534, A49

Haisch, Jr., K. E., Lada, E. A., & Lada, C. J. 2001, ApJ, 553, L153

Harsono, D., Jørgensen, J. K., van Dishoeck, E. F., et al. 2014, A&A, 562, A77

Hartmann, L. 2009, Accretion Processes in Star Formation: Second Edition (Cambridge University Press)

Hatchell, J., Fuller, G. A., & Ladd, E. F. 1999, A&A, 344, 687

Helou, G. & Walker, D. W., eds. 1988, Infrared astronomical satellite (IRAS) catalogs and atlases. Volume 7: The small scale structure catalog, Vol. 7, 1–265

Herbst, E. & van Dishoeck, E. F. 2009, ARA&A, 47, 427

Högbom, J. A. 1974, A&AS, 15, 417

Hogerheijde, M. R., van Dishoeck, E. F., Blake, G. A., & van Langevelde, H. J. 1998, ApJ, 502, 315

Hollenbach, D. & Salpeter, E. E. 1970, J. Chem. Phys., 53, 79

Horn, A., Møllendal, H., Sekiguchi, O., et al. 2004, ApJ, 611, 605

Hunter, J. D. 2007, Computing In Science & Engineering, 9, 90

Imai, M., Sakai, N., Oya, Y., et al. 2016, ApJ, 830, L37

Inutsuka, S.-I. & Miyama, S. M. 1992, ApJ, 388, 392

Inutsuka, S.-i. & Miyama, S. M. 1997, ApJ, 480, 681

Isella, A., Guidi, G., Testi, L., et al. 2016, Physical Review Letters, 117, 251101

Jacobsen, S. K., Jørgensen, J. K., van der Wiel, M. H. D., et al. 2017, ArXiv e-prints

Jacobsen, S. K., Jørgensen, J. K., Van der Wiel, M. H. D., et al. 2018, accepted by A&A (arxiv: 1712.06984), [J2018]

Jeans, J. H. 1902, Philosophical Transactions of the Royal Society of London Series A, 199, 1

Jiménez-Serra, I., Caselli, P., Martín-Pintado, J., & Hartquist, T. W. 2008, A&A, 482, 549

Jørgensen, J. K. 2004, A&A, 424, 589

Jørgensen, J. K., Bourke, T. L., Myers, P. C., et al. 2007, ApJ, 659, 479

Jørgensen, J. K., Bourke, T. L., Myers, P. C., et al. 2005a, ApJ, 632, 973

Jørgensen, J. K., Bourke, T. L., Nguyen Luong, Q., & Takakuwa, S. 2011, A&A, 534, A100

Jørgensen, J. K., Favre, C., Bisschop, S. E., et al. 2012, ApJ, 757, L4

Jørgensen, J. K., Lahuis, F., Schöier, F. L., et al. 2005b, ApJ, 631, L77

Jørgensen, J. K., Schöier, F. L., & van Dishoeck, E. F. 2002, A&A, 389, 908

Jørgensen, J. K., Schöier, F. L., & van Dishoeck, E. F. 2004, A&A, 416, 603

Jørgensen, J. K., Schöier, F. L., & van Dishoeck, E. F. 2005c, A&A, 437, 501

Jørgensen, J. K., van der Wiel, M. H. D., Coutens, A., et al. 2016, A&A, 595, A117

Jørgensen, J. K., van Dishoeck, E. F., Visser, R., et al. 2009, A&A, 507, 861

Jørgensen, J. K., Visser, R., Williams, J. P., & Bergin, E. A. 2015, A&A, 579, A23

Kahane, C., Ceccarelli, C., Faure, A., & Caux, E. 2013, ApJ, 763, L38

Klapper, G., Lewen, F., Gendriesch, R., Belov, S., & Winnewisser, G. 2000, Journal of Molecular Spectroscopy, 201, 124

Klapper, G., Lewen, F., Gendriesch, R., Belov, S. P., & Winnewisser, G. 2001, Zeitschrift für Naturforschung A, 56

Klapper, G., Surin, L., Lewen, F., et al. 2003, ApJ, 582, 262

Knez, C., Boogert, A. C. A., Pontoppidan, K. M., et al. 2005, ApJ, 635, L145

Knude, J. & Hog, E. 1998, A&A, 338, 897

Kristensen, L. E., Klaassen, P. D., Mottram, J. C., Schmalzl, M., & Hogerheijde, M. R. 2013, A&A, 549, L6

Kuan, Y.-J., Huang, H.-C., Charnley, S. B., et al. 2004, ApJ, 616, L27

Lada, C. J. 1987, in IAU Symposium, Vol. 115, Star Forming Regions, ed. M. Peimbert & J. Jugaku, 1–17

Lada, C. J. & Wilking, B. A. 1984, ApJ, 287, 610

Ladd, E. F., Adams, F. C., Casey, S., et al. 1991, ApJ, 366, 203

Larson, R. B. 1969, MNRAS, 145, 271

Lee, C.-F., Hirano, N., Zhang, Q., et al. 2014, ApJ, 786, 114

Lee, C.-F., Ho, P. T. P., Li, Z.-Y., et al. 2017a, Nature Astronomy, 1, 0152

Lee, J.-E., Lee, S., Dunham, M. M., et al. 2017b, Nature Astronomy, 1, 0172

Lee, K. I., Dunham, M. M., Myers, P. C., et al. 2016, ApJ, 820, L2

Li, Z.-Y., Banerjee, R., Pudritz, R. E., et al. 2014, Protostars and Planets VI, 173

Ligterink, N. F. W., Coutens, A., Kofman, V., et al. 2017, MNRAS, 469, 2219

Lindberg, J. E., Jørgensen, J. K., Brinch, C., et al. 2014, A&A, 566, A74

Lique, F., Spielfiedel, A., & Cernicharo, J. 2006, A&A, 451, 1125

Loinard, L., Chandler, C. J., Rodríguez, L. F., et al. 2007, ApJ, 670, 1353

Loinard, L., Torres, R. M., Mioduszewski, A. J., & Rodríguez, L. F. 2008, ApJ, 675, L29

Loinard, L., Zapata, L. A., Rodríguez, L. F., et al. 2013, MNRAS, 430, L10

Lombardi, M., Lada, C. J., & Alves, J. 2008, A&A, 480, 785

Looney, L. W., Mundy, L. G., & Welch, W. J. 2000, ApJ, 529, 477

Lykke, J. M., Coutens, A., Jørgensen, J. K., et al. 2017, A&A, 597, A53

Makiwa, G. 2014, PhD thesis, University of Lethbridge (Canada)

Maret, S., Ceccarelli, C., Caux, E., et al. 2004, A&A, 416, 577

Maury, A. J., Belloche, A., André, P., et al. 2014, A&A, 563, L2

McKee, C. F. & Ostriker, E. C. 2007, ARA&A, 45, 565

McMullin, J. P., Waters, B., Schiebel, D., Young, W., & Golap, K. 2007, in Astronomical Society of the Pacific Conference Series, Vol. 376, Astronomical Data Analysis Software and Systems XVI, ed. R. A. Shaw, F. Hill, & D. J. Bell, 127

Menten, K. M., Serabyn, E., Guesten, R., & Wilson, T. L. 1987, A&A, 177, L57

Mizuno, A., Fukui, Y., Iwata, T., Nozawa, S., & Takano, T. 1990, ApJ, 356, 184

Moriarty-Schieven, G. H. & Snell, R. L. 1988, ApJ, 332, 364

Müller, H. S. P., Belloche, A., Xu, L.-H., et al. 2016, A&A, 587, A92

Müller, H. S. P., Schlöder, F., Stutzki, J., & Winnewisser, G. 2005, Journal of Molecular Structure, 742, 215

Müller, H. S. P., Spezzano, S., Bizzocchi, L., et al. 2013, Journal of Physical Chemistry A, 117

Mundy, L. G., Wootten, A., Wilking, B. A., Blake, G. A., & Sargent, A. I. 1992, ApJ, 385, 306

Murillo, N. M., Lai, S.-P., Bruderer, S., Harsono, D., & van Dishoeck, E. F. 2013, A&A, 560, A103

Murillo, N. M., Van Dishoeck, E. F., Van der Wiel, M. H. D., et al. submitted, A&A, (subm. Aug. 2017; in revision)

Nan, R., Li, D., Jin, C., et al. 2011, International Journal of Modern Physics D, 20, 989

Nelson, A. F. & Marzari, F. 2016, ApJ, 827, 93

Noble, J. A., Theule, P., Borget, F., et al. 2013, MNRAS, 428, 3262

Öberg, K. I., Bottinelli, S., Jørgensen, J. K., & van Dishoeck, E. F. 2010, ApJ, 716, 825

Öberg, K. I., Garrod, R. T., van Dishoeck, E. F., & Linnartz, H. 2009, A&A, 504, 891

Offner, S. S. R., Kratter, K. M., Matzner, C. D., Krumholz, M. R., & Klein, R. I. 2010, ApJ, 725, 1485

Ohashi, N., Saigo, K., Aso, Y., et al. 2014, ApJ, 796, 131

Okuzumi, S., Tanaka, H., Kobayashi, H., & Wada, K. 2012, ApJ, 752, 106

Ortiz-León, G. N., Loinard, L., Kounkel, M. A., et al. 2017, ApJ, 834, 141

Ossenkopf, V. & Henning, T. 1994, A&A, 291, 943

Ostriker, J. 1964, ApJ, 140, 1056

Oya, Y., Moriwaki, K., Onishi, S., et al. 2018, ApJ, 854, 96

Oya, Y., Sakai, N., López-Sepulcre, A., et al. 2016, ApJ, 824, 88

Oya, Y., Sakai, N., Watanabe, Y., et al. 2017, ApJ, 837, 174

Padovani, M., Walmsley, C. M., Tafalla, M., Galli, D., & Müller, H. S. P. 2009, A&A, 505, 1199

Parker, N. D. 1988, MNRAS, 235, 139

Parker, N. D., Padman, R., & Scott, P. F. 1991, MNRAS, 252, 442

Pech, G., Loinard, L., Chandler, C. J., et al. 2010, ApJ, 712, 1403

Pineda, J. E., Maury, A. J., Fuller, G. A., et al. 2012, A&A, 544, L7

Pollack, J. B., Hubickyj, O., Bodenheimer, P., et al. 1996, Icarus, 124, 62

Ricci, L., Testi, L., Natta, A., et al. 2010, A&A, 512, A15

Richer, J. S., Hills, R. E., & Padman, R. 1992, MNRAS, 254, 525

Robitaille, T. & Bressert, E. 2012, APLpy: Astronomical Plotting Library in Python, Astrophysics Source Code Library

Rodgers, S. D. & Charnley, S. B. 2003, ApJ, 585, 355

Rucinski, S. M. & Krautter, J. 1983, A&A, 121, 217

Safronov, V. S. 1969, Evoliutsiia doplanetnogo oblaka.

Saftly, W., Baes, M., & Camps, P. 2014, A&A, 561, A77

Sakai, N., Oya, Y., Sakai, T., et al. 2014a, ApJ, 791, L38

Sakai, N., Sakai, T., Hirota, T., et al. 2014b, Nature, 507, 78

Sakai, N., Sakai, T., Hirota, T., & Yamamoto, S. 2009, ApJ, 702, 1025

Sakai, N., Sakai, T., & Yamamoto, S. 2006, PASJ, 58, L15

Salama, F. 2008, in IAU Symposium, Vol. 251, Organic Matter in Space, ed. S. Kwok & S. Sanford, 357–366

Sandford, S. A. & Allamandola, L. J. 1993, ApJ, 417, 815

Schneider, J., Dedieu, C., Le Sidaner, P., Savalle, R., & Zolotukhin, I. 2011, A&A, 532, A79

Schöier, F. L., Jørgensen, J. K., van Dishoeck, E. F., & Blake, G. A. 2002, A&A, 390, 1001

Schöier, F. L., Jørgensen, J. K., van Dishoeck, E. F., & Blake, G. A. 2004, A&A, 418, 185

Schöier, F. L., van der Tak, F. F. S., van Dishoeck, E. F., & Black, J. H. 2005a, A&A, 432, 369

Schöier, F. L., Van der Tak, F. F. S., Van Dishoeck, E. F., & Black, J. H. 2005b, A&A, 432, 369

Shirley, Y. L., Evans, II, N. J., & Rawlings, J. M. C. 2002, ApJ, 575, 337

Shirley, Y. L., Evans, II, N. J., Rawlings, J. M. C., & Gregersen, E. M. 2000, ApJS, 131, 249

Shirley, Y. L., Huard, T. L., Pontoppidan, K. M., et al. 2011, ApJ, 728, 143

Shu, F. H. 1977, ApJ, 214, 488

Skrutskie, M. F., Cutri, R. M., Stiening, R., et al. 2006, AJ, 131, 1163

Spezzi, L., Alcalá, J. M., Covino, E., et al. 2008, ApJ, 680, 1295

Spielfiedel, A., Feautrier, N., Najar, F., et al. 2012, MNRAS, 421, 1891

Stahler, S. W. & Palla, F. 2005, The Formation of Stars, 865

Stark, R., Sandell, G., Beck, S. C., et al. 2004, ApJ, 608, 341

Strauss, M. A., Davis, M., Yahil, A., & Huchra, J. P. 1990, ApJ, 361, 49

Tabone, B., Cabrit, S., Bianchi, E., et al. 2017, A&A, 607, L6

Tafalla, M., Myers, P. C., Mardones, D., & Bachiller, R. 2000, A&A, 359, 967

Takakuwa, S., Ohashi, N., Bourke, T. L., et al. 2007, ApJ, 662, 431

Taquet, V., López-Sepulcre, A., Ceccarelli, C., et al. 2015, ApJ, 804, 81

Terebey, S., Shu, F. H., & Cassen, P. 1984, ApJ, 286, 529

Tobin, J. J., Hartmann, L., Chiang, H.-F., et al. 2012, Nature, 492, 83

Tobin, J. J., Hartmann, L., Chiang, H.-F., et al. 2013, ApJ, 771, 48

Tobin, J. J., Kratter, K. M., Persson, M. V., et al. 2016a, Nature, 538, 483

Tobin, J. J., Looney, L. W., Li, Z.-Y., et al. 2016b, ApJ, 818, 73

Tóth, L. V., Marton, G., Zahorecz, S., et al. 2014, PASJ, 66, 17

van Cittert, P. H. 1934, Physica, 1, 201

Van der Tak, F. F. S., Black, J. H., Schöier, F. L., Jansen, D. J., & Van Dishoeck, E. F. 2007, A&A, 468, 627

van der Tak, F. F. S., van Dishoeck, E. F., Evans, II, N. J., Bakker, E. J., & Blake, G. A. 1999, ApJ, 522, 991

Van der Wiel, M. H. D., Van der Tak, F. F. S., Ossenkopf, V., et al. 2009, A&A, 498, 161

van Dishoeck, E. F. 2006, Proceedings of the National Academy of Science, 103, 12249

van Dishoeck, E. F., Blake, G. A., Jansen, D. J., & Groesbeck, T. D. 1995, ApJ, 447, 760

Visser, R., van Dishoeck, E. F., & Black, J. H. 2009, A&A, 503, 323

Wahhaj, Z., Cieza, L., Koerner, D. W., et al. 2010, ApJ, 724, 835

Watanabe, N. & Kouchi, A. 2002, ApJ, 571, L173

Weingartner, J. C. & Draine, B. T. 2001, ApJ, 548, 296

Wiesenfeld, L. & Faure, A. 2013, MNRAS, 432, 2573

Wilson, T. L. & Rood, R. 1994, ARA&A, 32, 191

Winnewisser, G., Belov, S. P., Klaus, T., & Schieder, R. 1997, Journal of Molecular Spectroscopy, 184, 468

Wolf, S., Schegerer, A., Beuther, H., Padgett, D. L., & Stapelfeldt, K. R. 2008, ApJ, 674, L101

Wootten, A. 1989, ApJ, 337, 858

Xiang, D. & Turner, B. E. 1995, ApJS, 99, 121

Yamamura, I., Makiuti, S., Ikeda, N., et al. 2010, VizieR Online Data Catalog, 2298

Yang, B., Stancil, P. C., Balakrishnan, N., & Forrey, R. C. 2010, ApJ, 718, 1062

Yang, Y.-L., Evans, II, N. J., Green, J. D., Dunham, M. M., & Jørgensen, J. K. 2017, ApJ, 835, 259

Yeh, S. C. C., Hirano, N., Bourke, T. L., et al. 2008, ApJ, 675, 454

Yen, H.-W., Takakuwa, S., Koch, P. M., et al. 2015, ApJ, 812, 129

Zapata, L. A., Loinard, L., Rodríguez, L. F., et al. 2013, ApJ, 764, L14

Zernike, F. 1938, Physica, 5, 785

Zhou, S. 1995, ApJ, 442, 685